VAAL UNIVERSITY
OF TECHNOLOGY

Inspiring thought. Shaping talent.

PRODUCTION OF ADSORPTIVE MATERIAL FROM MODIFIED NANOCRYSTALS CELLULOSE FOR INDUSTRIAL APPLICATION

This thesis is submitted in fulfilment of the requirements for the degree Doctor of philosophy: Chemical engineering

Vaal University of Technology, Main Campus

Private Bag X021, Vanderbijlpark 1900, South Africa

Name of student: BANZA MUSAMBA JEAN CLAUDE

Student number: 208067310

Supervisor/Promoter: PROF. H.L. RUTTO

Vaal university of technology

Co-Supervisor/Promoter: PROF. T. SEODIGENG

Vaal university of technology

May 2022

DECLARATION BY CANDIDATE

I hereby declare that the thesis submitted for the degree Doctor of Philosophy: Chemical Engineering, at the Vaal University of Technology, is my own original work and has not previously been submitted to any other institution of higher education. I further declare that all sources cited or quoted are indicated and acknowledged by means of a comprehensive list of references" I understand that my thesis may be made electronically available to the public.

ACKNOWLEDGEMENT

I would like to thank God for His guidance, protection, and strength throughout this process "The hand of the LORD was on me, and he brought me out by the Spirit of the LORD and set me in the middle of a valley; it was full of bones…" (EZEKIEL 37:1-14).

First and foremost, I would like to register my heartfelt gratitude and sincere appreciation to my thesis promoter: Professor Hilary LIMO RUTTO, for his patience, time, support, and guidance throughout my doctoral studies. His observations, advice and immense knowledge helped me to establish the overall direction of the research and to move forward with investigation in depth. Without his contribution, this endeavor would not have been accomplished. I extend my deepest gratitude to my co-promoter professor TUMISANG SEODIGENG for his exceptional research philosophy and high standard of excellence that he has instilled in me.

I am thankful to the Department of Chemical and Metallurgical Engineering at the Vaal University of Technology for providing equipment and other laboratory services essential for completion of the test work and all the staff members of Chemical and Metallurgical engineering who directly or indirectly helped me during my research work. I gratefully acknowledge the funding received towards my PhD from the paper association manufacturers of south Africa (PAMSA) and Department of science and innovation (DSI). Very special thanks go to Julie BORLAND (PAMSA research unit) and Samantha CHOLES (PAMSA communication specialist) for organizing the young engineer webinar series which gave me the platform to present my research work.

My respectful thanks to Dr. Ephraim IGBERASE, Katlego MPHAHLELE, Dr. Robert TEWO and Dr. Lawrence KOECH for their time, critical comments and suggestions which have helped to improve this work. I would also like to convey my sincere gratitude to all people who have directly or indirectly helped me in completing this academic work. Many thanks to my fellow postgraduate colleagues: Pascal MWENGE, Cedric MUSAVULI, Boitumelo MATSHEDISO, Nathan FUNDJI, Lucky MALISE, Given SEOWA, Robert SOMEO, Robert MBEDZI, Salvation MUTHUBI and Chris ITUMELENG for their scientific help and fruitful discussions.

My deepest thanks go to my family George MWENGE, Marthe MARUV, Mwenge SANKY, Sanky NKULU, Mireille BONDO, Huguette YUMBA, Daniel BANZA, Olivier LUNDA, Dida MWENGE, Harcel NUMBI, Espace MUKAZ, Merveille MALOBA for their support

throughout my life. I dedicate my thesis to my parents for their unconditional love and belief in me, this thesis is simply impossible without them. Thank you, I love you so very much! Last, but not least, I am truly grateful to God for all the blessings that have come to my family!

I am thankful to my church Mission of Eternal Salvation and pastor Michel for prayers and spiritual support During my studies.

CONTRIBUTION OF AUTHORS

All the manuscripts presented in this thesis were entirely written by Jean Claude BANZA MUSAMBA and were co-authored with Professor Hilary LIMO RUTTO and professor TUMISANG SEODIGENG (Clean Technology and Applied Materials Research Group, Department of Chemical and Metallurgical Engineering, Vaal University of Technology) All of the research presented in this thesis from chapter 3 - 8 was planned, executed and analyzed by Jean Claude BANZA MUSAMBA, with guidance from Professor Hilary LIMO RUTTO and Professor TUMISANG SEODIGENG.

PREFACE

Chapter 1 presents an introduction on the source of cellulose and cellulose nanocrystals extraction, the significance and problem statement and the main and specifics objective of the study.

Chapter 2 describes the literature survey for cellulose, extraction of cellulose nanofibers and cellulose nanocrystals, properties of cellulose nanocrystals and fields of application of cellulose nanocrystals. Different techniques for modification of cellulose nanocrystals for heavy metals ion removal were explained. Factors affecting adsorption of heavy metal ions onto cellulose nanocrystals, kinetics, isotherms , modeling of packed bed column , errors analysis functions, and quantum mechanism simulation were study in details.

Chapter 3 explores the potential extraction of cellulose nanocrystals from millet husk waste. Three main parameters homogenization speed, acid concentration, and acid to cellulose ratio were evaluated. The yield and swelling capacity were investigated and optimized using the Box Behnken design (BBD) method in response surface methodology.

Chapter 4 presents the selective removal of Chromium (VI) using modified cellulose nanocrystals with succinic anhydride and Ethylenediaminetetraacetic acid. The possible isotherms, kinetics, and thermodynamics properties were explored. The recycled studies on the modified cellulose nanocrystals were performed.

Chapter 5 looks at the possibility of modelling the adsorption of Cadmium (VI) onto cellulose nanocrystals modified with chitosan powder. Artificial neural network (ANN) and response surface methodology (RSM) modelling approaches were used to optimize the process. Quantum chemical performance was determined using the binding energy gaps HOMO-LUMO.

Chapter 6 presents the effectiveness of removing Nickel (II) from an aqueous solution using an adsorption method in a laboratory size reactor. An artificial neural network (ANN) and an adaptive neuro-fuzzy inference system (ANFIS) were used in this study to predict blend hydrogels adsorption potential in the removal of nickel (II) from aqueous solution.

Chapter 7 compares the effectiveness of artificial neural network (ANN) and an adaptive neuro-fuzzy inference system (ANFIS) and response surface methodology (RSM)

modelling approaches for predicting the removal efficiency of Chromium (VI) from wastewater using modified nanocellulose.

Chapter 8 describes a novel cellulosic hydrogel nanocomposite material for the absorption of Cu^{2+}, Ni^{2+}, Zn^{2+}, and Cd^{2+} ions from an aqueous solution in a packed bed adsorption column. The influence of breakthrough factors such as bed height, influent concentration and the feed flow rate was assessed. Bed Depth Service Time, Thomas, and Yoon-Nelson models were studied.

Chapter 9 gives a summary of the study and provides all the key findings. As the concluding chapter, it highlights all the recommendations on the future research studies.

LIST OF RELATED PUBLICATIONS: CONFERENCES PROCEEDINGS AND JOURNAL ARTICLES

1. Banza, M., Rutto, H. 2021. Fabrication of biodegradable cellulose nanocomposite hydrogel for heavy metal ions removal: characterization, adsorption behavior, and kinetic study. **Proceedings of SEEP2021, 13-16 September 2021, BOKU, Vienna, Austria**

2. Banza, M., Rutto, H. 2021. Selective removal of lead (II) from wastewaterusing modified cellulose nanocrystals with EDTA: isotherm and kinetics. **Proceedings of SBP2021, 13-15 December 2021, CAPTOWN, South Africa.**

3. Banza, M., Rutto, H. 2021. Extraction of cellulose nanocrystals from millet (Eleusine coracana) husk waste: optimization using Box Behnken design in response surface methodology (RSM) . **International journal of nano letters (Published).**

4. Banza, M., Rutto, H. 2021 selective removal of Cr(VI) from hydrometallurgical effluent using modified cellulose nanocrystals (CNCs) with succinic anhydride and (EDTA) ethylenediaminetetraacetic acid: isotherm, kinetics, and thermodynamic studies. **Canadian journal of chemical engineering (Published).**

5. Banza, M., Rutto, H. 2021. Modeling of adsorption of cd $^{2+}$ on cellulose-chitosan nanocomposites using response surface methodology (RSM) and artificial neural network (ANN) techniques: isotherm, kinetics, and quantum chemical performance. **Journal of Environmental science and health, part A (Under review).**

6. Banza, M., Rutto, H. 2022. modeling of adsorption of nickel (II) by blend hydrogels (cellulose nanocrystals and corn starch) from aqueous solution using adaptive neuro-fuzzy inference systems (ANFIS) and artificial neural networks (ANN).**Canadian journal of chemical engineering (Accepted for Publication).**

7. Banza, M., Rutto, H. 2021. continuous fixed-bed column study and adsorption modelling removal of Ni^{2+}, Cu^{2+}, Zn^{2+} and Cd^{2+} ions from synthetic acid mine drainage by nanocomposite cellulose hydrogel. **Journal of Environmental science and health, part B (Published).**

8. Banza, M., Rutto, H. Seodigeng, T. 2022. Comparison study of ANFIS, ANN, and RSM and Mechanistic modeling for chromium (VI) removal using modified cellulose nanocrystals-sodium alginate. **Arabian journal for science and engineering(under review).**

ABSTRACT

Water is the essence of life, yet it is progressively polluted by dyes, heavy metal ions, food additives, medicines, detergents, agrochemicals, and other toxins from industrial, municipal, and agricultural sources. Among the different wastewater treatment technologies, adsorption is a technique that, when used in conjunction with a well-designed system, produces high-quality treated water at a reasonable cost. For water treatment, activated carbon is the most often employed adsorbent. Its manufacture, on the other hand, is energy demanding, costly, and creates greenhouse emissions. As a result, finding low-cost alternative adsorbents from industrial and agricultural waste and biomass has attracted a lot of interest. In this context, developing sustainable platforms for wastewater treatment using sustainable nanomaterials such as cellulose nanocrystals (CNCs) is a unique technique with a low carbon footprint. CNCs, which are made by hydrolyzing pulp fibers in sulfuric acid, are rod-like nanomaterials with a lot of remarkable qualities including high specific surface area, high specific strength, hydrophilicity, biodegradability, and surface functionalization.

These characteristics, as well as their accessibility, make them suitable candidates for water treatment applications. However, because of their great colloidal stability and nano-dimensions, extracting these CNCs after usage in water treatment is difficult. To overcome this problem, including these CNCs into nanocomposite systems that can be readily separated after usage in batch and continuous water treatment processes is a great concept. Furthermore, pure CNCs have low selectivity towards a wide range of water pollutants, necessitating surface functionalization to provide this selectivity. As a result, this thesis investigates the extraction of CNCs from millet husk waste and waste papers, the development of CNC-incorporated nanocomposites and evaluation of their adsorption characteristics using batch and fixed bed column adsorption studies, and (ii) the evaluation of the selective adsorption characteristics of surface functionalized CNCs and their ability to tailor the nanocomposites' characteristics for use in water treatment applications. The response surface methodology, artificial neural network, and adaptive neuro-fuzzy inference systems were also applied to model the removal of heavy metal ions.

The first part of the research (cellulose nanocrystals extraction and optimization)

The cellulose nanocrystals were extracted from millet husk residue waste using a homogenized acid hydrolysis method. The effects of the process variables homogenization speed (A), acid concentration (B), and acid to cellulose ratio (C) on the yield and swelling capacity were investigated and optimized using the Box Behnken design (BBD) method in response surface methodology. The numerical optimization analysis results showed that the maximum yield of CNCs and swelling capacity from cellulose was 93.12 % and 2.81 % obtained at homogenization speed, acid concentration, and acid to cellulose ratio of 7464.0 rpm, 63.40 wt %, and 18.83 wt %, respectively. ANOVA revealed that the most influential parameter in the model was homogenization speed for Yield and acid concentration for swelling capacity. The TGA revealed that cellulose had greater heat stability than CNCs. The functional groups of CNCs and cellulose were identical according to the FTIR data. When compared to cellulose, the SEM picture of CNCs is porous and shows narrow particle size with needle-like shape. The XRD pattern revealed an increase in CNC intensity.

The second part of the research (CNCs modification for selective removal)

A novel type of recyclable adsorbents with outstanding adsorption capability was produced using CNCs with succinic anhydride and EDTA. and their adsorption properties were studied in detail utilizing batch adsorption experiments of Chromium (VI) in aqueous solution. The effects of several factors on Cr (VI) adsorption were examined, including contact duration, adsorbent dose, starting concentration, pH, and temperature. The cellulose nanocrystals treated with succinic anhydride and EDTA possessed a needle-like form, high porosity, and a narrow particle size distribution. The carboxylate transition of the carboxyl group of cellulose was verified by FTIR. XRD analysis of particles after modification revealed the presence of additional phases, which were attributed to succinic anhydride and EDTA modification. A spontaneous exothermic adsorption process was validated by the observed thermodynamic characteristics. The best model for describing adsorption kinetics and mechanism was a pseudo-second order kinetic and intra-particle diffusion model. The Langmuir adsorption isotherm was seen in equilibrium adsorption data, with a maximum adsorption capacity (q_{max}) of 387.25± 0.88 mgL^{-1}. We showed that the removal effectiveness of Cr (VI) maintained at 220± 0.78 $mg.g^{-1}$

after 6 adsorption-desorption cycles, and that the CNC-ALG hydrogel beads are excellent adsorbents for the selective removal of Cr (VI) from wastewaters.

The third part of the research (modeling of removal of heavy metal ions using RSM, ANN and quantum mechanism studies)

The effects of contact time , pH, nanoparticle dose, and beginning Cd2+ concentration on Cd2+ removal were examined using the central composite design (CCD) technique. The performance and prediction capabilities of Response Surface Methodology (RSM) and Artificial Neural Network (ANN) modelling methodologies were explored, as well as their performance and prediction capacities of the response (adsorption capacity). The process was also described using the adsorption isotherm and kinetic models. Statistical data, on the other hand, revealed that the RSM-CCD model beat the ANN model technique. The optimum conditions were determined to be a pH of 5.73, a contact time of 310 minutes, an initial Cd^{2+} concentration of 323.04 mg/L, a sorbent dosage of 16.36 mg, and an adsorption capacity of 440.01 mg/g. The spontaneous adsorption process was well characterized by the Langmuir model, and chemisorption was the dominant regulator. The binding energy gaps HOMO-LUMO were used to find the preferred adsorption sites.

The fourth part of research (optimization of removal using ANN and ANFIS)

An artificial neural network and an adaptive neuro-fuzzy inference system were utilized to predict the adsorption capability of mix hydrogels in the removal of nickel (II) from aqueous solution. Four operational variables were evaluated in the ANFIS model to determine their influence on the adsorption study, including starting Ni (II) concentration (mg/L), pH, contact time (min), and adsorbent dosage (mg/L) as inputs and removal percentage (percent) as the single output. In contrast, 70% of the data was employed to develop the ANN model, while 15% of the data was used in testing and validation. To train the network, feedforward propagation with the Levenberg-Marquardt algorithm was used. To optimise, design, and develop prediction models for Ni (II) adsorption using blend hydrogels, (ANN) and (ANFIS) models were employed for trials. The results demonstrate that the ANN and ANFIS models are viable prediction techniques for metal ion adsorption.

The fourth part of research (mechanistic modeling and optimization of removal using ANN, RSM and ANFIS)

An artificial neural network, response surface methodology and an adaptive neuro-fuzzy inference system were utilized to predict the adsorption capability of modified cellulose nanocrystals and sodium alginate for the removal of Cr (VI) from aqueous solution. Four variables such as time, pH, concentration, and adsorbent dose were evaluated to determine their influence on the adsorption study. To examine the viability of the models, five statistical functions (RMSE, ARE, SSE, MSE, and MPSD) were applied. absorption mechanism was described via four mechanistic models (Film diffusion, Weber and Morris, Bangham, and Dummwald-Wagner models. Further statistical indices supported ANFIS as the best prediction model for adsorption compared to ANN and RSM. Film diffusion was identified as the rate-limiting process via mechanistic modelling.

The sixth part of research (continuous fixed-bed column study)

The hydrogel's technical feasibility for adsorption of Cu2+, Ni2+, +Cd2+, and Zn2+ ions from the packed bed column's produced AMD was assessed. The hydrogel was considered to have a high potential for significant interactions with dangerous metal ions. This characteristic, together with the adsorbent's availability, low cost, and efficient regeneration of the spent adsorbent, distinguishes it from the many other adsorbents described in the literature by other researchers. With a bed height of 25 cm, an influent metal ion concentration of 10 mg/l, and a flow velocity of 10 ml/min, the bed performed better. As a consequence, the breakthrough curve for the packed bed experiment shows that the breakthrough points were approached sooner by increasing the flow rate and influent concentration, and later by increasing the bed height. The experimental results were satisfactorily described by the BDST, Yoon–Nelson, and Thomas models. The hydrogels had a net-work structure and more homogeneous porosity, according to the SEM, TGA, XRD, and FTIR results for CNCs. The hydrogels revealed varied degrees of opacity and heavy metal ions absorption capacity depending on the temperature of the analysis. Diffraction confirmed the existence of crystalline structures and the presence of carboxyl and amide groups.

TABLE OF CONTENTS

LIST OF FIGURES

LIST OF TABLES

ABBREVIATION/ NOMENCLATURE

AAS: Atomic Absorption Spectroscopy

AMD: Acid mine drainage

ANFIS: adaptive neuro-fuzzy inference system

ANN: Artificial neural network

ANOVA: Analysis of variance

ARE: Average relative errors

AARE: Absolute average relative errors

APS: ammonium persulfate

BBD: Box Behnken Design

BDST: Bed Depth Service Time model

BET: Brunauer-Emmett-Teller

BP: Back-propagation

CCD: Central Composite Design

CNCs: Cellulose nanocrystals

D-R: Dubinin- Radushkevich isotherm

EDTA: Ethylenediaminetetraacetic acid

FTIR: Fourier Transform Infrared Spectroscopy

ICP: Inductively coupled plasma

IX : Ion exchange

MSE: Mean square errors

MPSD: Marquardt's percent standard deviation

OFAT: One factor at a time design

RMSE: Root means square errors

RSM: Response Surface Methodology

SEM: Scanning electron microscopy

TGA: Thermogravimetric analysis

SWC: Swelling capacity

XRD: X-ray diffraction

Symbols

Ce	Concentration of metal ions left in the solution at equilibrium (mg/L)
C_i	Initial concentration of metal ions (mg/L)
B	Temkin isotherm constant for equilibrium adsorption
D	Temkin isotherm constant associated with adsorption intensity
N	Empirical parameter related to the adsorption intensity of the adsorption process
B_L	Langmuir isotherm constant (L/mg)
B	Polanyi potential which is related to the equilibrium concentration
E	Mean energy of the adsorption process (kJ/mol)
q_e	Concentration of the metal ions adsorbed at equilibrium (mg/g)
q_m	Maximum adsorption capacity (mg/g)
q_s	Maximum adsorption capacity for D-R isotherm model (mg/g)
q_t	Concentration of the metal ions adsorbed at time t (mg/g)
K_0	Energy constant for D-R isotherm model (mol^2/kJ^2)
K_1	Pseudo-first order kinetic model rate constant (min^{-1})
K_2	Pseudo-first order kinetic model rate constant (g/mg.min)
K_F	Freundlich isotherm constant (L/mg)
K_i	Intraparticle diffusion rate constant ($g/mg/min^{0.5}$)
R	Gas constant 8.314 (kJ/mol.K)
T	Temperature (K)
ΔG	Gibbs free energy change (kJ/mol)
ΔH	Change in enthalpy (kJ/mol)
ΔS	Change in entropy (kJ/mol)
K_d	Distribution coefficient (mLg^{-1})
N	Number of measurements
P	Number of parameters in the model
$q_{e(pred)}$	Predicted concentration of the metal ions adsorbed at equilibrium (mg/g)

$\mathbf{q_{e(exp)}}$ Experimental concentration of the metal ions adsorbed at equilibrium (mg/g)

$\mathbf{Y_{(act)}}$ Experimental maximum percentage removal of metals ion (%)

$\mathbf{Y_{(pred)}}$ Predicted maximum percentage removal of metals ion (%)

$\mathbf{X^2}$ Chi-square test

mH amount of the hydrogel in the column (g)

$\mathbf{N_o}$ saturation concentration (mg/L)

$\mathbf{K_T}$ Thomas rate constant

qe adsorption capacity (mg/g)

Qv volumetric flow rate (mL/min)

Z bed depth of the column (cm)

Zm critical bed depth (cm)

Veff effluent volume (mL)

$\mathbf{K_Y}$ Yoon-Nelson rate constant (min^{-1})

T time needed for adsorbate breakthrough (min)

Te exhaustion time (min)

Tb breakthrough time (min)

CHAPTER ONE

1. INTRODUCTION

1.1 Background

With an increasing interest in nanotechnology and nanoscience, the synthesis and modification of nanomaterials with specific functionalities and clear structure has become one of the most challenging and versatile topics (Thomas, Latha and Thomas, 2018). Recent advances in nanotechnology have streamlined the development of functionalized nanoparticles, which are believed to revolutionize applications in the fields of energy production, electronics, biomaterials, and medicine. Nevertheless, a large proportion of the chemicals used to synthesize such nanomaterials are from petroleum resources and the processes involve the use of harmful reagents that can affect the environment (Meng *et al.*, 2019). Because of the interest in global warming and sustainable development, there is a need to replace conventional resources with materials derived from renewable resources or nature. Moreover, the ability to take an abundant and cheap material and generate products with value-added properties is desirable and worthy of exploration (Bruel *et al.*, 2019).

The source of cellulose can change from plants, such as cotton, bacteria species, and tunicates (Thomas, Latha and Thomas, 2018; Zhou *et al.*, 2019). The amount of cellulose extracted depends on the source 40% for wood and 90% for cotton. For synthetic polymers, Cellulose is produced via an enzymatic process. In all organisms which can produce cellulose, the synthesizing enzymes are grouped in final complexes. Theses complexes coordinate simultaneous crystallization and the extrusion of cellulose molecules. Micro crystallites are created in this way(Abu-danso *et al.*, 2017; Luzi *et al.*, 2019; Niamsap, Tien and Sukyai, 2019). This biogenesis gives a cellulose a perfect morphology and structure that does not exist in synthetic polymers.

From elementary cellulose fibers, cellulose nanocrystals (CNC) and cellulose nanofibers (CNF) can be extracted via acid hydrolysis or mechanical treatment. It very important to keep in mind that even if the starting materials to produce nanocellulose is the same, the cellulose nanocrystals (CNC) and cellulose nanofibers (CNF) should be considered as two completely different families of nanomaterials (different flexibility, crystallinity, and aspect ratio). Cellulose nanocrystal (CNC) derivate from the acid hydrolysis of cellulose-

based material has predominantly been used to reinforced composites and polymers because it has remarkable strength that equals carbon nanotubes.

Cellulose nanocrystal is the main structural building block of plant and can be extracted from bacterial cellulose, plant fibers, and wood. The hydrolysis of nanocrystalline regions of native cellulose results in cellulose nanocrystal rigid, rod-shaped crystalline cellulose with 6 to 20nm diameter and tens to hundreds of nm in length. The development of technologies for the application of cellulose nanocrystal has been pursued by various groups in USA, Europe, and Canada. As renewable and abundant nanomaterial, cellulose nanocrystal is carried to be used to manufacture and develop an extensive range of high-value products, such as (i) medical materials for pharmaceuticals, tooth repair and bone replacement; (ii) additives for cosmetics, paints, food, coatings, pigments; (iii) advance composite materials (high strength fibers and textiles, innovative bioplastic and smart packaging) ; (iv) structural components for papermaking, transportation, building and aerospace; (v) optical switchable materials.

In chemical processes, there is a need to remove fine solid contaminants less than 5 microns (μm), from process liquids. When the suspended solids content is dilute, less than 1% (wt.%), the removal process is called filtration or clarification to produce a clean product. Applications include polymer and resins, pharmaceutical ingredient, catalyst recovery, removal of unreacted chemicals and byproducts and water treatment.

Frequently in water treatment applications, the solids are amorphous or very fine which can be a severe issue during filtration. When filtered, the solids will make a thin coating over the filter media and will reduce the filtration rate to an unacceptable level. Pretreatment can be used to improve filtration properties and efficiently remove the solids from process liquids. Physical or chemical pretreatment such as flocculants can be used to change the nature of the suspended solids.

The use of nanomaterials for water and wastewater treatment has become an attractive research area in recent years. Nanomaterials are defined as materials smaller than 100 micrometers in dimension. Nanomaterials are characterized by different chemical, physical and biological properties compared to larger sizes. The efficiency of larger conventional adsorbent is normally limited by available sorption sites or surface area which results in lack of selectivity and slow adsorption kinetics. Nanocrystal cellulose

allows significant improvements with their high surface area associated with adsorption sites and short intraparticle diffusion resulting in fast kinetics. Several studies demonstrate that nanocrystal cellulose not only have higher adsorption capacities than activated carbon for heavy metal ions such Cu(II), Zn(II), Cd(II) but also faster adsorption kinetics due to the highly accessible adsorption sites and short intraparticle diffusion distance(Lu *et al.*, 2016; Basu *et al.*, 2019; Oyewo *et al.*, 2019).

The high specific area of Cellulose nanocrystal is required to provide many available active sites on the surface of the adsorbent to immobilize metal ions. The functional groups functioning as metal-binding sites on the biomass are responsible for the immobilization of heavy metal ions. The presence of hydroxyl groups on the surface of Cellulose nanocrystal allows a platform for surface modification. The surface modifications of Cellulose nanocrystal include oxidation, amidation, esterification, phosphorylation, sulfonation, etc. all the major metal-binding groups for adsorption can be introduced trough surface modification. Many physical and chemical properties of Cellulose nanocrystal

Cellulose nanocrystals could be modified using several techniques and chemicals (Oyewo *et al.*, 2019). Most of these techniques are expensive, and most of chemicals are toxic. Sodium nitrite as low cost and non-toxic chemical can be used. The first step is the deprotonation of Cellulose nanocrystals and formation of sodium salt with addition of sodium nitrite. The second step is to introduce the carbonyl group which open bond to yield anionic oxygen groups on the surface of modified Cellulose nanocrystals with addition of sodium bicarbonate(Oyewo *et al.*, 2019). Hexadecyltrimethylammonium Bromide (HDTMA) is available and inexpensive can be explored in the modification process of Cellulose nanocrystals to increase stability without affecting the crystalline structure and size dimension(Basu *et al.*, 2019).

Polyethyleneimine composite (PEI) can be used to modify the Cellulose nanocrystals via amidation (reaction between hydroxyl and carboxyl group from CNC and the amino group from PEI. The (CNC-PEI) contained carboxyl and hydroxyl group from CNC surface, as well as unreacted amino group from PEI. Amino groups have excellent adsorption capacities for Cr(VII) and Cr(IV)(Liu *et al.*, 2017).

Hydrogel adsorbent can be developed by mixing biodegradable polymers such as Chitosan found in exoskeletons of crustaceans, insects, and arthropods and gelatin from the skins of pigs, cows or demineralized animal bones to Cellulose nanocrystals to remove heavy metal ions Pb(II), Cr(III), Cd(II) and Hg(II)(Perumal *et al.*, 2019).

1.2 Significance and problem statement

Our planet has a sustainability issue. The problem was created by the overutilization of natural resources by the human with little knowledge on the long-term effects of these activities until the last few decades. Substitutes to the virgin materials that are being used so quickly need to be developed and brought to the market. Developing materials that can be easily regenerated as a source, sustainable and easy to manipulate is a challenge, nevertheless, requiring researchers to develop and modify the material in attempt to maintain performance.

A promising development is to extract cellulose from plant matter. Cellulose is a naturally occurring polymer with a building block in the cell walls of nearly all plants. Cellulose is biodegradable, natural, can be used itself or as additive, and can be synthesized into sugars to create fuel. Cellulose is also very strong, similar strength to steel. The material in its raw form is incredibly tiny (100 nm size), they were named cellulose nanocrystals (CNCs). The ability to extract cellulose in larger scale is a challenge, the issue lies in being able to extract the material safely and effectively and scale it up to sustainable production without harm to the planet. However, cellulose nanocomposites, especially those modified with gelatin, chitosan or starch, have not been subjected to intensive scientific studies. Nanocomposites comprising biopolymers like cellulose have the potential to replace conventional materials such as synthetic polymers.

The properties of nanocomposite materials depend not only on the properties of their components but also on morphological and interfacial characteristics arising from the combination of distinct materials. Incorporation of polymers like gelatin, chitosan or starch to cellulose nanocrystals to form nanocomposites can allow the exploitation of various formulations depending on envisaged functionalities. Critical studies of these nanocomposites will pave the way to a better understanding the different characteristics and applications of such materials.

Due to strict legislation on the discharge of harmful or toxic metal ions in water bodies, developing various technologies that will remove or reduce these pollutants to their allowable limits becomes crucial. Several traditional treatment processes have been used to remove heavy metals from AMD or wastewaters, such as chemical precipitation, membrane filtration, ion exchange, reverse osmosis and electrodialysis. These methods have proven to be quite expensive and labor intensive. Recent studies have shown adsorption to be the most promising method of heavy metal removal. However, materials with high binding capacity have been studied as adsorbents (activated carbon, chitosan, clinoptilolites, and resins) to remove heavy metal ions from AMD and wastewater. It has been found that modified cellulose nanocrystals increased metal ions adsorption; for this reason, modified cellulose nanocrystals will be examined to remove heavy metal ions from industrial wastewater.

1.3 Motivation of the research

The use of cellulose-based material is omnipresent in a broad number of industries, including food processing, pharmaceuticals, chemicals, municipal water treatment, waste treatment and mining. Adsorbent based cellulose is:

- **Economical**

The use of cellulose adsorptive material is up to 80% less when compared with mineral products. This reduced consumption and less sludge which is frequently associated with time consuming and expensive disposal. Reduce sludge contains less filtrate which results in less product loss due to disposal. The adsorbent is made of organic, can be compressed or made in briquette. Due to the structure of cellulose, compacted, stable materials are obtained which can be recycled.

- **High effective and reliable**

Due to the structure, the surface as well as the large pore volume, high flow rates are obtained with cellulose-based materials compared to mineral products. The adsorbent last longer due to the structure of fibers that react elastically to pressure. The damage spots in the material done by the use of the inner bonding make the cleaning process easier. Because the organic materials are nonabrasive and soft, equipment such as pumps and conveying elements are well-protected.

- **Environmentally -friendly disposal**

Cellulose materials are completely biodegradable, the uncontaminated adsorbent residue can be profitably recycled through use in composting, crop production and animal feed. The contaminated filter residues can be recycled thermally due the presence of organic as well as low ash content. Worthful materials such as catalyst filtration can be recovered through the incineration of organic filter aids which are previously removed using filtration process.

1.4 Research objectives

The aim of this study is to develop and optimize cellulose filter aids that allow economic and ecological filtration and to develop a cellulose-based adsorbent for water treatment.

Specific objectives are as follows:

i. To produce and characterize the Cellulose filter aids using analytical methods such as X-ray Diffraction (XRD), Scanning electron microscope (SEM), Transmission electron microscopy (TEM), Fourier transform infrared spectroscopy (FTIR), Brunauer-Emmett-Teller (BET), and Thermogravimetric analysis (TGA).
ii. To examine the physical attribute such as swelling capacity and nanocrystals yield on the CNCs extraction.
iii. To develop the cellulose-based adsorbent for selective removal of heavy metal ions.
iv. To study the adsorption kinetics, isotherms, thermodynamics, mechanistic and the chemical quantum mechanism on the removal of heavy metal ions using modified cellulose nanocrystals.
v. To optimize the removal of heavy metal ions using artificial neural network, adaptive neuro-fuzzy inference systems and response surface methodology.
vi. To design and set up a bench unit with high reproducibility and repeatability for the continuous adsorption process using cellulose nanocrystals.

1.5 References

Abu-danso, E., Srivastava, V., Sillanpää, M., & Bhatnagar, A. 2017. International Journal of Biological Macromolecules Pretreatment assisted synthesis and characterization of cellulose nanocrystals and cellulose nanofibers from absorbent cotton. *Int. J. Biol. Macromol.* 102:248–257.

Basu, H., Saha, S., Mahadevan, I.A., & Pimple, M.V. 2019. Journal of Water Process Engineering Humic acid coated cellulose derived from rice husk : A novel biosorbent for the removal of Ni and Cr. *J. Water Process Eng.* 32100892.

Bruel, C., Tavares, J.R., Carreau, P.J., & Heuzey, M. 2019. The structural amphiphilicity of cellulose nanocrystals characterized from their cohesion parameters. *Carbohydr. Polym. Elsevier*. 205:184–191.

Du, H., Liu, W., Zhang, M., Si, C., Zhang, X., & Li, B. 2019. Cellulose nanocrystals and cellulose nano fi brils based hydrogels for biomedical applications. *Carbohydr. Polym.* 209:130–144.

Hemmati, F., Mahdi, S., Kashaninejad, M., & Barani, M. 2018. International Journal of Biological Macromolecules Synthesis and characterization of cellulose nanocrystals derived from walnut shell agricultural residues. *Int. J. Biol. Macromol.* 120:1216–1224.

Hivechi, A., Bahrami, S.H., & Siegel, R.A. 2019. International Journal of Biological Macromolecules Investigation of morphological , mechanical and biological properties of cellulose nanocrystal reinforced electrospun gelatin nano fi bers. *Int. J. Biol. Macromol.* 124:411–417.

La, D.D.E., Universite, C., & Alpes, G. 2017. Development of stimuli-responsive cellulose nanocrystals hydrogels for smart applications.

Liu, C., Jin, R., Ouyang, X., & Wang, Y. 2017. Applied Surface Science Adsorption behavior of carboxylated cellulose nanocrystal — polyethyleneimine composite for removal of Cr (VI) ions. *Appl. Surf. Sci.* 408:77–87.

Lu, J., Jin, R., Liu, C., Wang, Y., & Ouyang, X. 2016. International Journal of Biological Macromolecules Magnetic carboxylated cellulose nanocrystals as adsorbent for the removal of Pb (II) from aqueous solution. *Int. J. Biol. Macromol.* 93:547–556.

Luzi, F., Puglia, D., Sarasini, F., Tirillò, J., Ma, G., Zuorro, A., Lavecchia, R., Kenny, J.M., & Torre, L. 2019. Valorization and extraction of cellulose nanocrystals from North African grass : Ampelodesmos mauritanicus (Diss). 209:328–337.

Meng, F., Wang, G., Du, X., Wang, Z., Xu, S., & Zhang, Y. 2019.Extraction and characterization of cellulose nanofibers and nanocrystals from liquefied banana pseudo-stem residue. *Compos. Part B.* 160:341–347.

Niamsap, T., Tien, N., & Sukyai, P. 2019. Production of hydroxyapatite-bacterial

nanocellulose sca ff old with assist of cellulose nanocrystals. *Carbohydr. Polym. Elsevier*. 205:159–166.

Oyewo, O.A., Mutesse, B., Leswi, T.Y., & Onyango, M.S. 2019. Journal of Environmental Chemical Engineering Highly e ffi cient removal of nickel and cadmium from water using sawdust- derived cellulose nanocrystals.

Paulo, J., Oliveira, D., Pinheiro, G., Lisie, S., Cleber, F., Renato, A., Dias, G., & Zavareze, R. 2019. International Journal of Biological Macromolecules Cellulose nanocrystals from rice and oat husks and their application in aerogels for food packaging. *Int. J. Biol. Macromol.* 124:175–184.

Perumal, S., Atchudan, R., Yoon, D.H., Joo, J., & Cheong, I.W. 2019. Spherical Chitosan/Gelatin Hydrogel Particles for Removal of Multiple Heavy Metal Ions from Wastewater. *Ind. Eng. Chem. Res. American Chemical Society*. 58:9900–9907.

Priscila, A., Silva, M., Vitória, A., Pontes, S.M.A., Pereira, A.L.S., De, M., Filho, M.S., Rosa, M.F., & Azeredo, H.M.C. 2019. Mango kernel starch fi lms as a ff ected by starch nanocrystals and cellulose nanocrystals. 211:209–216.

Shaheen, T.I. & Emam, H.E. 2018. International Journal of Biological Macromolecules Sono-chemical synthesis of cellulose nanocrystals from wood sawdust using Acid hydrolysis. *Int. J. Biol. Macromol.* 107:1599–1606.

Tang, J. 2016. Functionalized Cellulose Nanocrystals (CNC) for Advanced Applications.

Thomas, D., Latha, M.S., & Thomas, K.K. 2018. Journal of Drug Delivery Science and Technology Synthesis and in vitro evaluation of alginate-cellulose nanocrystal hybrid nanoparticles for the controlled oral delivery of rifampicin. *J. Drug Deliv. Sci. Technol.* 46:392–399.

Won, S., Paolo, J., Soriano, E., Rajan, A., Yeon, J., Hee, C., & Sang, C. 2018. International Journal of Biological Macromolecules Development of bioactive cellulose nanocrystals derived from dominant cellulose polymorphs I and II from Capsosiphon Fulvescens for biomedical applications. *Int. J. Biol. Macromol.* 110:531–539.

Yue, Y. 2011. A comparative study of cellulose I and II and fibers and nanocrystals.

Zhou, J., Li, Y., Li, H., & Yao, H. 2019. Colloids and Surfaces B : Biointerfaces Cellulose nanocrystals / fluorinated polyacrylate soap-free emulsion prepared via RAFT-assisted Pickering emulsion polymerization. *Colloids Surfaces B Biointerfaces*. 177:321–328.

CHAPTER TWO

2. LITERATURE REVIEW

2.1 Introduction to cellulose

Cellulose was first discovered and isolated in 1838 by Anselme Payen (Shaheen & Emam, 2018). cellulose is the most abundant organic biomass in nature and renewable with an annual production around 75 billion tons (Basu *et al.*, 2019). it is extracted from several marine animals such as fungi, bacteria, algae, and plants with plants producing the majority of occurring cellulose. Cellulose is generally isolated from the plant cell using isolation methods involving chemical, enzymatic and physical isolation techniques, while bacteria produces cellulose using the bottom up approach from the assembly of glucose units (Shaheen & Emam, 2018). Its abundance, renewability, and properties (chemical and physical) have led to the exponential growth in the application and study of cellulose in various areas such as personal care products, packaging, coatings, textiles, and more importantly composite materials (Hemmati *et al.*, 2018a). the worldwide interest in sustainability and green technologies favors the utilization of cellulose-based materials for the replacement of petroleum-based products, therefore, opening up new markets for this renewable material for advanced applications and consumer needs (Tang *et al.*, 2017a).

2.2.1 Cellulose, an important substance

Cellulose is considered the most abundant naturally occurring organic compound on earth. Cellulose metabolism is an important part of the biosphere's carbon cycle. This carbohydrate is found mainly in plant cell, where its principal function is to provide the protection and structural support to the cells. It can also be found in various organisms such as animal tunicates, fungi, bacteria, and amoeba, even though the content of cellulose is negligible compared with plant (Shaheen & Emam, 2018). cellulose is naturally replenished (renewable) resource available all over the world. Further, it is biodegradable and non-toxic to living organisms, including humans. Cellulose has played an important role in the life of human being, from prehistoric to present time and its applications could even present a turning point in the understanding of human evolution. Cellulose-based materials (wood) have been used to many purposes for thousands of years

as source of heating for cooking and industrial production, engineering materials for buildings, ships, furnishes, bridges etc. in its pure form, such as cotton and flax fibers, cellulose has been used as clothing and writing material back to the time in Egypt (Valone *et al.*, 2016). the first industrial scale product based on cellulose was created in 1870 from nitrocellulose by the Hyatt manufacturing company, the first thermoplastic polymer material as celluloid (Salari *et al.*, 2019).

Presently, cellulose plays a great economic importance, it is use as feedstock in several industries and gives rise to a broad of products and materials, from biomedical to packaging field. The paper and cardboard industries are the greatest consumers of cellulose. Only a small amount of cellulose is used to produce films, textile fibers and a larger number of cellulose derivatives, such as cellulose esters and ethers (Basu *et al.*, 2019; Ishak *et al.*, 2019a; Onur *et al.*, 2018). For instance, carboxymethylcellulose is a cellulose derivative utilized in pharmaceuticals, detergents, cosmetics, coatings, paints, plastics and adhesives etc. although cellulose can be derived from a broad variety of sources (bagasse, bamboo, cotton, sisal, ramie, jute etc) wood is the most important raw material for commercial production of cellulose (Priscila *et al.*, 2019).

When it comes to sustainable raw materials for demands of materials, energy and chemicals, cellulose has great importance because of its renewability and abundance. For this reason, intensive research efforts have been dedicated to searching efficient processing methods for conversion of this biomass into multiple value added bioproducts. Hence, cellulose is a promising various resource with potential to reduce the dependence on petroleum-based products and at the same time assist the increasing need for carbon neutral, biocompatible and environmentally friendly products (Grishkewich *et al.*, 2017a). however, numerous technical challenges must be overtaking to enable the efficient and profitable utilization of cellulose to produce chemicals, materials, and energy.

2.2.2 Cellulose structure

Cellulose has been used for decades in diverse applications, nevertheless its chemical structure, morphology and composition remained very long ignored. Though the early work of (ref) concerning the acid hydrolysis of the substance constituting plant cell walls goes back to the beginning of the 19th century (Bruel *et al.*, 2019), it was the French Chemist

Anselme Payen (1795-1871) who demonstrated that the principal constituent of all plant has unique chemical structure (Payen, 1819) "cellulose" (Latin: rich in small cells) for the first time in 1838. In his research, Anselme reported that when diverse plant tissues were treated with acid-ammonia treatment, followed by subsequent extraction in water, alcohol, and ether a constant fibrous material was formed. He deducted the molecular formula to be $C_6H_{10}O_5$ by elemental analysis and observed the isomerism with starch (Halász, 2014).

It is only later, due to the research of the German chemist Herman Staudinger (1881-1965) at the beginning of the 20th century that the macromolecular nature of cellulose was recognized. Trough acetylation and deacetylation of cellulose, he suggests that its structure does not consist of an aggregation of D-glucose units. The glucose units were found to be connected to each other covalently to form long molecular chains. This marked the discovery of the polymeric state of molecules and represents the origin of polymer science. Despite the degree to which cellulose has been investigated, its molecular structural features have not been identified with clarity and new information appeared in the literature by employing technological advances alongside conventional analytical tools. Hence, the progress of knowledge on cellulose is nearly associated to the evolution of characterization techniques, such as electron microscopy, X-ray diffraction, nuclear magnetic resonance etc. (Abdelraof *et al.*, 2019a; Candido & Gonçalves, 2019). Various books and reviews have been published reporting the state of knowledge of this fascinating polymer (Kaboorani & Riedl, 2015; Menezes-silva *et al.*, 2019a; Shaheen & Fouda, 2018; Won *et al.*, 2018a)

Cellulose exhibits unusual chemical and physical properties arising from its structural architecture, such as: Good thermal constancy. But it decomposes prior the onset of melting, it is non-thermoplastic material.

Resistant to chemicals attack. Cellulose is resistant to chemical derivatization, and added groups are rarely distributed. However, there is a large industry based on derivatization of cellulose as previously mentioned.

- Good mechanical properties. Cellulose fibers with high stiffness and tensile strength which makes the cellulose fibers useful
- Thermal conductivity and low density.

- ❖ Highly hydrophilic nature. Even so, it is insoluble in water and in conventional organic solvents.

Therefore, to understand properly the macroscopic properties of cellulose it is essential to have knowledge of its structural architecture from the atomic scale, all the way up to the macro scale. In that cases, the cellulose biosynthesis, its hierarchical organization, and molecular structures inside the cell must be considered.

A schematic of the tree hierarchical structure is presented **in Figure 2.1.**

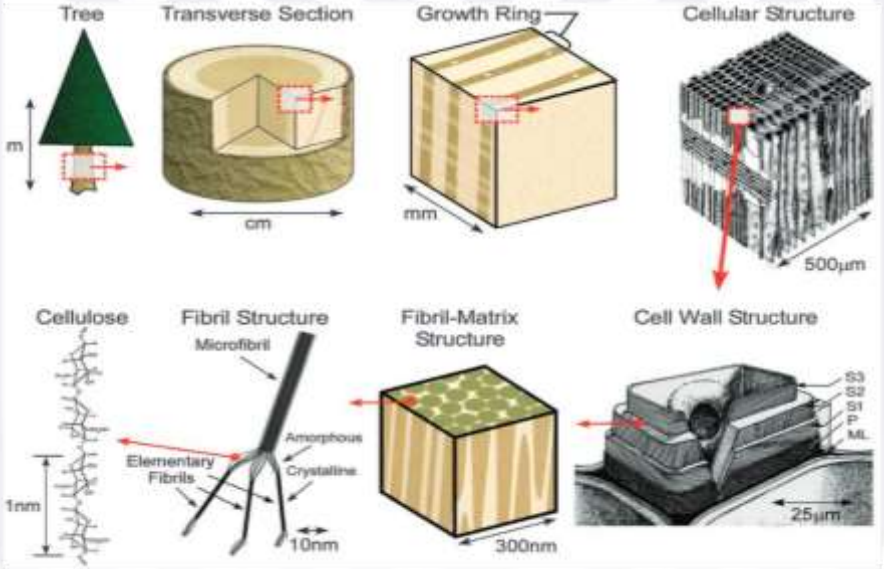

Figure 2.1: Schematic of the tree hierarchical structure (Bruel et al., 2019)

2.2.3 Molecular features of Cellulose

Cellulose is a semi crystalline long chain linear homopolymer, consisting of (glucose) of β-glucopyranose molecules covalently connected through acetal functions formed by β -(1,4)-glycosidic bonds (**Figure 2.2**), this glycosidic bond has a strength on the order of 360 Kj/mol. Since a molecule of water is lost when an alcohol and a hemiacetal react to form an acetal linkage, each glucose molecule in cellulose is referred to as anhydroglucose unit. The anhydroglucose are joined to one another in head-to-tail orientation and the C-O-C angle between two anhydroglucose rings is 116°. To accommodate the preferred bond angles of this acetal oxygen bridges formed by β 1→4 links, each anhydroglucose ring is rotated 180° in the plane with respect to its neighbor. In this manner, two adjacent

anhydroglucose rings define the repeating structural unit of cellulose polymer (cellobiose).

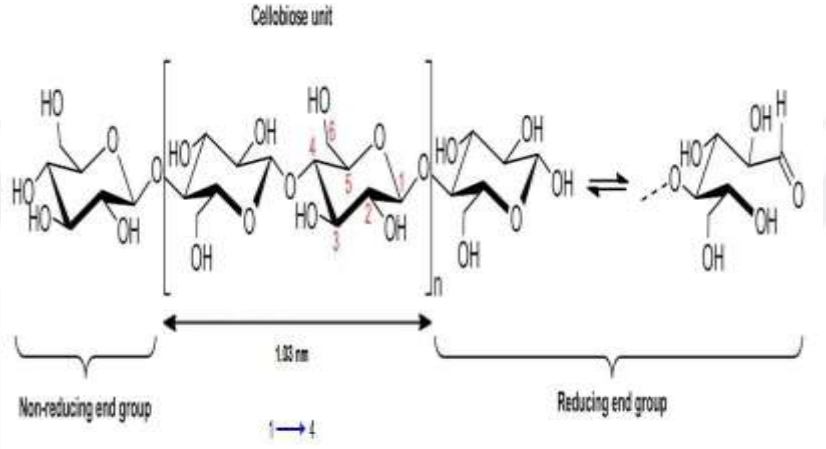

Figure2.2: Structure of cellobiose, representing the cellobiose (Henschen *et al.*, 2019a)

Taking the cellobiose as the basic unit, cellulose can be considered as an isotactic polymer of cellobiose. Each of the anhydroglucose contains three hydroxyl group at the C_6 position is a primary alcohol, while the hydroxyl groups at the C_2 and C_3 positions are secondary alcohols. These hydroxyl groups are all accessible sites for chemical reactions. Unlike simple alcohols, even so, the reactivity of these hydroxyl groups is usually controlled more by molecular interactions than would be expected based on the inherent reactivity of the different hydroxyl groups. The cellulose molecule has a directional asymmetry with respect to the termini of its chain axis: one end is a hemiacetal which is in equilibrium with the aldehyde structure (reducing end); and the other end has a pendant hydroxyl group, the nominal non-reducing end (Najwa and Amin, 2016; Basu *et al.*, 2019).

The β configuration allows cellulose to form long, straight, "fully extended "molecular chains are stretched out in a straight line, in the opposite to the 1→4 glucan of α- anomers, amylose, which is hexicalled shaped. All β-D-glucopyranose rings adopt a $^4C_1$ chair conformation, the lowest free energy conformation of the molecule, in which, the glycosidic bonds and the ring substituents are all positioned in the ring plane (equatorial), while the hydrogen atoms are in the vertical position (axial) (Niamsap *et al.*, 2019). This way, as represented in **Figure 2.3**, the cellulose molecule takes the form of a flat ribbon with hydroxyl groups protruding laterally along the extend chain and, as a consequence,

these hydroxyl groups are readily available for hydrogen bonding, either within the same cellulose chain (intramolecular) or between different chains (intermolecular).

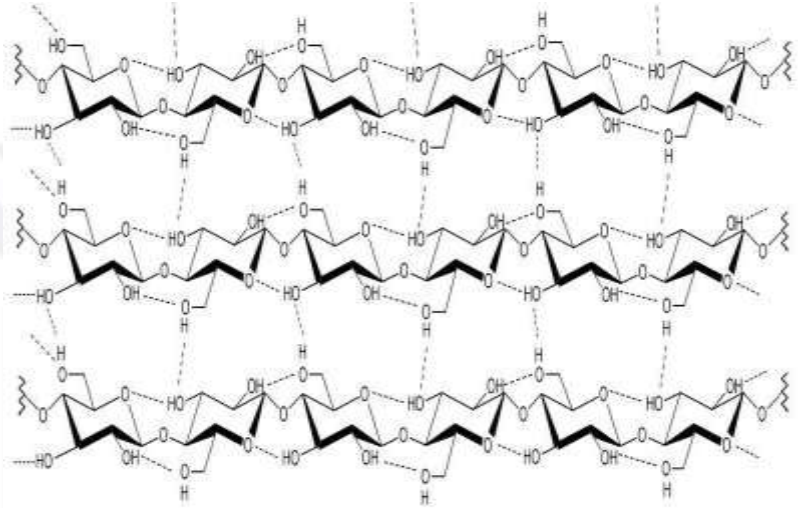

Figure 2-3: Schematic of the intra-and intermolecular hydrogen bonding network in cellulose (Wu *et al.*, 2018a).

The presence of intramolecular hydrogen bonds is of high relevance regarding single chain conformation of cellulose, since they block the free rotation of the rings along their linking glycoside bonds resulting in the constraining of the cellulose chain. These intramolecular hydrogen bonds between adjacent anhydroglucose unit rings stabilize the glycosidic linkage in so much that the linear integrity and the rigidness of the polymer chain are increased. The intermolecular hydrogen bonds are normally responsible for the aggregation state of cellulose and the cohesion between chains (Meng *et al.*, 2019).

Therefore, this complex and strong hydrogen bonding network present in cellulose is highly important for the specific characteristics of cellulose such as solubility, mechanical properties, thermal stability, and the reactivity. For example, it affects:

(i) the solubility, the high number of hydroxyl groups in a molecule should lead to a great solubility in water, but the cellulose is insoluble in most formal solvents and water, since to solubilize it the solute-solvent attraction have to be stronger than the high intermolecular attractive forces which bind the cellulose molecules together.

(ii) mechanical properties, the inter and intra-chain hydrogen bonding system gives to cellulose fibrils a relatively good strength and high axial stiffness.

(iii) the thermal stability, high energy in the form of heat is required to overtake the high cohesive energy between the cellulose molecules, this explains why cellulose does not have a liquid state, it means that the total bonding force between the cellulose molecules is harder than the covalent intramolecular bonds.

(iv) the reactivity of the hydroxyl groups, particularly of the C_3 hydroxyl group, which hydrogen binds strongly to the endocyclic oxygen of the anhydroglucose unit in the same chain.

Another important characteristics is from the position of the hydroxyl groups, the hydrogen atoms in the pyranose ring (H atoms are oriented axially to the ring plane, while OH group are equatorial) and the flat ribbon-like shape of cellulose molecule. The formation of sites with distinguishable polarities: the hydrophilic sites parallel to the ring plane and hydrophobic sites perpendicular to the ring are described in **Figure 2.4**, and is required to substantially influence both macroscopic and microscopic properties of cellulose (Luzi *et al.*, 2019; Pei *et al.*, 2019a).

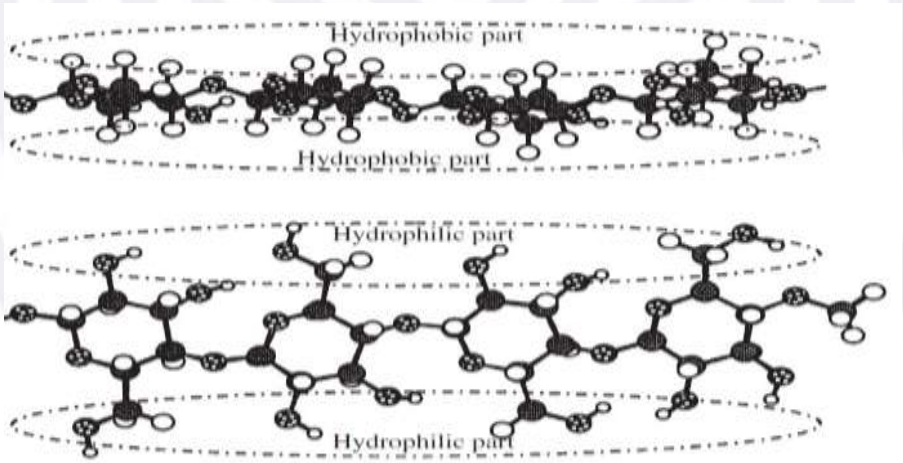

Figure 2.4: Hydrophilic and hydrophobic part of the cellulose molecules showing the hydroxyl groups located on the equatorial positions of the rings and the C-H bonds on the axial position of the rings(Halász, 2014)

2.2.4 Degree of polymerization of cellulose

The size of the cellulose molecule, showed by degree of polymerization (DeP) or molecular weight (MW), has a great influence on the biological, solution, mechanical and physiological properties of cellulose. It is believed that a β (1→4) linked glucan with DeP

around 20-30 can offer all properties of cellulose (Shaheen & Emam, 2018). Values of DeP ranging from hundreds and various tens of thousands have been reported. The DeP is dependent on the source of cellulose (e.g., 45000 in valonia, 15000 in cotton and 10000 in native wood), and in less degree on the isolation and purification methods (e.g., 350-500 in regenerated cellulose and 1000 in bleached Kraft pulp). The combination of methods expected to isolate and purify cellulose necessarily causes some degradation during analysis leading in chains cutting. value of DeP obtained are therefore minimum and depend on the method used to determine it. For similar reasons, the distribution of chain lengths of cellulose is not well established. Even so, some researchers proposed that the molecular mass distribution must be homogeneous for cellulose of a given source (Basu *et al.*, 2019; Onur *et al.*, 2018; Singh *et al.*, 2017; Thomas *et al.*, 2018). In its commonly used form, isolated cellulose is always a polydisperse polymer, viz., like nearly all polymers it is a mixture of molecules that have the same basic composition but differ in the chain length. Thereby, the molecular mass and the DeP, the fibrils are quite long. For example, given a glucose unit as 0.515 nm long, for DeP value of 10000, the cellulose may have average length around 5 μm by considering stretched chains.

2.2.5 Cellulose biosynthesis and microfibril formation

In nature, cellulose does not occur as an isolated molecule, but it is found as assemblies of individual chains forming a fiber-like structure. This is because cellulose is polymerized as individual molecules, which undergo crystallization and spinning in a hierarchical order at the site of biosynthesis resulting in fibrillary supramolecular structures (Bruel *et al.*, 2019). That way, the biosynthesis of cellulose can be described as a complex sequential multistep phenomenon, involving coupled processes

(i) the enzymatic polymerization of individual β-(1,4)-D-glucopyranose chains from glucose monomers, and (ii) the assemble of these glucan chains, through spinning and crystallization, to form fibrillary supramolecular structures.

Cellulose biosynthesis process take place at plasma membrane-bound enzyme system in the cell wall, known as cellulose synthase complexes (CS). The cellulose synthase complexes have functional specialization roles in gene expression, regulation, and catalytic functions (Halász, 2014). The model proposed by Delmer & Amor introduces the cellulose synthase through the cytoplasmic membrane within the plant cell in **Figure 2.5.**

The model describes the growth of glycosidic chains and the catalytic role of the main enzyme system whose main family is named cellulose synthase (CS), which cannot function without the presence of enzyme called sucrose synthase (SUSY). The sucrose synthase hydrolyzes sucrose to fructose by creating uridine diphosphate glucose unit (UDP) and dimerization of glucose. The growing chains are secreted via a pore and the crystallization event is brought about by a protein, which should facilitate alignment of the chains to promote precise crystallization into metastable cellulose.

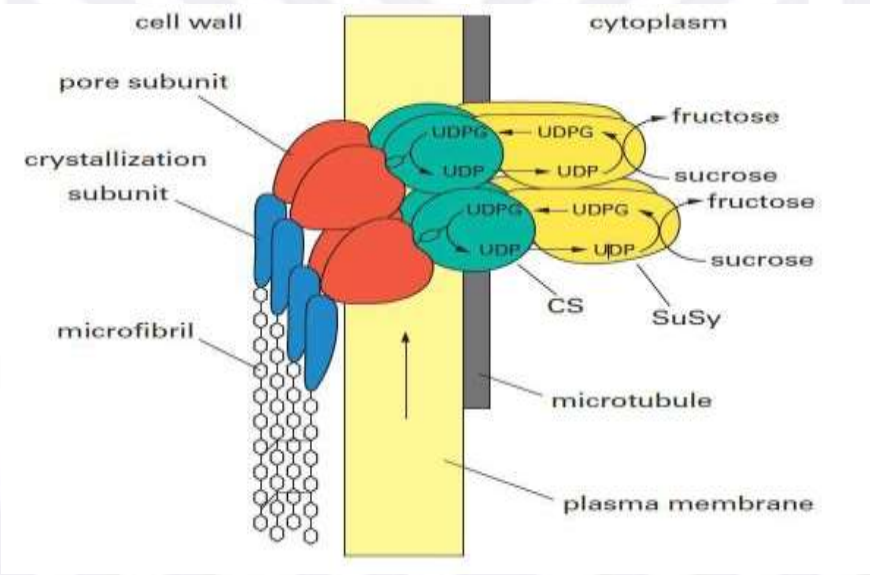

Figure 2.5: Model of a cellulose synthase complex in the plasma membrane (Halász, 2014).

2.3 Nanocellulose: Cellulose Nanofibrils (CNF) and Cellulose Nanocrystals (CNC)

The terms used to identify cellulose nanomaterials have not been standardized and because of this there is an inconsistent use of terms in the literature to describe several cellulose particles (Kaboorani & Riedl, 2015). Generally, people tend to divide cellulose nanomaterials into two categories, cellulose nanocrystals (CNC) and cellulose nanofibers (CNF) as shown in **Figure 2.6.**

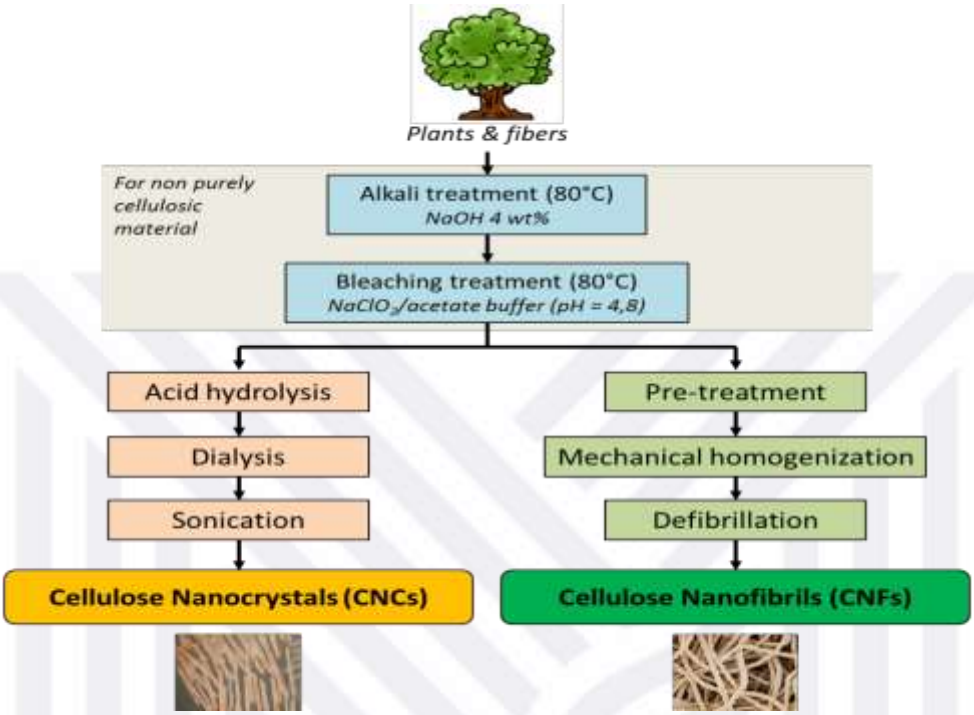

Figure 2.6: General procedure to obtain nanocellulose (Gicquel et al., 2017)

These two categories of cellulose nanomaterials differ from each other based on the size distribution and crystalline fraction. The cellulose nanofibers have larger diameter (5-60 nm), longer length (more than 10 μm) and lower crystalline fraction (Du *et al.*, 2019a) and may contain non cellulose components. The cellulose biomass can be treated in various ways to yield either CNC or CNF. A recent paper (Tang, 2016), presents the results of four methods to prepare wood cellulose nanomaterials. The methods include enzymatic hydrolysis by endoglucanase enzyme, sulfuric hydrolysis, mechanical treatment, and TEMPO mediated oxidation (Kaboorani & Riedl, 2015). it is evident from this study that the method of preparation can alter the shape, size, crystalline faction, and surface chemistry of the cellulose nanomaterial, even when using the same starting material (**Table 1.1 and Figure 2.7**). As shown in **Figure 2.8**, the CNCs produced by acid hydrolysis is much smaller than the CNF produced by any of the other 3 methods, because the CNF retains disordered cellulose regions that link the small cellulose nanocrystals.

Table 2.1: Different preparation methods lead to different types with varying crystalline fractions and different surface functional groups (Hynninen *et al.*, 2019).

Cellulose source/ method	Particle type	Crystalline fraction	Surface chemistry
Wood-mechanically refined	CNF	0.30	Hydroxyl
Wood-enzymatic	CNF	0.55	hydroxyl
Wood-TEMPO mediated oxidation	CNF	0.05	Hydroxyl/ carboxylate
Wood-Sulfuric acid hydrolysis	CNC	0.60	Sulphate Hydroxyl

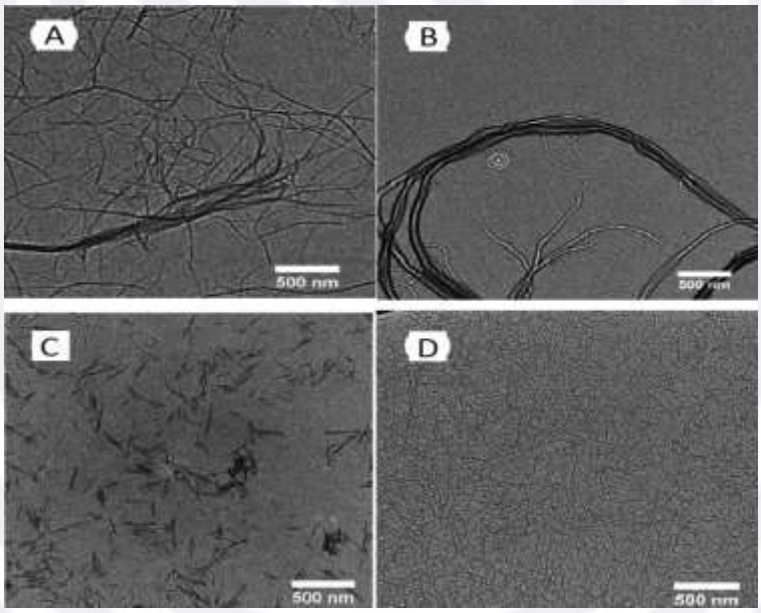

Figure 2.7: TEM images of cellulose nanomaterials: (a) CNF from enzyme treatment, (b) CNF from mechanical refining, (c) CNC from sulfuric acid hydrolysis, (d) CNF from TEMPO oxidation (Du et al., 2019b).

2.3.1 Cellulose nanofibers (CNF)

Cellulose nanofibers (CNF) with diameters as low as 5nm (elementary fibril level) and lengths in the micron scale containing both crystalline and amorphous sections, can be isolated from cellulose microfibers. Cellulose nanofibers are obtained by mechanical fibrillation (microfluidization or ultrafine grinding, homogenization) of cellulose biomass depending on the cellulose source and pretreatments (Du *et al.*, 2019b). In some cases, pretreatments (chemical pretreatment, mechanical pretreatment, or enzymatic pretreatment) are carried out on cellulose nanofibers to reduce energy input, enhance cellulose nanofibers quality, or achieve other functions.

2.3.2 Cellulose nanocrystals (CNC)

These nano particles are generally called cellulose nanocrystals (CNC) although their nomenclature in the literatures is poorly stated and they have also been called "Nano Crystalline Cellulose (NCC)" (Ishak *et al.*, 2019b). There are various ways to prepare the CNC with acid hydrolysis using sulfuric acid being the most used method. The treatment of cellulosic microfibers by acid hydrolysis results in the dissolution of their amorphous domains. The glyosidic bonds of the cellulose chains are cut longitudinal to form the microfibers and rod like near perfect cellulose nanocrystals (Awang *et al.*, 2019a).

Hydrolysis using sulfuric grafts sulphate groups onto the surface hydroxyl groups through esterification. The presence of theses negatively charged groups promotes the dispersion cellulose nanocrystals in water by increasing unfavorable electrostatic repulsions and leads to stable colloidal suspensions. Hydrolysis with hydrochloric acid gives only hydroxyl groups on the surface, resulting to neutral cellulose nanocrystals that aggregate and are difficult to disperse. Phosphoric acid, ammonium persulfate (APS) oxidation, hypochlorite acid and nitric acids have also been employed for the preparation of cellulose nanocrystals with different surface groups. All methods except the hydrochloric acid hydrolysis give mixtures of surface functional groups. Some of the original hydroxyl groups always remain on the cellulose nanocrystals surface (Kaboorani & Riedl, 2015). Some examples of cellulose nanocrystals surface chemistry using different preparation methods are shown in **Figure 2.8.**

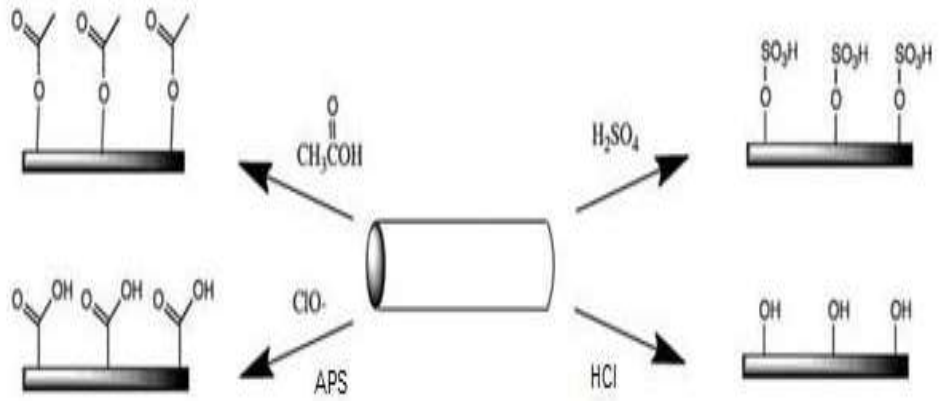

Figure 2.8: Cellulose surface by different methods: sulfuric acid hydrolysis provides sulfate esters (top right), acetic acid hydrolysis gives acetyl (top left), ammonium persulfate (APS) oxidation or hypochlorite hydrolysis allows carboxyl (bottom left) and hydrochloric hydrolysis provides hydroxyl (bottom right) (Halász, 2014).

For cellulose nanocrystals produced by sulfuric acid hydrolysis with 65.0 wt.% acid for about 2h, the length of cellulose nanocrystal is generally between 100 and 500 nm, width is less than 10 nm and its yield is 30% based on initial weight of the cellulose source (Ishak *et al.*, 2019b). The effects of varying the acid to pulp ratio and reaction time on the nanocrystals produced by sulfuric acid hydrolysis of bleached softwood pulp was studied by (Kaboorani & Riedl, 2015). Shorter nanoparticles with a narrow polydispersity were generated when longer hydrolysis times were used. A method to control the size distribution has been discussed by (Kaboorani & Riedl, 2015). Results in that paper shows that acid hydrolysis of cotton in 67% sulfuric acid for 45 min at temperature of 45 to 70 °C can produce cellulose nanocrystals with different size distributions. Shorter crystals were obtained when the temperature increased, although it is still unclear whether temperature influences the width of the crystal.

When the method of cellulose preparation is kept constant, the size, yield, and crystallinity index of the nanoparticles are determined by the cellulose source. (Tang, 2016), measured size, yield, and crystallinity index (CRI) for cellulose nanocrystals obtained from several cellulose sources (**Table 2.2**). The TEM images of cellulose nanocrystal from different biomasses which have different shapes are shown in **Figure 2.9.**

Table 2.2: The yield, crystallinity index (CRI), length and diameter of cellulose nanocrystals produced from several cellulosic sources. XRD with integral method was used for CRI estimation (Tang, 2016).

CNC source	Yield (%)	CNC CRI (%)	Length (nm)	Diameter (nm)
Flax	28	75	144	3.8
Flax shives	22	63	296	5.1
Hemp	36	73	147	5.8
Tunicate	31	74	1160	4.2
Paper	80	90	120	6.7
Wood pulp	35	81	124	6.0
Bacterial	15	72	88	6.5

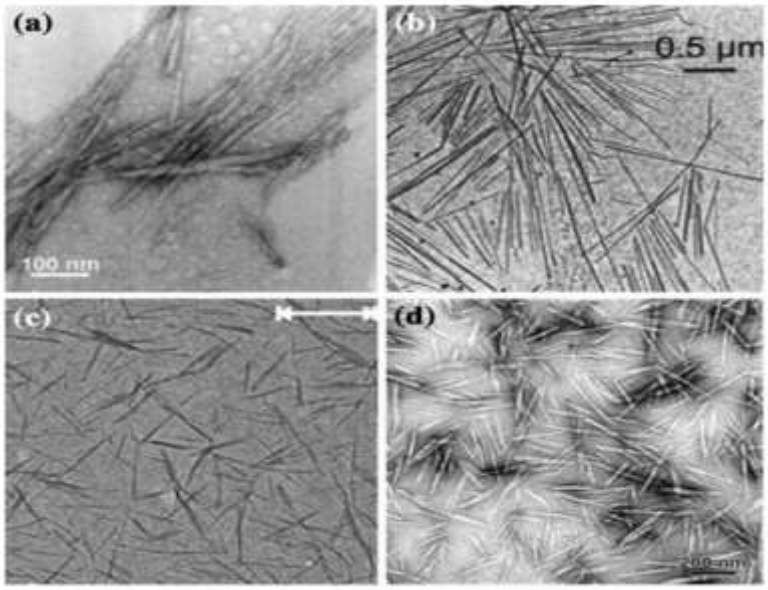

Figure 2.9: Transmission electron microscopy images of cellulose nanocrystals, from acid hydrolysis of (a) wood, (b) tunicate, (c) cotton and (d) ramie (Al-Qahtani, 2016)

2.3.4 Cellulose nanocrystals isolation

Cellulose nanocrystals preparation requires a chemical acid hydrolysis process aimed to dissolved amorphous chains from cellulose fibers, and to release crystal domains after the sonication process. The cellulose nanocrystals are the smallest building blocks that can be extracted from cellulose.

Cellulose crystallites were isolated the first time by Harble and Nickersson in the 1940s. They found that the degradation induced by boiling cellulose fibers in acidic solution (sulfuric and hydrochloric acids) reached a limit after a specific time of treatment. The work of Ranby and Ribi in 1951 revealed that cellulose nanocrystals from hydrolysis of cotton pulp and wood present negative charge and well-dispersed suspension at the pH range of 3 to 11.

Chemical isolation of cellulose nanocrystal consists of exhibiting the cellulosic material to acid hydrolysis under controlled time, temperature and agitation speed followed by sonication to separate the crystal domains. The amorphous cellulose regions are oriented in a spaghetti-like arrangement heading to lower density cellulose compared to the nanocrystalline areas. The amorphous regions act as structural defects which are susceptible to be attacked by acid and, under controlled conditions, they may be removed leaving crystalline regions intact (Awang *et al.*, 2019b; Du *et al.*, 2019b). During the acid hydrolysis process, the hydronium ions can penetrate the cellulose chains in the amorphous domains promoting the hydrolytic segmentation of the glycosidic bonds and taking out individual crystallites. Sulfuric (H_2SO_4) and hydrochloric acids (HCl) are typically used as hydrolyzing agents. Various other mineral and organic acids have been tested such hydrobromic acid, phosphoric acid, nitric acid or subcritical water (Niamsap *et al.*, 2019; Tang, 2016; Tang *et al.*, 2017b; Yue, 2011).

The isolation of cellulose nanocrystals from cellulosic source follows various step. For non-purely cellulosic materials, bleaching and chemical pre-treatment steps are necessary to removed hemicellulose and lignin from the material. The removal of hemicellulose and lignin is necessary to ensure maximum crystallinity of the produced cellulose nanocrystals(La *et al.*, 2017). As reported previously, the third step is the acid hydrolysis. Sulfuric acid is the common method used in literature and was reported in details by (Bruel *et al.*, 2019). The morphology and final yield are affected by parameters such as acid choice and concentration and cellulose source, hydrolysis cellulose nanocrystals. From cellulose fiber to cellulose nanocrystals its temperature and functionalization time. Time of hydrolysis using traditional methods was (64 wt.% sulfuric acid, 40°C, 30 min) shown the greatest impact on the final yield. It has been reported by (Tang *et al.*, 2017b; Thomas *et al.*, 2018) that with increased reaction time the yield decreases because of the destruction of cellulose nanocrystals. To cease the isolation

process of cellulose nanocrystals, the hydrolyzed mixture is diluted to suppress the reaction. Then the suspension is subjected to various separations (filtration and centrifugation) and washing process such as dialysis to removed salt residues and remaining reagents. Final centrifuge separation or micro-filtration are used to remove agglomerates (Wu *et al.*, 2018b). The last step in the process is ultrasonic treatment to help the dispersion of the crystalline cellulose in the suspension (Du *et al.*, 2019b). **Figure 2.10** shows a schematic of the cellulose nanocrystals isolation procedure with sulfuric acid hydrolysis. The process will introduce the negatively charge ester-sulfate on the cellulose nanocrystals surface. These negative charges cause repulsive forces between cellulose nanocrystals, which makes stable colloidal suspension in aqueous solution.

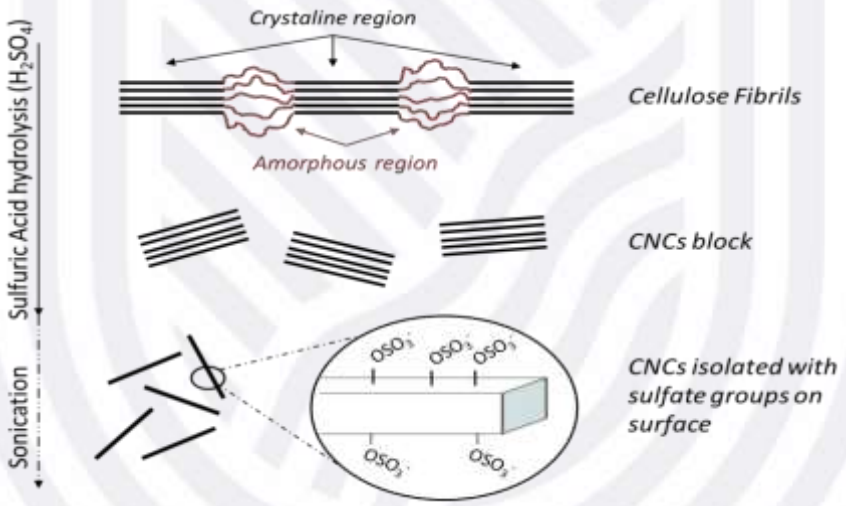

Figure 2.10: Schematic of the cellulose nanocrystals isolation procedure with sulfuric acid hydrolysis which brake down amorphous region and isolates nanocrystals (Halász, 2014)

2.3.5 Cellulose nanocrystal safety and toxicology

The raising interest on cellulose nanocrystals causes the question of safety and nano-toxicology issues. Cellulose is considered as non-toxic materials (no impact on health). Regarding the high specific area and size, the question of interactions with physiological medium is still under investigation. Various studies have reported that cellulose nanocrystals seem to be non-toxic (Awang *et al.*, 2019b; Errezma *et al.*, 2018; Onur *et al.*, 2018). In November 2012, the Canadian government added the cellulose nanocrystals nanomaterial to the list of "domestic substances list" with no suspicion of toxicity. The list

is an inventory of substances that may be imported or manufactured in Canada in food and drug applications. Very recent studies also investigate the impact of cellulose nanocrystals in immune toxicology and genotoxicity (Candido & Gonçalves, 2019), the impact of surface modified cellulose nanocrystals on their toxicity (Luzi *et al.*, 2019) and review the oral, dermal, pulmonary and cytotoxicity of cellulose nanocrystals (Kaboorani & Riedl, 2015).

2.3.6 Cellulose nanocrystal properties

Cellulose nanocrystals are good in terms of abundance, renewability, and biodegradability. They present many advantages and interesting properties. **Figure 2.11** illustrates the Chemical and physical properties of Cellulose nanocrystals.

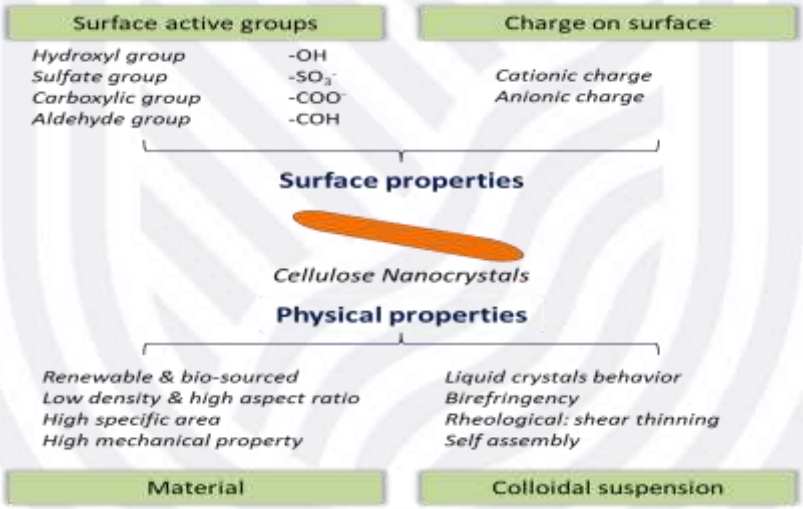

Figure 2.11: The Chemical and physical properties of Cellulose nanocrystals.

Cellulose nanocrystals have a density of 1.606 g/cm^3 and displayed a high aspect ratio with a diameter of 5nm to of tens nanometers and the length of 100 to 110 nm (Habibi *et al.,* 2010). As described, their shape, size and surface properties depend on the hydrolysis conditions and cellulosic source (Awang *et al.*, 2019b; La *et al.*, 2017; Salari *et al.*, 2019; Won *et al.*, 2018b). Considering the mechanical properties, high crystallinity (70~90%), high elastic modulus (~150 GPa) and high tensile strength (~7.5 GPa). These specific properties cause reinforcement of mechanical properties with addition of nanocellulose into polymer matrix as reported in several reviews (Mariano *et al.,* 2014; Oksman *et al.,* 2016). Cellulose nanocrystals suspension demonstrates interesting properties to self-organize into liquid crystalline phases. The suspension phase separates into an upper isotropic

phase and lower anisotropic chiral nematic phase. The chiral nematic structure of Cellulose nanocrystals have been studied by researchers to get iridescent dried films. The Cellulose nanocrystals materials demonstrate a colloidal stability in aqueous media due to the presence of SO_3^- on the surface. The rheological behavior of Cellulose nanocrystals suspension is explained in works (Shafiei-Sabet et al., 2012; UreñaBenavides et al., 2011). These research works explain that Cellulose nanocrystals suspension rheological behavior depend on the concentration. At higher concentrations >3 wt.% a shear thining behavior is observed due to the organization of particles in the sense of the flow. At low concentrations< 3 wt.% suspension appear as a near Newtonian fluid with small thining behavior at high shear rate. Researchers and industries are attracted by the isolation of nanoparticles with a surface area > 200 $m^2 \cdot /g$ to produce materials such as hydrogels, nanocomposites, aerogels, etc. Cellulose nanocrystals show a high surface area of 180-850 m^2/g and can be used to create hybrid materials with minerals or metals (Hoeng *et al.,* 2015; Kaushik and Moores, 2016a; Majoinen *et al.,* 2016; Rezayat *et al.,* 2014). Due to the presence of hydroxyl groups in each anhydroglucose unit, cellulose nanocrystals present good surface reactivity and allow the introduction of new groups.

2.3.7 Cellulose nanocrystals Applications

Cellulose nanocrystals are great candidates for the design and development of high-performance nanomaterials in many applications due to several attractive features such as, high surface area, hydroxyl groups for functionalization, low toxicity, chirality, morphology, colloidal stability, and mechanical strength. Since the last decade, around the world, several large-scale manufacturing facilities have been commissioned to produce cellulose nanocrystals. Some of these facilities include the following:

- Cell force 1000 kg/day (Canada),
- American Process 500 kg/day (USA),
- Holmen 100 kg/day (Sweden),
- Alberta Innovates 20 kg/day (Canada),
- US Forest Products Lab 10 kg/day (USA),
- Blue Goose Biorefineries 10 kg/day (Canada), and
- India Council for Agriculture Research 10 kg/day (India) (Halász, 2014).

Thanks to these facilities, the average price for 1 kilogram of dried CNCs is around 400 €. This promising interest of scientific community has allowed several recent reviews on

potential applications of cellulose nanocrystals and functionalized cellulose nanocrystals (Du *et al.*, 2019b; Ishak *et al.*, 2019b; Kaboorani & Riedl, 2015; Tang, 2016). **Figure 2.12** shows different field of applications with Cellulose nanocrystals.

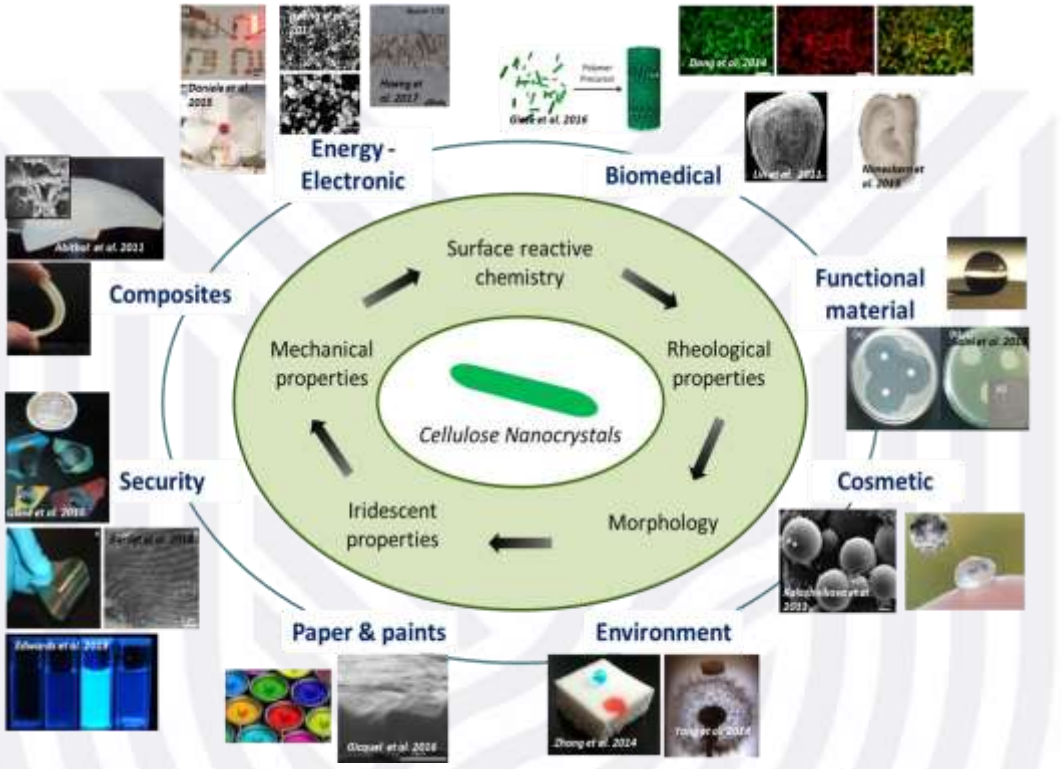

Figure 2.12: Different cellulose nanocrystals field of application (Halász, 2014)

Biomedical: Because of the possibility of chemical modification, colloidal stability, chirality for template and bio compatibility, the field of biomedical research is one of the most recent application area for cellulose nanocrystals based materials (Kaboorani & Riedl, 2015). Several examples are present in literature using cellulose nanocrystals as drug delivery (Basu *et al.*, 2019; Hemmati *et al.*, 2018b)), fluorescent labeling for bio-imaging (Du *et al.*, 2019b), tissue engineering and 3D printing for tissue (Ishak *et al.*, 2019b) as a template for medical devices and injectable hydrogel (Du *et al.*, 2019b).

Cosmetics: The rheological behavior of cellulose nanocrystals is used in this field of application and, the possibility of cellulose nanocrystals to create Pickering emulsions for foam formation (Du *et al.*, 2019b).

Energy and electronics: This field takes advantages from the reactive surface of cellulose nanocrystals and their unique morphology in order to realize conductive bio-sourced inks

(Voisin *et al.*, 2017; Wu *et al.*, 2018b), flexible piezo electric devices (Tang, 2016), semiconductors (Grishkewich *et al.*, 2017b), to stabilize metal particles (Hu *et al.*, 2018), and other material applications (Lihong *et al.*, 2011).

Paper and paints: this field encompasses several applications such as food packaging, hygienic tissues, specific paper, printing papers or paints facilities (Liu *et al.*, 2017).

Composites: material applications take advantage of the outstanding mechanical properties of cellulose nanocrystals. Used as a reinforcement or a crosslinker, several works investigate the effect of cellulose nanocrystals in polymeric matrices (Abdelraof *et al.*, 2019b; Thomas *et al.*, 2018; Yalç *et al.*, 2019). A recent review on this field of material science are present in literature (Valone *et al.*, 2016).

Environment: Wastewater (Kaboorani & Riedl, 2015) and pollution adsorbent (Song *et al.*, 2019; Tang, 2016) are important fields of research to help with protecting the environment, which is possible due to the high specific area of cellulose nanocrystals. In the same area, cellulose nanocrystals are used to increase the thermal isolation of materials to their possible configuration in aerogels (Won *et al.*, 2018b).

Functional materials: antimicrobial properties (Menezes-silva *et al.*, 2019b), barrier to water, air, or oil (Hynninen *et al.*, 2019; Luzi *et al.*, 2019), or super-hydrophobic surfaces.

Security: Iridescent properties combined with unique morphology of cellulose nanocrystals open the possibility of use in security paper and inks (Lei *et al.*, 2019).

2.3.8 Modification of cellulose nanocrystals

The abundance of hydroxyl groups on the surface of cellulose nanocrystals allows different chemical modifications, such as esterification, etherification, oxidation, silylation, polymer grafting, etc. Noncovalent surface modification is also possible using surfactants. Covalent or noncovalent modifications have been conducted mainly to:

- Transform the hydroxyl groups on the surface of cellulose nanocrystals for further modification.
- Impart positive or negative charges on the surface of cellulose nanocrystals to obtain better dispersion.

- ❖ Change the surface energy characteristics of cellulose nanocrystals to improve compatibility, especially when they are used in hydrophobic matrices in nanocomposites.

The main challenge is to modify only the surface of cellulose nanocrystals, while preserving the original morphology of nanocrystal.

2.3.8.1 Tempo Mediated oxidation

Hydroxymethyl groups at the surface of the cellulose nanocrystals can be converted to carboxylic groups using 2,2,6,6–tetramethylpiperidine-1-oxyl(TEMPO) reagent in the presence of NaBr and NaOCl.

This technique has been used since it was first reported by de Ma et al., 2019 who showed that only primary hydroxyl groups of polysaccharides were oxidized, while secondary hydroxyl groups were left intact (Ma *et al.*, 2019). However, all primary hydroxyl groups of cellulose nanocrystals are not prone to be oxidized. The morphology and the crystal axis of the cellulose nanocrystals are important factors in determining the accessibility of the hydroxymethyl groups. It was reported that only half of the hydroxymethyl groups are available to react because the other half is buried within the crystalline structure of cellulose nanocrystals (Onur *et al.*, 2019; Won *et al.*, 2018b) Tempo-mediated oxidation of cellulose nanocrystalline was first reported by Araki et al.., 2020 It was used as an intermediate step to graft polymeric chains. They demonstrated that cellulose nanocrystals maintained its initial morphological integrity after oxidation and formed a homogeneous suspension when dispersed in water due to the permanent charges on the surface of cellulose nanocrystals. Habibi et al (2019) also performed TEMPO-mediated oxidation of cellulose nanocrystals isolated from tunicate by HCl hydrolysis. They demonstrated that the degree of oxidation could be controlled by using specific amounts of the primary oxidizing agent, NaOCl.

2.3.8.2 Cationization

Abdelroaf et al (2019) described a single step method to impart positive charges on the surface of cellulose nanocrystals by grafting epoxypropyl trimethylammonium chloride (EPTMAC) onto cellulose nanocrystals surface. Alkali activated surface hydroxyl groups made nucleophilic addition to the epoxy moiety of EPTMAC. This modification reversed

the surface charge and reduced the total surface charge density. These modifications led to the stable aqueous suspensions having unexpected gelling properties.

2.3.8.3 Acetylation

Sassi and Chanzy have studied the homogeneous and heterogeneous acetylation of cellulose nanocrystals extracted from valonia and tunicate using acetic anhydride in acetic acid. The model for the acetylation of cellulose nanocrystals was based on a no swelling reaction mechanism suggesting that only the cellulose chains on the surface of nanocrystals was affected by the reaction. In the case of homogenous acetylation, the partially acetylated cellulose chains entered the acetylating medium when they were sufficiently soluble, however in the case of heterogeneous acetylation, the cellulose acetate remained insoluble and surrounded the crystalline core of unreacted cellulose chains (Meng *et al.*, 2019).

Yuan et al. (2016) reported a simple chemical modification route involving low reagent consumption. They mixed alkyenyl succinic anhydride (ASA) emulsion with cellulose nanocrystals suspension, freeze dried and heated to 105°C. Highly hydrophobic whiskers were obtained, which could easily be dispersible in solvents with widely different polarities; for example, they were both dispersible in N,N-dimethyl sulfoxide (DMSO) having a very high (dielectric constant) of 46.45 and 1,4-dioxane that has a quite low of 2.21. A one-step methodology for hydrolyzing cellulose and making acetylation of hydroxyl groups simultaneously has been reported (Ishak *et al.*, 2019b). A mixture of hydrochloric and organic acid (acetic and butyric acid) was used to carry out the reaction. HCl was used to produce the cellulose nanocrystals and organic acid was used to functionalize the surface of cellulose nanocrystals. The dimensions of the obtained crystals are similar to those obtained by hydrochloric acid hydrolysis alone. More than 50% of the surface hydroxyl groups were substituted under the employed reaction conditions. The obtained nanocrystals were dispersible in ethyl acetate and toluene.

2.3.8.4 Silylation

Cellulose isolated from tunicate were silylated by alkyldimethylchlorosilanes, with alkyl groups ranging from isopropyl to *n*-butyl, *n*-octyl and *n*dodrecyl (Pei *et al.*, 2019b). It has been demonstrated that the whiskers became readily dispersible in solvents of low polarity (THF and acetone) with the degree of substitution (DS) between 0.6 and 1, while

their morphological integrity was preserved. However, when the degree of silylation is high (DS >1) the chains in the core of the crystals became silylated that resulted in the loss of morphology.

2.3.8.5 Aldehyde functionalization

Drogat et al (2018) used periodate oxidation to generate aldehyde groups on the surface of cellulose nanocrystal. These aldehyde groups are used as reductive sites, thus avoiding the use of another reducing agent like $NaBH_4$ to prepare Ag nanoparticles on the surface of cellulose nanocrystals. Periodate oxidation breaks the bond between the carbon atoms possessing secondary hydroxyl groups and gives two aldehyde groups per reacting anhydroglucose unit.

2.3.8.6 Polymer grafting

There are two main strategies to graft a polymer on the surface of cellulose nanocrystals, namely, "grafting-to" and "grafting-from". The "grafting-to" approach involves the attachment of a pre-synthesized polymer chain to the hydroxyl groups using a coupling agent. In the "grafting-from" approach, the polymer grows from the CNC surface via the atom transfer radical polymerization (ATRP) (Henschen *et al.*, 2019b). Habibi and Dufresne used the "grafting-to" approach to graft different molecular weights of polycaprolactone (PCL) to the cellulose nanocrystals via the isocyanate-mediated coupling reaction (Bruel *et al.*, 2019). It was found that PCL chains at the surface were able to crystallize when the grafting density was sufficiently high. Errezma et al (2018) also made a similar effort in the grafting process of pre-synthesized water-borne polyurethane polymers via a one-pot process. Peptide coupling reaction was also utilized to graft amine-terminated polymer on cellulose nanocrystals.

Paulo et al (2019) used this method to graft poly (ethylene glycol) on cellulose nanocrystals particles. cellulose nanocrystals particles were firstly carboxylated by TEMPO-mediated oxidation, and then EDC-NHS carbodiimide reaction was used to couple - Recently, Cudjoe et al. grafted thermo-responsive polymers onto cellulose nanocrystals via a peptidic coupling reaction. They reported that the modified cellulose nanocrystals show unusual properties, such as colloidal stability at high ionic strength, surface activity and thermo reversible aggregation. They also reported a thermo reversible aggregation, which could open a new way to design stimuli-responsive biobased nanocomposite materials.

The “grafting-from” approach uses ATRP technique allowed to produce well-defined monodispersed particles (Leng, 2016). This technique has two steps: the first step is the reaction of surface hydroxyl groups with 2-bromoisobuturyl bromide (BIBB), which is followed by the polymerization of monomers (Hynninen *et al.*, 2019).

Lin et al (2016) used styrene to study surface initiated ATRP, and they reported various grafting products with different grafting densities and molecular weights (Lin, 2016). Yi et al. (2019) used N,N-dimethyl aminoethyl methacrylate (DMAEMA) as a monomer to study the temperature-induced chiral nematic phase behavior of PDMAEMA-grafted cellulose nanocrystals suspensions (Voisin *et al.*, 2017). Habibi et al. (2019) reported the first “grafting from” approach by grafting polycaprolactone onto the surface of cellulose nanocrystals via ring-opening polymerization. They used stannous octonate ($Sn(Oct)_2$) as a grafting and polymerization agent. Du et al. (2019) and Lu et al. (2016) used microwave radiation to conduct similar grafting reactions with high grafting efficiency (Du *et al.*, 2019b; Lu *et al.*, 2016). Errezma et al. studied in situ polymerization of furfuryl alcohol catalyzed by sulfonic acid residues from the cellulose nanocrystals surface (Errezma *et al.*, 2018).

2.4 Nanotechnology for heavy metals ions removal

The use of nanomaterials for water purification has become a fascinating research area in the recent years. Nanomaterials are typically defined as materials smaller than 100 nm in at least one dimension. At the nanoscale level, materials are characterized by different physical, chemical, and biological properties compared to their larger size counterparts. Efficiency of conventional adsorbents is usually limited by their surface area or available sorption sites, the lack of selectivity and the slow adsorption kinetics. Nano-adsorbents provide significant improvements with their extremely high specific surface area associated with sorption sites and short intraparticle diffusion distance leading to fast kinetics (Oyewo *et al.*, 2019). For instance, the arsenic adsorption capacity onto nano-magnetite increased more than 100 times, when its particle size decreased from 300 to 11 nm. Several studies show that carbon nanotubes not only have higher adsorption capacities than activated carbon for heavy metals (e.g., Cu(II), Pb(II), Zn(II), Cd(II)), but also faster adsorption kinetics due to the highly accessible adsorption sites and the short intraparticle diffusion distance (Basu *et al.*, 2019). Other advantages of the properties of

nano-adsorbents are including enhanced redox, superparamagnetic, photocatalytic properties, etc. depending on the type of nano-sized adsorbents (Song *et al.*, 2019) For example, as the size decreased lower than the critical value (around 40 nm), magnetite (Fe_3O_4) particles become super-paramagnetic, losing permanent magnetic moments while responding to an external magnetic field, which allow easy separation and recovery after water treatment by low-gradient magnetic field.

Nanocellulose, which offers a combination of biosorption, nano dimensions and unique cellulosic nature, has a tremendous potential for a new and green route to solve the current heavy metal pollution problems. **Figure 2.12** shows the benefits of nanocellulose as adsorbents for heavy metal ions from the perspectives of cellulosic nature, biosorption and its nanosized.

High specific area of nanocellulose is expected to provide large number of active sites on the surface of bio sorbent to immobilize metal ions. The specific surface area of cellulose nanofiber prepared using a supercritical drying process, can be as high as 480 m^2/g (Oyewo *et al.*, 2019).

The surface functional groups functioning as metal-binding sites on the biomass irrespective of micro or nanoscale are considered responsible for immobilization of heavy metal ions. The presence of abundant hydroxyl groups on the surface of nanocellulose provides a unique platform for significant surface modification to graft a myriad of functional groups or molecules onto the cellulosic structure. The surface modifications of nanocellulose include sulfonation, TEMPO-mediated oxidation, phosphorylation, esterification, etherification, silylation, amidation, etc. All the major metal binding groups for biosorption displayed in Table 2-3 can be introduced via surface modification. In the meantime, many other physical and chemical properties of nanocellulose can be tailored by surface modifications to meet the requirements of applications.

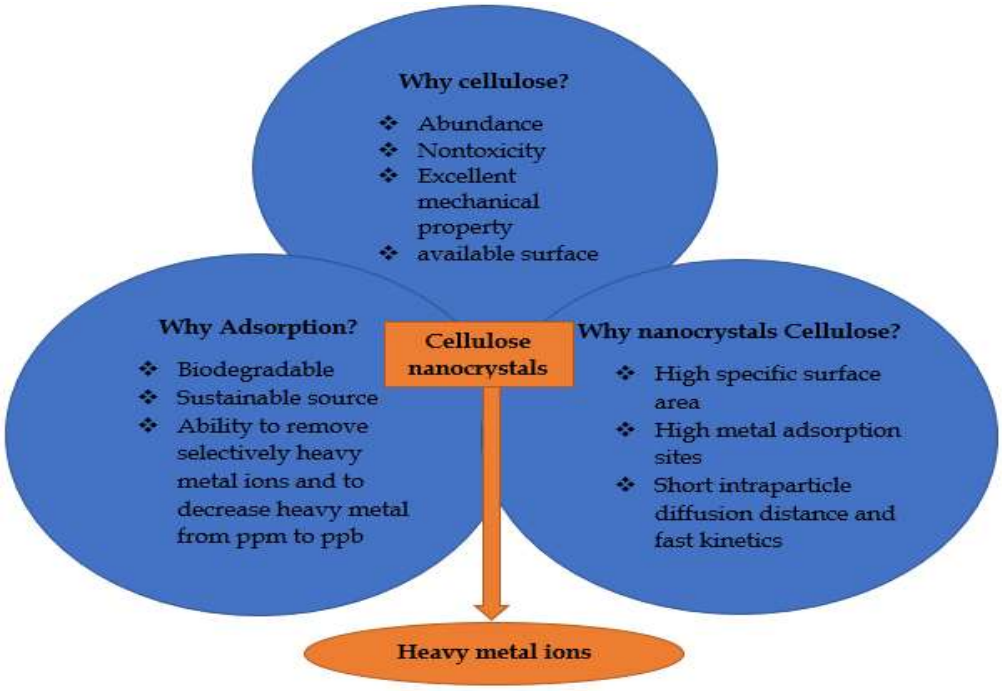

Figure 2.12: Benefits of nanocellulose as adsorbents for heavy metal ions from the perspectives of cellulosic nature, biosorption and the nanosized (Voisin et al., 2017)

Nanocellulose has good mechanical strength and rigidity that can offer adsorbents with potential for use in high-pressure environments in real water treatment applications. Stability in water environment as well as hydrophilicity of nanocellulose is also of advantage while using in water treatment. The hydrophillity is expected to reduce bio-fouling and organic fouling (Song *et al.*, 2019). Furthermore, nanocellulose, especially for cellulose nanocrystal, usually have high crystallinity, which makes the adsorbents resistant to chemical and biological corrosion in aqueous environment. However, some challenges for using nanocellulose in water purification maybe related to its agglomeration, regeneration potential, immobilization, cost effectiveness and long-term performance.

Very few studies were reported on the heavy metal adsorption properties of cellulose nanocrystals before 2012, and in the last few years, more studies are available. The adsorption efficiency of heavy metal ions, including Pb (II), Cd (II), Ni (II), As (V), Cr (III) and Cr (VI) onto cellulose nanocrystals and the chemical modified derivatives were investigated. Ma et al. (2012) reported that radioactive U(II) ions (UO_2^{2+}) in solution coordinated to the carboxylate groups of TEMPO-oxidized cellulose nanocrystals up to

167 mg/g, which is 2–3 times greater than that achieved with traditional adsorbents (i.e., montmorillonite, polymer particles, silica particles, and hydrogels (Ishak *et al.*, 2019b). The adsorption of organic contaminants, such as oils and cyclohexane has also been demonstrated with modified nanocellulose matrix grafted with hydrophobic or oleophilic functionalities (Voisin *et al.*, 2017). The removal of sorbed metallic ions was achieved through acid washing, whereas the removal of organic compounds could be achieved by submersion in organic solvents or by evaporation.

2.5 Heavy metal ions

Heavy metals in general have a density greater than 5 g per cubic centimeter and atomic weights between 63.5 and 200.6 (Jha *et al.*, 2016). The pollution of water due to the release of heavy metals into ecosystem has been a global challenge. The major sources of heavy metals are the wastewaters from industries such as metal plating facilities, battery manufacturing, fertilizer, mining, paper, and pesticides, metallurgical, fossil fuel, tannery, and production of different plastics such as polyvinyl chloride. Consequently, rapid industrialization in the past years has contributed enormously to heavy metals discharge into the environment (Igberase *et al.*, 2017). Heavy metals tend to accumulate in living organisms as they are non-biodegradable, unlike organic contaminants. Toxic heavy metals are of major concern, in the treatment of industrial wastewaters including lead, chromium, cadmium, nickel, copper and zinc. The toxic effects of these heavy metals on human health have been studied vastly. The possible symptoms of the toxic metals include high blood pressure, speech disorders, fatigue, sleep disabilities, aggressive behavior, poor concentration, irritability, mood swings, depression, increased allergic reactions, autoimmune diseases, vascular occlusion, and memory loss (Hernández-Hernández *et al.*, 2017). Though, our body needs some heavy metals such as chromium, copper and zinc but become harmful when a large amount is ingested (Li *et al.*, 2017). **Table 2.3** summarizes the allowable concentrations limits for the selected heavy metals, as reported by United State Environmental Agency (USEPA) and World Health Organization (WHO). Consequently, detailed information about these heavy metals are presented in sub-sections 2.5.1 – 2.5.4.

Table 2-3: WHO and EPA limitations of some heavy metal in drinking water .

Contaminant	Maximum allowable limit (mg/L)	Maximum allowable limit goal (mg/L)	WHO provisional guideline value (mg/L)
Lead	0.015	0	0.01
Copper	1.3	1.3	2
Zinc	5	-	3
Cadmium	0.005	0.005	0.003

2.5.1 Lead

Lead is a non-biodegradable toxic heavy metal that easily accumulates in the human body. The major source of lead in the human body is the drinking water, containing a substantial amount of lead. Initially, it can enter the body through the digestive tract and lungs and, spread by blood throughout the body. The presence of large quantity of lead in drinking water can result into; anemia, cancer, renal kidney disease, nervous system damage and mental retardation (Igberase & Osifo, 2015).

2.5.2 Copper

Copper has several applications in industrial and agricultural processes. Copper can be released into the environment from many sources. Drinking water can be a potential source for an intense copper exposition. Copper is highly toxic in drinking water, and mercury is the only metal more toxic than copper (Ihsanullah *et al.*, 2016). Although copper is important for human and animal metabolism, the excessive intake of copper brings about serious threats, such as increased blood pressure and respiratory rates damaged in kidney and liver, convulsions, cramps, vomiting, or even death (Ramos *et al.*, 2016).

2.5.3 Zinc

Zinc plays a vital role in regulating many biochemical processes and physiological functions of living tissue. However, the presence of zinc in excess causes eminent health problems, such as stomach nausea, skin irritations, cramps, vomiting, and anemia (Tian *et al.*, 2017). The industrial sources of zinc include brass platting, wood pulp production, ground and newsprint paper production, steel works with galvanizing lines, zinc and brass metal works. Waste concentrations of zinc range from less than 1 to more than

48,000 mg/L in various waste streams described in the literature (Ghassa *et al.*, 2017). Zinc is released into the environment from sediment remobilization or entrainment, agricultural activities, groundwater intrusion or from a combination of these sources (Race *et al.*, 2016).

2.5.4 Cadmium

Cadmium is a heavy metal found in natural deposits containing other elements. This element is highly toxic and considered as one of the major priority pollutants in drinking water. Cadmium was found to accumulate primarily in the kidneys and has a relatively long biological half-life in human bodies of 10–35 years (Tang *et al.*, 2016). As a drinking water pollutant, the kidney is the main target organ for cadmium toxicity. Cadmium metal is mainly used in steel and plastics industries. Therefore, the potential sources of cadmium contamination in drinking water contamination are the industrial wastewater discharge to the environment. Other industrial sources of cadmium contamination include cooling tower blow down, electroplating, metal plating and coating operations. Cadmium is also used in nickel–cadmium batteries, in thin film solar cells and in pigments. One major source of non-industrial sourced cadmium contamination in drinking-water is impurities in the zinc of galvanized pipes and some metal fittings (Wei *et al.*, 2016)

Table 2.4: Sources of contamination and potential health effects of some heavy metals

Metal	Health effects	Available sources	Uses	Ref
Lead	Anaemia, carcinogenic, abdominal muscle and joint pains, and high blood pressure	Lead acid batteries, paints, e-waste, smelting operations, coal-based thermal power plants, ceramics, and bangle industries	Car batteries, pigments, lead crystal glass, radiation protection and architecture	Fu and Wang, 2011
Copper	Stomachache, irritation of nose, mouth and eyes, headaches	Mining, electroplating, smelting operations	Electrical wiring, stoves, portable CD players, transmission wires, copper alloys and coins	Liu *et al.*, 2011
Zinc	Stomach cramps, skin irritations, vomiting, nausea, respiratory, disorders, anaemia and metal fever.	Smelting, electroplating, pig, and poultry manures	Batteries, coating, compounds, crops, diecasting alloys	Fu and Wang, 2011; Deliyanni *et al.*, 2007.
Cadmium	Carcinogenic, lung fibrosis, dyspnea, chronic lung disease and testicular degeneration	Smelting, waste batteries, e-waste, paint sludge, incineration, and fuel combustion	Electroplating of steel, nickel-cadmium batteries, cellular telephones, laptop computers and camcorders.	Ihsanullah *et al.*, 2015; Vukovic *et al.*, 2004

2.6 Factors affecting adsorption of heavy metal ions onto cellulose nanocrystals

In general, the adsorption of metal ions is known to proceed through the following steps:

(a) Transfer of metal ions from bulk solution to the adsorbent surface which is usually mentioned as external diffusion.

(b) Migration of metal ions into pores which is usually mentioned as internal diffusion (intraparticle diffusion).

(c) Interaction of metal ions with available sites on the interior surface of pores.

However, there are some crucial factors affecting adsorption and these factors are discussed in the sub-sections 2.6.1 – 2.6.5.

2.6.1 Effect of pH

During the adsorption process, solution pH is one of the significant variables that affect the speciation of metal and the surface characteristics of modified cellulose adsorbents (MCA). Thus, some research groups have investigated the effects of pH on heavy metal ion adsorption onto MCA (Oyewo *et al.*, 2019). For most heavy metal cation removal by MCA, the optimum pH was observed between pH 5.0 - pH 6.0, and heavy metal ion removal increased with the increase in pH and decreased or increased at higher pH. Under lower pH, various functional groups in MCA are protonated and thus resulted in the positively charged surface of MCA. Electrostatic repulsion will occur between cationic metal ions and positively charged MCA surface at low pH. However, the presence of hydrogen ions in the aqueous solution may also compete with the cationic metal ions for the available binding sites on MCA, which results in a lower adsorption at low solution pH. In several cases, similar trends were observed in divalent metal cation removal on various MCA. These divalent metal cations include Pb (II), Cu (II), Cd (II), Hg (II), and Ni (II). For example, adsorption of Pb (II) by modified cellulose sharply increased with increasing pH from 1.0 to 5.0 and the maximum adsorption capacity was 50.23 mg/g at pH 5.0 (Song *et al.*, 2019). The authors suggested that the low adsorption observed at low pH was due to the electrostatic repulsion between Pb (II) ions and carboxyl group on the surface of the adsorbent. In a study, Cu (II) adsorption by modified cellulose composite beads was investigated in the pH range of 2.0–5.5 (Voisin *et al.*, 2017). The results showed that the adsorption capacity of Cu (II) increased with increasing pH (from 2.0 to 4.5), then decreased when pH increased up to 5.5. According to the authors the concentration of OH ions is high enough to interact with metal ions, reducing the availability of metal ions in their free form, hence a decrease at higher pH value. Adsorption of Cu(II), Pb(II) and Cd(II) onto modified cellulose was studied in the pH range of 2.0–5.0 (Liu *et al.*, 2014). Increasing pH from 2.0 to 5.0, maximum uptakes were increased 3.5 and 8 times respectively, which was caused by metal ions having a competitive advantage in binding more adsorption sites due to the reduction of hydronium ions.

However, a higher removal efficiency of heavy metal cations on MCA was also reported even in a lower solution pH, which is possible due to ion exchange with carboxyl groups through proton exchange or anion exchange, the counter ion is exchanged with the metal ion (Zhou *et al.*, 2011). Removal of Cr(VI) onto magnetic chitosan-iron (III) hydrogel was explored in the pH range of 2.0–8.0 and the highest Cr(VI) adsorption was reached at pH 3.0. The authors suggested that Cr(VI) could be adsorbed by positively charged magnetic chitosan-iron (III) hydrogel through electrostatic attraction and ion-exchange interaction while the latter is the controlling mechanism. Huang *et al.* (2011), reported that the adsorption of Cd(II) onto bentonite modified with N-2-hydroxypropyl trimethyl ammonium chloride chitosan can be carried out via a physical cation exchange mechanism, and they found that the optimum pH was obtained at 7. Besides, at a higher pH range, the H^+ ions decrease, and the surface of the adsorbent becomes negatively charged, so the adsorptions of metal cations became favorable due to electrostatic interactions. Moreover, many researchers have explored the effects of solution pH on heavy metal oxyanion adsorption by MCA and it was observed that the stability of metal speciation and the charge status of adsorbents were pH-dependent.

2.6.2 Effect of temperature

Temperature is perceived as an important parameter for the adsorption of metal ions by adsorbents. That's mostly because the temperature of the solution may affect the solid/liquid interfaces, the swelling property of adsorbents and the mobility of metal ions. Along with solution temperature, thermodynamic parameters of an adsorption reaction were also applied to determine the nature of the adsorption process, then further investigate whether the temperature is favorable for an adsorption process (Oyewo *et al.*, 2019). Adsorption of Cd(II) and Zn(II) onto modified cellulose was studied in the temperature range from 20 to 40 °C and the optimum temperature was observed at 30 °C (Ihsanullah *et al.*, 2016). Further, the thermodynamic results indicated the feasible, spontaneous and exothermic nature of the adsorption process. A similar trend was observed in the case of Cr(VI) adsorption by modified cellulose adsorbent (Ma *et al.*, 2019). They reported that the equilibrium constant decreased with increasing temperature and the exothermic adsorbent–adsorbate interaction is favorable at lower temperature. Apart from the exothermic process, some studies reported that adsorption of metal ions onto modified cellulose increased with the increase in temperature. Adsorption of Pb(II),

Cd(II) and Zn(II) on modified cellulose was studied at five temperatures (25–65 °C) (Oyewo *et al.*, 2019). The results suggested that the adsorption capacity increased slightly with the increase in temperature and the positive value of ΔH° also proved the endothermicity of the adsorption process.

2.6.3 Effect of adsorbent dosage

To maximize the interactions between metal ions and adsorption sites of the adsorbent, getting an optimum dosage of the adsorbent is necessary. Thus, the effects of the adsorbent dosage on metal ion adsorption have been investigated by many. Oyewo *et al.* (2019) reported that the adsorption of Cr(VI) on cellulose composites increased from 77.7 to 95.0 % with an increasing dosage from 0.01 to 0.10 g, while the maximum adsorption capacity (mg/g) decreased considerably. An increase of the dose of the adsorbents may multiply the number of available adsorption sites, thus leading to the raise of the removal efficiency. However, when nearly all the heavy metals in the aqueous solutions were adsorbed by the adsorbents, the number of unoccupied active adsorption sites grew, which results in a decrease of adsorption capacities of the adsorbents. Adsorption of Cu(II), Cd(II) and Pb(II) on modified cellulose adsorbent was explored with an increasing dosage from 0.5 to 1.5 g/L (Oyewo *et al.*, 2019). The authors observed that the removal efficiency increased greatly with an increase of dosage from 0.5 to 1.0 g/L and then reached a plateau, but the adsorption capacity has no significant changes in the range from 0.5 to 1.0 g/L and then decreases remarkably. In a recent study adsorption of Cd(II) and Pb(II) cellulose beads, was studied by varying dosages from 1.5 to 6.5 g/L (ref), they found that removal capacity increased sharply from 1.5 to 4.5 g/L then reached a plateau, which could be due to increased adsorption sites.

2.6.4 Effect of contact time

It has been found that the contacts time of the absorbent and adsorbate have greatly affect the efficiency of the adsorption process. Besides, in the practical usage of absorbents, the contact time directly reflects the economic efficiency of the process, which is related to the adsorption kinetics. So, we can conclude that the contact time of the adsorption process is an important influential factor. (Huang *et al.*, 2017) observed that the removal efficiency of Cu(II) onto modified cellulose increased with increasing contact time, and the maximum removal was observed at 360 min. ref, studied the effects of contact time on

the adsorption of Pb(II) with cellulose composites and reported that the adsorption process attained equilibrium only after 60 min. A similar trend was observed in the case of nickel and lead adsorption on cellulose composite (Oyewo *et al.*, 2019). The authors observed that the total adsorption of the adsorbent for all studied ions did not change remarkably after 30 min. (Voisin *et al.*, 2017), studied the effects of contact time on the adsorption of Pb(II), Cd(II), Cu(II) and Ni(II) onto the cellulose membrane, and the results showed that more than 80% of total adsorption of metal ions occurred within the first 60 min and then reached adsorption equilibrium after approximately 120 min. Adsorption of Cr(VI) onto cellulose was studied in the contact time range of 0–400 min, and the study suggested that the concentration of Cr(VI) decreased obviously during the first 30 min, then decreased gradually and finally reached the equilibrium state within 400 min (ref).

2.6.5 Effect of co-existing ions

The presence of co-existing ions (viz. Na^+, Cl^-, NO_3^-, SO_4^-, PO_4^- and other metal cations) in solutions will lead to competitive adsorption, affecting the removal efficiency of heavy metal ions onto modified cellulose. Song *et al.* (2019) reported that adding Cl^-, NO_3^-, SO_4^-, and HCO_3^- ions resulted in a slight increase in Cu(II) adsorption. The adsorption capacity varied between 118 and 120 mg/g in the presence of common ions, while it was 126 mg/g in the absence of common ions. In addition, the influence of ionic strength and electrolyte type (NaCl and $NaNO_3$) on the adsorption of Pb (II) and Cu (II) ions was explored by (Kaboorani & Riedl, 2015). They found that the removal of Pb (II) and Cu (II) decreased with increasing ionic strength of the electrolyte solutions when cellulose was used as an adsorbent, attributed to increased competition for adsorption sites. Voisin *et al.* (2017) reported that the addition of cations (Ca^{2+} and Mg^{2+}) did not affect the adsorption capacity of Cr(VI) by third-generation polyamidation chitosan beads. By contrast, anions like SO_4^-, and HCO_3^- have marginal interfering effects on Cr(VI) adsorption while the effect of Cl^- and NO_3^- is not significant.

2.7 Batch Adsorption Kinetics

The kinetics of a system influences the metal ions residence time. It is controlled by the physical and chemical properties of the adsorbent which also has an impact on the binding mechanism (Fang *et al.*, 2014). Most studies apply the pseudo-first order kinetics of Lagergren, (Lagergren, 1898), the pseudo-second order kinetic model that was

introduced by Ho and McKay (Ho and Mckay, 1999), intra-particle diffusion and external diffusion model as shown in Equations 2.1-2.4 respectively, to describe kinetic data. These models are used to investigate the controlling mechanism of the adsorption process.

$$log(q_e - q_t) = log(q_e) - t\frac{K_1}{2.303} \quad (2.1)$$

where q_e and q_t represents the amount of metal ions absorbed on the adsorbent (mg/g) at equilibrium and time t, respectively. K_1 (min^{-1}) is the rate constant of the pseudo-first order kinetics. The value of adsorption rate constant, K_1 can be calculated from the straight-line plot of $\log(q_e - q_t)$versus t. The pseudo-second order kinetic model is given as:

$$\frac{t}{q_t} = \frac{1}{K_2 q_e^2} + \frac{1}{q_e}t \quad (2.2)$$

where K_2 (g/mg.min) is the rate constant for a pseudo-second order model and the definitions of q_e and q_t remains the same. The slope and intercept of the linear plot of t/q_t versus t, gives the values of q_e and K_2 respectively.

Intra-particle diffusion model is very vital in that it is the rate-determining step in any liquid/solid adsorption system (Race *et al.*, 2016). This model describes three stages of adsorbate binding process by adsorbents. In stage one, binding occurs on the exterior surface of adsorbent until the exterior surface is filled with metal ions. In stage two, the metal ions at the surface of the adsorbent enter the pores creating increased diffusion resistance due to crowding. The third stage is very slow due to reduced adsorbate concentration in the mixture and at this stage, equilibrium is established between the metal ions in solution and the adsorbed ions (Race *et al.*, 2016). Intra-particle diffusion model as shown in Equation 2.3 varies directly with the rate constant and the square root of time.

$$q_t = K_{id}\sqrt{t} \quad (2.3)$$

t is the time (min), K_{id} (g/mg.g$min^{1/2}$) is the intra-particle diffusion rate constant. The slope of the linear plot of q_t against $t^{1/2}$ give the value of K_{id}. The Eolic model is shown in equation 2.4

$$q_t = \frac{1}{A}\ln \alpha A + \frac{1}{A}\ln t \quad (2.4)$$

where q_t ($mg.g^{-1}$) is the adsorption capacity at time t, and qe ($mg.g^{-1}$) is the equilibrium adsorption capacity. $K_a(min^{-1})$ is the pseudo-first-order rate constant, A ($g.mg^{-1}$) is the amount of surface coverage and active energy.

2.8 Equilibrium model

Frequently, the adsorption loading process is defined as an equilibrium-controlled process. The analysis of isotherm data is essential to develop an equation which accurately represents the results which can be used to optimize an operating procedure and for design purpose. The most frequently applied isotherms in solid/liquid systems are Langmuir and Freundlich model (Favvas *et al.*, 2016; Xu *et al.*, 2018). The simplicity of their empirical equation, easy estimation of the adjustable variable and the straightforward interpretability are some of the reasons for the extensive use of these models. At the same time, linear regression has frequently been used to evaluate the model parameters (Favvas *et al.*, 2016). However, equilibrium such as discussed by Temkin, Redlich-Peterson and Dubinin-Radushkevitch (D-R), Langmuir-Freundlich (Sips isotherm), can also be used to model experimental data (Amphlett *et al.*, 2018).

2.8.1 Langmuir isotherm model

The Langmuir isotherm model, also called monolayer model, was developed to represent chemisorption (Huang *et al.*, 2017). Langmuir theoretically examined the adsorption of gases on solid surfaces and considered sorption as a chemical phenomenon. The Langmuir equation shows the content of molecules on a solid surface at a fixed temperature. This isotherm assumes that the adsorption process is limited to monolayer coverage, all the surfaces sites are similar, and that it only accommodates one adsorbed molecule. The ability of a molecule to be adsorbed on a given site is independent of another site occupation. The adsorption process is reversible and the adsorbed molecule cannot move over the surface or interact with other molecule (Borandegi & Nezamzadeh-Ejhieh, 2015). By applying these assumptions and the kinetic principle (rate of adsorption and desorption from the surface is equal), the Langmuir isotherm model can be written in the following linear Equation (2.7).

$$\frac{C_e}{q_e} = \frac{C_e}{q_{max}} + \frac{1}{bq_{max}} \qquad (2.7)$$

where C_e is the equilibrium concentration (mg/L) and q_e the amount adsorbed at equilibrium (mg/g). The Langmuir constant q_{max} (mg/g) represent the maximum adsorption capacity and *b* relates to the rate of adsorption. Higher values of *b* indicate much stronger affinity of metal ion adsorption(Kushwaha *et al.*, 2017).

2.8.2 Freundlich isotherm model

The Freundlich isotherm was originally of an empirical nature but later interpreted as sorption to heterogeneous surfaces or surfaces supporting sites of various affinities. This isotherm is derived from the assumption that the adsorption sites are distributed exponentially with respect to the heat of adsorption (Pawar *et al.*, 2016). It is also assumed that the stronger binding sites are occupied first and that binding strength decreases with an increasing degree of site occupation (Igberase & Osifo, 2015). The Freundlich isotherm describes the adsorption of organic and inorganic compounds on a wide variety of adsorbents (Kushwaha *et al.*, 2017). According to this model, the adsorbed mass per mass of solvent can be expressed by a power law function of the solute concentration.
This model is described in Equations (2.8).

$$\text{Log } q_e = \log K_f + \frac{1}{n} \log C_e \qquad (2.8)$$

Where K_f is the Freundlich constant related to adsorption capacity (mg/g), *n* is the heterogeneity coefficient (dimensionless). Favorable adsorption tends to have a Freundlich constant *n* between 1 and 10. A larger value of *n* (smaller value of 1/*n*) implies a stronger interaction between the adsorbent and adsorbate while 1/*n* equal to 1 indicates linear adsorption leading to identical adsorption energies for all sites. Linear adsorption generally occurs at very low solute concentration and low loading of the adsorbent.

2.8.3 The Dubinin- Radushkevich isotherm

The Dubinin-Radushkevich isotherm is applied to estimate the characteristic porosity and the apparent free energy of adsorption. This isotherm model does not assume a homogenous surface or constant sorption potential (Amphlett *et al.*, 2018). It enables researchers to distinguish between the chemical and physical sorption of metal ions. The Dubinin- Radushkevich isotherm offers a three-parameter equation, used to represent solute adsorption data on heterogeneous surfaces in Equation (2.9)

$$\ln q_e = \ln q_{max} - k\beta^2 \qquad (2.9)$$

where q_e is the amount of ion adsorbed in (mg/g), q_{max} is the D-R monolayer capacity(mg/g), k is energy constant in (mol^2/kJ^2) and β is the Polanyi potential which is related to the equilibrium concentration which is defined in equation (2.10)

$$\beta = RT \ln\left(1 + \frac{1}{C_{eq}}\right) \tag{2.10}$$

where R is the gas constant 8.314 in kJ/mol.K, T is the temperature in K and C_e is the equilibrium concentration in solution (mg/L). The slope of the plot of ln q_e versus β gives k (mol^2/Kj^2) and of the intercept yields the adsorption capacity q_{max} (mg/g).

The energy required to remove each molecule of metal ion from the solution to the adsorption site can be calculated using Equation (2.11)

$$E = \frac{1}{\sqrt{-2K_{ad}}} \tag{2.11}$$

The value of free energy E is vital and can be used to obtain the nature of the adsorption process. If the value of E is ≤ 8 kJ/mol, the adsorption process is physical in nature, but if it is between 8 and 16 kJ/mol, then it can be explained by the ion exchange mechanism.

2.9 Determination of enthalpy and entropy of adsorption

The original ideal of thermodynamics is based on the assumption that in a system that is kept isolated, where energy cannot be gained or lost to the surroundings, the entropy change is the driving force. In environmental engineering practice, both energy and entropy factors must be considered to decide what processes will occur spontaneously (Raval *et al.,* 2016). The entropy and enthalpy change associated with the process can be calculated from Equation 2.12.

$$\ln K = -\frac{\Delta H^o}{RT} + \frac{\Delta S^o}{R} \tag{2.12}$$

The Gibbs free energy change, ΔG^o, is the fundamental criterion of spontaneity. Reactions occur spontaneously at a given temperature if ΔG^o is a negative quantity (Safarzadeh & Miller, 2016). The free energy of the adsorption reaction in relation to the enthalpy, entropy and adsorption equilibrium constant is given by Equation 2.13

$$\Delta G^\circ = \Delta H^\circ - T\Delta S^\circ = -RTIn\text{k} \tag{2.13}$$

The equilibrium constant 'K' as defined mathematically by Liu *et al.* 2008, is given in Equation 2.14.

$$K = \frac{q_e}{C_e} \tag{2.14}$$

ΔS^o is the entropy change while ΔH^o is the enthalpy change. Equilibrium adsorption experiment carried out at different temperatures can be used to determine ΔH^o and ΔS^o which can be calculated from the slope and intercept of a plot of lnK as a function of 1/T of Equation 2.12.

2.10 Modelling of packed bed column

Packed bed columns are applied in most large-scale operation. The behavior of packed bed column is often illustrated with breakthrough curves. The adsorbent material is packed in a column and fluid flows continuously through the column where dynamic adsorption takes place. As the process continues, the amount adsorbed in the column becomes in equilibrium with the adsorbate influent concentration. This is called the saturation zone. Thereafter, can be observed a region with increasing concentration of the adsorbate in which the mass transfer occurs, also referred to as the mass transfer zone (MTZ), or sometimes referred as the shock wave front. The depth of this zone is controlled by many variables such as characteristics of the adsorbate and the adsorbent, flow velocities and bed height. This zone advances to the bottom of the column where the adsorbate concentration in the fluid starts to rise gradually. This breakthrough point eventually turns into exhaustion point. Normally the breakthrough curve takes an S-shape. Systems with high film transfer coefficients, high internal diffusivities or favorable isotherms result in steeper slopes (Hernández-Hernández *et al.*, 2017).

In the design of a packed bed column for adsorption process, the time for breakthrough and shape of the breakthrough curve are key factors in determining the operation and dynamic performance of an adsorption packed column (Khadhri *et al.*, 2019; Zhang *et al.*, 2015, , 2016). The breakthrough curve is usually obtained by plotting the ratio of effluent concentration to influent concentration against time. Mathematical models enable the design and assessment of full tests necessary to optimize operating conditions and design parameters. Several mathematical modellings have been applied to simulate adsorber

column, and the four models considered for this study are BDST model, Thomas Model, Yoon Model, and Swan model.

2.10.1 Bed Depth Service Time (BDST)

This model is used to investigate the relationship between bed depth (Z) and breakthrough time (t_b) for a given effluent concentration. The BDST model was modified by Hudchins from Bohard-Adams model and was derived on the assumption that forces such as intra-particle diffusion and external mass transfer resistance are not worth considering and that the adsorbate is directly adsorbed on the surface of the adsorbent (Saha *et al.*, 2012). This model is presented in Equation 2.15.

$$t_b = \frac{N_o}{C_o U_o} Z - \frac{1}{K_a C_o} Ln\left(\frac{C_o}{C} - 1\right) \quad (2.15)$$

Where, N_o is the saturation concentration (mg/L), C_o is the influent concentration (mg/L), C is the effluent concentration (mg/L), K_a is the adsorption rate constant (L/mg/min), Z is the bed depth (cm) and t_b is the breakthrough time of the packed column in relation to these conditions (min). Equation 2.15 can be arranged into a linear or straight-line equation as presented in Equation 2.16.

$$y = ax - c \quad (2.16)$$

where, a is the slope of BDST, defined by Equation 2.17 and c, the intercept is defined by Equation 2.18.

$$a = \frac{N_o}{C_o U_o} \quad (2.17)$$

$$c = \frac{1}{K_a C_o} Ln\left(\frac{C_o}{C} - 1\right) \quad (2.18)$$

N_o and K_a can be calculated from a and c respectively, when the breakthrough time is plotted against bed height.

2.10.2 Yoon-Nelson model

This model is quite simple to apply and requires no detailed information about the characteristics of the pollutant, the type of adsorbing material and the physical properties of adsorption (Pérez-morales & Sánchez-galván, 2019). Consequently, it is often applied to describe breakthrough curves, and this model is based primarily on the assumption that the rate of decrease, is the probability of adsorption for each molecule, and is proportional

to the probability of breakthrough. This model is expressed in non-linear and linear form in Equations 2.19 and 2.20 respectively.

$$\frac{C}{C_o - C} = exp(k_{YN}t - \tau k_{YN}) \quad (2.19)$$

$$ln\left(\frac{C}{C_o - C}\right) = k_{YN}t - \tau k_{YN} \quad (2.20)$$

where k_{YN} is the rate constant (min^{-1}), τ is the breakthrough time (min). The slope and intercept of the linear plot of $\ln\left(\frac{C}{C_o - C}\right)$ versus t give the values of k_{YN} and τ respectively.

2.10.3 Thomas model

The Thomas model is one of the mostly used model today and is applied in evaluating the rate constant and the maximum adsorption capacity of a pollutant in a packed column. In this model, the prediction of breakthrough curve is allowed hence contributes meaningfully in the design of a packed column for adsorption process. This model takes into consideration that the rate of driving force obeys second order reversible reaction and was proposed based on the assumption of Langmuir kinetics of adsorption-desorption with no axial dispersion. Thomas model is expressed in non-linear and linear form in Equations. 2.21 and 2.22 respectively.

$$\frac{C}{C_o} = \frac{1}{1 + exp\left[\frac{k_{Th}}{Q_v(q_e m_c - C_o Q_v t)}\right]} \quad (2.21)$$

$$\ln\left(\frac{C_o}{C} - 1\right) = \frac{k_{Th} q_e m_c}{Q_v} - K_{Th} C_o t \quad (2.22)$$

where k_{Th} is the Thomas rate constant, Q_v is the flow rate, m_c is the amount of adsorbent in the column and q_e is the adsorption capacity. The values of k_{Th} and q_e can be obtained respectively from the slope and intercept of the straight-line plot of $\ln\left(\frac{C_o}{C} - 1\right)$ versus t.

2.11 Optimisation process

The optimisation can be assessed using statistical analysis design software (Mini-tab, Design Expert stat-ease 6.0.8, design expert 7 to 13) . There are different approaches such as response surface method (RSM), factorial design, fractional factorial, crossed and mixture design used to discuss and explain the removal of heavy metals generated from experiment (Kaboorani & Riedl, 2015).

Fractional factorial is used to estimate the main effect, interaction and screening many factors to find significant few. This factorial can be irregular, general, D-optimal, placket Burman and Tagucchi OA. Response surface methodology is used to investigate the influence of parameters of the process, to predict optimum condition as well as to minimize the number of experiments. These properties may be determined by using different approaches such as central composite design, Box Behnken, 3-level factorial, hybrid, pentagonal, hexagonal, D-optimal, distance based, modified distance, user-defined and historical data.

In this research, response surface methodology (RSM) was applied for data analysis with the Central Composite Design (CCD) and Box Behnken Design (BBD) technique tool to achieve optimum condition for CNCs extraction and heavy metal ions removal. This also was used to determine which variables have an impact on the response interest. The choice of design technique was due to its ability to give multiple responses and its ability to used more than three factorial levels (Menezes-silva *et al.*, 2019a).

2.11.1 Response surface methodology (RSM)

RSM is simple, based on linear function and is the most frequently used method for statistical analyses in the optimisation of recovery or removal of heavy metals. The objective of RSM is to explain the interaction effects among process variables obtained from experimental data. To construct a 3D response surface and contour plot following a regression model. This experimental design methodology offers not only an efficient way of assessing uncertainty but also provide inference with a minimum number of experiments. There two major classes of RSM: Central Composite Design (CCD) and Box Behnken design (BBD). These two methods have different structures. Before applying RSM, it is essential to apply an experimental design that would define which experiment design should be carried out in the study area

2.11.1.1 Box Behnken design (BBD)

Each numerical factor is varied over three levels and has fewer runs than three level factorials. The factors are placed at one of the three space value -1, 0, +1 and the design must fit the quadratic model. The ball is located inside the box defined by a wire frame that is composed of the edges of the box. This method does not need many central points because the points on the outside are closed to the middle. The box Behnken design has

limited capability to orthogonal blocking as compared to CCD and is used for many variables (Shaheen & Fouda, 2018).

2.11.1.2 Central Composite Design (CCD)

CCD is a standard RSM design tool used to study the removal and recovery of heavy metals parameters and predict the variables. CCD is suitable for sequential experiment and fits the quadratic surface, which usually works well for process optimisation (Koech *et al.*, 2015). In CCD all the corner points lay on the surface by using a ball. Each number of factors is varied over five levels, plus and minus alpha (axial point), plus and minus one (factorial point) and center point. CCD design performs a more detailed designed as compared to box Behnken design. Artificial neural networks (ANNs), also known as neural networks (NNs), are computer systems that are modelled after the biological neural networks that make up animal brain (Won *et al.*, 2018a).

2.11.2 Artificial neural network (ANN)

Artificial neurons are a set of connected units or nodes in an ANN that loosely replicate the neurons in a biological brain. Each link can send a signal to other neurons, just like synapses in a human brain. An artificial neuron receives a signal, analyses it, and then sends signals to neurons it is connected to. Each neuron's output is generated by some non-linear function of the sum of its inputs, and the "signal" at a connection is a real number. Edges are the terms for the connections. The weight of neurons and edges is frequently adjusted as learning progresses. The signal strength at a connection is increased or decreased by the weight. Neurons may have a threshold that allows them to send a signal only if the aggregate signal exceeds it. Neurons are usually grouped into layers. On their inputs, separate layers may apply different transformations. Signals go from the first layer (input layer) to the last layer (output layer), possibly multiple times. (Dolatabadi *et al.*, 2018).

2.11.3 Adaptive neuro-fuzzy inference systems (ANFIS)

An adaptive neuro-fuzzy inference system (ANFIS), also known as an adaptive network-based fuzzy inference system, is a type of artificial neural network based on the Takagi–Sugeno fuzzy inference system. It offers the ability to incorporate the benefits of both neural networks and fuzzy logic principles in a single framework since it blends both. Its

inference system is made up of a collection of fuzzy IF–THEN rules with the capacity to approximate nonlinear functions through learning. As a result, ANFIS is regarded as a universal estimator. The best parameters acquired by genetic algorithm may be used to employ the ANFIS in a more efficient and optimal manner. It's used in intelligent energy management systems that are aware of their surroundings (Zhu & Wang, 2022).

2.12 Error analysis functions

To demonstrate the adequacy of the models, the chi square (χ^2) , Root mean square error (RMSE), Root means square errors (RMSE), Sum of the squares of errors (SSE), Sum of absolute errors (SAE), Hybrid fractional error function (HYBRID), Average relative errors (ARE), Mean square errors (MSE), Absolute average deviation (ADD), and Marquardt's percent standard deviation (MPSD), test of statistical analysis were applied. These are non-linear technique used to compare data from the experiment and model predicted data as given in relation to q_e in Equations 2.23 to 2. 30 (Ahmad *et al.*, 2021; Dolatabadi *et al.*, 2018; Ehteram *et al.*, 2021).

The chi square $\frac{\left(q_{e(exp)}-q_{e(pred)}\right)^2}{q_{e(pred)}}$ (2.23)

The RMSE $\sqrt{\frac{1}{N}\sum_{i=1}^{n}\left(\frac{\left(q_{e(exp)}-q_{e(pred)}\right)^2}{q_{e(exp)}}\right)}$ (2.24)

The SSE $\sum_{i=1}^{n}\left(q_{e(exp)}-q_{e(pred)}\right)^2$ (2.25)

The SAE $\sum_{i=1}^{n}[\left(q_{e(exp)}-q_{e(pred)}\right)]$ (2.26)

The HYBRID $\frac{1}{N-P}\sum_{i=1}^{n}\left(\frac{\left(q_{e(exp)}-q_{e(pred)}\right)^2}{q_{e(exp)}}\right)x100$ (2.27)

The ARE $\frac{100}{N}\sum_{i=1}^{n}\left([\frac{\left(q_{e(exp)}-q_{e(pred)}\right)^1}{q_{e(exp)}}]\right)$ (2.28)

The MSE $\frac{1}{N}\sum_{i=1}^{n}\left(q_{e(exp)}-q_{e(pred)}\right)^2$ (2.29)

$\text{MPSD} = 100\sqrt{\frac{1}{N-P}\sum_{i=1}^{n}\left(\frac{\left(q_{e(exp)}-q_{e(pred)}\right)^2}{q_{e(exp)}}\right)i}$ (2.30)

where the number of observations is N, the number of variables in the model is P, $q_{e(pred)}$ and $q_{e(exp)}$ are predicted and experimental adsorbent capacity, respectively.

2.13 Quantum mechanism simulation

DFT is a computer quantum mechanical modelling approach used in physics, chemistry, and materials science to study the electronic structure (or nuclear structure) (principally the ground state) of many-body systems, such as atoms, molecules, and condensed phases. The features of a many-electron system may be defined using functionals, or functions of other functions, according to this theory. These are the functionals of the spatially dependent electron density in DFT. In condensed-matter physics, computational physics, and computational chemistry, DFT is one of the most common and adaptable approaches. In general, density functional theory is finding growing use in chemistry and materials science for interpreting and predicting complicated system behaviour at the atomic scale. DFT computational approaches are used specifically for synthesis-related systems and processing parameters (Mo *et al.*, 2021).

Experimental research in such systems are frequently hampered by inconsistent results and non-equilibrium situations. Studying the impact of dopants on phase transition behaviour in oxides, magnetic behaviour in dilute magnetic semiconductor materials, and magnetic and electronic behaviour in ferroelectrics and dilute magnetic semiconductors are some examples of modern DFT applications. It has also been demonstrated that DFT produces good results in predicting the susceptibility of various nanostructures to environmental contaminants such as sulphur dioxide or acrolein, as well as mechanical properties (Xu *et al.*, 2021).

2.14. Reference

Abdelraof, M., Hasanin, M.S., Farag, M.M., & Ahmed, H.Y. 2019a. International Journal of Biological Macromolecules Green synthesis of bacterial cellulose / bioactive glass nanocomposites : Effect of glass nanoparticles on cellulose yield , biocompatibility and antimicrobial activity. *Int. J. Biol. Macromol.* 138:975–985.

Al-Qahtani, K.M. 2016. Water purification using different waste fruit cortexes for the removal of heavy metals. *J. Taibah Univ. Sci. Taibah University*. 10(5):700–708.

Amphlett, J.T.M., Ogden, M.D., Foster, R.I., Syna, N., Soldenhoff, K., & Sharrad, C.A. 2018. Polyamine functionalised ion exchange resins: Synthesis, characterisation and uranyl uptake. *Chem. Eng. J.* 334:1361–1370.

Awang, N.W., Ramasamy, D., Kadirgama, K., Samykano, M., Najafi, G., Azwadi, N., & Sidik, C. 2019a. International Journal of Heat and Mass Transfer An experimental study on characterization and properties of nano lubricant containing Cellulose Nanocrystal (CNC). *Int. J. Heat Mass Transf.* 130:1163–1169.

Basu, H., Saha, S., Mahadevan, I.A., & Pimple, M.V. 2019. Journal of Water Process Engineering Humic acid coated cellulose derived from rice husk : A novel biosorbent for the removal of Ni and Cr. *J. Water Process Eng.* 32:100892.

Borandegi, M. & Nezamzadeh-Ejhieh, A. 2015. Enhanced removal efficiency of clinoptilolite nano-particles toward Co(II) from aqueous solution by modification with glutamic acid. *Colloids Surfaces A Physicochem. Eng. Asp.* 479:35–45.

Bruel, C., Tavares, J.R., Carreau, P.J., & Heuzey, M. 2019. The structural amphiphilicity of cellulose nanocrystals characterized from their cohesion parameters. *Carbohydr. Polym.* 205:184–191.

Candido, R.G. & Gonçalves, A.R. 2019. Industrial Crops & Products Evaluation of two di ff erent applications for cellulose isolated from sugarcane bagasse in a biore fi nery concept. 142.

Errezma, M., Ben, A., Magnin, A., Dufresne, A., & Bou, S. 2018. Surfactant-free emulsion Pickering polymerization stabilized by aldehyde- functionalized cellulose nanocrystals. 202:621–630.

Fang, F., Kong, L., Huang, J., Wu, S., Zhang, K., Wang, X., Sun, B., Jin, Z., Wang, J., Huang, X.J., & Liu, J. 2014. Removal of cobalt ions from aqueous solution by an amination graphene oxide nanocomposite. *J. Hazard. Mater.* 270:1–10.

Favvas, E.P., Tsanaktsidis, C.G., Sapalidis, A.A., Tzilantonis, G.T., Papageorgiou, S.K., & Mitropoulos, A.C. 2016. Clinoptilolite, a natural zeolite material: Structural characterization and performance evaluation on its dehydration properties of hydrocarbon-based fuels. *Microporous Mesoporous Mater.* 225:385–391.

Ghassa, S., Noaparast, M., Shafaei, S.Z., Abdollahi, H., Gharabaghi, M., & Boruomand, Z. 2017. A study on the zinc sulfide dissolution kinetics with biological and chemical ferric reagents. *Hydrometallurgy*. 171:362–373.

Grishkewich, N., Mohammed, N., Tang, J., & Tam, K.C. 2017a. Current Opinion in Colloid & Interface Science Recent advances in the application of cellulose nanocrystals. *Curr.*

Opin. Colloid Interface Sci. 29:32–45.

Halász, K. 2014. theses of the ph . d . dissertation Effect of montmorillonite nanoplatelet , cellulose micro- and nanocrystal on the properties of poly (lactic acid) matrix.

Hemmati, F., Mahdi, S., Kashaninejad, M., & Barani, M. 2018a. International Journal of Biological Macromolecules Synthesis and characterization of cellulose nanocrystals derived from walnut shell agricultural residues. *Int. J. Biol. Macromol.* 120:1216–1224.

Henschen, J., Li, D., & Ek, M. 2019a. Preparation of cellulose nanomaterials via cellulose oxalates. *Carbohydr. Polym.* 213:208–216.

Hernández-Hernández, L.E., Bonilla-Petriciolet, A., Mendoza-Castillo, D.I., & Reynel-Ávila, H.E. 2017. Antagonistic binary adsorption of heavy metals using stratified bone char columns. *J. Mol. Liq.* 241:334–346.

Hu, Z., Mohamed, A., & Yu, D. 2018. International Journal of Biological Macromolecules Fabrication of carboxylated cellulose nanocrystal / sodium alginate hydrogel beads for adsorption of Pb (II) from aqueous solution. 108:149–157.

Huang, Y., Wang, W., Feng, Q., & Dong, F. 2017. Preparation of magnetic clinoptilolite/CoFe2O4 composites for removal of Sr2+ from aqueous solutions: Kinetic, equilibrium, and thermodynamic studies. *J. Saudi Chem. Soc. King Saud University*. 21(1):58–66.

Hynninen, V., Mohammadi, P., Wagermaier, W., & Hietala, S. 2019. Methyl cellulose / cellulose nanocrystal nanocomposite fibers with high ductility. *Eur. Polym. J.* 112:334–345.

Igberase, E. & Osifo, P. 2015. Equilibrium, kinetic, thermodynamic and desorption studies of cadmium and lead by polyaniline grafted cross-linked chitosan beads from aqueous solution. *J. Ind. Eng. Chem. The Korean Society of Industrial and Engineering Chemistry*. 26:340–347.

Ihsanullah, Abbas, A., Al-Amer, A.M., Laoui, T., Al-Marri, M.J., Nasser, M.S., Khraisheh, M., & Atieh, M.A. 2016. Heavy metal removal from aqueous solution by advanced carbon nanotubes: Critical review of adsorption applications. *Sep. Purif. Technol.* 157:141–161.

Ishak, N.S., Ishak, K.M.K., Bustami, Y., & Rokiah, H. 2019a. ScienceDirect Evaluation of Cellulose Nanocrystals (CNCs) as Protein Adsorbent in stick water. *Mater. Today Proc.* 17:516–524.

Ishak, N.S., Ishak, K.M.K., Bustami, Y., & Rokiah, H. 2019b. ScienceDirect Evaluation of Cellulose Nanocrystals (CNCs) as Protein Adsorbent in stick water. *Mater. Today Proc.* 17:516–524.

Jha, M.K., Kumari, A., Panda, R., Rajesh Kumar, J., Yoo, K., & Lee, J.Y. 2016. Review on hydrometallurgical recovery of rare earth metals. *Hydrometallurgy*. 165:2–26.

Kaboorani, A. & Riedl, B. 2015. Surface modification of cellulose nanocrystals (CNC) by a cationic surfactant. *Ind. Crop. Prod.* 65:45–55.

Khadhri, N., El, M., Saad, K., & Moussaoui, Y. 2019. Journal of Environmental Chemical Engineering Batch and continuous column adsorption of indigo carmine onto activated

carbon derived from date palm petiole. *J. Environ. Chem. Eng.* 7(1):102775.

Kushwaha, A.K., Gupta, N., & Chattopadhyaya, M.C. 2017. Dynamics of adsorption of Ni(II), Co(II) and Cu(II) from aqueous solution onto newly synthesized poly[N-(4-[4-(aminophenyl)methylphenylmethacrylamide])]. *Arab. J. Chem. King Saud University*. 10:S1645–S1653.

La, D.D.E., Universite, C., & Alpes, G. 2017. Development of stimuli-responsive cellulose nanocrystals hydrogels for smart applications.

Lei, W., Zhou, X., Fang, C., Song, Y., & Li, Y. 2019. Eco-friendly waterborne polyurethane reinforced with cellulose nanocrystal from o ffi ce waste paper by two di ff erent methods. *Carbohydr. Polym.* 209:299–309.

Leng, T. 2016. Cellulose Nanocrystals : Particle Size Distribution and Dispersion in Polymer Composites Tianyang Leng MSc degree in Chemistry.

Li, X., Lei, Z., Qu, J., Hu, H., & Zhang, Q. 2017. Separation of copper from nickel in sulfate solutions by mechanochemical activation with CaCO3. *Sep. Purif. Technol.* 172:107–112.

Lihong, D.U., Xu, C., Wenping, L.I., & Qixin, Z.H.U. 2011. A Study on Enhancement of Filtration Process with Filter Aids Diatomaceous Earth and Wood Pulp Cellulose. *Chinese J. Chem. Eng. Chemical Industry and Engineering Society of China (CIESC) and Chemical Industry Press (CIP)*. 19(5):792–798.

Lin, N. 2016. Cellulose nanocrystals : surface modification and advanced materials To cite this version : HAL Id : tel-01296967 Cellulose Nanocrystals : Surface Modification and Advanced Materials.

Liu, C., Jin, R., Ouyang, X., & Wang, Y. 2017. Applied Surface Science Adsorption behavior of carboxylated cellulose nanocrystal — polyethyleneimine composite for removal of Cr (VI) ions. *Appl. Surf. Sci.* 408:77–87.

Lu, J., Jin, R., Liu, C., Wang, Y., & Ouyang, X. 2016. International Journal of Biological Macromolecules Magnetic carboxylated cellulose nanocrystals as adsorbent for the removal of Pb (II) from aqueous solution. *Int. J. Biol. Macromol.* 93:547–556.

Luzi, F., Puglia, D., Sarasini, F., Tirillò, J., Ma, G., Zuorro, A., Lavecchia, R., Kenny, J.M., & Torre, L. 2019. Valorization and extraction of cellulose nanocrystals from North African grass : Ampelodesmos mauritanicus (Diss). 209:328–337.

Ma, M., Liu, Z., Hui, L., Shang, Z., Yuan, S., Dai, L., & Liu, P. 2019. International Journal of Biological Macromolecules Lignin-containing cellulose nanocrystals / sodium alginate beads as highly effective adsorbents for cationic organic dyes. *Int. J. Biol. Macromol.* 139.

Menezes-silva, R., Medeiros, B., Oliveira, B. De, Henrique, P., Fernandes, M., Yukari, L., Vargas, F., Flávia, A., Borges, S., Afonso, M., Buzalaf, R., Corrêa, R., Sidhu, S.K., Fidela, M., & Navarro, D.L. 2019a. Effects of the reinforced cellulose nanocrystals on glass-ionomer cements. *Dent. Mater. The Academy of Dental Materials* :1–10.

Meng, F., Wang, G., Du, X., Wang, Z., Xu, S., & Zhang, Y. 2019. Extraction and characterization of cellulose nanofibers and nanocrystals from liquefied banana pseudo-stem residue. *Compos. Part B*. 160:341–347.

Najwa, K. & Amin, M. 2016. Cellulose Nanocrystals Reinforced Thermoplastic Polyurethane Nanocomposites.

Niamsap, T., Tien, N., & Sukyai, P. 2019. Production of hydroxyapatite-bacterial nanocellulose sca ff old with assist of cellulose nanocrystals. *Carbohydr. Polym.* 205:159–166.

Onur, A., Shanmugam, K., Ng, A., Garnier, G., & Batchelor, W. 2019. Cellulose fibre- perlite depth filters with cellulose nanofibre top coating for improved filtration performance. *Colloids Surfaces A. Elsevier*. 583:123997.

Oyewo, O.A., Mutesse, B., Leswi, T.Y., & Onyango, M.S. 2019. Journal of Environmental Chemical Engineering Highly e ffi cient removal of nickel and cadmium from water using sawdust- derived cellulose nanocrystals. 7.

Pawar, R.R., Lalhmunsiama, Bajaj, H.C., & Lee, S.M. 2016. Activated bentonite as a low-cost adsorbent for the removal of Cu(II) and Pb(II) from aqueous solutions: Batch and column studies. *J. Ind. Eng. Chem. The Korean Society of Industrial and Engineering Chemistry*. 34:213–223.

Pei, C., Ou, Q., Yu, T., & Pui, D.Y.H. 2019a. Separation and Puri fi cation Technology Loading characteristics of nano fi ber coated air intake fi lter media by potassium chloride , ammonium sulfate , and ammonium nitrate fi ne particles and the comparison with conventional cellulose fi lter media. *Sep. Purif. Technol.* 228:115734.

Pérez-morales, J.M. & Sánchez-galván, G. 2019. Continuous dye adsorption and desorption on an invasive macrophyte (Salvinia minima). *Environmental Science and Pollution Research*. :5955–5970.

Priscila, A., Silva, M., Vitória, A., Pontes, S.M.A., Pereira, A.L.S., De, M., Filho, M.S., Rosa, M.F., & Azeredo, H.M.C. 2019. Mango kernel starch fi lms as a ff ected by starch nanocrystals and cellulose nanocrystals. 211:209–216.

Race, M., Marotta, R., Fabbricino, M., Pirozzi, F., Andreozzi, R., Cortese, L., & Giudicianni, P. 2016. Copper and zinc removal from contaminated soils through soil washing process using ethylenediaminedisuccinic acid as a chelating agent: A modeling investigation. *J. Environ. Chem. Eng.* 4(3):2878–2891.

Ramos, S.N. do C., Xavier, A.L.P., Teodoro, F.S., Gil, L.F., & Gurgel, L.V.A. 2016. Removal of cobalt(II), copper(II), and nickel(II) ions from aqueous solutions using phthalate-functionalized sugarcane bagasse: Mono- and multicomponent adsorption in batch mode. *Ind. Crops Prod.* 79:116–130.

Raval, N.P., Shah, P.U., & Shah, N.K. 2016. Adsorptive removal of nickel(II) ions from aqueous environment: A review. *J. Environ. Manage.* 179:1–20.

Salari, M., Sowti, M., Rezaei, R., Ghanbarzadeh, B., & Samadi, H. 2019. International Journal of Biological Macromolecules Preparation and characterization of cellulose nanocrystals from bacterial cellulose produced in sugar beet molasses and cheese whey media. 122:280–288.

Shaheen, T.I. & Emam, H.E. 2018. International Journal of Biological Macromolecules Sono-chemical synthesis of cellulose nanocrystals from wood sawdust using Acid

hydrolysis. *Int. J. Biol. Macromol.* 107:1599–1606.

Singh, S., Gaikwad, K.K., Park, S., & Lee, Y.S. 2017. International Journal of Biological Macromolecules Microwave-assisted step reduced extraction of seaweed (Gelidiella aceroso) cellulose nanocrystals. *Int. J. Biol. Macromol.* 99:506–510.

Song, K., Qian, X., Li, X., Zhao, Y., & Yu, Z. 2019. Fabrication of a novel functional CNC cross-linked and reinforced adsorbent from feather biomass for e ffi cient metal removal. *Carbohydr. Polym.* 222:115016.

Tang, J. 2016. Functionalized Cellulose Nanocrystals (CNC) for Advanced Applications.

Tang, J., Sisler, J., Grishkewich, N., & Tam, K.C. 2017a. Journal of Colloid and Interface Science Functionalization of cellulose nanocrystals for advanced applications. *J. Colloid Interface Sci.* 494:397–409.

Tang, J., Sisler, J., Grishkewich, N., & Tam, K.C. 2017b. Journal of Colloid and Interface Science Functionalization of cellulose nanocrystals for advanced applications. *J. Colloid Interface Sci.* 494:397–409.

Tang, X., Li, Q., Wu, M., Lin, L., & Scholz, M. 2016. Review of remediation practices regarding cadmium-enriched farmland soil with particular reference to China. *J. Environ. Manage.* 181:646–662.

Valone, M.C., Youngblood, J., Martinez, C., Youngblood, J., & Bahr, D. 2016. Effect of humidity on the creep response of cellulose nanocrystals films Is approved by the final examining committee : Approved by Major Professor (s):

Voisin, H., Bergström, L., Liu, P., & Mathew, A.P. 2017. Nanocellulose-Based Materials for Water Purification.

Wei, M., Chen, J., & Wang, X. 2016. Removal of arsenic and cadmium with sequential soil washing techniques using Na2EDTA, oxalic and phosphoric acid: Optimization conditions, removal effectiveness and ecological risks. *Chemosphere*. 156:252–261.

Won, S., Paolo, J., Soriano, E., Rajan, A., Yeon, J., Hee, C., & Sang, C. 2018a. International Journal of Biological Macromolecules Development of bioactive cellulose nanocrystals derived from dominant cellulose polymorphs I and II from Capsosiphon Fulvescens for biomedical applications. *Int. J. Biol. Macromol.* 110:531–539.

Won, S., Paolo, J., Soriano, E., Rajan, A., Yeon, J., Hee, C., & Sang, C. 2018b. International

Wu, W., Song, R., Xu, Z., Jing, Y., Dai, H., & Fang, G. 2018a. Sensors and Actuators B : Chemical Fluorescent cellulose nanocrystals with responsiveness to solvent polarity and ionic strength. *Sensors Actuators B. Chem.* 275:490–498.

Xu, J., Koivula, R., Zhang, W., Wiikinkoski, E., Hietala, S., & Harjula, R. 2018. Separation of cobalt, neodymium and dysprosium using amorphous zirconium phosphate. *Hydrometallurgy*. 175:170–178.

Yue, Y. 2011. A comparative study of cellulose I and II and fibers and nanocrystals.

Zhang, Z.-Z., Cheng, Y.-F., Zhou, Y.-H., Buayi, X., & Jin, R.-C. 2015. A novel strategy for accelerating the recovery of an anammox reactor inhibited by copper(II): EDTA washing combined with biostimulation via low-intensity ultrasound. *Chem. Eng. J.* 279:912–920.

CHAPTER THREE

EXTRACTION OF CELLULOSE NANOCRYSTALS FROM MILLET (*ELEUSINE CORACANA*) HUSK WASTE: OPTIMIZATION USING BOX BEHNKEN DESIGN IN RESPONSE SURFACE METHODOLOGY (RSM)

ABSTRACT

Cellulose nanocrystals (CNCs) and their applications have attracted growing interest in both research and industry due to their appealing properties such as excellent mechanical properties, high surface area, rich hydroxyl groups for modification, and natural properties are 100% environmentally friendly. Cellulose nanocrystals were extracted from millet husk residue waste using a homogenized acid hydrolysis method. The effects of the process variables homogenization speed (A), acid concentration (B), and acid to cellulose ratio (C) on the yield and swelling capacity were investigated and optimized using the Box Behnken design (BBD) method in response surface methodology. The cellulose and nano-cellulose obtained were characterized using transform infrared microscopy (FTIR), X-ray diffraction (XRD), thermogravimetric analysis (TGA), and scanning electron microscopy (SEM). The numerical optimization analysis results showed that the maximum yield of CNCs and swelling capacity from cellulose was 93.12 % and 2.81 % obtained at homogenization speed, acid concentration, and acid to cellulose ratio of 7464.0 rpm, 63.40 wt %, and 18.83 wt %, respectively. ANOVA revealed that the most influential parameter in the model was homogenization speed for Yield and acid concentration for swelling capacity. The mathematical models to predict cellulose nanocrystals' yield and swelling capacity were developed with R^2 of 98.9 % and 97.9%, respectively. The TGA showed that the thermal stability of cellulose was higher than that of CNCs. FTIR results showed functional groups of CNCs, and cellulose were similar. SEM image of CNCs is porous and displayed narrow particle size with needle-like morphology compared to cellulose. The XRD pattern presented an increase in the intensity of CNCs.

Keywords: Cellulose nanocrystals, Extraction, Response surface method, Box Behnken

GRAPHICAL ABSTRACT

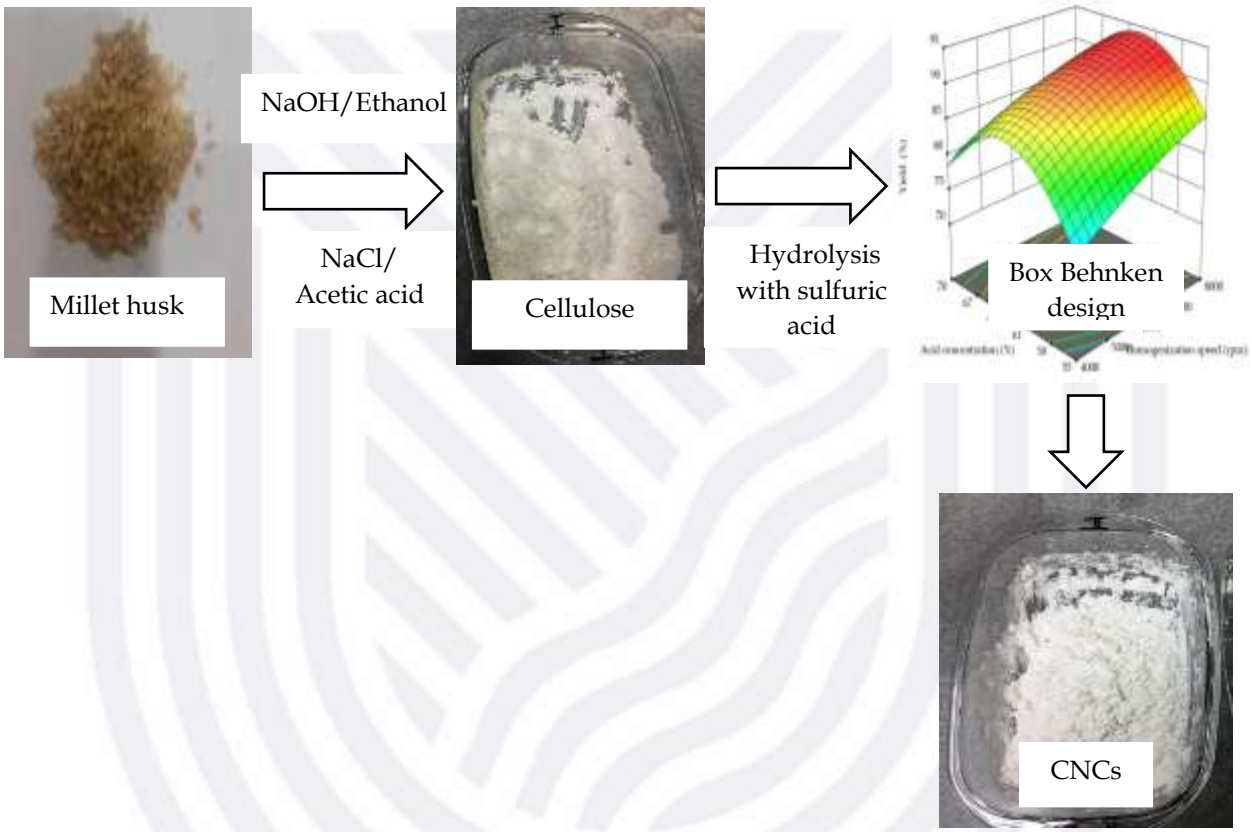

3.1. INTRODUCTION

In nanotechnology, the modification and synthesis of nanomaterials with distinct configurations and functions are gaining increasing interest due to their multiple potential uses. Nanomaterials have been used in many applications, such as nanocarriers, packaging materials, drug delivery systems, biomaterials, and water treatments (Leszczy *et al.*, 2018a; Niamsap *et al.*, 2019). However, most of the chemicals used in the production of nanomaterials come from petroleum-derivated resources which, are toxic and detrimental to the environment. Alarms about global warming towards attaining sustainable development are of great concern, and there is a critical need to substitute the traditional non-renewable materials with renewable resources (Onur *et al.*, 2019). Also, the ability to convert abundant and cheap materials to produce high-value products offers benefits.

Renewable energy is by the future the fastest-growing fuel source and gives about 14% of principal energy (Abdelraof *et al.*, 2019). Cellulose fibers synthesized from animals, plants, and bacteria are the most available resources used as renewable materials. Cellulose is the furthermost specific kind of linear homopolymer produced in billions of tons yearly, consisting of β-D glucoproprenose (1→4) fused through the hydrogen bonds (Lei *et al.*, 2019). Cellulose predominately exists in the cell walls of plants and is crucial for the rigidity of the cell wall (Hynninen *et al.*, 2019). Cellulose is applied in many applications because it is stable, biodegradable, environmentally friendly, and readily available (Awang *et al.*, 2019).

In recent years, the use of cellulose has been in nanotechnology materials (Meng *et al.*, 2019a). Acidic/alkaline hydrolysis extraction methods with sulfuric acid proceed with the removal of amorphous regions within the molecular structure of cellulose, while the crystalline parts called nanoparticles are undamaged (Wu *et al.*, 2018). Cellulose nanocrystals are produced via alkaline/acidic hydrolysis, steam explosion, enzymatic hydrolysis, high-pressure symmetry, sonication, and grinding processes (Awang *et al.*, 2019; Hemmati *et al.*, 2018).

The physical and chemical properties of cellulose nanocrystals can vary depending on the extraction method and the source of cellulose. Cellulose nanocrystals have been extracted from alkali/hydrolysis methods using wall nutshells, banana peels, palm date fiber, sawdust, sago seed, and waste paper (Meng *et al.*, 2019b; Oyewo *et al.*, 2019; Priscila *et al.*, 2019; Shafiei *et al.*, 2010; Souza *et al.*, 2017). CNCs is used in the cosmetic and pharmaceutical industries as excipient, binder, and adsorbent. They also serve as an additive, emulsifier, stabilizer, thickener, fat substitute, anti-caking agent, gelling agent, and suspending agent in the beverage and food industries.

The two types of millets that are grown in Sub-Saharan Africa are the pearl millet (Pennisetum glaucum) and finger millet (Eleusine coracana) for nutritional values as it contains high amounts of calcium (Du *et al.*, 2019). After harvesting, the husks are discarded as agricultural waste and be a source of cellulose.

There have been few published studies on optimization studying the extraction of cellulose nanocrystals from finger millet husk using response surface methodology. The response surface methodology is employed to analyze the impact of process parameters and predict the optimum condition at a minimized number of experiments. Optimization and investigating the effect of process variables can be determined using 3-level factorials, central composite design, hybrid, pentagonal, hexagonal, D-optimal, distance-based, and box Behnken (Zolgharnein *et al.*, 2017).

In this study, the Box Behnken design (BBD) in response surface methodology tool was used to determine the optimum conditions for extracting cellulose nanocrystals from millet husk. The selection of the design method was due to its capability to allow multiple responses. The individual numerical factor is varied over three levels and has fewer runs associated with the three-level factorials (Yalç *et al.*, 2019). This method does not require several central points since the points on the surface are closer towards the midpoint. Because the model proposed by the combinations does not incorporate the study of the components in their upper and lower limits concurrently, the advantage of using BBD is to avoid doing experiments under extreme conditions.

The effects of process variables on the CNCs yield and swelling were determined and numerically optimized. Analysis of variance (ANOVA) was, used as a statistical and diagnostic checking test tool. The novelty is focused on using millet husk waste as a new

biomass material for generating CNCs particles. We also look at how to extract CNCs from raw millet husk waste by using varied acid hydrolysis reaction durations, homogenization speed and acid/cellulose ratio. The resulting CNCs were characterized to assess the production yield and swelling capacity. To clearly understand the change in attributes of CNCs particles, their physical chemistry, crystallinity, and thermal stability were also assessed.

3.2. MATERIALS AND METHODS

3.2.1 Materials

Millet husk residues (with a density of 0.950 g/cm^3 and melt flow index of 7.2 g/10 min) were obtained from a millet farm in Kenya. Sigma Aldrich and Merck Chemical South Africa provided analytical grades of sulfuric acid, sodium chlorite, sodium hydroxide, acetic acid, and ethanol.

3.2.2. Production of cellulose from millet husk waste

The millet husk waste was washed, air-dried, milled, and sieved with a 45-mesh sieve. The oil was removed from the ground husk by solvent extraction with ethanol at 65°C for 6 hours. The unextracted sample was dried in an oven at 65°C for 15 hours and was stored in a tight polythene bag. 50 g of cellulose was mixed with 500 ml of 7.0 percent aqueous sodium hydroxide. At 25°C, the mixture was agitated for 60 minutes.

To eliminate wax and oil, the pretreated sample was rinsed with 90 percent ethanol severely filtered at 25°C. The cellulose was then dried in an oven at 65°C for 18 hours. Finally, 200 mL of deionized water, 1.5g sodium chlorite, and 25 mL acetic acid were added to decolourize the cellulose. At 70°C, the mixture was stirred for 3 hours and filtered. The cellulose produced was thoroughly washed with deionized water. The final cellulose was dried for 24 hours in an oven. The cellulose obtained was used to produce cellulose nanocrystals.

3.2.3 Cellulose nanocrystals extraction

The acidic hydrolysis technique was used to produce cellulose nanocrystals from cellulose 65 wt % sulfuric acid was used. Cellulose was mixed with the acid to cellulose ratio (1:15, 1:20, 1:25) using a homogenizer at speeds of (4000, 6000, 8000 rpm) for 10 min at 50 °C. After that, the suspension formed was diluted five times with deionized water to

discontinue the hydrolysis process. The suspension was centrifuged for 15 minutes to remove excess sulphuric acid before discarding the supernatant. The suspension was placed in a dialysis bag and repetitively rinsed with deionized water to achieve a pH of 7. For 15 minutes, the washed sample was homogenized in an ultrasonic setup. For 72 hours, the CNCs were, dried and to prevent microorganism contamination, a drop of chloroform was added before storing the cellulose nanocrystal powder in a tight, impenetrable vessel.

3.2.4 Physical and chemical properties of cellulose nanocrystals

3.2.4.1 Yield of cellulose nanocrystals

The samples were precisely measured using a digital balance. The measurements were performed in triplicates, and the average and standard deviations values were recorded. The yield of CNCs was calculated using Equation (3.1).

$$\text{Yield}\ (\%) = \frac{m_1 - m_2}{m_3} \times 100 \qquad (3.1)$$

Where m_1 (g) is the weight of cellulose nanocrystals with the vial, m_2 (g) is the weight of the vial, and m_3 (g) is the weight of cellulose used.

3.2.4.2 Cellulose nanocrystals swelling capacity

2g of CNCs sample was weighed and placed in a conical flask, followed by 20 mL of distilled water. The volume is measured after being left for 24 hours in a controlled room temperature environment. Equation (3.2) was used to calculate swelling capacity

$$\text{SWC}\ (mg/L) = \frac{V_2 - V_1}{m} \times 100 \qquad (3.2)$$

Where m (g) is the weight of the cellulose nanocrystals, V_1 (mL) is the initial volume of the CNCs, and V_2 (mL) is the volume of the CNCs together with the absorbed water.

3.2.5 Experimental design and optimization

3.2.5.1 RSM-Box Behnken experimental design

The evaluation of the linear, cubic, and quadratic effects on the yield and the swelling capacity of CNCs was studied using the Box Behnken design in RSM. The choice of this design technique was to permit multiple responses and its capability to use three levels of factorials. Each numerical factorial is varied over three levels and has fewer runs than the three-level factorials (Yalç *et al.*, 2019). The BBD was designed by considering the response

as the yield and swelling capacity and the independent variables as homogenization speed (A), acid concentration (B) and acid/cellulose ratio (C). The mathematical correlation amongst the independent variables and dependent variable in the response is explained by the second-order polynomial using Equation (3.3).

$$Y = \gamma_0 + \gamma_a A + \gamma_b B + \gamma_c C + \gamma_{aa} A^2 + \gamma_{bb} B^2 + \gamma_{cc} C^2 + \gamma_{ab} AB + \gamma_{ac} AC + \gamma_{bc} BC \quad (3.3)$$

Where Y is the predicted response, γ_0 is the model constant, A, B, and C are independent variables. γ_a, γ_b and γ_c are linear coefficients and γ_{ab}, γ_{ac} and γ_{bc} are cross-product coefficients, and γ_{aa}, γ_{bb} and γ_{cc} are the quadratic coefficients. The various stages of CNCs extraction based on RSM are presented in **Figure 3.1.** Homogenization speed (4000-8000 rpm), acid concentration (55-70 %) and acid/cellulose ratio(15-25) are taken as input variables (**see Table 3. 1**). **Table 3.2** shows the Box Behnken set of experiments conducted and their results.

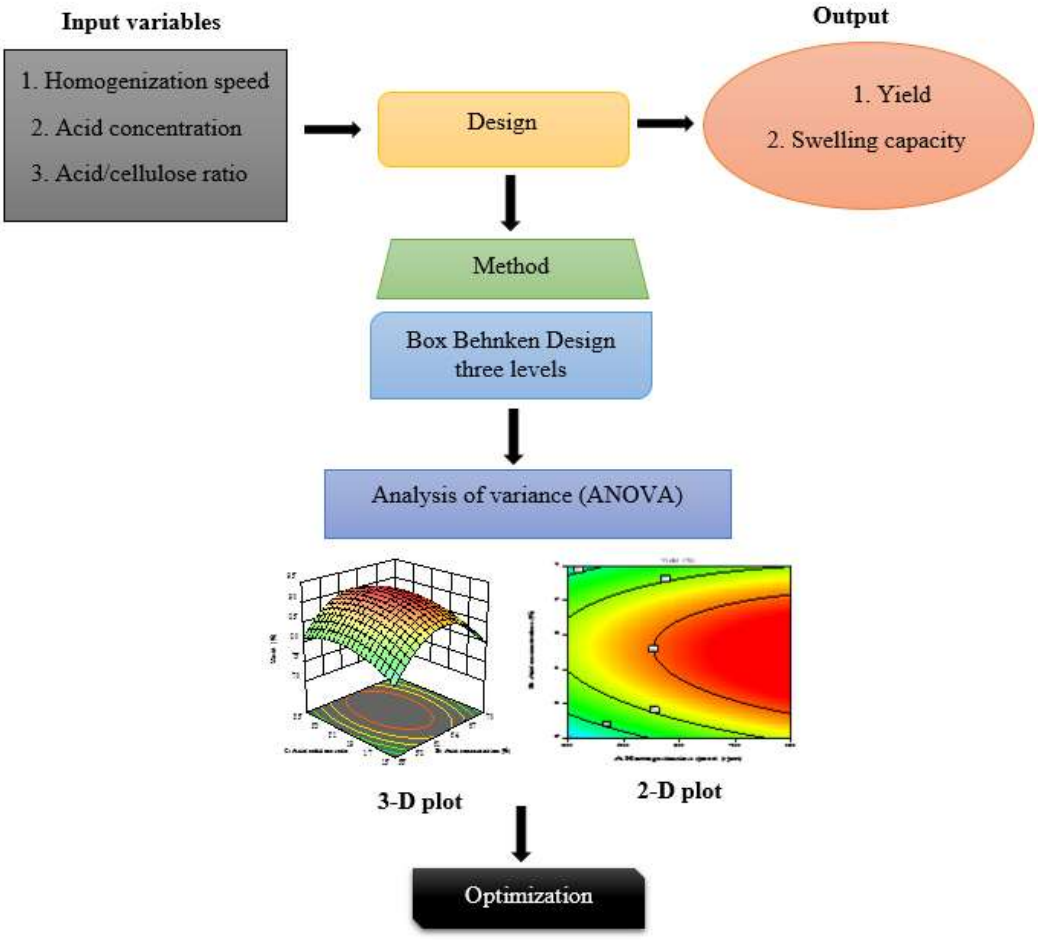

Figure 3.1: RSM technique for optimum condition for CNCs extraction

Table 3.1: Range of factors and their levels used in the Box Behnken design.

Variable	Coded symbol	Coded level		
		-1	0	+1
Homogenization speed(rpm)	A	4000	6000	8000
Acid concentration (wt %)	B	55	62.5	70
Acid to cellulose ratio (wt %)	C	15	20	25

3.2.5.2 Model fitting, statistical analysis, and numerical optimization

A design expert (Version 13) was, used to fit experimental data to the second-order mathematical polynomial regression model. The statistical importance evaluation of the model was determined using ANOVA and optimized numerically.

3.2.6 Characterization of cellulose and cellulose nanocrystals from millet husk

3.2.6.1 Fourier transform infrared spectroscopy (FTIR)

Fourier transform infrared spectroscopy analysis of samples was performed using a VARIAN 7000 spectrometer at a resolution of 4 cm^{-1} and a range of 500- 4500 cm^{-1}.

3.2.6.2 Scanning electron microscopy (SEM)

A scanning electron microscope (Philips XL 30FEG) was employed to examine the morphology. All samples were coated with platinum using the sputtering technique.

3.2.6.3 X-Ray diffraction (XRD)

X-ray diffraction of samples was using Cu kα radiation source in a Phillips X'pert Model 0993. The diffraction intensity was recorded between 5 and 90º (2θ angle range) with a scanning speed of 0.4ºC per min. The relative crystallinity index of the model was calculated by following Equation (3.4).

$$CI\ (\%) = \frac{I_{02} - I_{an}}{I_{02}} \times 100 \qquad (3.4)$$

I_{02} is the maximum diffraction intensity of the plane, and I_{an} represents the diffraction intensity of the amorphous part.

3.2.6.4 Thermogravimetric analysis (TGA)

Thermogravimetric analysis was determined using a thermogravimetric analyzer (NETZSCH5 209F3). The temperature was ramped 50 to 700ºC at the heating rate of 10°C/min under nitrogen gas.

Table 3.2: Box Behnken design and results for yield and swelling capacity of CNCs

Run	A: Homogenization speed (rpm)	B: Acid concentration (%)	C: Acid to cellulose ratio	Yield (%)	Swelling (%)
1	6000	62.50	20.00	87 ± 1.8	2.6 ± 2.9
2	4000	55.00	20.00	72 ± 2.3	3.7 ± 1.5
3	8000	62.50	15.00	85 ± 1.1	2.7 ± 3.8
4	6000	55.00	25.00	78 ± 1.2	3 ± 1.8
5	6000	55.00	15.00	80 ± 1.8	3.1 ± 2.6
6	8000	70.00	20.00	88 ± 3.2	2.8 ± 3.4
7	6000	62.50	20.00	92 ± 2.5	2.6 ± 3.6
8	4000	62.50	15.00	83 ± 2.7	2.5 ± 1.6
9	6000	70.00	15.00	80 ± 1.4	2.1 ± 3.2
10	6000	62.50	20.00	92 ± 2.1	2.57 ± 4.1
11	4000	70.00	20.00	77 ± 1.7	2.6 ± 2.3
12	6000	62.50	20.00	92 ± 2.5	2.59 ± 3.5
13	8000	55.00	20.00	87 ± 2.3	3.9 ± 1.4
14	6000	62.50	20.00	92 ± 1.9	2.6 ± 3.3
15	6000	70.00	25.00	77 ± 1.6	2.4 ± 2.2
16	8000	62.50	25.00	92 ± 1.2	2.8 ± 4.2
17	4000	62.50	25.00	87 ± 3.1	2.7 ± 3.9

3.3 RESULTS AND DISCUSSION

3.3.1 The development of quadratic equation for predicting yield and swelling capacity of CNCs

The insignificant terms were eliminated, using the Fischer's test, and the resulting final equation for predicting the yield and swelling capacity of CNCs are shown in Equation (3.5) and Equation (3.6), respectively.

$$\text{Yield (\%)} = 91.48 + 4.04A + 0.59B + 0.83C - 0.90AB + 0.81AC - 0.19BC - 1.22A^2 - 9.31B^2 - 3.54C^2 \quad (3.5)$$

$$\text{SWC (\%)} = 2.58 + 0.09A - 0.46B + 0.06C + 0.05AB - 0.01AC + 0.19BC + 0.33A^2 + 0.32B^2 - 0.25C^2 \quad (3.6)$$

The negative and positive signs in the quadratic models to predict the yield and swelling capacity of CNCs expresses the antagonist and synergic effect, respectively.

The regression coefficient (R^2) values of the obtained models are 0.989 for the yield and 0.979 for the swelling capacity of CNCs. As shown in **Figure 3.2** 98.9% and 97.9% of the experimental data are explained.

3.3.2 ANOVA for regression results for yield and swelling capacity of CNCs

Table 3.3 and Table 3.4 show the ANOVA for the regression model for predicting the yield and swelling of CNCs, respectively. The quadratic model equations show that F= 672.80 and F= 413.55 for the yield and swelling capacity of CNCs, respectively, with P <0.0001 suggesting that the models are significant in predicting the yield and the swelling capacity. The ANOVA results, shown in **Table 3.3**, indicate that the homogenization speed and acid to cellulose ratio individual terms are significant terms in the model the acid concentration term is insignificant. In the case, ANOVA results shown in **Table 3.4** for predicting the swelling capacity of CNCs in all individual terms are significant in the model. The interaction terms are insignificant and, all quadratic terms are significant in the model for predicting the yield and swelling capacity of CNCs.

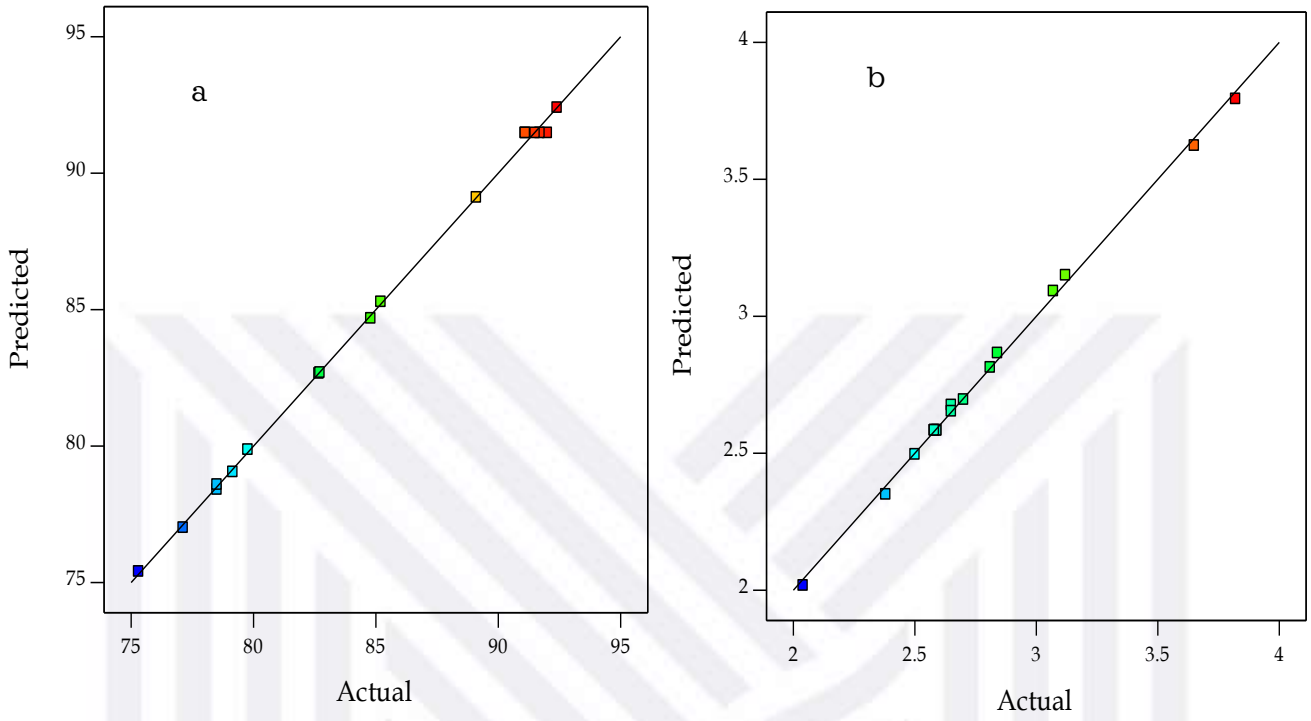

Figure 3.2: A plot between the predicted and experimental values for yield (a) and (b) for swelling capacity of cellulose nanocrystals.

Table 3.3: ANOVA for regression model equation for the yield of CNCs when insignificant terms are removed.

Source	Sum of Squares	Df	Mean Square	F-value	p-value	Significance
Model	594.12	9	66.01	672.80	< 0.0001	significant
A-Homogenization speed	130.49	1	130.49	1329.95	< 0.0001	
B-Acid concentration	2.87	1	2.87	29.23	0.001	
C-Acid to cellulose ratio	5.51	1	5.51	56.17	0.0001	
AB	3.26	1	3.26	33.21	0.0007	
AC	2.66	1	2.66	27.08	0.0012	
BC	0.14	1	0.14	1.47	0.0264	
A^2	6.31	1	6.31	64.26	< 0.0001	
B^2	364.85	1	364.85	3718.53	< 0.0001	
C^2	52.65	1	52.65	536.63	< 0.0001	
Residual	0.68	7	0.098			

Table 3.4: Results of ANOVA for regression model for the swelling capacity of CNCS when insignificant terms are removed.

Source	Sum of Squares	Df	Mean Square	F-value	p-value	Significance
Model	3.05	9	0.3394	413.55	< 0.0001	significant
A-Homogenization speed	0.0648	1	0.0648	78.96	< 0.0001	
B-Acid concentration	1.76	1	1.76	2141.81	< 0.0001	
C-Acid to ratio	0.0378	1	0.0378	46.07	0.0003	
AB	0.0001	1	0.0001	0.1218	0.7373	
AC	0.0004	1	0.0004	0.4874	0.5076	
BC	0.038	1	0.038	46.33	0.0003	
A^2	0.4704	1	0.4704	573.17	< 0.0001	
B^2	0.4359	1	0.4359	531.11	< 0.0001	
C^2	0.27	1	0.27	329.04	< 0.0001	
Residual	0.0057	7	0.0008			

3.3.3 The effect of process variables on the yield and swelling capacity of CNCs

3.3.3.1 Effects of homogenization speed and acid concentration on the yield of CNCs

The maximum yield was predicted to be 94.9%, according to the RSM. **Figure 3.3** shows the effect of homogenization speed and acid concentration on the yield of CNCs; the acid to cellulose mass ratio is held constant at 20 wt %. At high acid concentrations (64%), the yield of CNCs is much higher than at low acid concentrations. Because, at low acid concentration, the acid can not access and attack the amorphous regions of the cellulose. At a high acid concentration, as time and homogenization speed increases, the formation of glucose takes place as cellulose degrades and hence a reduction in the number of cellulose nanocrystals produced. As the homogenization speed increases to 8000 rpm, the yield of CNCs increases due to the more chances at which the cellulose particles are dispersed throughout the sulphuric acid. Another explanation could be that as the homogenization speed increases, there are more collisions between the cellulose and the sulphuric acid molecules. The glycosidic bond breaks down between cellulosic chains resulting in the reduction of amorphous chains and more crystalline structure. The circular nature contour plot revealed that homogenization speed and acid concentration significantly interact with yield performance(Lei *et al.*, 2019).

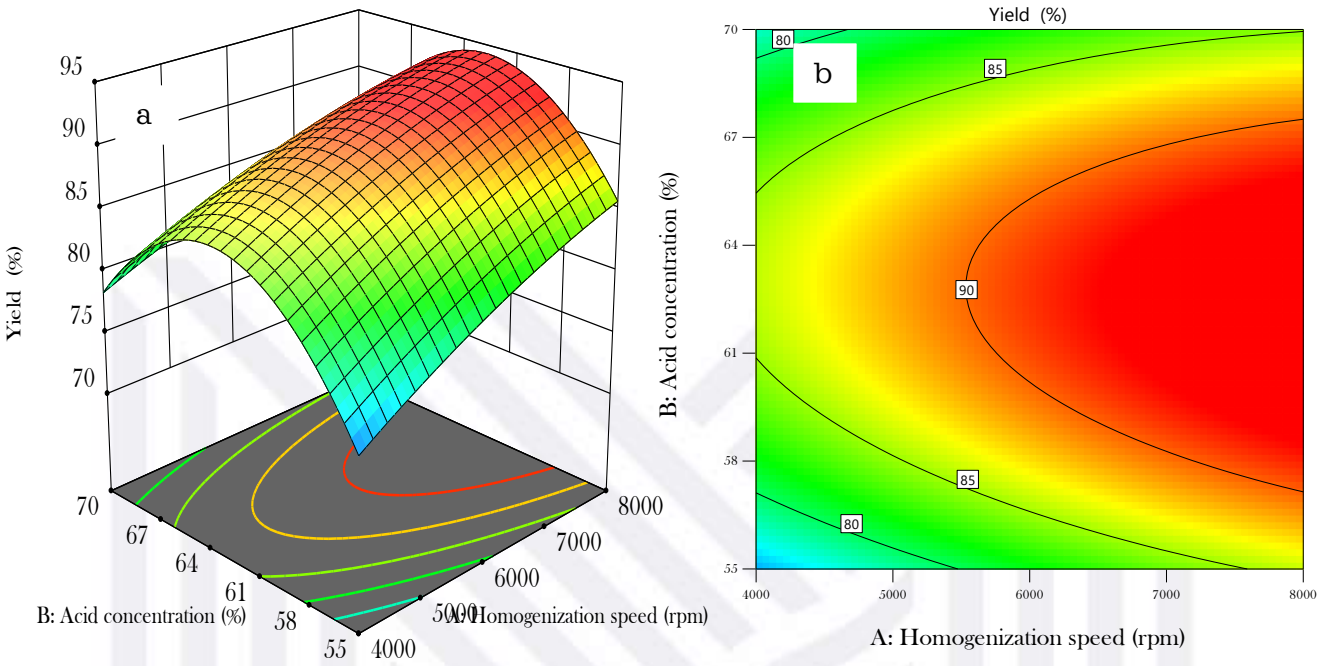

Figure 3.3: Effect of homogenization speed and acid concentration on the yield of cellulose nanocrystals (a) response surface and (b) two-dimension plot with acid concentration.

3.3.3.2 Effects of acid to cellulose ratio and acid concentration on the yield of CNCs

Figure 3.4 shows the effect of acid to cellulose ratio and acid concentration on the yield of CNCs; the homogenization speed is held constant at 6,000 rpm. A high yield of 93.5 % was obtained with an acid concentration of 64 % and an Acid: sample ratio of 20. The percentage yield declined gradually to 80.0 % when the acid concentration was increased to 70%, and the Acid: sample ratio was increased to 25. At higher acid to cellulose mass ratio, the yield of CNCs is higher than at low acid to cellulose ratio. This is due to the presence of cellulose to be attacked per unit volume of acid. As the acid concentration increases, the yield increases to a maximum level and then decreases. The main reason could be as the acid concentration increases, the crystalline part of the cellulose decomposes. This results in less yield of CNCs as the glucosidic bond between cellulosic chains breaks down, resulting in shorter chains with irregular structures (Henschen *et al.*, 2019; Souza *et al.*, 2017).

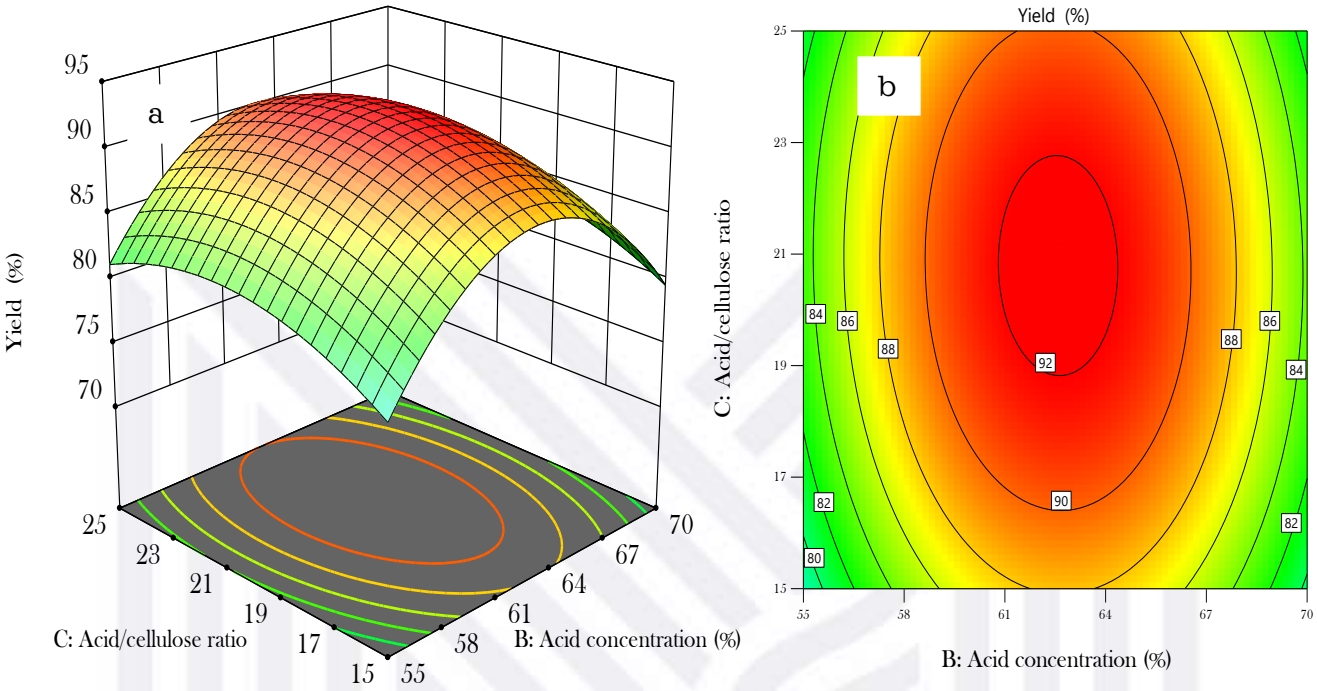

Figure 3.4: Effect of acid to cellulose ratio and acid concentration on the yield of cellulose nanocrystals (a) response surface and (b) two-dimension plot with acid to cellululose ratio.

3.3.3.3 Effects of homogenization speed and acid concentration on the swelling capacity of CNCs

Figure 3.5 shows the effect of homogenization speed and acid concentration on the swelling capacity of CNCs; the acid to cellulose ratio is held constant at 20 wt %. The curve demonstrates that the acid concentration is significant than the homogenization speed. The swelling percentage was enhanced to 3.5 % by increasing the acid concentration to 55% and increasing the homogenization speed to 8000rpm. At high acid concentrations, the swelling capacity of CNCs is much lower than at low acid concentrations. The explanation could be the generation of glucose at the start of the process results in degradation, which reduces the amount of CNCs and thus lowers the swelling capacity at high acid concentrations.

Swelling capacity decreases and then increases as homogenization speed increases (Minimax behaviour). As the homogenization speed increases, the cellulose configuration

is broken and converted to nano-cellulose, which causes extreme changes in the physical and chemical properties, increasing the swelling capacity (Yao *et al.*, 2019).

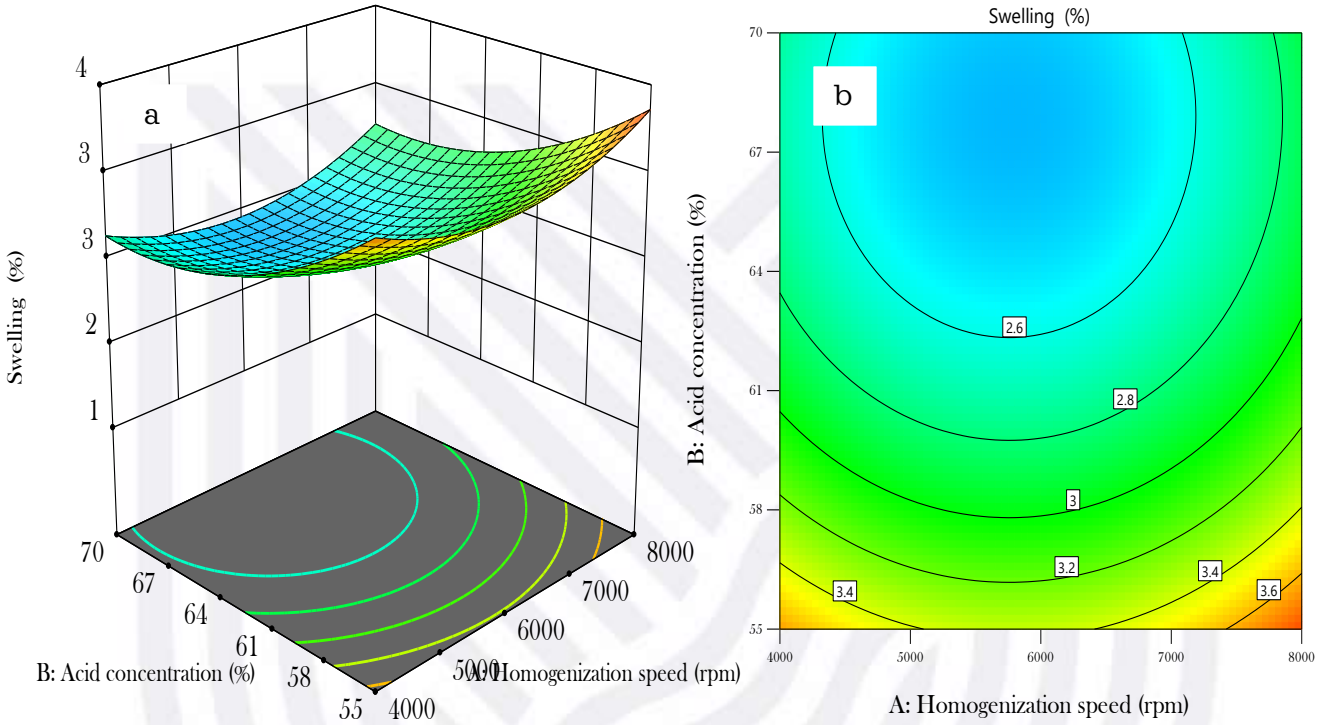

Figure 3.5: Effect of homogenization speed and acid concentration on the swelling capacity of cellulose nanocrystals (a) response surface and (b) two-dimension plot with acid concentration.

3.3.3.4 Effects of acid to cellulose ratio and acid concentration on the swelling of CNCs

Figure 3.6 shows the effect of acid to cellulose ratio and acid concentration on the swelling of CNCs; the homogenization speed is held constant at 6000 rpm. At low acid to cellulose ratio of 15, the swelling capacity is lower (2.5%) than at high acid to cellulose ratio of 25. This is because there is more cellulose to be attacked per unit volume of acid and, hence swelling capacity of CNCs increases. As the acid concentration increases, the swelling capacity decreases since the degradation starts with the most accessible region of the cellulose fiber, and this reduces the end groups and the crystalline regions drastically and hence the swelling capacity drops (Chen *et al.*, 2012).

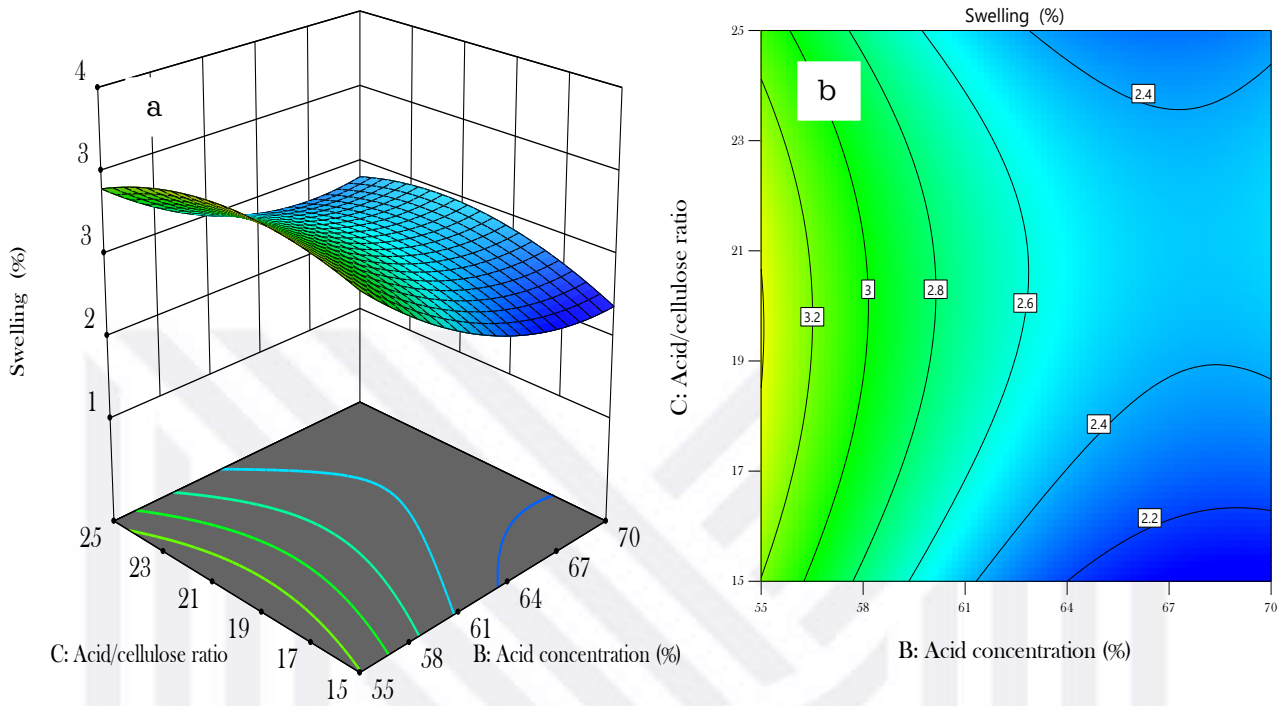

Figure 3.6: Effect of acid to cellulose ratio and acid concentration on the yield of cellulose nanocrystals (a) response surface and (b) two-dimension plot with acid to cellulose mass ratio

3.3.4 Individual influence of process variables on the yield and swelling capacity of CNCs from cellulose.

As shown in **Figure 3.7**, the perturbation plot shows the effect of process variables on the yield and swelling capacity of CNCs from cellulose. The influence of one factor was evaluated and plotted alongside the yield and the swelling capacity when the other variables remained constant.

As ompared to the acid concentration, the homogenization speed and acid to cellulose ratio have a more significant influence on the yield of CNCs from cellulose, as shown in **Figure 3.7a.** As shown in **Figure 3.7b**, the homogenization speed and acid concentration significantly influence the swelling capacity of CNCs, as compared to the acid to cellulose ratio has the least. According to the perturbation plot, the yield and swelling capacity of CNCs from cellulose decrease as the acid concentration and acid to cellulose ratio increase and increase as the homogenization speed increases. The outcome is in perfect agreement with the result of the analysis of variance (ANOVA).

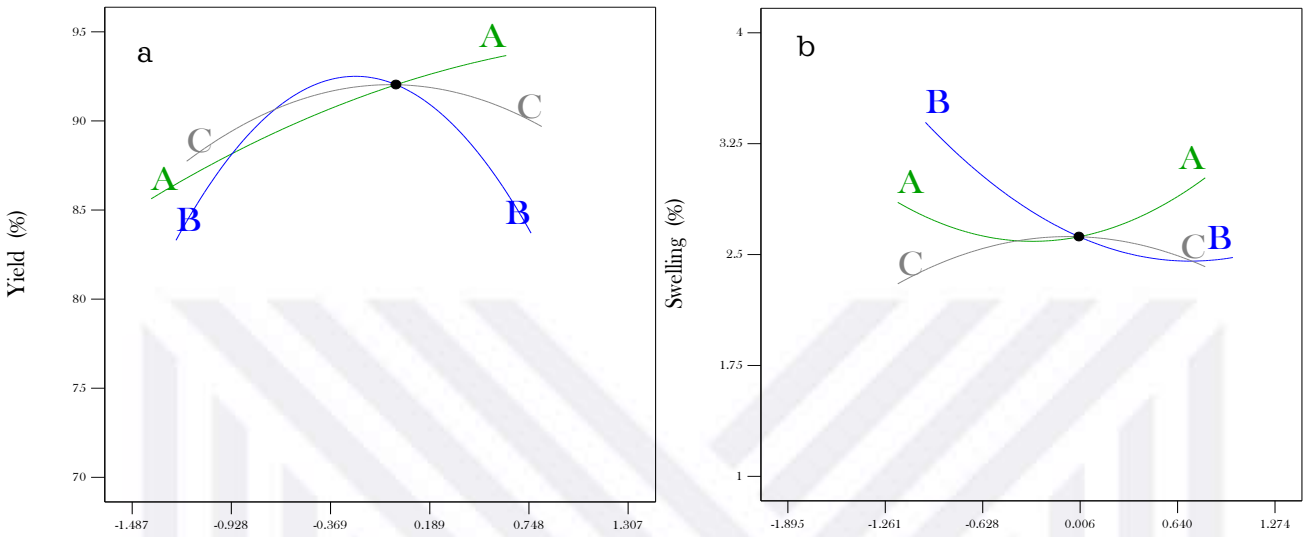

Figure 3.7: Pertubation plots showing the effects of (A) homogenization speed, (B) acid concentration, and (C) cellulose to acid ratio on the yield and swelling capacity.

3.3.5 Numerical optimizations

The numerical optimization technique in the design expert software was applied due to the maximum and minimum detected in the three-dimensional response surfaces in **Figure 3.8**. The objective function, which is the yield and swelling capacity of CNCs, was set to a maximum value, and process parameters were set to a range for optimization.

The numerical optimization analysis results showed that the maximum yield of CNCs from cellulose was 93.12 % and was obtained at homogenization speed, acid concentration, and acid to cellulose ratio of 7464.0 rpm, 63.40 wt %, and 18.83 wt %, respectively. A maximum swelling capacity of 2.81 % was obtained at homogenization speed, acid concentration, and acid to cellulose ratio of 80000 rpm, 62.5 wt %, and 25 wt %, respectively.

The desirability of 0.996 and 0.998 for CNC yield and swelling capacity of CNCs, respectively, were obtained, indicating that the response is within the desired limits and that the optimized operational conditions can be trusted in achieving the maximum yield and swelling capacity CNCs provided by the model.

Table 3.5 compare the extraction of CNCs from various raw material and different uses. Enzymatic hydrolysis and mechanical isolation are simple techniques. CNCs are produced without the use of very corrosive reagents or a large amount of water. Furthermore, minimum energy consumption, small amounts of water, and various commercial enzyme systems allow this technique to be performed by non-specialists.

However, the yields obtained are often lower than those obtained from purely physical-chemical methods. CNCs have been produced from walnut shells using a mix of alkali/acidic hydrolysis, homogenization, and ultrasonic radiation. CNCs have been observed to have a yield of (87.96 %) and medium crystallinity degree (49%). As it can be observed, the present study revealed that the CNCs were successfully extracted from Millet husk waste as raw material via acidic hydrolysis (93.12%) and crystallinity degree (70 %). As a result, millet husk waste could be a suitable alternative feedstock for the future manufacture of CNCs materials.

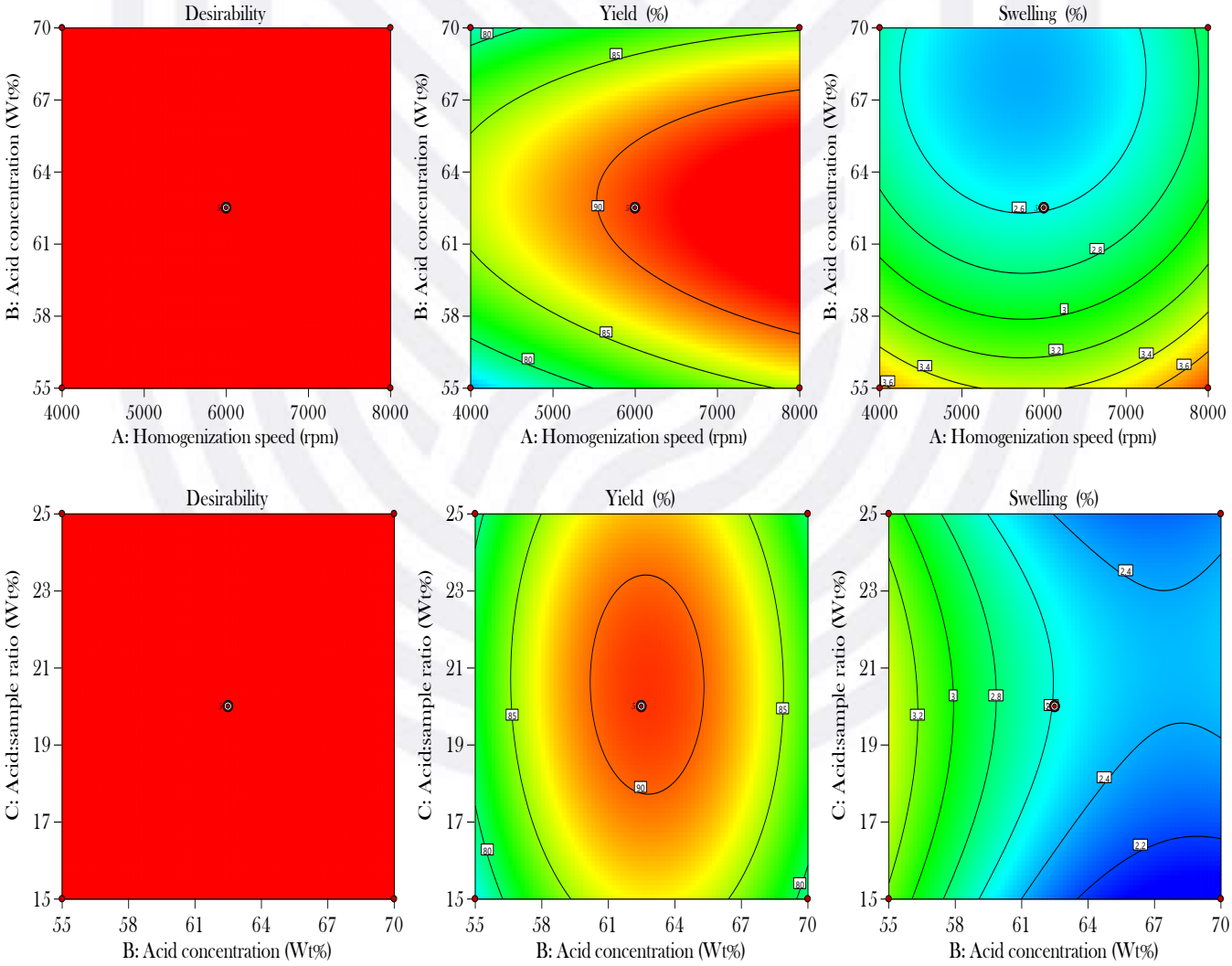

Figure 3.8: Optimal conditions for yield and swelling capacity

3.4 CHARACTERIZATION RESULTS

3.4.1 Fourier-transform infrared spectroscopy (FTIR)Analysis

Figure 3.9 shows FTIR functional groups for cellulose and cellulose nanocrystals (CNC). The wideband between 3100-3600 cm^{-1} is assigned to the vibration O-H group. This is due to the hydrogen bonds caused by molecular interactions in cellulose. Also, the bands at 2880cm^{-1} and 2780 cm^{-1} are corresponding to the stretching vibration C-H group. The band at 1650 cm-1 present for CNCs is assigned to the O-H group. The band was not present in the original cellulose (Hemmati *et al.*, 2018). This factor may be related to the sulfate groups existing on the external surface of the cellulose nanocrystals in the aqueous phase of CNCs, which will increase the hydrophilicity of the CNCs. The band at 1600 cm^{-1} is assigned to C=C, which shows the magnetism of the aromatic cycle due to lignin formation. The band at 1430 cm^{-1} is linked to the OH and C-H group available in the cellulose. The groups are reduced in the CNCs due to the hydrolysis process (Meng *et al.*, 2019b). The band at 1320 cm-1 is assigned to the bending vibration of CH_2. Other band includes 1030 cm^{-1} for morphological modification in C-O and 890 cm^{-1} which shows the standard configuration of cellulose with the β glycoside bonds in the glucose ring.

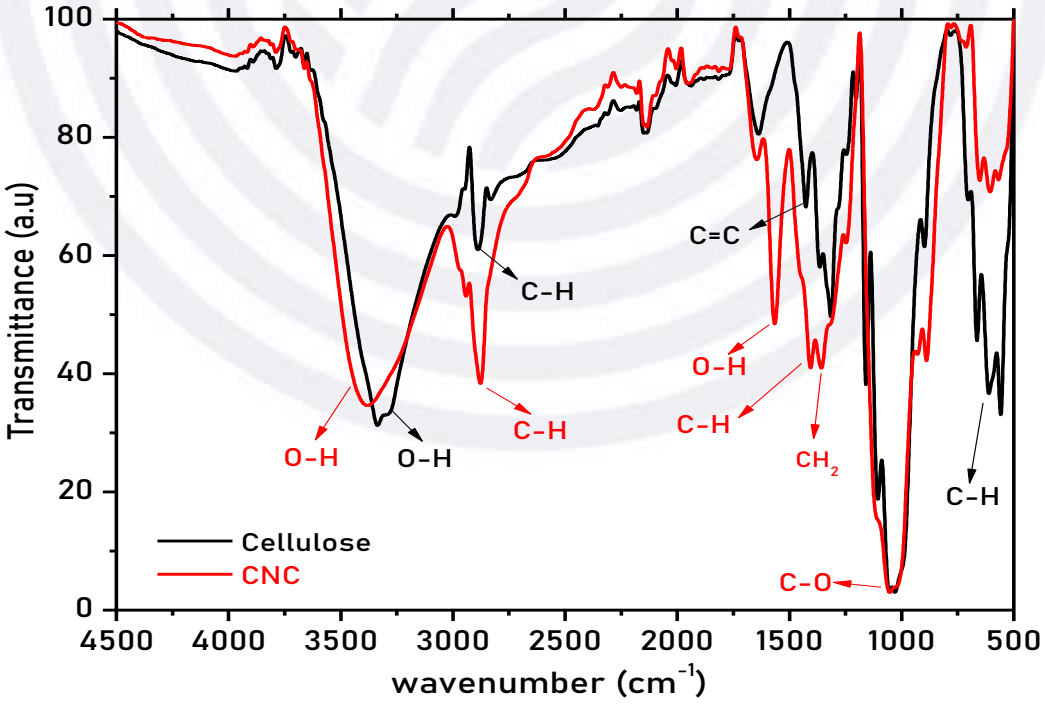

Figure 3.9: FT-IR transmittance of cellulose and cellulose nanocrystals

3.4.2 X-ray diffraction (XRD) pattern

Figure 3.10. elucidates the XRD analysis of cellulose and CNCs. The three typical peaks were observed for cellulose and CNCs at 2θ angles of 16.6°, 27.4°, and 40.0°regions. The crystalline index of cellulose was 48%, based on Fig. 8. The alkali hydrolysis and lignin in cellulose are removed by concentrated sulfuric acid, the amorphous region in the cellulose configuration is detached, and the crystallinity index is improved (Oyewo *et al.*, 2019). After acid hydrolysis, the crystallinity index was around 70%. The % degree of crystallinity is influenced by the source of cellulose, the period of CNCs purification, and the process conditions of hydrolysis. There is a straight connection between the degree of crystallinity and the hardness of the cellulose. The more complex the cellulose, the higher the crystallinity index (Ishak *et al.*, 2019). The crystallinity index of walnut shells and sawdust is 36.7° and 55°respectively, similar to the crystallinity index measured in this study (Hemmati *et al.*, 2018; Oyewo *et al.*, 2019).

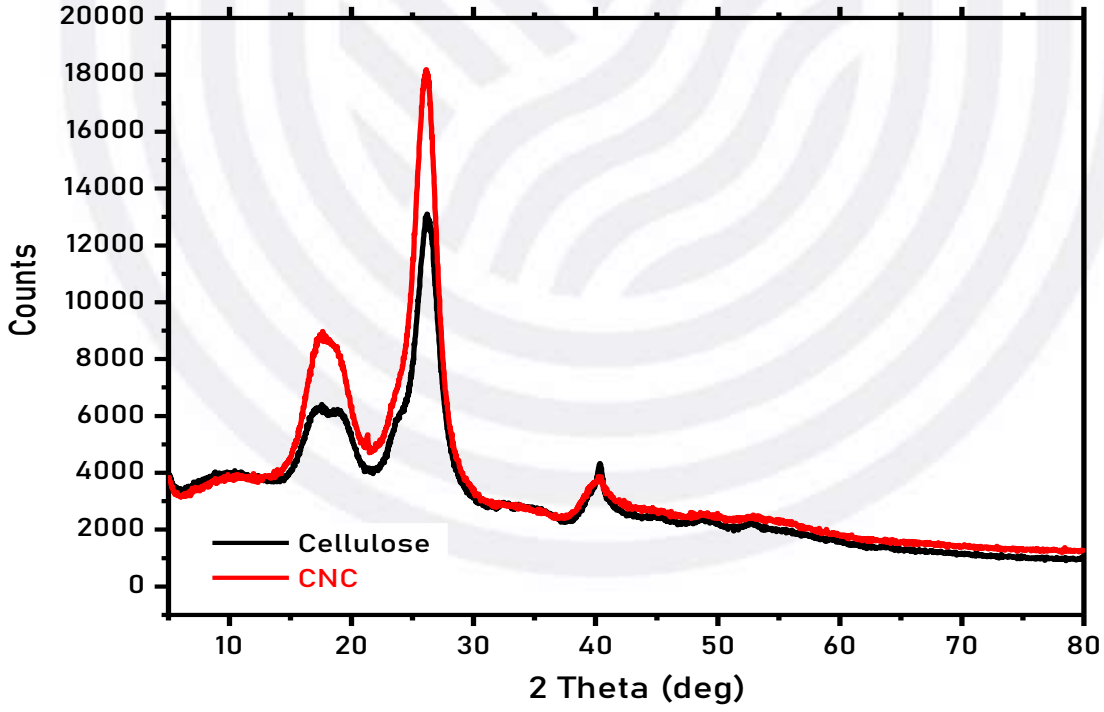

Figure 3.10: XRD patterns of cellulose and cellulose nanocrystals

3.4.3 Thermogravimetric analysis (TGA)

The thermal stability of cellulose and cellulose nanocrystals (CNCs) is shown in **Figure 3.11**. As depicted in the graph, the temperature decreased slightly between 60 and 100°C

for cellulose and CNCs graphs, indicating water loss. The weight loss of both samples at this stage is less than 6%. There was a further loss at the temperature range between 260 to 400°C, due to the decomposition of alpha-cellulose and lignin. At this phase, the mass loss of 85% of the cellulose occurs. This was due to the destructions of chains in the cellulose due to the disintegrations of glycosyl cellulose chains (Hemmati *et al.*, 2018). At temperatures above 400°C, the mass loss is due to the oxidation and the formation of residual ash in low-weight gases. At this phase, the residual content is less than 10% at 600°C.

The CNCs showed a dissimilar thermal stability trend as compared to cellulose. The mass loss of CNCs occurred at the temperature range between 240 to 380°C and, the sample lost 79% of its initial weight. For the CNCs, degradation occurred over the wide temperature range as compared to cellulose. The large surface area of CNCs can play a crucial role in decreasing the thermal stability because, in the CNCs, the contact surface advances the heat transfer. Furthermore, through acid hydrolysis with sulfuric acid, both amorphous and crystalline structures decompose causing, the arrangements within the CNCs to be more sensitive to heat l (Leszczy *et al.*, 2018b).

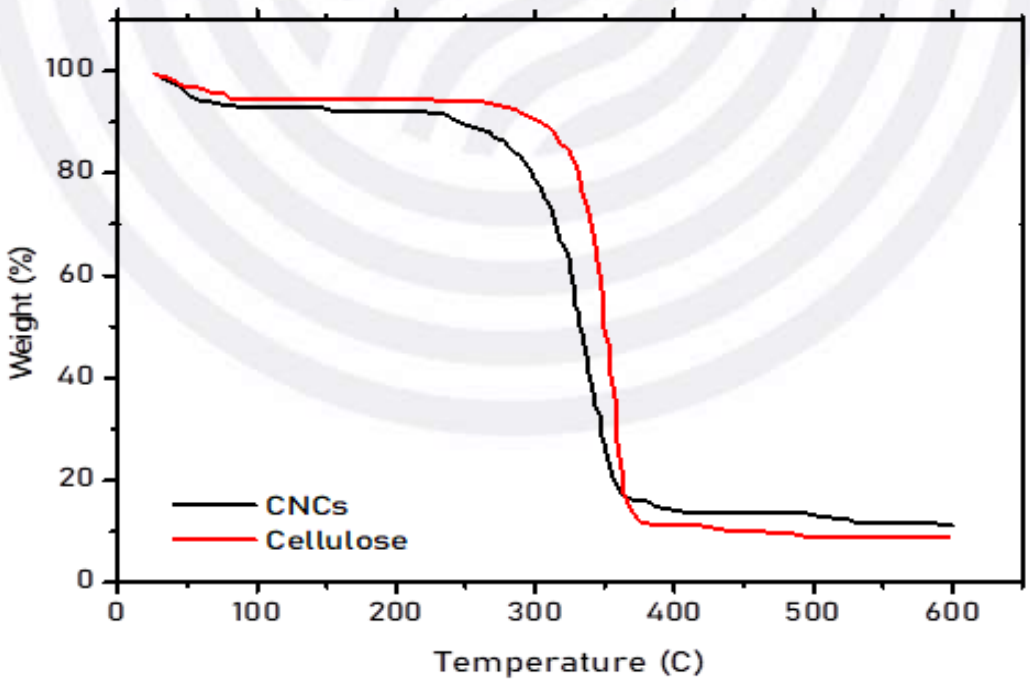

Figure 3.11: TGA graph for cellulose and cellulose nanocrystals

3.4.4 Scanning electron microscopy (SEM) analysis

Figure 3.12 shows the SEM images of cellulose and cellulose nanocrystals (CNCs). The SEM images depict that the alpha-cellulose fibers were relatively easy to see and with more regular surfaces were observed after elimination of non-cellulosic components. On the other hand, the cellulose nanocrystals (CNCs) cover the surface in the form of short fibers and fine fibers and is probably because sulfuric acid penetrated the amorphous region of cellulose, causing the hydrolysis and degradation of glucopyranose linkage. The actual structure of the cellulose nanocrystals is visible, probably due to the drying process, and the presence of nanocrystals cluster around ice crystals is the result of the large number of hydrogen bonds formed between the surfaces.

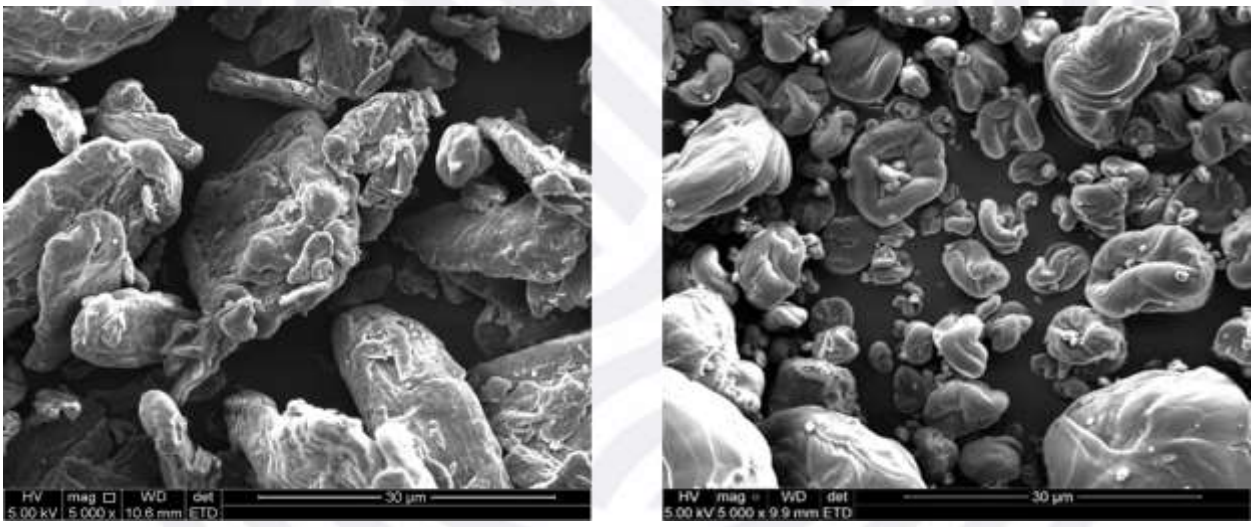

Figure 3.12: SEM image of cellulose (A) and cellulose nanocrystals (B)

3.5 CONCLUSION

This study shows that it is possible to extract cellulose nanocrystals (CNCs) from cellulose using millet husk residue waste. A Box Behnken design was used to investigate and optimize the effect of homogenization speed, acid concentration, and acid to cellulose ratio on the yield and swelling capacity of CNCs. Results show the yield and swelling capacity of CNCs from cellulose decreases as the acid concentration and acid to cellulose ratio increases and increases with an increase in homogenization speed. The maximum yield of CNCs of 93.12 wt % was obtained at homogenization speed, acid concentration, and acid to cellulose ratio of 7464.0 rpm, 63.40 wt %, and 18.83 wt %, respectively. An optimum maximum swelling capacity of 2.81 % was obtained, at homogenization speed, acid concentration, and acid to cellulose ratio of 8000 rpm, 62.5 wt %, and 25 wt %, respectively. The mathematical models to predict cellulose nanocrystals' yield and swelling capacity were developed with R^2 of 98.9 % and 97.9%, respectively. The cellulose and nano-cellulose obtained were characterized using transform infrared microscopy (FTIR), X-ray diffraction (XRD), thermogravimetric analysis (TGA), and scanning electron microscopy (SEM). The TGA showed that the thermal stability of cellulose was higher than that of CNCs. The FTIR results showed functional groups of CNCs and cellulose were similar. The SEM image of CNCs is porous and displayed a narrow particle size with needle-like morphology compared to cellulose. The XRD pattern presented an increase in the intensity of CNCs.

3.6 REFERENCES

Abdelraof, M., Hasanin, M.S., Farag, M.M., & Ahmed, H.Y. 2019. International Journal of Biological Macromolecules Green synthesis of bacterial cellulose / bioactive glass nanocomposites : Effect of glass nanoparticles on cellulose yield , biocompatibility and antimicrobial activity. *Int. J. Biol. Macromol.* 138:975–985.

Awang, N.W., Ramasamy, D., Kadirgama, K., Samykano, M., Najafi, G., Azwadi, N., & Sidik, C. 2019. International Journal of Heat and Mass Transfer An experimental study on characterization and properties of nano lubricant containing Cellulose Nanocrystal (CNC). *Int. J. Heat Mass Transf.* 130:1163–1169.

Chen, D., Lawton, D., Thompson, M.R., & Liu, Q. 2012. Biocomposites reinforced with cellulose nanocrystals derived from potato peel waste. *Carbohydr. Polym.* 90(1):709–716.

Du, H., Liu, W., Zhang, M., Si, C., Zhang, X., & Li, B. 2019. Cellulose nanocrystals and cellulose nano fi brils based hydrogels for biomedical applications. *Carbohydr. Polym.* 209:130–144.

Hemmati, F., Mahdi, S., Kashaninejad, M., & Barani, M. 2018. International Journal of Biological Macromolecules Synthesis and characterization of cellulose nanocrystals derived from walnut shell agricultural residues. *Int. J. Biol. Macromol.* 120:1216–1224.

Henschen, J., Li, D., & Ek, M. 2019. Preparation of cellulose nanomaterials via cellulose oxalates. *Carbohydr. Polym.* 213:208–216.

Hynninen, V., Mohammadi, P., Wagermaier, W., & Hietala, S. 2019. Methyl cellulose / cellulose nanocrystal nanocomposite fibers with high ductility. *Eur. Polym. J.* 112:334–345.

Ishak, N.S., Ishak, K.M.K., Bustami, Y., & Rokiah, H. 2019. ScienceDirect Evaluation of Cellulose Nanocrystals (CNCs) as Protein Adsorbent in stick water. *Mater. Today Proc.* 17:516–524.

Lei, W., Zhou, X., Fang, C., Li, Y., Song, Y., Wang, C., & Huang, Z. 2019. New approach to recycle office waste paper: Reinforcement for polyurethane with nano cellulose crystals extracted from waste paper. *Waste Manag.* 95:59–69.

Leszczy, A., Radzik, P., Hara, K., & Pielichowski, K. 2018a. Thermochimica Acta Thermal stability of cellulose nanocrystals prepared by succinic anhydride assisted hydrolysis. 663:145–156.

Leszczy, A., Radzik, P., Hara, K., & Pielichowski, K. 2018b. Thermochimica Acta Thermal stability of cellulose nanocrystals prepared by succinic anhydride assisted hydrolysis. 663:145–156.

Meng, F., Wang, G., Du, X., Wang, Z., Xu, S., & Zhang, Y. 2019a. Extraction and characterization of cellulose nanofibers and nanocrystals from liquefied banana pseudo-stem residue. *Compos. Part B.* 160:341–347.

Niamsap, T., Tien, N., & Sukyai, P. 2019. Production of hydroxyapatite-bacterial nanocellulose sca ff old with assist of cellulose nanocrystals. *Carbohydr. Polym.* 205:159–166.

Onur, A., Shanmugam, K., Ng, A., Garnier, G., & Batchelor, W. 2019. Cellulose fibre- perlite depth filters with cellulose nanofibre top coating for improved filtration performance. *Colloids Surfaces A.* 583:123997.

Oyewo, O.A., Mutesse, B., Leswi, T.Y., & Onyango, M.S. 2019. Journal of Environmental Chemical Engineering Highly e ffi cient removal of nickel and cadmium from water using sawdust- derived cellulose nanocrystals. 7.

Priscila, A., Silva, M., Vitória, A., Pontes, S.M.A., Pereira, A.L.S., De, M., Filho, M.S., Rosa, M.F., & Azeredo, H.M.C. 2019. Mango kernel starch fi lms as a ff ected by starch nanocrystals and cellulose nanocrystals. 211:209–216.

Shafiei, M., Karimi, K., & Taherzadeh, M.J. 2010. Palm Date Fibers : Analysis and Enzymatic Hydrolysis.

Souza, A.G. De, Kano, F.S., & Bonvent, J.J. 2017. Cellulose Nanostructures Obtained from Waste Paper Industry : A Comparison of Acid and Mechanical Isolation Methods. :1–6.

Wu, W., Song, R., Xu, Z., Jing, Y., Dai, H., & Fang, G. 2018. Sensors and Actuators B : Chemical

Fluorescent cellulose nanocrystals with responsiveness to solvent polarity and ionic strength. *Sensors Actuators B. Chem.* 275:490–498.

Yalç, A., Ersus, S., & Cesur, S. 2019. Optimum alkaline treatment parameters for the extraction of cellulose and production of cellulose nanocrystals from apple pomace. 215:330–337.

Yao, Y., Wang, H., Wang, R., & Chai, Y. 2019. International Journal of Biological Macromolecules Novel cellulose-gelatin composite fi lms made from self-dispersed microgels : Structure and properties. *Int. J. Biol. Macromol.* 123:991–1001.

Zolgharnein, J., Dalvand, K., Rastgordani, M., & Zolgharnein, P. 2017. Adsorptive removal of phosphate using nano cobalt hydroxide as a sorbent from aqueous solution; multivariate optimization and adsorption characterization. *J. Alloys Compd.* 725:1006–1017.

CHAPTER FOUR

SELECTIVE REMOVAL OF Cr(VI) FROM HYDROMETALLURGICAL EFFLUENT USING MODIFIED CELLULOSE NANOCRYSTALS (CNCs) WITH SUCCINIC ANHYDRIDE AND ETHYLENEDIAMINETETRAACETIC ACID: ISOTHERM, KINETICS, AND THERMODYNAMIC STUDIES

ABSTRACT

Biological sources are renewable basic resources that may be used for several purposes, including the development of green material for the removal of heavy metal ions. CNCs extracted from waste papers via acid hydrolysis were modified and utilized as adsorbents to remove Cr (VI) ions from metallurgical effluent in this work. XRD, SEM, FTIR, TGA, and zeta potentiometer were used to characterize the CNCs. The CNCs treated with succinic anhydride and EDTA have thin particle sizes and are porous. The carboxylate functional group is primarily engaged in the coordination and selective removal of metal ions (-COO^{2-}), thermal degradation of 85% observed at temperature between (250-380°C). On the surface of the modified CNCs, the zeta potential data showed a decrease in negative value. The results revealed that the modified CNCs had a maximum adsorption capacity of 387.25± 0.88 mgL^{-1} at pH 5, CNCs dose 25 mgL^{-1} and 400 mgL^{-1} as a starting concentration. The adsorption equilibrium period was 300 minutes and temperature 313 K. The equilibrium results fit the Langmuir isotherm model with R^2 of 0.993 and qmax of 340± 0.97, and the Chi-square (X^2) and Marquardt's percent standard deviation (MPSD) tests confirms that the adsorption process was pseudo-second-order with R^2 of 0.998 and The Elovich model revealed that Cr (VI) complexed with the adsorbent's functional groups. The reaction was endothermic due positive ΔH, spontaneous due and negative ΔG, The positive ΔS indicates that the adsorption process enhances the unpredictability of the solid/liquid interface, according to thermodynamic analysis. After acid treatment, the CNCs may be effectively reused for 6 cycles with adorption capacity of 220± 0.78 $mg.g^{-1}$.

Keywords: Adsorption, cellulose nanocrystals, Cr (VI) removal, succinic anhydride

GRAPHICAL ABSTRACT

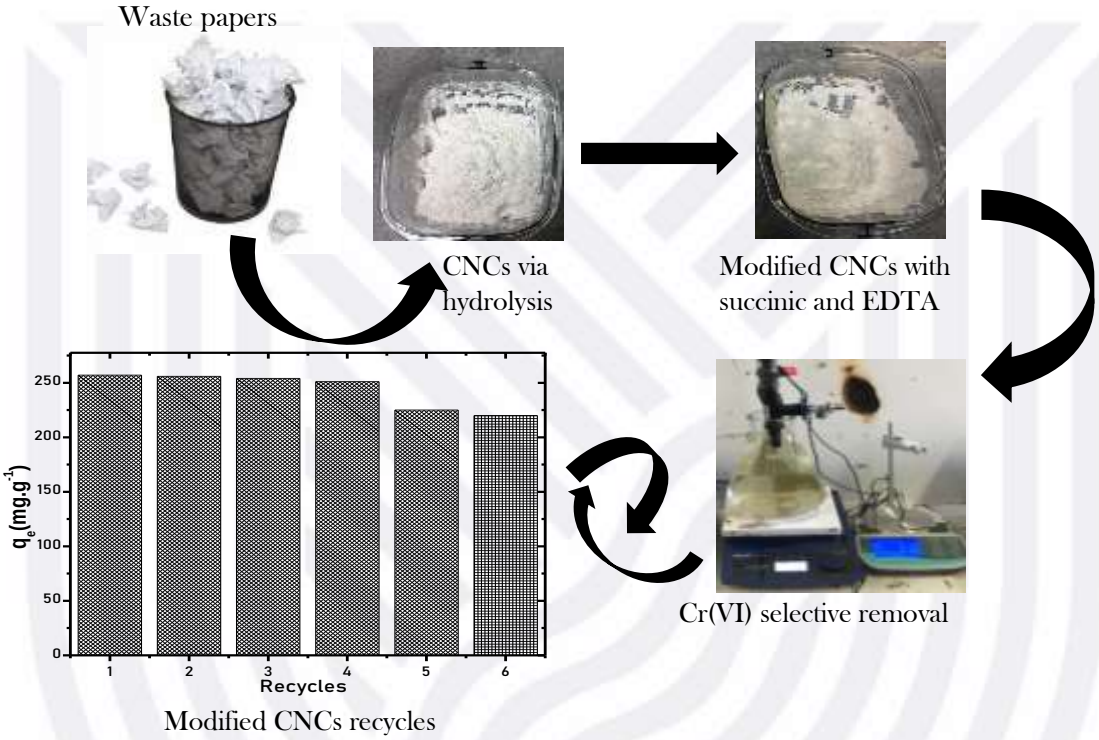

Highlights

- As a bioadsorbent, a novel functionally modified cellulose nanocrystals was developed for selective removal of Chromium (VI).
- Carboxylate functionalization on the surface of of modified cellulose nanocrystals provides the capacity to absorb the Chromium (VI) ions.
- Adsorption occurs mainly on the surface and also has a homogenous distribution of adsorption energy.
- Kinetic investigations indicate the significance of surface carboxylate in the mechanism of metal ion adsorption.
- The mechanism and driving forces of adsorption on bioadsorbent have been described.

4.1. INTRODUCTION

Many environmental concerns, such as heavy metal contamination in water, have become more prevalent as a result of global industrialization, posing a threat to human health, the ecosystem, and the environment. Chromium is a hazardous wastewater pollutant that is extensively distributed. Chromium is widely found in aquatic systems in both trivalent and hexavalent oxidation forms, each of which has different toxicity. Cr(III) traces are reasonably harmless, yet it is an essential nutrient for animals and plants because it regulates glucose metabolism (Zaman *et al.*, 2017). Cr(VI), on the other hand, is more hazardous due to its high mobility in the environment and ability to induce cancer in living organisms (Igberase *et al.*, 2017). Lung congestion, severe diarrhea, and liver damage are all possible side effects. Cr(VI) can be hazardous to humans if it accumulates in the food chain even in low concentrations (Nordin *et al.*, 2021).

Chromium discharge limitations in water are set on a national level, although they might vary widely depending on the kind of company or receiving water body (marine water, lake, river, sewer system). In the tanning industry, the concentration of chromium in wastewater discharged volume from the tanning process ranges from 500-1500mg/L, from coal mine wastewater 150mg/L and electroplating wastewater the Cr(VI) concentration ranges from 500 to 2000 mg/L. In most countries, pollution control authorities do not permit the presence of more than 2 mg/L of Cr(VI) in the treated effluent (Zainol & Nicol, 2009).

Many studies have employed microbes, organic acids, and other chemical reagents to convert Cr(VI) to Cr(III), and many studies have used microorganisms, organic acids, and other chemical reagents to convert Cr(VI) to Cr(III) (Nordin *et al.*, 2021). However, this necessitates a high number of organic reagents, which jeopardizes the solution's stability. Metal polishing, electroplating, paint production wastewater, and chromium mining effluent are all examples of industrial sources of chromium (Cheng *et al.*, 2016). Heavy metal ions have been removed from water using traditional methods such as physical and chemical procedures. Ion exchange (Kabuba & Banza, 2020), electrochemical precipitation (Banza *et al.*, 2021), reverse osmosis (Salcedo *et al.*, 2016), membrane separation (Xu *et al.*, 2018), and adsorption (Saxena *et al.*, 2017; Zolgharnein *et al.*, 2017) are some of these techniques. Most of these techniques, however, have drawbacks that restrict

their use in wastewater treatment, such as high operating costs, secondary pollutant generation, limited yield, and increased sewage sludge formation (Qi *et al.*, 2016).

Because of its significant benefits, such as design simplicity, cost-effectiveness, ease of operation, and the lack of secondary contamination, Cr(VI) adsorption is regarded as the ideal treatment method (Durano *et al.*, 2012; Kumar *et al.*, 2013; Mohan *et al.*, 2011). Activated carbon, organic solvents, and inorganic compounds have all been investigated for their capacity to extract Cr(VI) from aqueous solutions (Cheng *et al.*, 2016; Liu *et al.*, 2017). These adsorbents, however, exhibit unfavorable characteristics such as weak adsorption, limited selectivity, and poor regeneration, which restrict their applicability. As a result, novel adsorbent materials with high adsorption capacity, wide surface areas, and increased stabilities are required (Vishnu Priyan *et al.*, 2021).

In wastewater treatment, nanomaterials are becoming increasingly important (Hu *et al.*, 2018; Oyewo *et al.*, 2019). The use of nanoparticles for metal removal has several advantages, including improved reactivity and a large specific surface area. Carboxylated cellulose nanocrystals (CNCs) are cellulose nanocrystals having a significant number of carboxylic acid functional groups that may bind metal ions. Several cellulosic materials, including bacterial cellulose, wood straw, microcrystalline cellulose, and cotton (Hemmati *et al.*, 2018a), can be used to extract cellulose nanocrystals. CNCs have a higher strength and crystallinity, as well as a higher specific area, as compared to natural celluloses (Kaboorani & Riedl, 2015).

There are several methods for preparing the CNC, the most common of which is acid hydrolysis with sulfuric acid. The amorphous domains of cellulosic microfibers dissolve when they are treated with acid hydrolysis. Several steps are involved in isolating cellulose nanocrystals from a cellulosic source. Bleaching and chemical pre-treatment procedures are required for non-purely cellulosic materials to remove hemicellulose and lignin (Oyewo *et al.*, 2019).To guarantee optimum crystallinity of the cellulose nanocrystals generated, hemicellulose and lignin must be removed. This is followed by a series of separations (filtration and centrifugation) and washing processes such as dialysis to remove salt residues and residual chemicals from the suspended solution. agglomerates are removed by centrifuge separation or microfiltration. Finally, the crystalline cellulose is dispersed by ultrasonic treatment (Hemmati *et al.*, 2018a).

As a result, several functional cellulose-based nanocomposites have been produced in a variety of fields (Lin *et al.*, 2016). The CNCs are an excellent adsorbent due to their high number of specific surface areas and active sites, which have already been utilized to adsorb oils (José *et al.*, 2019), dye (Nordin *et al.*, 2021), and heavy metal ions (Oyewo *et al.*, 2019). CNCs have a large specific area to offer a large number of active accessible sites on the surface to stabilize metal ions. Heavy metal ions are stabilized by functional groups that act as metal-binding sites on biomass. Surface changes are possible due to the presence of hydroxyl groups on the surface of cellulose nanocrystals (Leszczy *et al.*, 2018). Surface modification can be used to introduce all of the main metal-binding groups for adsorption. Modified CNCs are used to remove cadmium and nickel from aqueous solutions. For the elimination of lead from an aqueous solution, carboxylated CNCs/sodium alginate hydrogel beads were created(Cheng *et al.*, 2016). Humic acid-modified CNCs for nickel and chromium removal (Basu *et al.*, 2019).

This research is part of a wider initiative to produce cellulose nanocrystal-based environmental products. To create a green adsorbent, CNCs are treated using low-cost, non-toxic chemicals. Succinic acid is a viable CNCs modification agent because it allows the insertion of aliphatic chains containing carboxyl groups, which enables the selective removal of metal ions from water. Variations in pH, CNCs dose, contact duration, starting concentration, and temperature were used to assess the adsorbent's performance. Isothermal models, kinetic processes, and thermodynamic factors were also investigated. To assess the morphology and a plausible mechanism for selective removal of Cr(VI), chemical and physical characteristics such as surface modification, structures, and functional groups have been investigated. The new aspect of this study is the incorporation of succinic anhydride and Ethylenediaminetetraacetic acid tetrasodium salt to CNCs produced from a low-cost source: wastepapers. The comparison of the properties of original and modified CNCs clearly demonstrates that the modication of cellulose nanocrystals increases the selective removal of Chromium (VI) from hrydrometallurgical effluent without compromising the environment and no secondary pollution.

4.2. MATERIALS AND METHODS

4.2.1 Materials

The cellulose nanocrystals (CNCs) utilized in this study were extracted from waste papers via acid hydrolysis((≥90%). The water samples were taken in a 1000 ml polypropylene plastic container from metallurgical effluent plant. Before the trials, the samples were placed in the refrigerator and maintained overnight. The zeta potential was measured using a Zetasizer Malvern Nano ZS at 25°C. CNCs were treated using succinic anhydride and Ethylenediaminetetraacetic acid tetrasodium salt (≥99%), and the pH of the solution was adjusted with NaOH (≥98%)and HCl (37%) using a pH meter (Hanna HI 8421). The Purity water system (Model Select Analyst HP40) provided the deionized water for the solution preparation. All chemicals utilized were analytical grade reagents from Sigma Aldrich in South Africa.

4.2.2 Modification of cellulose nanocrystals (CNCs)

The following are the surface modifications made with Ethylenediaminetetraacetic acid tetrasodium salt (EDTA)/succinic anhydride: To allow the reaction to take place, 0.05M EDTA tetrasodium salt was added to the reactor containing CNCs at an agitation speed of 100 rpm for 60 minutes. After that, 10 mL of hydrochloric acid was added, and the agitation time was increased to 6 hours. The modified product was centrifuged for 30 minutes at 500 rpm and rinsed to remove unreacted compounds until the pH reached 7. Treatment of the CNCs suspension with 0.05 M succinic anhydride at 25°C for 3 hours resulted in further alterations of the CNCs. The pH of the modified CNCs was adjusted to about 7.

4.2.3 The chemistry of CNCs modification

Many procedures and substances can be used to modify cellulose nanocrystals.[26] The majority of these techniques are costly, and nearly all of the chemicals used to modify them are hazardous. This study utilized EDTA tetrasodium and succinic anhydride as a low-cost, non-toxic chemical. The addition of EDTA tetrasodium to CNCs in an aqueous solution resulted in the creation of sodium salt and cellulose depletion, while the addition of succinic anhydride to the -COOH group resulted in bonding openings to create anionic oxygen groups on the surface of the CNCs. The inclusion of anions boosted the material's

sensitivity and selectivity to the complex's interaction with metal ions via coordinate bonds.

4.2.4 Characterization of unmodified and modified CNCs

The functional groups present in the CNCs, as well as the resultant structural modifications, were studied using Fourier transform infrared spectroscopy (FTIR, Varian 7000). The morphological surface of the CNCs was assessed using scanning electron microscopy (SEM, Philips XL30FEG). X-ray diffraction was used to accomplish the qualitative and quantitative analyses (XRD, Philips expert 0993). A thermal thermogravimetric analyzer was used to determine the CNC's thermal stability (TGA, NETZSCH5 209F3).

4.2.5 Batch removal experiments

A 200 mL beaker was used in batch studies in the thermostatic shaker. Modified CNCs were used to remove Cr (VI) from hydrometallurgical effluent for 5 hours at 185 rpm. A conical flask holding 100 mL of the heavy metal ion solution was combined with 5 g of modified CNCs. The starting concentration ranged from 100 to 500 mg/L, the pH of the solution was between 2 and 8, and the temperature was between 25 and 40°C (**Figure 4.1**). 10 mL of suspension from the mixture was filtered every 1-hour interval, and the resultant solutions were analyzed using atomic absorption spectroscopy (AAS, thermoelectric corporation 3300).

The following equations were used to determine the adsorption capacities at equilibrium (qe, mg.g-1) at any time t (qt, $mg.g^{-1}$):

$$q_e = \frac{(C_i - C_{eq}) \times V}{Ms} \quad (4.1)$$

$$q_t = \frac{(C_i - C_t) \times V}{Ms} \quad (4.2)$$

where C_i ($mg.L^{-1}$) denotes the initial Cr(VI) concentration, Ct (mgL^{-1}) denotes the concentration at time t, C_{eq} (mgL^{-1}) denotes the concentration at equilibrium, M_s (mg) denotes the mass of dry CNCs employed, and V (L) is the volume of Cr(VI) solution used for selective removal.

The removal rate (%) was assessed using the following equation:

$$\text{Removal}\,(\%) = \frac{(C_O - C_e)}{C_O} \times 100 \qquad (4.3)$$

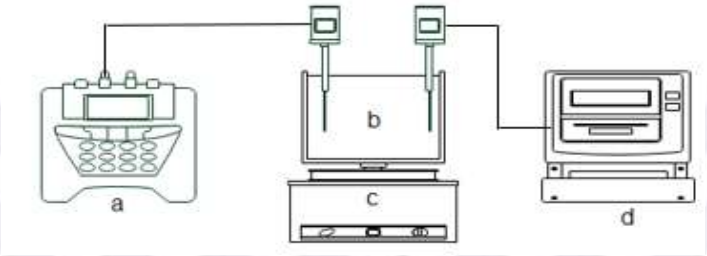

a: Temperature control

b: Hydrometallurgical effluent with modified CNCs

c: Heating plate

d: pH control

Figure 4.1: schematic representation of the experimental set-up for removal of Cr(VI)

4.3. RESULTS AND DISCUSSION

4.3.1 Characterization of CNCs

4.3.1.1 FTIR analysis

The FTIR spectrum of unmodified and modified CNCs is shown in **Figure 4.2.** The stretching vibration O-H and C-O groups correspond to the broad peaks of CNCs (**Figure 2B**) at 3350 cm-1 and 890 cm^{-1}. When comparing the spectra in **Figures 4.2 (A)** and **(B)**, it can be noted that the modified CNCs have a larger peak area at 3350 cm-1, which may be attributed to the position of the carboxyl group stretching vibration formed by the interaction CNCs and succinic anhydride. Furthermore, the CH_2 expansion and contraction are linked to the band at 1330 cm^{-1}. Furthermore, the CH_2 expansion and contraction are linked to the band at 1330 cm-1. The pyranose C-O-C skeletal vibration is allocated to the strong band at 1040 cm^{-1}, while the overall structure of cellulose with glucoside linkages is assigned to the weak band at 890 cm-1. The spectra of modified CNCs (Figure 1A) show three bands at 2500, 1630, and 1340 cm^{-1}, which correspond to carbonyl C=O stretching vibration, C-H stretching in CH_2 vibration, and C-O stretching vibration. As a result, it was shown that the succinic anhydride interacted with the carboxylate groups in the CNCs. The peaks of the -OH of -COOH signal are more strong and wider for

modified CNCs, making the strength of the signal harsher. This might indicate that CNCs have been successfully modified. These findings show that the modified CNCs surface's hydroxyl and carboxyl groups were important in the selective removal process.

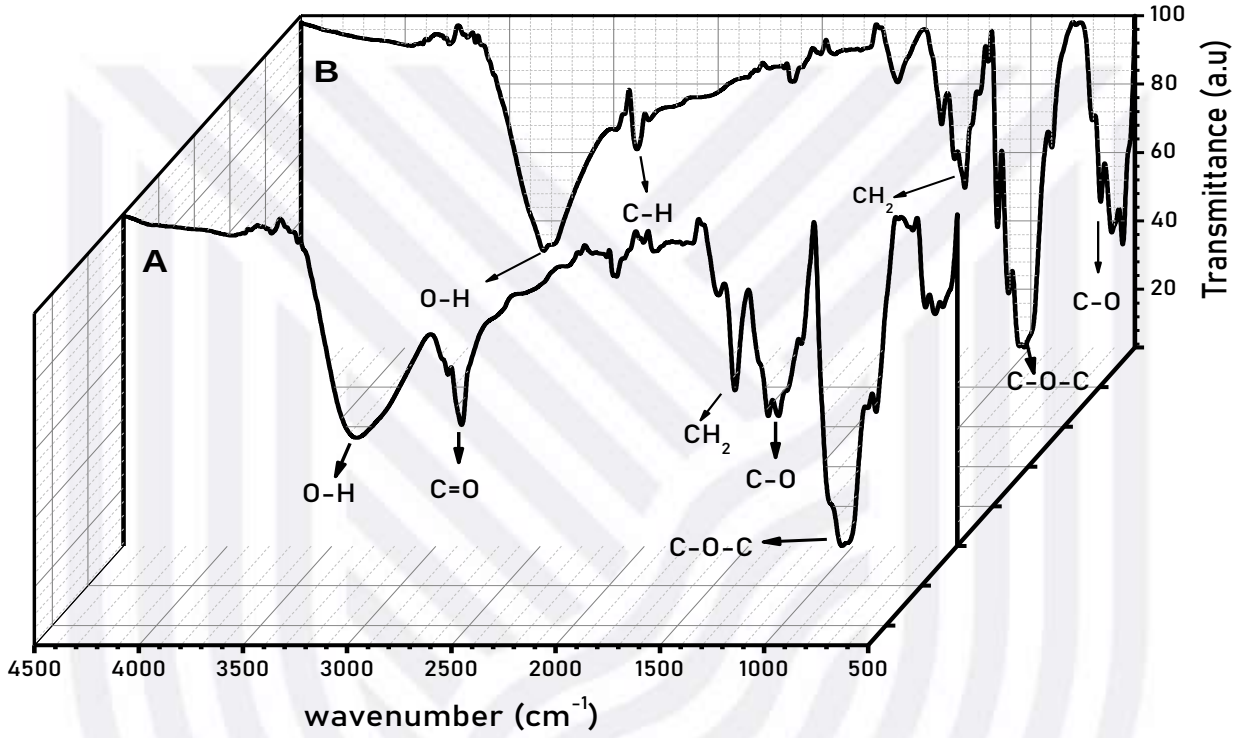

Figure 4.2: FTIR spectrum of (A) modified CNCs, and (B) CNCs

4.3.1.2 X-ray diffraction analysis

Figures 4.3 (A) and **(B)** depict cellulose nanocrystal phase identification and crystallinity analyses (raw CNCs and modified CNCs). Diffraction peaks at 2θ angles 11° and 25° ($C_2H_{192}O_{16}$ and $C_{60}H_{88}O_8$) are attributed to cellulose phases 1β and 1α in the XRD spectra obtained in these CNCs samples. The crystalline sodium in these samples is ascribed to the peaks at 13°, 23°, and 40° in modified CNCs, suggesting a very strong connection between the sodium units and the cellulose structure. Due to the presence of Ethylenediaminetetraacetic acid tetrasodium in the modification of CNCs, the emergence of ($C_{16}H_{32}O_4$ and $C_{36}H_{36}N_4O_8$) was also seen following the modification of CNCs. Due to stronger crystallinity than the unmodified CNCs, the CNCs exhibit the sharpest and narrowest at 2θ = 25°. The increase in the crystallinity of the modified CNCs was to improve the rigidity and strength. As a result, it was assumed that the potential mechanical

behavior and strengthening capacity of cellulose nanocrystals would increase (Lu *et al.*, 2016a; Meng *et al.*, 2019).

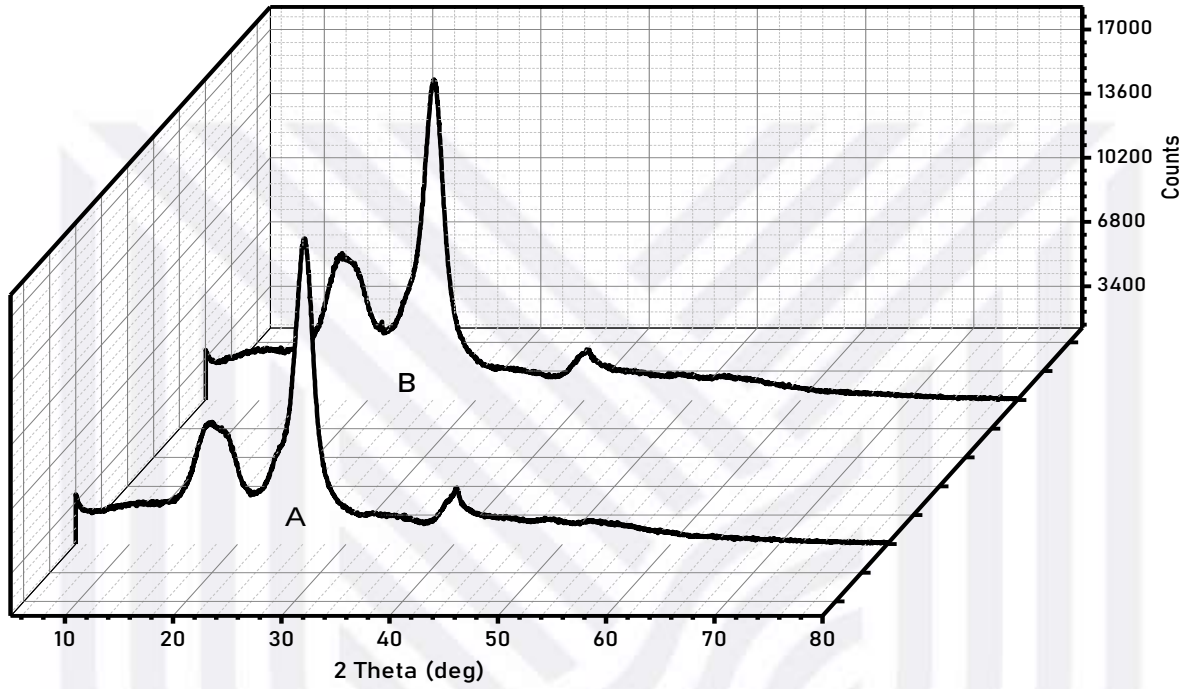

Figure 4.3: XRD spectra of (A) CNCs and (B) modified CNCs

4.3.1.3 Thermogravimetric analysis

The thermal properties of cellulose nanocrystals and modified cellulose nanocrystals were investigated under a nitrogen flow rate of 10°C/min and temperature ranging from 25°C to 600°C. CNCs and modified CNCs are shown in **Figures 4.4 (A)** and **(B)**. The TGA of both samples from 25°C to 130°C showed a slight weight loss (5%) due to residual water desorption and moisture. This may be explained by the heat absorption that occurs between 40°C to 130°C. the second degradation was observed due to the thermal decomposition of the CNCs at higher temperatures (250-380°C) about 85%, this may be related to the destruction of CNCs chains as well as the disintegration of glycosyl cellulose units and the breakdown of pyranose rings (Wu *et al.*, 2016). Followed by relatively slow degradation (10%) at 380-410°C which is consistent with the decomposition of CNCs and modified CNCs and clearly shows the success of the modification process.

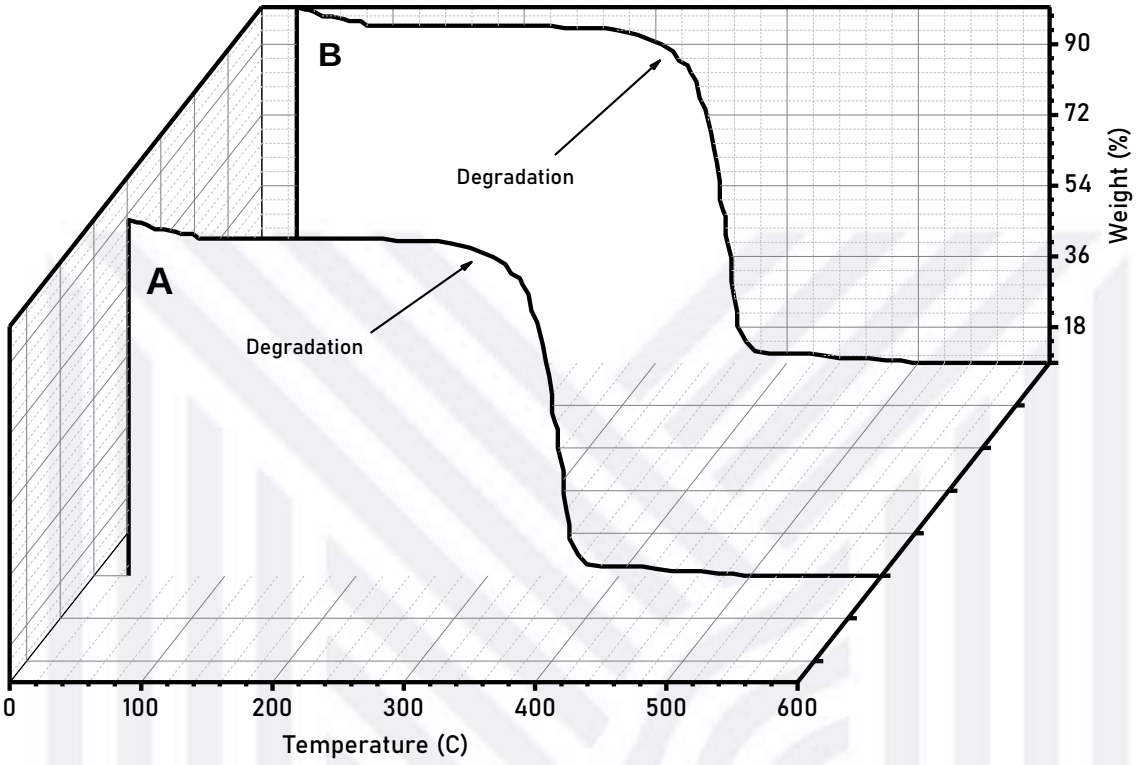

Figure 4.4: TGA curves of the studied (A) CNCs and (B) modified CNCs

4.3.1.4 SEM analysis

SEM analysis was used to examine the morphological structures of original and modified CNCs, as illustrated in **Figure 4.5 (A-B)**. **Figure 5A** demonstrates the porosity of CNCs, with pores uniformly dispersed throughout the smooth rough surface. Figure 5B, on the other hand, shows an increase in the ratio of particle width to length, which might be attributable to the influence of transformation on the surface of CNCs. This might also imply that the density of the materials is affected by the modification (Oyewo *et al.*, 2019). The presence of needle-shaped fibers (**Figure 5B**) was also noticed, confirming the reality of the material change, and demonstrating that the reaction is occurring at particular areas on the CNCs surface. On the surface of the modified CNCs, the development of well-distributed flocs was observed.

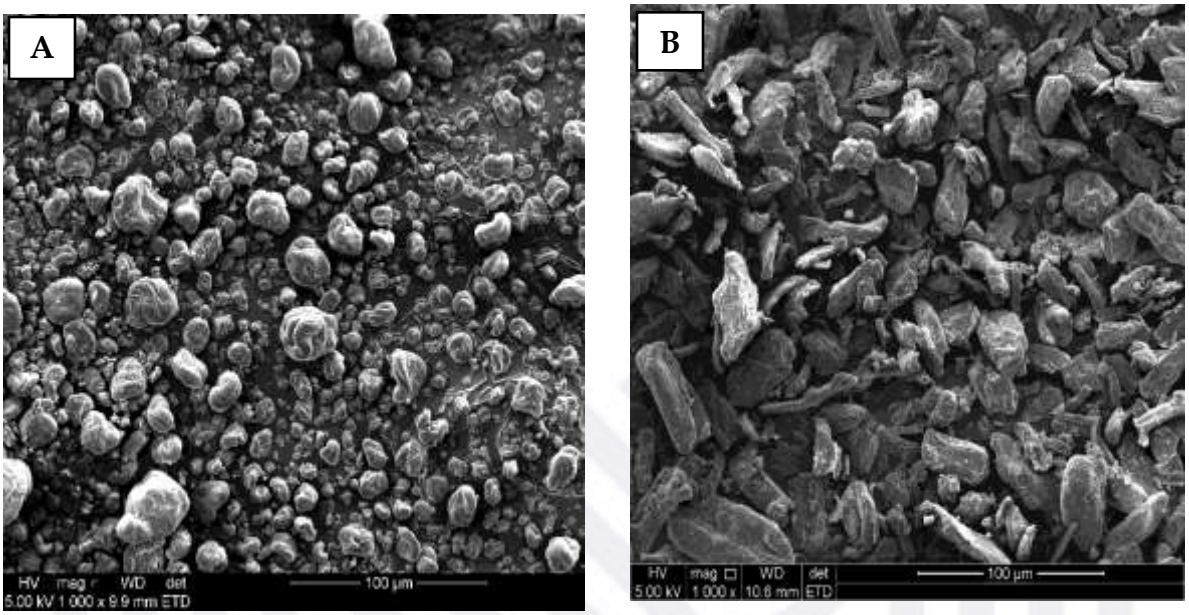

Figure 4.5: SEM images of (A) Raw CNCs (unmodified) and (B) modified CNCs

4.3.2 Cellulose nanocrystals Zeta potential

Changes in reaction, attraction, or repulsion can occur due to the strong surface reactivity of the cellulose nanocrystals. This behavior is described by the zeta potential, which also explains nanoparticle stability and surface potential. When the zeta potential values are more than +30 mV or less than -30 mV, the particles are said to be stable (Banza *et al.*, 2021). The zeta potential of unmodified CNCs and modified CNCs as a function of pH is shown in **Figure 4.6**. Two distinct features have been identified. First, across the entire pH range, both substances have a negative surface. Second, as compared to raw CNCs, the modified CNCs have a lower surface load. This last finding shows that the modified CNCs are more stable than the unmodified CNCs due to the presence of EDTA and Succinic anhydride. Nanoparticle stability facilitates some applications, thus stable nanoparticles with low zeta potential decrease electrostatic interactions between particles (Meng *et al.*, 2019). It also allows the particles to get closer together, resulting in more dense particles. CNCs with lower surface charges should be able to remove metal ions more selectively.

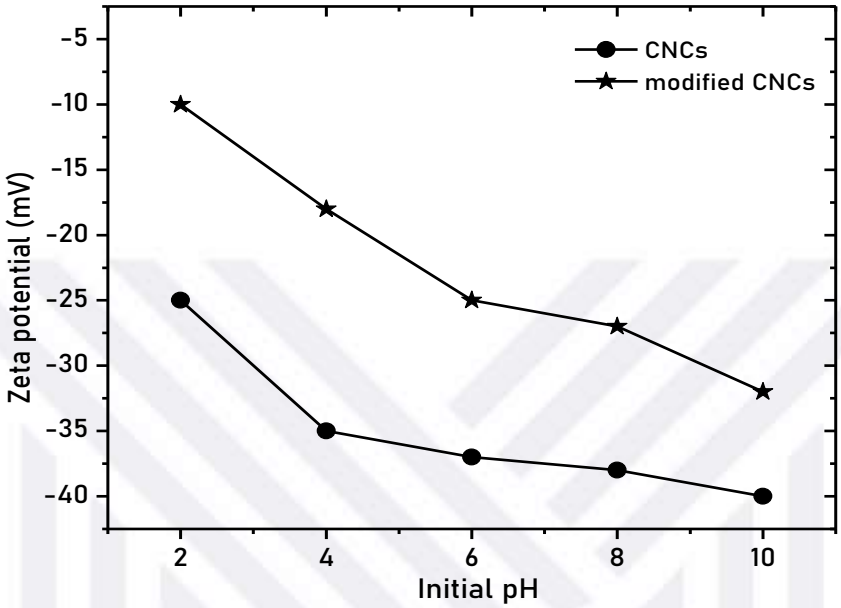

Figure 4.6: Effect of pH on zeta potential of CNCs

4.3.3 Adsorption studies

Figure 4.7 depicts the adsorption experimentation method. In the following studies, factors such as pH, contact duration, starting concentration, and CNCs dose were varied to understand the mechanism and characteristics of adsorption.

4.3.3.1 Effect of contact time

Figure 4.7A shows the effect of contact time on adsorption capacity and removal % when utilizing the modified CNCs. Because the accessible site on the modified CNCs is not initially entirely occupied, the percentage removal and qt grow fast from 0 to 100 min as the contact time increases: the Cr (VI) is immediately and easily absorbed. Over 300 minutes, Cr (VI) adsorption progressively achieves equilibrium, resulting in a Cr (VI) removal efficiency of about 96± 0.85%, with no notable change in R% or q_t. As a result, for the batch adsorption tests, a contact time of 300 minutes was used

4.3.3.2 Effect of pH

Figure 4.7B depicts the impact of pH for Cr (VI) removal. The adsorption capacity of modified CNCs was shown to be strongly influenced by the pH of the solution. When the pH is raised from 2 to 5, q_e rises from 260± 0.96 to 287± 0.79 (mg.g-1), and R% rises from 75± 0.48 to 96± 0.81 ($mg.g^{-1}$). The findings show that a high pH environment is advantageous for

the removal of Cr (VI). Under acidic circumstances, the groups present in modified CNCs are protonated, reducing the propensity to adsorb positively charged Cr (VI) to the positively charged surface CNCs. The modified CNCs surface, on the other hand, can be negatively charged at higher pH and attract Cr (VI) cations (Ran *et al.*, 2017). Figure 6 indicates that beyond pH 5, qe and R% do not change because abundant OH- ions in the solution generate competition between the negative surface of CNCs and OH^- ions, reducing Cr (VI) removal. It has been found that the modified CNCs outperform the raw CNCs. The zeta potential indicated that the magnitude of the negative charge for modified CNCs had decreased. As a result, the forces between CNCs particles are reduced, and the removal of positively charged Cr is increased (VI). As a result, tests were carried out at pH 5 to avoid Cr (VI) precipitation.

4.3.3.3 Effect of initial concentration

Figure 4.7C summarizes the effect of the initial Cr (VI) concentration on the performance of the modified CNCs in terms of adsorption capacity and % removal. It can be shown that raising the starting dosage from 10 to 500 mgL^{-1} has a positive effect, the q_e increased from 20± 0.96 $mg.g^{-1}$ to 320± 0.81 $mg.g^{-1}$, and the removal efficiency decreased from 98± 0.75%to 75± 0.50%. This might be due to the concentration gradient's increasing driving power. As long as the adsorbent aggregate's accessible sites are not saturated, higher concentrations improve metal ion removal. Modified CNCs are highly competitive compared to other materials available because of their high adsorption capacity values (Nordin *et al.*, 2021). The great holding capacity in water treatment has an economic advantage since it requires fewer CNCs to remove heavy metal ions from hydrometallurgical effluent, saving costs on adsorbent and sludge management.

4.3.3.4 Effect of CNCs dosage

The effects of modified CNCs dosage on q_e and R% equilibrium values were in the range of 5 - 25 mgL^{-1}. For the constant volume of Cr (VI), (**Figure 4.7D**) is used. With increasing dosage, q_e decreases under the same adsorption circumstances. R%, on the other hand, rises until it reaches 94± 0.89 %at 25 $mg.L^{-1}$. Because a large number of CNCs gives a greater surface area and more accessible sites for adsorption, the removal percentage initially increases with dosage. However, because the adsorption efficiency is not fully saturated, excessive modified CNCs in the solution may impair adsorption effectiveness. The dosage

of 5mgL^{-1} was chosen for the following adsorption studies to determine the best removal of Cr (VI) and the most effective usage of modified CNCs.

4.3.3.5 Effect of temperature

The adsorption capacity of the modified CNCs and the removal % of Cr (VI) increased marginally with increasing temperature in **Figure 4.7E**. The adsorption capacity increased from 285± 0.80 mg.L^{-1} at 293 K to 290± 0.71 mg.L^{-1} At 313 K. As a result, the adsorption reaction consumes energy. Changes in Gibbs, enthalpy, and entropy (ΔG, ΔH, and ΔS, respectively) are thermodynamic characteristics that help predict the path and direction of adsorption.

The change in Gibbs for adsorption was calculated from the following equations:

$$\Delta G = \Delta H - T\Delta S \quad (4.4)$$

$$\Delta G = -RTLn\, K \quad (4.5)$$

$$K = \frac{q_e}{C_e} \quad (4.6)$$

Where the gas constant is R(8.314 Jmol^{-1}K^{-1}), and the absolute temperature is T (K).

Table 1 shows the estimated value (from 293 to 313 K) with a starting concentration of 400 mgL^{-1}. The negative ΔG confirmed the spontaneous character of the process; the increase in temperature is proportional to ΔG, implying that higher temperatures promote adsorption. The positive ΔH readings corroborate this conclusion, indicating an endothermic reaction. The positive ΔS indicates that the adsorption process enhances the unpredictability of the solid/liquid interface (Banza *et al.*, 2018). The spontaneous nature of the process was confirmed by negative ΔG, the increase in temperature is proportional with ΔG implies that higher temperature favors the adsorption. This conclusion is supported by positive values of ΔH, which shows an endothermic process. The positive ΔS suggests that the adsorption process increases solid/liquid interface randomness(Saxena *et al.*, 2017).

Table 4.1: Thermodynamic parameters of adsorption for Cr (VI) on modified CNCs

ΔG (Kj/mol)T					**ΔH(kJ/mol**	**ΔS(J/mol K)**
293	289	303	308	313		
-5.78	-5.85	-5.97	-6.09	-6.10	8.74	39.41

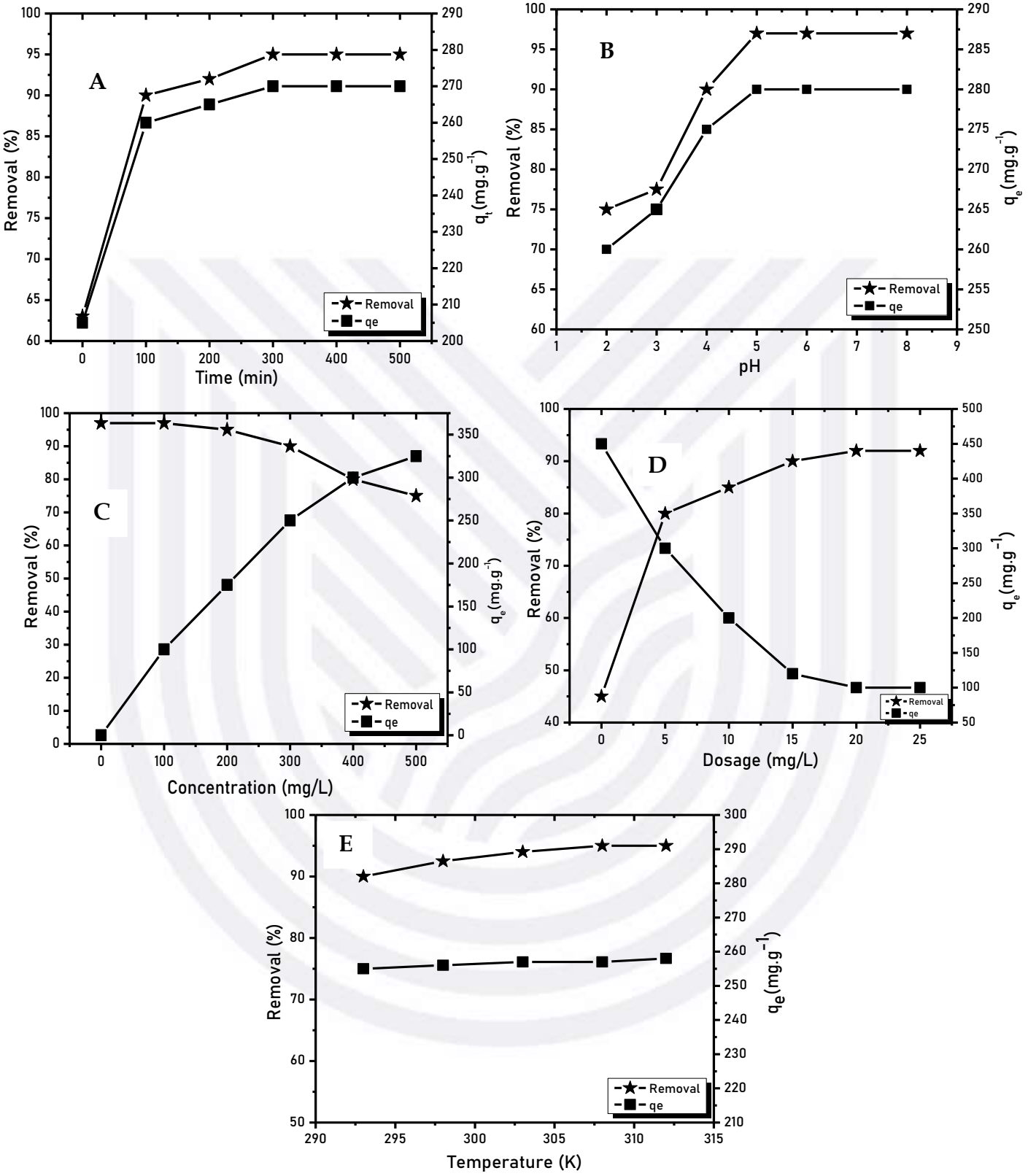

Figure 4.7: effect of (A) time, (B) pH, (C)concentration, (D)dosage, and (E) temperature on Cr (VI) adsorption

4.3.4 Equilibrium adsorption isotherm

Studying the equilibrium adsorption is important to optimize the adsorption, as it not only determines the adsorption capacity but also helps to understand the underlying mechanism. The adsorption isotherm of Cr (VI) on the modified cellulose was obtained at ambient temperature using various concentrations of Cr (VI) from 20- 500 mgL^{-1}. After 24 hours at a shaking speed of 185 rpm and pH of 5. **Equations (4.7-4.12)** were used to fit the data to the Langmuir (L), Freundlich (F), Dubini-Radushkevich (D-R), and Temkin (T) isotherm models (Kabuba & Banza, 2020) (see **Table 4.2**).

Langmuir (L)

$$\frac{C_{eq}}{q_e} = \frac{C_{eq}}{q_{max}} + \frac{1}{bq_{max}} \quad (4.7)$$

Freundlich (F)(Hu *et al.*, 2018)

$$\text{Log } q_e = \log K_f + \frac{1}{n}\log C_{eq} \text{ (Linear form)} \quad (4.8)$$

Dubini-Radushkevich (D-R)[7]

$$\ln q_e = \ln q_{max} - k\beta^2 \quad (4.9)$$

Where the Polanyi potential (β):

$$\beta = RT \ln\left(1 + \frac{1}{C_{eq}}\right) \quad (4.10)$$

and the energy (E):

$$E = \frac{1}{\sqrt{-2K_{ad}}} \quad (4.11)$$

Temkin (T)(Lu *et al.*, 2016b)

$$q_e = A \ln C_{eq} + K_t \quad (4.12)$$

where qe ($mg.g^{-1}$) is the equilibrium adsorption capacity; C_{eq} ($mg.L^{-1}$) is the equilibrium Cr (VI) concentration in the solution; q_{max} ($mg.g^{-1}$) is the maximum adsorption capacity; b ($L.mg^{-1}$) is the Langmuir isotherm model (L) constant; 1/n is the adsorption intensity, and K_F is the Freundlich (F) isotherm model constant; The free energy constant is k (mol^2J^2), the universal gas constant is R (8.314 J/mol), and the temperature is T (K). K_t ($L.g^{-1}$) is the

equilibrium binding constant for the Temkin isotherm (T), and A is the constant for the heat of adsorption.

Table 4.2 shows the values of the (R^2) correlation coefficients. The experimental data are satisfactory compatible with isotherm studies. The Langmuir isotherm model has a good fit. The q_{max} values obtained from the model agree with the experimental values of 340± 0.97 mg.g^{-1}). The B value was found to be 0.19 and R_L value pointed that the process is convenient when R_L is between 0 and 1, irreversible when R_L is equal to 0, and linear when R_L =1. The value obtained from the (F) Freundlich isotherm model shows that Cr (VI) is favorable onto modified CNCs with n values between 1 and 10. In the (D-R) Dubini-Radushkevich isotherm model, the estimated energy (E) for Cr (VI) was less than 8 Kj.mol^{-1} **(see Table 4.2**), indicating that the adsorption process is physical (Oyewo *et al.*, 2019).

Table 4.2: Parameters of isotherms models for the adsorption of Cr (VI) on modified CNCs at 289 K

	Langmuir				**Temkin**		
	q_{max}	**B**	**R_L**	**R^2**	**K_T**	**A**	**R^2**
Cr (VI)	340± 0.97	0.19	3.5x 10^{-3}	0.993	80.69± 0.85	0.62	0.682

	D-R				**Freundlich**		
	q_e	**K**	**E**	**R^2**	**n**	**K_F**	**R^2**
Cr (VI)	250± 0.84	9.10x 10^{-3}	6.98	0.967	4.23	78.65±0.65	0.958

4.3.5 kinetics studies and diffusion mechanism

4.3.5.1 kinetics studies

Kinetic studies are important because they reveal important details about the reaction pathway and adsorption mechanism (Hemmati *et al.*, 2018b). In this work, kinetics pseudo-first, pseudo-second-order, and Elovich kinetic models were used to predict the rate of selectivity of Cr (VI) removal from hydrometallurgical effluent.

Pseudo-first order model

$$\text{Log}\,(q_e\text{-}q_t) = \log qe - \frac{K_a}{2.3}t \qquad (4.13)$$

Pseudo-second order model

$$\frac{t}{q_t} = \frac{1}{K_b q_e^2} + \frac{1}{q_e} t \quad (4.14)$$

Elovich model

$$q_t = \frac{1}{A} \ln \alpha A + \frac{1}{A} \ln t \quad (4.15)$$

where q_t (mg.g^{-1}) is the adsorption capacity at time t, and qe (mg.g^{-1}) is the equilibrium adsorption capacity. K_a(min^{-1}) is the pseudo-first-order rate constant, and K_b is the pseudo-second-order rate constant; A (g.mg^{-1}) is the amount of surface coverage and active energy. For pseudo-second-order, the experimental data of adsorption kinetics was accepted adequately. Chi-square (X^2) and Marquardt's percent standard deviation (MPSD) were used to assess the adequacy of the pseudo-first and second-order models.

$$X^2 = \frac{\left(q_{e(\exp)} - q_{e(pred)}\right)^2}{q_{e(pred)}} \quad (4.16)$$

$$MPSD = 100 \sqrt{\frac{1}{N-P} \sum_{i=1}^{n} \left(\frac{\left(q_{e(\exp)} - q_{e(pred)}\right)^2}{q_{e(\exp)}} \right) i} \quad (4.17)$$

where N is the number of measurements, P is the number of model parameters, $q_{e(pred)}$ is the predicted adsorption capacity in mg.g^{-1}, and $q_{e(exp)}$ is the experimental adsorption capacity in mg.g-1 (mg.g^{-1}).

Table 4.3 : Kinetic parameters for Cr (VI) adsorption onto modified CNCs at 500 mg.L^{-1}

Cr (VI)	Equations	Constant	$q_{e\,(exp)}$	R^2	X^2	MPSD
	Pseudo first order	K_1= 0.0493	285.18± 0.95	0.853	0.02	11.28
	Pseudo second order	K_2= 0.0453	387.25± 0.88	0.998	0.0015	0.35
	Elovich	α= 6.07	B= 9.06	0.963		

With the pseudo-second-order model, R2 was high (0.998) and predicted qe values were in agreement with the experimental $q_{e\,(exp)}$. A pseudo-second order model was used to explain Cr (VI) adhesion to modified cellulosic materials. The rate-limiting phase was interpreted as an electron exchange between Cr (VI) and adsorbent. Chemisorption dominated the adsorption process. The pseudo-second-order rate constant K_2 was lower compared to K_1, indicating that the the pseudo second order had a quicker adsorption rate. The Elovich model revealed that Cr (VI) complexed with the adsorbent's functional

groups. This was most likely due to the high concentration of carboxyl group in the modified-cellulosic material.

4.3.6 Diffusion mechanism

Several sub-processes, such as pore diffusion, surface diffusion, and diffusion through the liquid are always involved in adsorption reactions. The adsorption of Cr (VI) was studied using a film diffusion-controlled, moving boundary process, and particle diffusion-controlled approach. (Refer to **Table 4.4**)

Film diffusion-controlled

$$\ln\left(1-\frac{q_t}{q_e}\right) = K_T \quad (4.18)$$

Particle diffusion

$$\ln\left(1-\frac{q_t}{q_e}\right)^2 = K_T \quad (4.19)$$

Moving boundary process

$$3-3\left(1-\frac{q_t}{q_e}\right)^{2/3}-2\frac{q_t}{q_e}=K_T \quad (4.20)$$

Table 4.4: Diffusion mechanism model

Cr (VI)	Kinetic diffusion model	Constant	R^2
	Film diffusion	0.0583	0.925
	Particle diffusion	0.0498	0.997
	Moving boundary	-0.086	0.725

The findings of the kinetics diffusion model suggest that particle diffusion may better represent the adsorption of Cr (VI) on the modified CNCs with a K_T of 0.0498 min-1, as shown in **Table 4.4.** The adsorption rate was found to match the particle diffusion model equation.

4.3.7 regeneration tests

The possibility to regenerate the Cr (VI) loaded adsorbent was achieved by acid treatment. **Figure 4.8** demonstrates that the adsorption capacity decreases as the number of cycles increases, resulting in decreases in the removal efficiency. Even if, the modified CNCs still

have good adsorption properties after being recycled 6 times, the Cr (VI) adsorption capacity of 220± 0.78 $mg.g^{-1}$ and the removal percentage around 75± 0.69 %. As a result, the CNCs generated in this experiment that has been treated with succinic anhydride and EDTA is a cost-effective and reusable adsorbent.

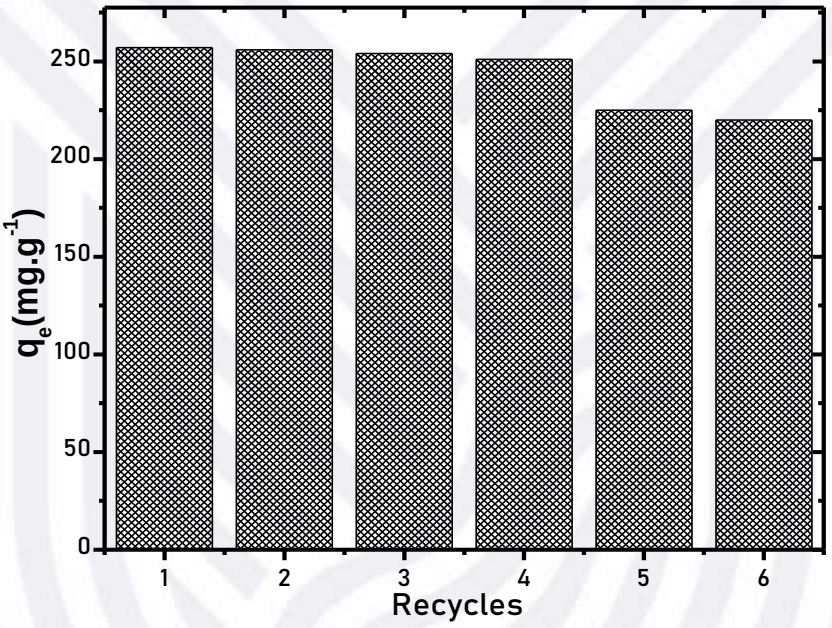

Figure 4.8: repeated adsorption studies for Cr (VI) onto modified CNCs

Table 5 compares modified CNCs with succinic and EDTA maximal sorption capacity to that of other natural sorbents for Cr (VI) adsorption capacity. As can be observed, CNCs modified with succinic and EDTA has an excellent and acceptable sorption capacity for chromium ions removal from the aqueous phase compared to other sorbents

Table 4.5: The Comparison of adsorption capacity between modified CNCs with other adsorbents

Sorbent	q_m (mg/g)	Reference
Modified Clinoptilolite	54.35	Banza et al.
Magnetic carboxylated cellulose	63.78	Liu et al.
Chitosan beads	154.25	Igberase et al.
Alginate sodium hydrogel	338.98	Hu et al.
Carboxylated cellulose	358.42	Wang et al.
Modified CNCs with succinic and EDTA	387.25	This work

4.4. CONCLUSION

The purpose of this study was to develop, characterize, and evaluate a new cellulose nanocrystals (CNCs) adsorbent for removing Cr (VI) from metallurgical effluent. The cellulose nanocrystals that had been treated with succinic anhydride and EDTA had high porosity, a narrow particle size distribution, and a needle-like shape. FTIR confirmed the carboxylate transition of the carboxyl group of cellulose. The existence of extra phases was shown by XRD analysis of particles following alteration, which was ascribed to succinic anhydride and EDTA modification. Changes in Cr (VI) concentration in solution confirmed the removal of metal ions; the modified CNCs exhibited significant Cr (VI) removal, which is attributed to the CNCs' high negative charge. The pH of the solution, the dosage of CNCs, and the starting concentration all impacted the adsorbent's efficacy. The removal of Cr (VI) was sightly affected by the temperature change. The adsorption capacity of the material deteriorated as the temperature rose. The highest Cr (VI) adsorption capacity was 387.25± 0.88 mgL^{-1}, with a 95± 0.79% removal. The findings on adsorption kinetics accord well with the pseudo-second-order model, whereas the equilibrium data fit well with the Langmuir isotherm model. The particle diffusion model describes the adsorption. According to the thermodynamic analyses, the process was spontaneous, exothermic, and unpredictable. CNCs modified is a potential adsorbent for selective removal of Cr (VI) ions from hydrometallurgical effluent, according to this study.

4.5. REFERENCES

Banza, M., Rutto, H., & Kabuba, J. Cobalt and Nickel Separation in Hydrometallurgy Using Modified Clinoptilolite with Dialkyl Phosphoric and Ethylenediaminetetraacetic Acid as an Ion Exchanger. Springer International Publishing.

Basu, H., Saha, S., Mahadevan, I.A., & Pimple, M.V. 2019. Journal of Water Process Engineering Humic acid coated cellulose derived from rice husk : A novel biosorbent for the removal of Ni and Cr. *J. Water Process Eng.* 32:100892.

Cheng, W., Ding, C., Wang, X., Wu, Z., Sun, Y., Yu, S., Hayat, T., & Wang, X. 2016. Competitive sorption of As (V) and Cr (VI) on carbonaceous nanofibers. *Chem. Eng. J.* 293:311–318.

Durano, D., Trochimczuk, A.W., & Beker, U. 2012. Kinetics and thermodynamics of hexavalent chromium adsorption onto activated carbon derived from acrylonitrile-divinylbenzene copolymer. 187:193–202.

Hemmati, F., Mahdi, S., Kashaninejad, M., & Barani, M. 2018a. International Journal of Biological Macromolecules Synthesis and characterization of cellulose nanocrystals derived from walnut shell agricultural residues. *Int. J. Biol. Macromol.* 120:1216–1224.

Hu, Z., Mohamed, A., & Yu, D. 2018. International Journal of Biological Macromolecules Fabrication of carboxylated cellulose nanocrystal / sodium alginate hydrogel beads for adsorption of Pb (II) from aqueous solution. 108:149–157.

Igberase, E., Osifo, P., & Ofomaja, A. 2017. The Adsorption of Pb, Zn, Cu, Ni, and Cd by Modified Ligand in a Single Component Aqueous Solution: Equilibrium, Kinetic, Thermodynamic, and Desorption Studies. *Int. J. Anal. Chem.* 2017.

José, C., Jr, S.G., Maia, A.D., Meira, H.M., Souza, T.C., Amorim, J.D.P., Almeida, F.C.G., Costa, A.F.S., & Sarubbo, L.A. 2019. Use of a bacterial cellulose fi lter for the removal of oil from wastewater. *Process Biochem.* 25:0–1.

Kaboorani, A. & Riedl, B. 2015. Surface modification of cellulose nanocrystals (CNC) by a cationic surfactant. *Ind. Crop. Prod.* 65:45–55.

Kabuba, J. & Banza, M. 2020. Modification of clinoptilolite with dialkylphosphinic acid for the selective removal of cobalt (II) and nickel (II) from hydrometallurgical effluent. 8:1–11.

Kumar, V., Pathania, D., Sharma, S., Agarwal, S., & Singh, P. 2013. Remediation of noxious chromium (VI) utilizing acrylic acid grafted lignocellulosic adsorbent. *J. Mol. Liq.* 177:343–352.

Leszczy, A., Radzik, P., Hara, K., & Pielichowski, K. 2018. Thermochimica Acta Thermal stability of cellulose nanocrystals prepared by succinic anhydride assisted hydrolysis. 663:145–156.

Lin, N., Ge, A., Wouessidjewe, D., Huang, J., & Dufresne, A. 2016. Biocompatible Double-Membrane Hydrogels from Cationic Cellulose Nanocrystals and Anionic Alginate as Complexing Drugs Codelivery.

Liu, C., Jin, R., Ouyang, X., & Wang, Y. 2017. Applied Surface Science Adsorption behavior of carboxylated cellulose nanocrystal — polyethyleneimine composite for removal of Cr

(VI) ions. *Appl. Surf. Sci.* 408:77–87.

Lu, J., Jin, R., Liu, C., Wang, Y., & Ouyang, X. 2016a. International Journal of Biological Macromolecules Magnetic carboxylated cellulose nanocrystals as adsorbent for the removal of Pb (II) from aqueous solution. *Int. J. Biol. Macromol.* 93:547–556.

Lu, J., Jin, R., Liu, C., Wang, Y., & Ouyang, X. 2016b. International Journal of Biological Macromolecules Magnetic carboxylated cellulose nanocrystals as adsorbent for the removal of Pb (II) from aqueous solution. *Int. J. Biol. Macromol.* 93:547–556.

Meng, F., Wang, G., Du, X., Wang, Z., Xu, S., & Zhang, Y. 2019.Extraction and characterization of cellulose nanofibers and nanocrystals from liquefied banana pseudo-stem residue. *Compos. Part B. Elsevier*. 160:341–347.

Mohan, D., Rajput, S., Singh, V.K., Steele, P.H., & Pittman, C.U. 2011. Modeling and evaluation of chromium remediation from water using low cost bio-char , a green adsorbent. *J. Hazard. Mater.* 188(1–3):319–333.

Musamba, B., Kabuba, J., & Rutto, H. 2018. Cobalt and Nickel Separation in Hydrometallurgy using Clinoptilolite as Ion- Exchanger. .

Nordin, A.H., Wong, S., Ngadi, N., Zainol, M.M., Aien, N., Abd, F., & Nabgan, W. 2021. Journal of Environmental Chemical Engineering Surface functionalization of cellulose with polyethyleneimine and magnetic nanoparticles for efficient removal of anionic dye in wastewater. *J. Environ. Chem. Eng.* 9(1):104639.

Oyewo, O.A., Mutesse, B., Leswi, T.Y., & Onyango, M.S. 2019. Journal of Environmental Chemical Engineering Highly e ffi cient removal of nickel and cadmium from water using sawdust- derived cellulose nanocrystals. 7:5-12.

Qi, W., Zhao, Y., Zheng, X., Ji, M., & Zhang, Z. 2016. Applied Surface Science Adsorption behavior and mechanism of Cr (VI) using Sakura waste from aqueous solution. *Appl. Surf. Sci.* 360:470–476.

Ran, J., Wu, L., He, Y., Yang, Z., Wang, Y., Jiang, C., Ge, L., Bakangura, E., & Xu, T. 2017. Ion exchange membranes: New developments and applications. *J. Memb. Sci.* 522:267–291.

Salcedo, A.F.M., Ballesteros, F.C., Vilando, A.C., & Lu, M.C. 2016. Nickel recovery from synthetic Watts bath electroplating wastewater by homogeneous fluidized bed granulation process. *Sep. Purif. Technol.* 169:128–136.

Saxena, A., Bhardwaj, M., Allen, T., Kumar, S., & Sahney, R. 2017. Adsorption of heavy metals from wastewater using agricultural–industrial wastes as biosorbents. *Water Sci. National Water Research Center*. 31(2):189–197.

Vishnu Priyan, V., Kumar, N., & Narayanasamy, S. 2021. Development of Fe3O4/CAC nanocomposite for the effective removal of contaminants of emerging concerns (Ce3+) from water: An ecotoxicological assessment. *Environ. Pollut. Elsevier Ltd.* 285:117326.

Wu, Y., Fan, Y., Zhang, M., Ming, Z., Yang, S., & Arkin, A. 2016. Functionalized agricultural biomass as a low-cost adsorbent : Utilization of rice straw incorporated with amine groups for the adsorption of Cr (VI) and Ni (II) from single and binary systems. *Biochem. Eng. J.* 105:27–35.

Xu, J., Koivula, R., Zhang, W., Wiikinkoski, E., Hietala, S., & Harjula, R. 2018. Separation of cobalt, neodymium and dysprosium using amorphous zirconium phosphate. *Hydrometallurgy*. 175:170–178.

Zainol, Z. & Nicol, M.J. 2009. Comparative study of chelating ion exchange resins for the recovery of nickel and cobalt from laterite leach tailings. *Hydrometallurgy*. 96(4):283–287.

Zaman, H.A., Sharif, S., Kim, D.W., Idris, M.H., Suhaimi, M.A., & Tumurkhuyag, Z. 2017. Machinability of Cobalt-based and Cobalt Chromium Molybdenum Alloys - A Review. *Procedia Manuf. Elsevier B.V.* 11:563–570.

Zolgharnein, J., Dalvand, K., Rastgordani, M., & Zolgharnein, P. 2017. Adsorptive removal of phosphate using nano cobalt hydroxide as a sorbent from aqueous solution; multivariate optimization and adsorption characterization. *J. Alloys Compd.* 725:1006–1017.

CHAPTER FIVE

MODELING OF ADSORPTION OF Cd^{2+} ON CELLULOSE-CHITOSAN NANOCOMPOSITES USING RESPONSE SURFACE METHODOLOGY (RSM) AND ARTIFICIAL NEURAL NETWORK (ANN) TECHNIQUES: ISOTHERM, KINETICS AND QUANTUM CHEMICAL PERFORMANCE

ABSTRACT

Heavy metal pollution posed an immediate hazard to human life and health. In this study, a new carboxyl, amide, and secondary amino group grafted cellulose nanocrystals derivative adsorbent (nanocomposites) was developed to remove the heavy metal Cd^{2+}. The FTIR, SEM, TGA and BET findings demonstrated that CNCs, Chitosan and Nanocomposites characteristics. Using the central composite design (CCD) approach, the effects of contact duration, pH, nanoparticles dosage, and starting Cd^{2+} concentration on the Cd^{2+} removal were investigated. Response Surface Methodology (RSM) and Artificial Neural Network (ANN) modelling approaches were used, and their performance and prediction capacities of the response (adsorption capacity) were also investigated. The adsorption isotherm and kinetic models were also used to describe the process. However, statistical findings showed that the RSM-CCD model outperformed the ANN model method. Initial pH of 5.73, contact time of 310 min, initial Cd^{2+} concentration of 323.04 mg/L, sorbent dose of 16.36 mg, and adsorption capacity of 440.01 mg/g were determined to be the optimal condition. The adsorption process was spontaneous, well explained by the Langmuir model and chemisorption was the primary control. The preferred adsorption sites were determined using the binding energy gaps HOMO-LUMO.

Keywords: Nanocomposites, Artificial neural network, Response surface method, central composite design, adsorption, quantum chemical simulation

GRAPHICAL ABSTRACT

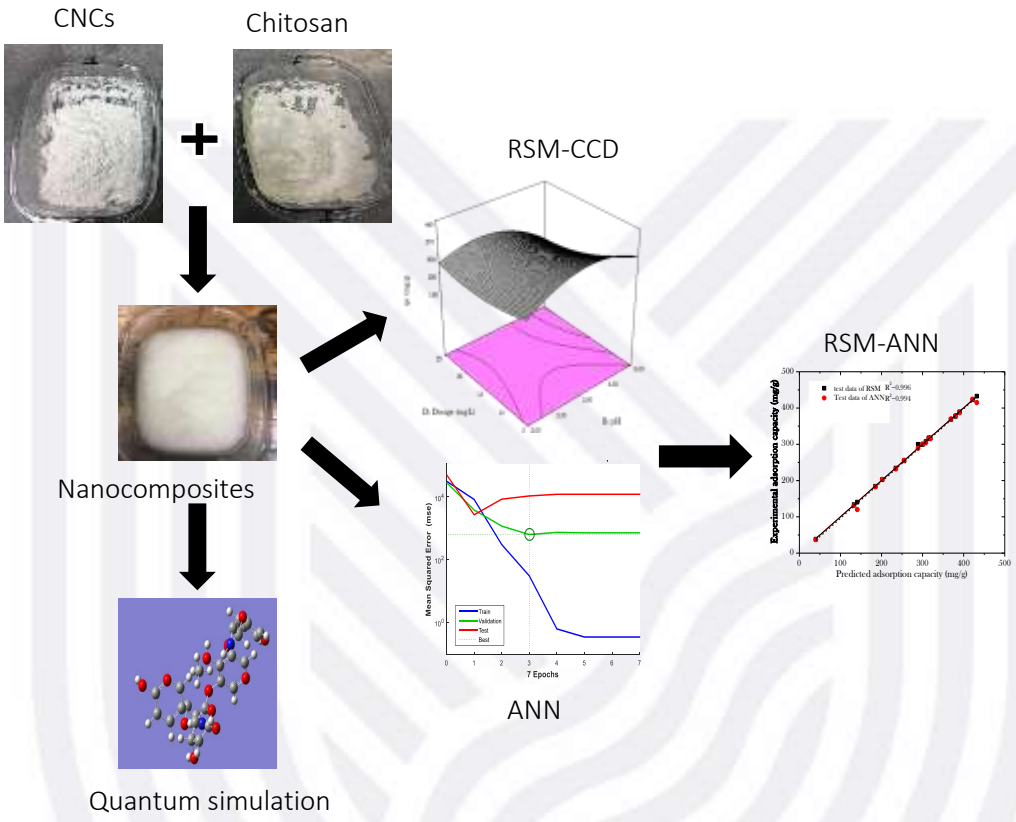

Highlight

- CNCs-Chitosan nanocomposites synthesis and characterization
- Response Surface Methodology (RSM) and Artificial Neural Networks (ANN) were used to model and optimise the removal of Cd^{2+} onto nanocomposites.
- The isotherm and kinetic parameters of the adsorption process are evaluated.
- The adsorption capacity of Cd^{2+} reached 440.01 mg/g.
- The sorbent's adsorption capacity and preferred sites were identified
-

5.1. INTRODUCTION

Metals used in the chemical, electroplating, leather, tanning, galvanizing, mining, pigment, and dye industries are among the world's most hazardous nonbiodegradable elements. It is a problem because industrial effluents containing a fair quantity of hazardous metal ions are released into the environment without potential treatment, resulting in environmental difficulties. As a result, the environmental protection agency (USEPA) has classified some metals as carcinogenic and bioaccumulative elements(Khadhri *et al.*, 2019; Oyewo *et al.*, 2019). Most heavy metals are not biodegradable and easy to gather in fish and plants and then enter the human body through the food chain. Once the accumulated heavy metal content is higher than the body's micronutrient levels, it will affect the enzyme's activity, resulting in various illnesses and even life-threatening.(Chen *et al.*, 2019)

Many approaches, such as chemical oxidation/reduction, precipitation, ion exchange and adsorption, and membrane filtration, have been used to reduce the harmful effects of heavy metals on the environment and humans.(Rahaman *et al.*, 2021; Salcedo *et al.*, 2016) There are two significant limitations for adsorption application: the cost and efficiency of adsorptive materials. As a result, an increasing number of researchers are concentrating their efforts on developing bioresource adsorbents. Cellulose is a bioresource, and its derivatives have piqued the interest of many people because of its renewability, biodegradability, and high stability.

Cellulose is made up of b-D-glucopyranose units linked by b1,4 glycosidic connections and has a high polymerization degree. Because of the solid intermolecular and intramolecular hydrogen interactions between the hydroxyl groups, cellulose tends to cluster into bundles and produce a highly crystalline structure, limiting its ability to remove heavy metals. On the other hand, many hydroxyl groups supply chemical modification properties to cellulose, allowing for superior adsorption performance and broad-scale use.(Shahnaz *et al.*, 2020)

Furthermore, earlier research has shown that cellulose nanocrystals(CNCs) nanocomposites are potential biosorbents for water purification due to their high affinity for various water contaminants among bio-based natural polymer nanocomposites. The presence of hydroxyl and amino groups in the gelatin chemical structure is a significant

benefit, as it facilitates the functionalization of cellulose nanocrystals/gelatin and subsequent modifications with nanomaterials. These cellulose nanocrystals modifications with nanomaterials like carbon nanotubes and inorganic nanoparticles like Fe_3O_4, ZnO and TiO_2 are ideal for improving the mechanical characteristics of CNCs, which are beneficial for water treatment.(Du *et al.*, 2019; Kaboorani & Riedl, 2015; Lu *et al.*, 2018; Tang, 2016) Furthermore, these functional cellulose nanocrystals modified with nanomaterials to introduce new functional groups are required to improve the chelating properties of cellulose nanocrystals, change the pH range for pollutant adsorption, improve the density of adsorption sites, and improve the adsorption selectivity for various water contaminants.(Voisin *et al.*, 2017) Due to the large surface area and many other excellent multifunctional properties of nanomaterials, such as carbon nanostructured and inorganic nanoparticles are critical for achieving a high adsorption capacity. Resulting from increased interactions between the adsorbate (pollutants) and active sites of cellulose-based nanocomposites.(Olad *et al.*, 2020)

Adsorption processes have a complicated mechanism. It is owing to the non-linear nature of these processes and the complex interplay of factors. As a result, determining the best experimental conditions is critical for achieving maximum efficiency. The traditional optimization approach (single variable optimization) is time-consuming and inefficient. Still, it also fails to portray the full impacts of the process parameters and overlooks the coupled interactions between physicochemical parameters. This technique can potentially lead to results being misinterpreted. Some statistical approaches have been tried to solve this challenge. Response surface methodology (RSM) has recently gained a lot of interest as a set of mathematical and statistical approaches for evaluating the impacts of several independent factors.(Shahnaz *et al.*, 2020)

RSM evaluates the connections between the response(s) and the independent factors and the influence of the independent variables in the processes, whether alone or combination. This technique offers many advantages, including being more cost-effective, requiring fewer trials, investigating the interaction between factors on response, anticipating a response, evaluating method appropriateness, and taking less time. This method uses low-order polynomial equations in a predefined area of the independent variables, which are then evaluated to find the optimal independent variable values for the best responses.(Saini *et al.*, 2019)

In addition, during the last ten years, a slew of data analysis tools based on biological phenomena have evolved into well-known modelling approaches, including artificial intelligence and evolutionary computing. Indeed, an artificial neural network (ANN) is a massively linked network structure consisting of many essential processing components capable of simultaneous data processing computation. This technique is effective when the mechanisms behind process performance are complicated. Because of its dependable and conspicuous qualities in capturing the non-linear connections that occur between variables, artificial neural networks (ANNs) have been intensively explored in recent years to solve environmental challenges.(Aversano *et al.*, 2021; Kabuba & Banza, 2020a) It can be used to solve situations for which traditional statistical approaches are ineffective. Because of their widespread use, aptitude, and ability to handle complex issues, ANNs have been evaluated. Chemical engineering uses ANNs for process modelling and simulation, especially when there is no analytical model available. The prediction and generalisation capacities, sensitivity analysis, and optimization efficiency of the ANN and RSM methods in heavy metal removal from wastewater were compared. The removal of Cu^{2+} from aqueous solutions using various sorbents has been studied. However, these sorbents must be focused on and studied more thoroughly.(Hernández-Hernández *et al.*, 2017)

The primary goal of this research is to assess cellulose nanocomposite adsorption capability as a natural and low-cost sorbent in cadmium removal using RSM and ANNs, estimate their performance in the water treatment process, and a comparison of ANN and RSM methods was conducted. The findings of the two models were then compared to the experimental data.

5.2. MATERIALS AND METHODS

5.2.1 Materials

Cellulose nanocrystals used were extracted from waste papers provided by Vaal university of technology. Chitosan commercial grade with a degree of acetylation of 75 %. Cadmium acetate dihydrate, acetic acid(>99%), sodium hydroxide(>99%), hydrochloric acid (>99%) and urea(>99.5%) were all purchased from Sigma-Aldrich.

5.2.2 Method

For cellulose nanocrystals dissolving, an aqueous solution comprising urea and water was produced, and frozen.10g of cellulose nanocrystals were dispersed with vigorous stirring in 200 mL of urea solvent, the mixture was frozen at −25°C for 5 minutes before being thawed at room temperature and agitated at 1000 rpm for 10 minutes to dissolve cellulose. 10 g of chitosan was mixed in 1% acetic acid at room temperature. The chitosan solution was dispersed in 200 mL of sodium hydroxide/urea/water solvent. The mixture was kept at -25°C until it was frozen. The frozen mixture was then thawed completely and stirred at 1000 rpm for 10 min. 25 mL of cellulose nanocrystals solution was added to 25 mL of Chitosan at the rate of 2mL per minute using a syringe. The bulk solution was stirred with a magnetic bar at 250 rpm during addition. After that, the cellulose-chitosan nanocomposites were collected and thoroughly washed with deionized water to remove the salts, followed by the drying process.

5.2.3 Batch experiments

batch adsorption experiments for Cd^{2+} removal by cellulose nanocrystals/chitosan nanocomposites were carried out in 250 mL glass flasks. 5–25 mg/L of the nanocomposites were mixed into 100 mL of Cd^{2+} solution with a known concentration ranging from 50 to 500 mg/L and pH from 2 to 8. 1 M HCl and 1 M NaOH were used to adjust the pH of the solution. Plastic paraffin film was used to cover the glass beakers. The sample was then placed on a shaker at a constant temperature (20–30°C) and agitated at a constant pace (180 rpm) for (0–360 minutes). The Cd^{2+} concentration in residual solutions was determined using a flame atomic absorption spectrophotometer after reaching equilibrium.

The quantity of cadmium ions adsorbed onto cellulose nanocrystals-chitosan nanocomposites (q_e) was determined using the equation below.

$$q_e = \frac{(C_i - C_{eq}) \times V}{M} \quad (5.1)$$

where C_i ($mg.L^{-1}$) denotes the initial concentration of Cd^{2+}, C_{eq} (mg/L) denotes the concentration at equilibrium, M (mg) denotes the mass of the nanocomposite used, and V (L) is the volume of the solution.

5.2.4 RSM (Response surface methodology)

When all other parameters are set to a specific value, one variable changes in the traditional way, experiments must be carried out using traditional methods, and the interaction between factors must be investigated. RSM is one of the essential branches of experimental design. The RSM method is used to assess the impact of several variables and their interactions on the system's response. It's a blend of mathematics and statistical techniques. This approach is practical for generating and improving independent variables and responses while also requiring fewer experimental runs. RSM is most commonly used in situations where a large number of factors influence the system response. As stated above, RSM consists of three phases: design of experiments, response surface modeling, and optimization. For this study, Central Composite Design (CCD) approach using Design expert software for the experimental design (version 13).

Table 5.1 shows the number of input variables taken into account, which ranges from one to three. As a result, the following factors were considered independent variables in the current study: Time (X_1), pH (X_2), Concentration (X_3)and Dosage (X_4). As response variables, The adsorption capacity (q_e) was selected.

Table 5.1: Range of factors and their levels used in the Central Composite Design.

Variable	Coded	Coded level		
Time (min)	A	0	180	360
pH	B	2	5	8
Concentration (mg/L)	C	50	250	500
Dosage (mg/L)	D	5	15	25

The second-order polynomial illustrates the mathematical relationship between independent process variables in Equation 5.2.

$$Y = \gamma_0 + \gamma_a A + \gamma_b B + \gamma_c C + \gamma_{aa} A^2 + \gamma_{bb} B^2 + \gamma_{cc} C^2 + \gamma_{ab} AB + \gamma_{ac} AC + \gamma_{bc} BC \quad (5.2)$$

Where Y is the predicted response, γ_0 is the model constant, A, B, and C are independent variables, γ_a, γ_b and γ_c are linear coefficients and γ_{ab}, γ_{ac} and γ_{bc} are cross-product coefficients, and γ_{aa}, γ_{bb} and γ_{cc} are the quadratic coefficients.(Kabuba & Banza, 2020a)

5.2.5 ANN (Artificial Neural Networks)

The artificial neural network (ANN) is a suitable model for the human brain and nerve systems, well-known for its exceptional capacity to learn and categorize data. ANNs are made up of an input and output layer and one or more hidden layers. Each neuron in the input and buried layers get input values. Neurons provide input values to the next layer of neurons, with the strength of these connections regulated by weights. As the optimum method for network training, the Levenberg–Marquardt backpropagation algorithm (LMA) was used. A three-layer feed-forward ANN was also constructed to forecast and simulate the nanocomposites adsorption capacity for Cd^{2+} removal (**Figure 5.1**), using a linear transfer function at the output layer and a tangent sigmoid transfer function at the hidden layer. Four input nodes, ten hidden layer neurons, and one output node were used in training, with an error of 0.0001. Artificial Neural Network Toolbox V4.0, MATLAB, 2015a was used to conduct the ANN method.

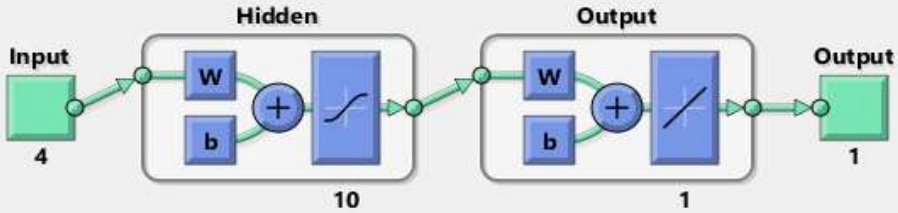

Figure 5.1: Artificial neural network architecture

5.2.6 Quantum mechanism simulation

Spin-polarized density functional theory was used to study the capacity of Cd^{2+} to bind to the adsorbent (DFT). The Gaussian 6.0 software was used to perform the density functional theory calculations. The positively charged Cd^{2+} was chosen as the model cadmium form, while the cellulose glucose was chosen as the model cellulose compound. Furthermore, the vibrational frequency was utilised to confirm that the molecules were correctly optimised, with the findings revealing that no negative wavenumber peak could be found in the spectrums.(Chen *et al.*, 2019) The adsorbent's highest occupied molecular orbital (HOMO) energy Eg(HOMO) and lowest unoccupied molecular orbital (LUMO) were computed to get a better understanding of the adsorption preferred locations. The ability of different functional group-modified cellulose derivatives and identifying the preferred adsorption sites were determined by comparing the Cd^{2+} binding and energy

gaps $Eg^{1/4}$ =Eg(HOMO)-Eg(LUMO).(Mo *et al.*, 2021; Xu *et al.*, 2021) The structure of the nanocomposites is presented in **Figure 5.2.**

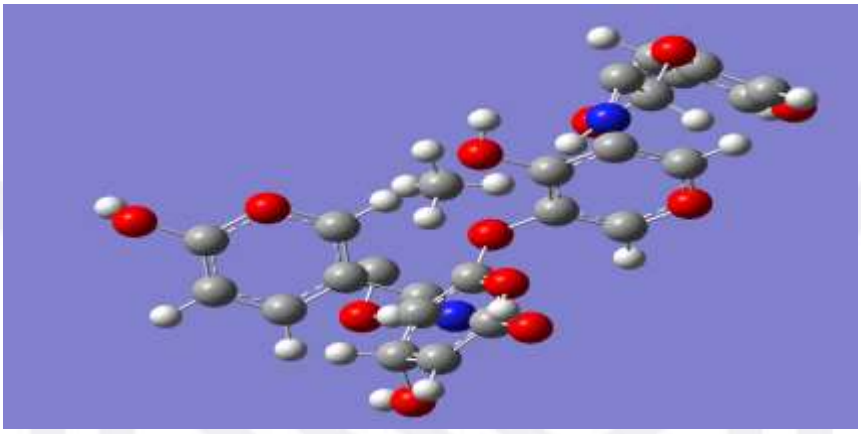

Figure 5.2: the optimized structure of the nanocomposite (3D). Black, red, blue, and light black denote carbon, oxygen, nitrate, and hydrogen atoms.

5.3. RESULTS AND DISCUSSION

5.3.1 FTIR analysis

A wideband in the 3286-3486 cm^{-1} range is seen in **Figure 5.3a**, which is attributed to the O-H stretching vibration. The absorption peak shows the C–H vibration of SP3 hybridised carbon at 2920 cm^{-1}. This band, which emerges in the SP^2 hybridised carbon area just above 3000 cm^{-1}, confirms the presence of a saturated bond surrounding the carbon atom. The stretching vibration of C–O is represented by a band at 1000 cm^{-1}. Still, a band around 1435 cm-1 represents the CH2 vibration, 790 cm^{-1} indicates the general structure of cellulose with glucoside bonds and is considered the crystallinity band in any cellulosic material.

Bands at 750 cm^{-1}, 800 cm^{-1}, 1020 cm^{-1}, 1550 cm^{-1},1650 cm^{-1}, 2800 cm^{-1} , 3000 cm^{-1}, and 3300 cm^{-1} are typical bounds for chitin.(Cheng *et al.*, 2019) In **Figure 3b**, O-H, N-H stretches are linked to the band at 3320 cm^{-1}. CH_2 and CH_3 stretches are responsible for the vibrations at 3000 and 2800 cm^{-1}. At 1650 cm^{-1}, a secondary amide stretch may be seen. At 1550 cm^{-1}, the N-H and C-N vibrations for amide II are seen. The C-O ring has an asymmetric elongation of 1020 cm^{-1}. C-O vibration at 820 cm^{-1} while N-H had single bounds at 750 cm^{-1}.

The hydroxyl and amine groups' absorption bands overlapped and formed a broad peak in the range of 3400-3600 cm^{-1} (**Figure 3c**). The stretch of CH_2 vibration in CNCs and Chitosan is connected to developing a peak of approximately 1500 cm^{-1} for the

nanocomposite samples. The apparent band at 1630 cm^{-1} is attributed to N-H vibration due to the overlapping stretching vibration of carbonyl groups of CNCs and Chitosan. The bending vibration mode of O-H groups has coupled with the absorption bands of C-O and C-N, resulting in overlapping absorption bands between 1150 cm^{-1} and 1350 cm^{-1}. The existence of N-H and C-O indicate that CNCs and Chitosan have been included in the composite.

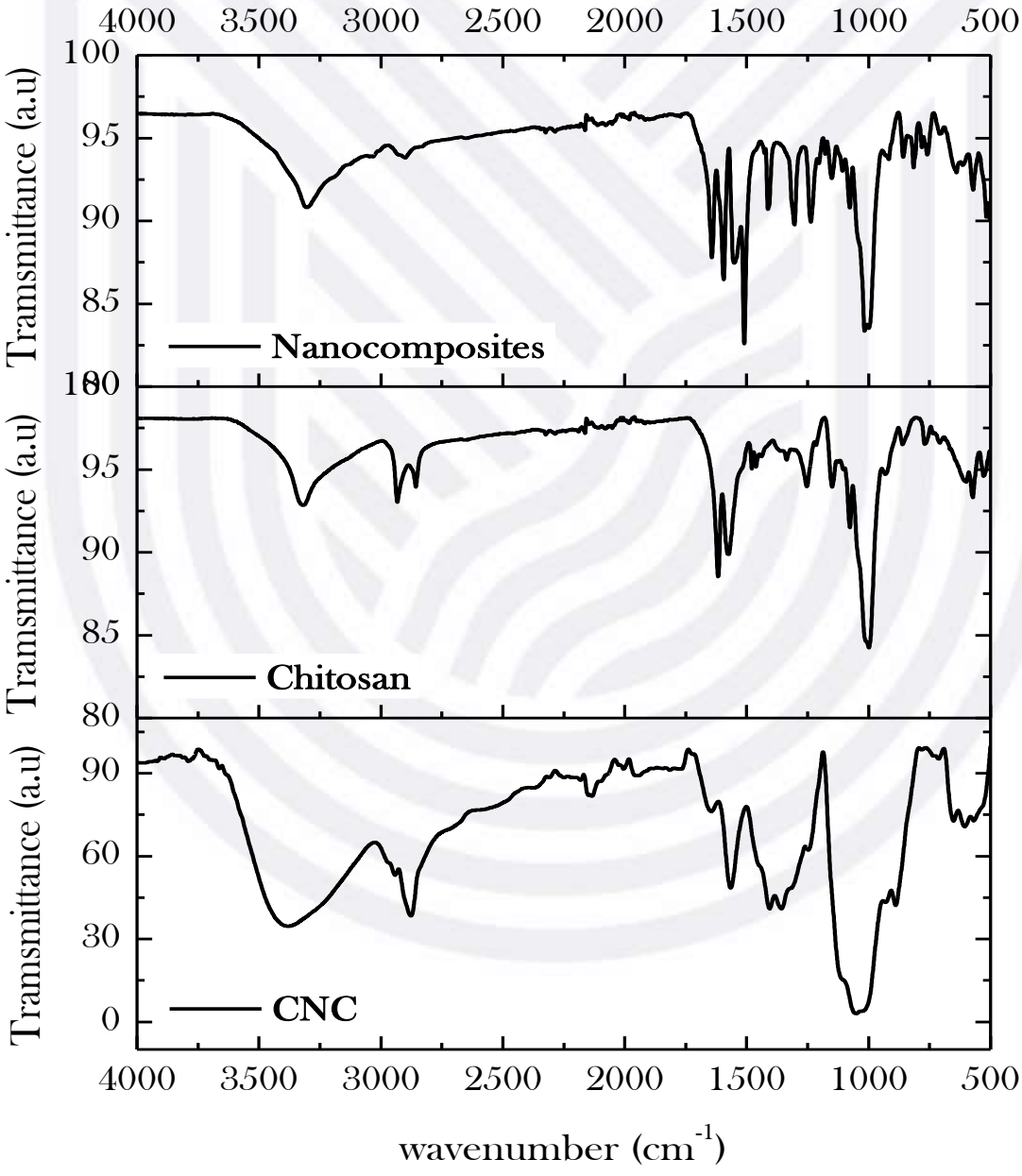

Figure 5.3: FTIR spectra (a) CNCS, (b) chitosan, and (c) Nanocomposites

5.3.2 Morphological analysis

Figure 5.4a reveals the porous nature of the CNCs, and the pores are uniformly distributed over the homogenous rough surface; the appearance of needle-shaped fibres was also noted. Pure chitosan SEM image (**Figure 5.4b**) revealed a nonporous, smooth membranous phase with dome-shaped orifices, microfibrils, and crystallites(Leudjo Taka *et al.*, 2021). SEM of the composites is shown in **Figure (5.4c)**. The nanocomposites exhibit a porous surface morphology, as observed in SEM pictures, attributed to physical crosslinking sites between CNCs chains and the grafted chitosan structure.(Lei *et al.*, 2019) By increasing the contact surface area in the swelling medium, this porous structure can boost the swelling rate of the nanocompites(Shojaeiarani *et al.*, 2019).

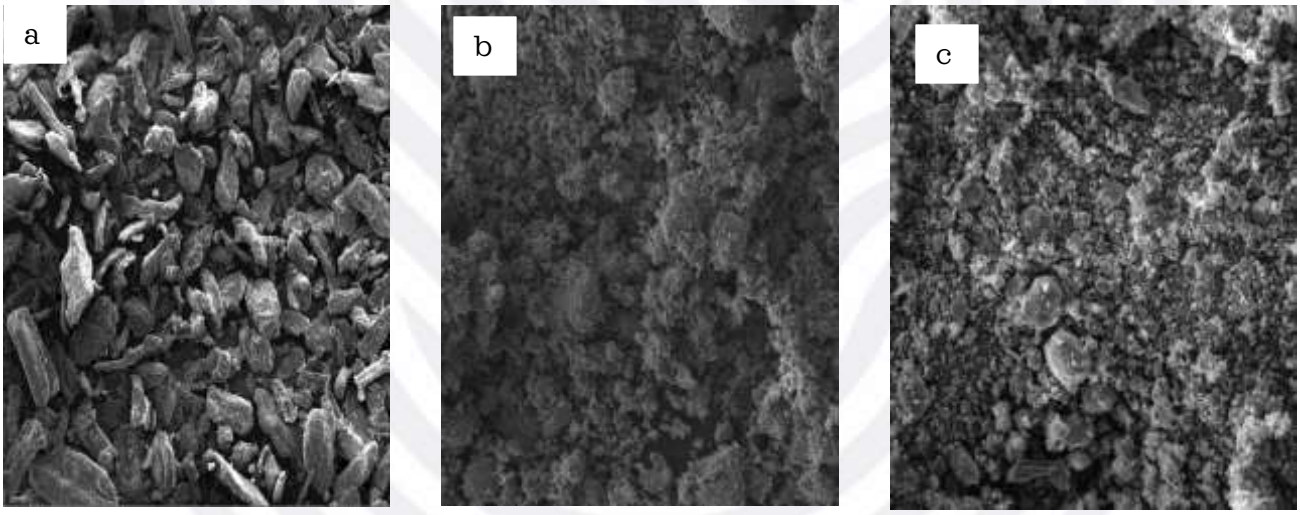

Figure 5.4. SEM image of (a) CNCS, (b) chitosan, and (c) Nanocomposites

5.3.3 TGA analysis

The TGA curves of CNCs, Chitosan, and Nanocomposites samples produced in an N_2 atmosphere at a 10 C min^{-1} heating rate are shown in **Figure 5.5.** The initial degradation stage at ambient temperature (20–100°C) is due to the evaporation of moisture and residual H_2O from the samples, with weight losses of 10%, 5%, and 5% for the nanocomposites, CNCs, and Chitosan, respectively. The following degradation phase was seen at higher temperatures due to the thermal breakdown of the CNCs-chitosan. The weight loss for CNCs was rapid at 250–300°C, followed by a more gradual decline at 300–400°C. The degradation of the pyranose rings in the backbone of CNCs is correlated with a distinctive degradation peak between 250 and 400°C.(Moharrami & Motamedi, 2020)

The second stage began at 250°C and ended at 350°C, with a 70% weight reduction. Above 400°C, there was a 5% weight loss in the third stage. The depolymerisation and breakdown of the acetylated units of Chitosan, and decomposition of Chitosan, respectively, correlate to the weight loss in the second and third phases.(Zhang *et al.*, 2016) Meanwhile, nanocomposites began to degrade around 250°C, similar to what was observed in CNCs. A third degradation stage occurred at 450–600°C, resulting in a 5% weight loss consistent with the breakdown of Chitosan and CNCs and demonstrated the effective synthesis process.

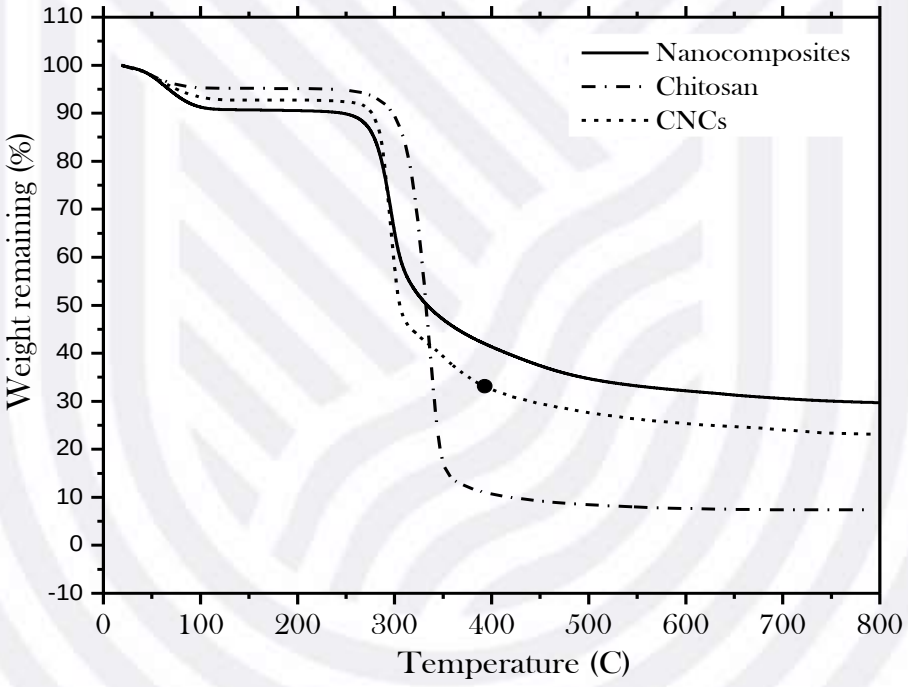

Figure 5.5. TGA of CNCs, Chitosan and Nanocomposites

5.3.4 BET analysis

The Brunauer–Emmett–Teller (BET) technique was used to calculate the specific surface area of CNC, Chitosan and Nanocomposites and the findings are summarised in **Table 5.2.** The width of the pore volume and the surface area distribution may be observed to follow an increasing order: Chitosan> CNCs> Nanocomposites. The nanocomposites' surface area and pore volume were increased by loading urea molecules during the modification process in the nanoparticles. The urea opened several CNCs and chitosan major channels, increasing N_2 diffusion via these channels, opening the surface area and pore volume

Table 5.2: BET analysis of CNCs, Chitosan, and Nanocomposites

Sample	Specific surface area (m^2/g)	Pore volume (cm^3/g)
CNCs	2.126	0.002
Chitosan	1.586	0.001
Nanocomposites	4.254	0.015

5.4 THE RSM MODELLING

Based on earlier investigations(Aden *et al.*, 2017; Chen *et al.*, 2019; Ihsanullah *et al.*, 2016; Nordin *et al.*, 2021; Oyewo *et al.*, 2019; Tang *et al.*, 2016; Vishnu Priyan *et al.*, 2021), the starting cadmium ions concentration, initial pH, time, and adsorbent dose were chosen as independent variables. The experiment response was chosen to be Cd^{2+} adsorption capacity (q_e). The sequence of the experimental runs was chosen at random from three levels. The experimental design runs were found to be twenty-one runs. The primary argument was repeated three times to examine the pure mistake. All of the experiments were duplicated. The performance of Cd^{2+} adsorption was studied using a centrale composite design. The experimental design and obtained results are reported in **Table 5.3.**

Table 5.3: Independent variables and experimental data for CCD

Run	A: Time (min)	B: pH	C:Concentration (mg/L)	D: Dosage (mg/L)	q_e Experimental (mg/g)	q_e Predicted (mg/g)	Residual
1	0	0	0	0	319.01	317.71	1.29
2	0	0	+1	0	289.06	290.91	-191
3	+1	+1	-1	-1	432.05	432.77	-0.77
4	+1	+1	+1	-1	369.00	368.5	0.48
5	+1	-1	-1	+1	422.03	422.77	-0.76
6	+1	0	0	0	379.05	378.41	0.59
7	0	0	0	0	316.06	317.71	-1.71
8	0	0	0	+1	202.01	202.77	-0.77
9	+1	-1	+1	+1	300.02	299.52	0.49
10	-1	+1	+1	+1	40.07	39.52	0.48
11	0	+1	0	0	235.01	2.34.41	0.59
12	-1	-1	+1	-1	141.02	140.52	-0.77
13	-1	0	0	0	185.03	184.41	0.59
14	-1	-1	-1	-1	202.05	202.77	0.58
15	0	0	0	0	317.06	317.71	-0.71
16	-1	+1	-1	+1	133.02	133.77	-0.78
17	0	0	0	0	315.03	317.71	-1.70
18	0	0	0	0	318.08	317.71	0.29
19	0	0	0	-1	390.02	389.41	0.59
20	0	0	-1	0	380.03	376.91	3.09
21	0	0	0	0	255.02	254.41	0.57

5.4.1 Model fitting and ANOVA analysis

The ANOVA findings for the generated response surface quadratic model are shown in **Table 5.4.** The ANOVA test determines if the generated response surface quadratic model is statistically appropriate for representing the process of Cd^{2+} adsorption on nanocomposites at the investigated range.

The model's F-value of 2843.43 indicates that it is significant. Noise has a 0.01 percent probability of causing such a high F-value in a model. P-values less than 0.0001 denote significant model terms. (Kabuba & Banza, 2020b) In this case, a, C, D, BD, CD, A^2, B^2, and D^2 are the signficant model terms. Model terms with P-values larger than 0.10 are not significant. The p-value represents the likelihood of rejecting the null hypothesis. The greater the Fisher's F-value, the more important the individual coefficients are, and the better the model is.(Shahnaz *et al.*, 2020) The lack of fit F-value of 10.54 indicates that the lack of fit is not statistically significant compared to the pure error. A large lack of fit F-

value, possibly due to noise, has a 4.21 percent chance of occurring. No significant lack of fit is good. Furthermore, the p-value for lack of fit is larger than 0.05, implying that the model fits the experimental data and that the independent process variables significantly influence the response. The coefficients of a specific process variable and two combined variables, respectively, explain the magnitude of the variable's influence and the interaction between two variables.(Derikvandi & Nezamzadeh-Ejhieh, 2017) Using the F-value, the following terms have the greatest influence on the model: A > C > B^2 > A^2 > D > D^2 > BD > CD > C^2 > B > AB > AC > BC > AD. The initial Cd^{2+}concentration was discovered to have the largest impact on the model, followed by the dosage. The predicted R^2 (0.992) is reasonably close to the adjusted R^2 (0.987). The coefficient of determination, R^2, of 0.987, representing the degree of fitness, indicates the strong connection between the predicted and experimental responses. These values are near to unity, confirming the model's validity.[32] Equation 3 shows the quadratic model equation that relates the response of Cd^{2+} removal efficiency to the independent process variables (pH, contact time, dosage, and initial Cd^{2+} concentration).

$$q_e = 371.71+97.00A- 10.00B- 43.00C-41.00D- 36.30A^2- 73.30B^2+ 16.20C^2+ 30.70D^2- 9.88AB- 3.88AC+ 1.38AD+ 3.37BC- 28.87BD- 11.37CD \quad (5.3)$$

The insignificant terms of the above model equation can be eliminated(Kabuba & Banza, 2020a). The standard probability plots of the residuals (normal percent probability against internally studentized residuals) (**Figure 5.6**) show no significant departure from the norm. Because the graphical points are on a straight line, no data transformation is necessary(Igwegbe *et al.*, 2019)

Table 5.4: Regression analysis and significance of the components in the model.

Factor	coefficient	Standard error	F-value	P-value	Significance
model	317.71	0.75	2843.43	<0.0001	significant
A	97.00	1.61	3633.42	<0.0001	
B	-10.00	1.61	38.62	0.0008	
C	-43.00	0.72	3570.09	<0.0001	
D	-41.00	1.61	649.14	<0.0001	
A^2	-36.30	1.42	649.36	0.0005	
B^2	-73.30	1.42	2648.07	<0.0001	
C^2	16.20	1.42	129.42	0.0005	
D^2	30.70	1.42	464.68	<0.0001	
AB	-9.88	1.80	30.13	0.0015	
AC	-3.88	0.80	23.19	0.0475	
AD	1.38	1.80	0.58	0.0014	
BC	3.37	0.80	17.59	0.0005	
BD	-28.87	1.80	257.58	<0.001	
CD	-11.37	0.80	199.86	<0.001	
Lack of fit			10.54	4.21	Not significant
R^2	**0.989**				
R^2 adjusted	**0.987**				
R^2 Predicted	**0.992**				

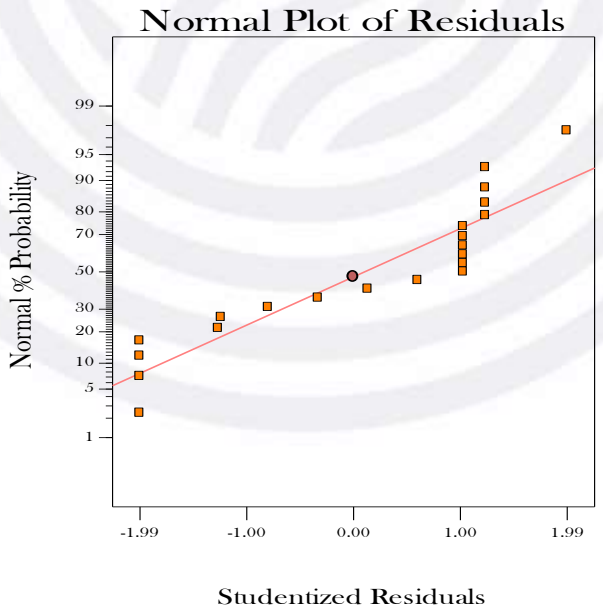

Figure 5.6: The normal percentage probability residuals and studentized for Cd^{2+}adsorption onto Nanocomposites

5.4.2 Response surface plots

To examine the impact of independent process factors on a response or responses, RSM is used. While the other process variables were kept at their central (0) level, two-dimensional (2D) contour plots, as well as three-dimensional (3D) response surface plots, were made to study the interaction of the different process variables and their corresponding effects on the response (Cd^{2+} removal efficiency).

pH and Dosage were shown in **Figure 5.7 (a)** and **(b)** as elliptic contour plots. According to the circular nature contour plot, pH and dosage strongly affect adsorbent capacity. Up to pH 5 and 5 mg/L dosage, the adsorbent increased. The reaction slowed down when the pH was more than six and the dosage greater than 20 mg/L. It may be due to the presence of cationic species in the nanocomposite sites, which can slow the approach of such ions to the surface. Cadmium may precipitate at a higher pH value as $Cd(OH)_2$, resulting in lower adsorption capacity(Banza *et al.*, 2021)

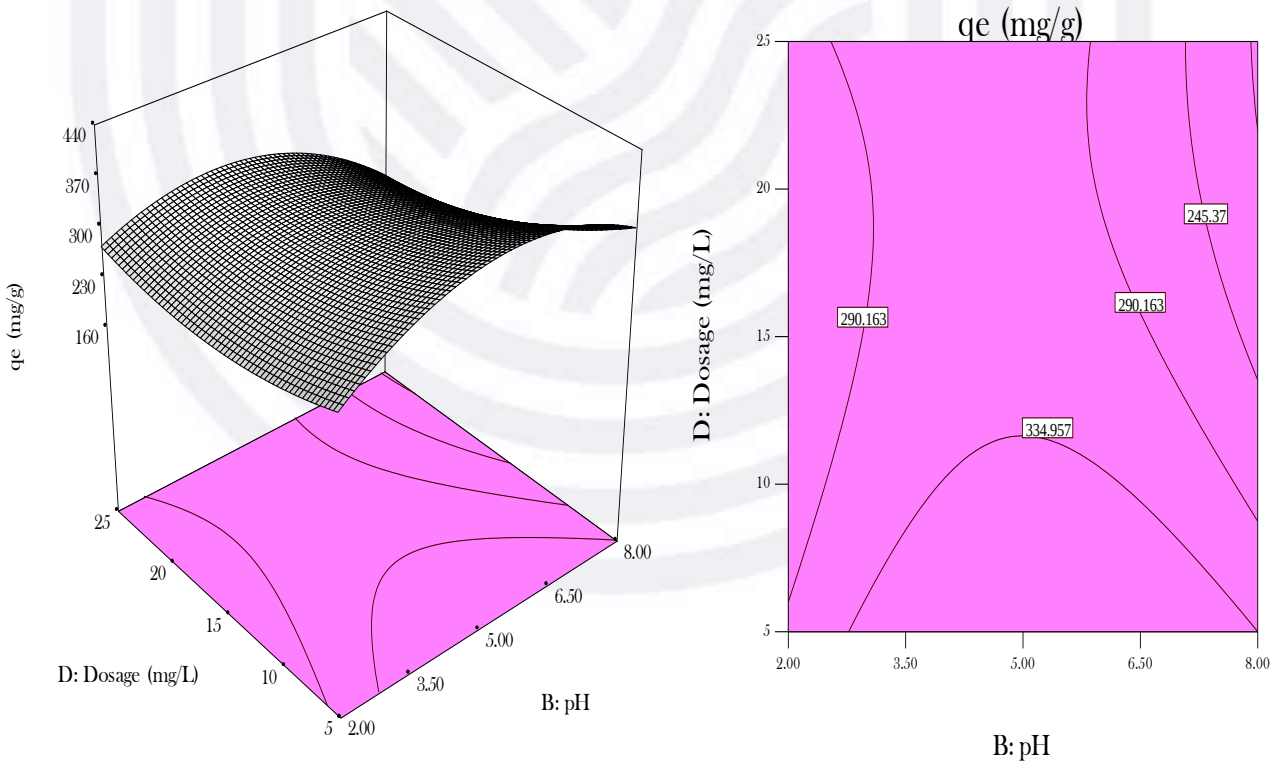

Figure 5.7. The 3D surface and 2D contour plots of the effect of pH and dosage on the Cd^{2+}removal efficiency using nanocomposites at constant time and concentration

Contact time and concentration are critical factors in the removal of Cd^{2+} from the solution. As shown in **Figure 5.8 (a)** and **(b)**, the contact time of the solution can impact the solution/solid interface and dosage, as well as the adsorption capacity of nanocomposites.(Musikavanhu *et al.*, 2019) The contour shows that the contact time of the nanocomposite is more significant than the concentration, and there is an interaction. In all procedures, the time of interaction is a critical factor. With increasing contact duration and the initial concentration, the adsorbate, Cd^{2+}, adsorption was enhanced. The availability of more active adsorption sites for the trapping of the Cd^{2+} and the existence of enough time for the adsorption process is responsible for the improvement in Cd^{2+} removal effectiveness(Chen *et al.*, 2019).

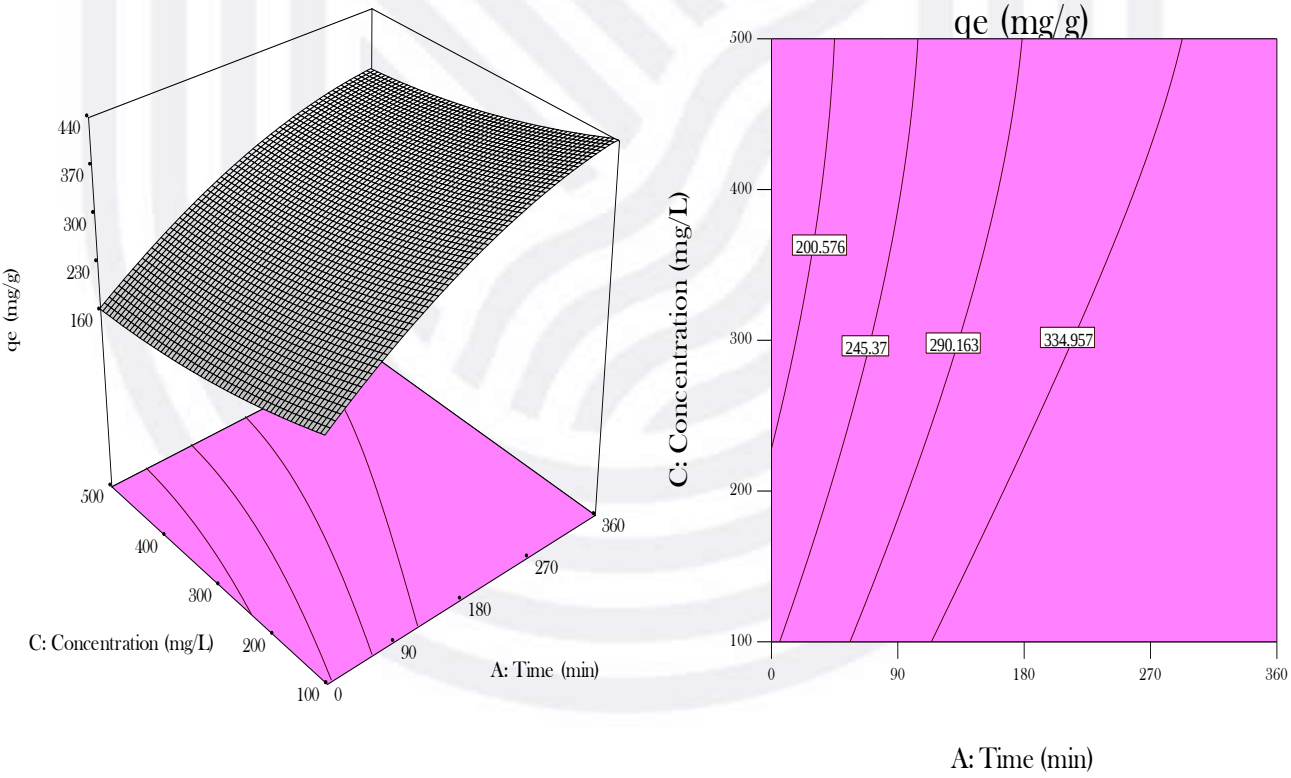

Figure 5.8: The 3D surface and 2D contour plots of the effect of Time and Concentration on the Cd^{2+} removal efficiency using nanocomposites at constant time and concentration

5.4.3 ANN (Artificial neural network) modelling

To anticipate the result and behaviour of systems, create novel processes, and analyse previously existing processes, Artificial Neural Networks (ANNs) are employed(Aversano *et al.*, 2021). An MLP is generally taught using the back-propagation method. Gradient descent (GD), conjugate gradient (CG), and Levenberge–Marquardt (LM) techniques can be used to minimise errors in MLP networks. The experiments generated using the CCD provided the input and output for the training. The multilayer perceptron (MLP) technique used in this study was created in MATLAB (The Math Works Inc. 2015a) with four input neurons representing the independent variables (pH, contact time, nanocomposite dose, and initial Cd^{2+} concentration), a ten neuron hidden layer, and a single neuron output layer representing the Cd^{2+} adsorption. To choose data, build, and train a network, the Neural Fitting application was utilised. The mean square error (MSE) and regression analysis coefficient (R^2), both available in the MATLAB programme, were used to evaluate its performance.

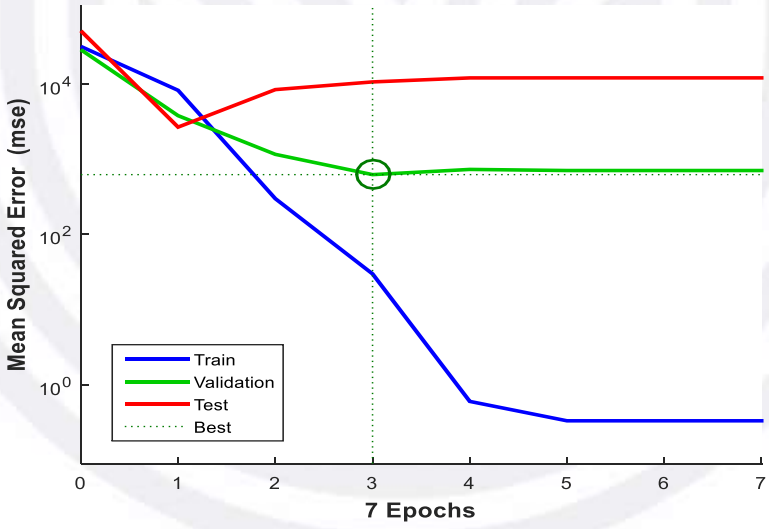

Figure 5.9: Performance plot for the ANN model

As long as the input is consistent and there are enough neurons in the hidden layer, a two-layer feed-forward network with hidden sigmoid neurons and linear output neurons can fit multi-dimensional mapping problems arbitrarily well. The Leven berg-Marquardt backpropagation method was used to train the network MLP (4:10:1). In general, this technique requires more memory, but it is faster. It occurs when the mean square error of the validation samples increases, indicating that generalisation is no longer improving.

This approach was used to determine the optimal number of neurons in the hidden layer, the optimal number of training and validating examples, and the optimal number of testing samples. For the ANN modelling, a total of 21 samples were employed; 75% (16 samples), 15% (3 samples), and 10% (2 samples) were used for training, validation of the training, and testing. Several neurons were selected by trial and error for the hidden layer and then trained for seven iterations to find the optimal number. An average regression coefficient, R^2, of 0.999 was found. The trained network's performance plots and regression plots are shown in **Figures 5.10.**

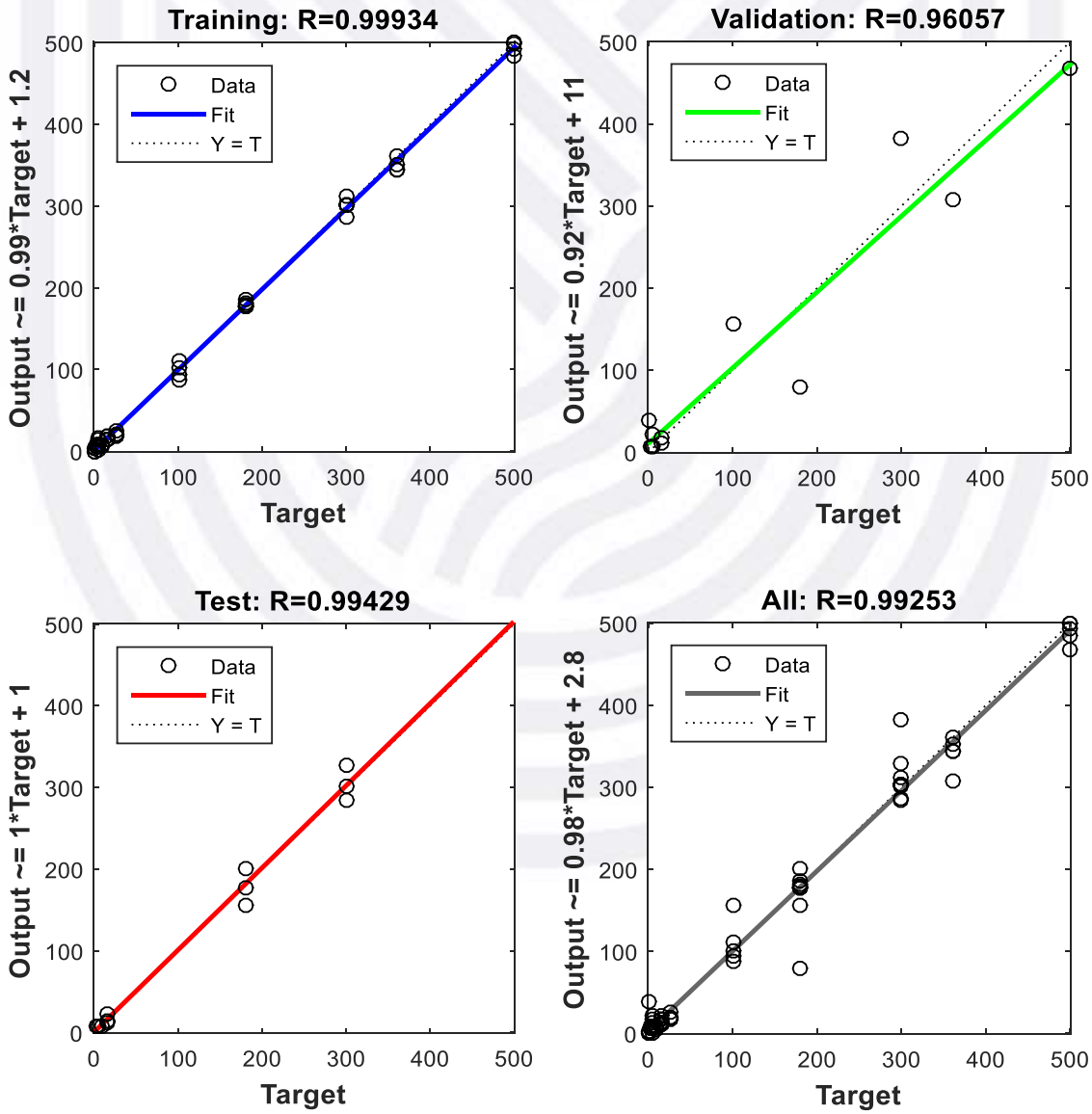

Figure 5.10: Regression analysis results for output and corresponding target(ANN).

5.4.4 Comparaison RSM-ANN

RMSE, MPSD, SSE, SAE, HYBRID, R^2, ARE, MSE, AAD, and X^2, were used to determine performance and the optimum modelling approach for predicting output responses. Table 5 presents the non-linear and linear errors function for ANN and RSM. The best fits are those with the lowest possible error functions. Compared to the ANN model, the RSM model is more acceptable since it has lower error function values. It might be because the current study only employed a small number of experimental runs. To perform better in network training, the ANN generally requires many data points(Aversano *et al.*, 2021; Dolatabadi *et al.*, 2018; Franco *et al.*, 2020). **Figure 5.11** presented the comparison between predicted and experimental data for RSM and ANN.

Table 5.5: Non-linear and linear error functions

Error function	RSM	ANN
Root means square errors (RMSE	0.0005	0.0011
Marquart's percentage standard deviation (MPSD)	0.4132	0.5838
Sum of the squares of errors (SSE)	0.1210	0.1387
Sum of absolute errors (SAE)	0.9950	0.9905
Hybrid fractional error function (HYBRID)	0.0012	0.0035
Regression coefficient (R^2)	0.9969	0.9941
Average relative errors (ARE)	2.5434	2.9821
Mean square errors (MSE)	0.0001	0.0002
Absolute average deviation (ADD)	0.0006	0.0048
Pearson's Chi-square (X^2)	0.0016	0.0008

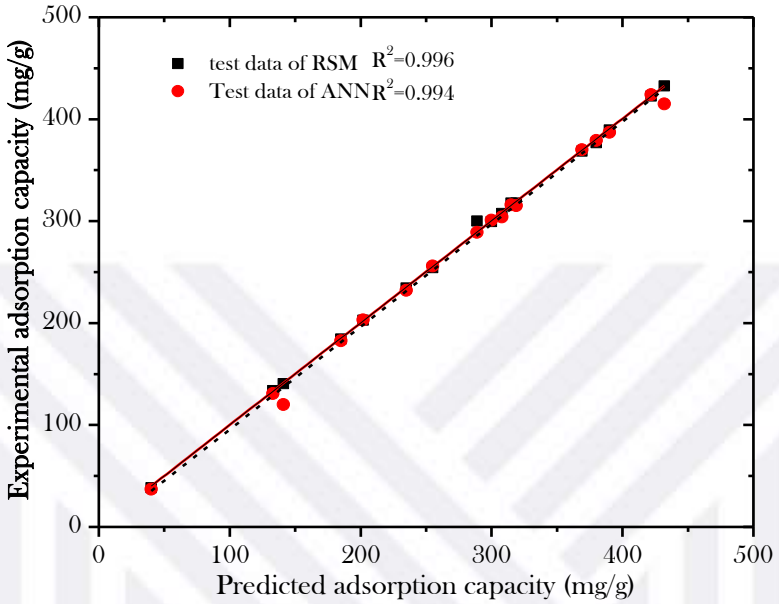

Figure 5.11: Comparison of the predicted vs experimental results (RSM-ANN)

Table 5.5: Experimental and predicted values for Cd2+ removal by RSM and ANN.

Time(min)	pH	Conc.(mg/L)	Dosage (mg/L)	q_e(exp) (mg/g)	q_e (exp) (mg/g) RSM	q_e(exp) (mg/g) ANN
284	3.60	467.04	15.70	335.23	335.52	334.87
274	5.09	297.75	12.14	315.53	315.20	316.29
141	3.82	377.96	10.65	305.80	304.99	302.99
233	4.43	472.20	15.62	378.87	380.10	382.07

Both models (RSM and ANN) accurately predicted the removal of Cd^{2+} from the nanocomposites, as shown in Table 6. To optimize the Cd^{2+} adsorption on nanocomposites, the RSM was applied.

5.4.5 Numerical optimization Centrale Composite Design (RSM)

The optimal conditions for Cd^{2+} adsorption on the nanocomposites were successfully defined using the Design expert programme (13.0 version). Table 4 shows the predicted optimal conditions for maximal Cd^{2+} adsorption capacity. The experimental result, 438.79 mg/g, was achieved by experimenting with the optimal parametric parameters in Table 4. The adsorption capacity was determined to be 440.05 mg/g, which was similar to the prediction. According to Tahareh et al. (Shojaeimehr *et al.*, 2014), a produced model is

acceptable when the desired value is near 1. The desirability of 1 means the model is widely accepted and applicable (**Table 5.6**)

Table 5.6: The optimum predicted conditions for maximum Cd^{2+} removal

Time (min)	pH	Conc.(mg/L)	Dosage (mg/L)	Adsorption capacity (mg/g)	Desirabiliyty
310	5.73	323.04	16.36	440.01	1.000
343	4.63	312..48	17.94	440.05	1.000

5.4.6 Adsorption isotherm and kinetics

An adsorption isotherm describes the connection between adsorbate and adsorbent, their interactions and their maximum adsorption capacity. Here, equilibrium investigations are carried out by fitting the experimental data to Temkin, Freundlich, Langmuir, and Dubinin–Radushkevich isotherm models, respectively.(Kabuba & Banza, 2020a) According to data, the fitted model was validated using regression analysis (R^2) and error functions (X^2). Table 8 lists the results. As may be observed, the most significant correlation coefficients ($R^2 > 0.995$) and lowest error function (0.011) are owned by The Langmuir model. This finding demonstrates that the Langmuir model is adequate. Compared to the Freundlich, Temkin, and D-R isotherms, this is the best way to describe the Cd^{2+} adsorption process on the nanocomposites. Following the Langmuir model, the active sites were distributed uniformly on the adsorbent surface, and the adsorption of Cd^{2+}on the nanocomposites occurred in a monolayer adsorption way. The mean adsorption energy, E, can be used to predict the physical and chemical properties of the reaction. When E is less than 8 kJ mol^{-1}, the adsorption process is physical; when E is between 8 and 16 kJ mol^{-1}, the adsorption process is chemical; and when E is greater than 20 kJ mol^{-1}, chemical adsorption occurs. The D-R model showed E for Cd^{2+}adsorption to be more than 8 kJ mol^{-1}, indicating that Cd^{2+} adsorption onto the adsorbent is a chemisorption process.(Kabuba & Banza, 2020c) The experimental data are fit and correlated with pseudo-first- and second-order kinetic models, Elovich, and intraparticle diffusion to study the adsorption process's mass transfer rate and mechanism. **Table 5.7** shows the kinetic parameters for each model.

The more significant correlation coefficient (R2 > 0.997) and the slight variance between $qe_{(exp)}$ and $qe_{(pred)}$ suggest the pseudo-second-order model's ability to demonstrate

experimental data. The kinetic findings were then analysed using an intraparticle diffusion model based on the Weber and Morris theory to determine the diffusion process. A Weber and Morris theory-based intraparticle diffusion model was then used to analyse the kinetic findings. According to the Morris hypothesis, a qt-versus-t1/2 regression line with an intercept B = 0 suggests that only intraparticle diffusion is responsible for controlling an adsorption process. A non-zero B value (not shown) was obtained, revealing that the Adsorption and pore diffusion is not the only rate-controlling stages. The C values explained the thickness of the boundary layer. The greater the boundary, the larger the intercept (B value).

Table 5.7: Isotherm, kinetic constant parameters and correlation coefficients for Cd^{2+} adsorption onto nanocomposites under RSM optimized condition

Model	Equation	Parameters	values	RMSE
Temkin	$q_e = A \ln C_{eq} + K_t$	Kt (Lmg^{-1})	300.204	0.027
		A	7.521	
		R^2	0.895	
Freundlich	$\text{Log } q_e = \log K_f + \frac{1}{n} \log C_{eq}$	K_f (Lmg^{-1})	289.524	0.033
		n	5.864	
		R^2	0.969	
Langmuir	$\frac{C_{eq}}{q_e} = \frac{C_{eq}}{q_{max}} + \frac{1}{Dq_{max}}$	q_{max} (mg/g)	435.018	0.011
		D (Lmg^{-1})	0.789	
		R^2	0.998	
Dubini-Radushkevich	$\ln q_e = \ln q_{max} - k\beta^2$ $\beta = RT \ln(1 + \frac{1}{C_{eq}})$	E ($Kj.mol^{-1}$)	816.715	0.039
		k (mol^2j^2)	$3.879.10^{-9}$	
		R^2	0.875	
First-order kinetics	$\text{Log } (q_e - q_t) = \log qe - \frac{K_I}{2.3} t$	K_I (min^{-1})	0.0279	0.025
		qe (mg/g)	258.962	
		R^2	0.972	
Second-order kinetics	$\frac{t}{q_t} = \frac{1}{K_S q_e^2} + \frac{1}{q_e} t$	K_S ($g.mg^{-1} min^{-1}$)	0.157	0.013
		qe(mg/g)	376.325	
		R^2	0.997	
Intraparticle diffusion	$qt = K_{dif} t^{1/2} + B$	K_{dif} ($g.mg^{-1} min^{0.5}$)	2.185	0.037
		B	0.018	
		R^2	0.923	
Elovich	$q_t = \frac{1}{A} \ln \alpha A + \frac{1}{A} \ln t$	A (gmg^{-1})	9.521	0.062
		α ($g.mg^{-1} min^{-1}$)	0.025	
		R^2	0.989	

Table 9 compares the maximal sorption capacity of nanocomposites with that of other natural sorbents for Cd $^{2+}$ adsorption capacity. As can be observed, the nanocomposites have an excellent and acceptable sorption capacity for removing cadmium ions from the aqueous phase compared to other sorbents.

Table 5.8: The comparison of the adsorption capacity between CNCs and other sorbents

Sorbent	q_{max} (mg/g)	Reference
Nanocomposite	53.81	Hajar Azad et al. (Azad *et al.*, 2021)
Chitosan beads	145.10	Igberase et al. (Igberase *et al.*, 2014)
Modified cellulose	401.10	Chen et al. (Chen *et al.*, 2019)
CNCs with succinic anhydride	259.70	Oyewo et al. (Oyewo *et al.*, 2019)
Amino Modified CNCs	137.60	Oyewo et al. (Oyewo *et al.*, 2019)
CNCs Nanocomposites	440.05	This study

5.4.7 Analysis of binding ability

Mechanistic study of the nanocomposite indicated that it had more active adsorption sites and higher adsorption ability. To further understand the binding energy and preferred adsorption sites between the adsorbents and Cd^{2+}, quantum chemical modelling was employed.(Chen *et al.*, 2019) Cellulose was simplified by using glucose as the structural unit. Three types of cellulose modified with various functional groups were restricted to examine and compare their contributions.

Table 6 shows equilibrium configurations of adsorbed Cd^{2+} on different group modified cellulose and the energy data. As the absolute amount of binding energy increases, the adsorbent's capacity to bind Cd^{2+} increases. The bond capacity followed the following order: CNCs < carboxyl-CNCs< Amide-CNCs. In contrast to the raw cellulose nanocrystals, the amide-CNCs had the most potent binding ability Adsorbents with more than one functional group modification showed the highest binding ability. It was due to N soliton's electron-donating solid capacity. It may be because the C=O depleted the N soliton's lone pair electrons.(Wang *et al.*, 2021)

To conclude, functional groups play an essential role in synergistic adsorption in the nanocomposite. **Table 5.9** shows a comparison of the nanocomposite and unmodified cellulose adsorbents, which supports this result. For heavy metal cations, our nanocomposite outperformed other adsorbents. The electron transition between the

HOMO of the adsorbent and the LUMO of Cd^{2+}can be considered as chemisorption by the adsorbent. Table 10 shows the HOMO of different functional group modified cellulose adsorbents, the LUMO of Cd^{2+}, and the energy gap (Eg) between Cd^{2+} and the adsorbent. The more significant the energy gap, the more likely an electronic spontaneous transition will occur, and the associated adsorbent will have a higher adsorption capacity. The energy gap in the multi-functional-groups modified cellulose was the largest; it's possible that the hydrogen bond between the amide group from Chitosan and the cellulose molecules was broken, and more active adsorption sites were introduced as a result of the modification, increasing the adsorbent's Cd^{2+} binding ability

Table 5.9: HOMO of the functional group present in the nanocomposite LUMO of Cd^{2+}, Energy gaps and binding energy between the adsorbent and Cd^{2+}

Matrix	E(HOMO)	E(LUMO)	Eg kcal/mol	Ekcal/mol
CNCs	-0.230	-0.298	47.8	-67.3
Carboxyl;-CNCs	-0.233	-0.298	46.7	-72.2
Amide-CNCs	-0.214	-0.298	59.1	-80.7

5.5. CONCLUSION

Using RSM and ANNs, the performance of the nanocomposites in Cd^{2+} removal from aqueous solution and the impacts of operational factors on adsorption capacity in the batch system was studied. The following are the most critical findings from this research:

- The SEM, TGA, BET, and FTIR findings for CNCs, Chitosan and Nanocomposites were remarkable. These findings suggested that the nanocomposites could remove metal ions from wastewater.
- The interaction impacts of the process variables were identified, as well as their optimal conditions. Initial pH of 5.73, contact time of 310 min, initial Cd^{2+} concentration of 323.04 mg/L, sorbent dose of 16.36 mg, and adsorption capacity of 440.01 mg/g were determined to be the optimal condition.
- Based on validation data, the findings of two RSM and ANN approaches revealed that RSM (R^2 = 0.996) and ANN (R^2 = 0.994) are helpful and accurate methods for predicting the adsorption process.

- The RSM had a better RMSE=0.0005, MPSD=0.4132, SSE= 0.1210, SAE= 0.990, HYBRID= 0.0012, ARE= 2.5434, MSE= 0.0001, AAD= 0.0006 and X^2= 0.0016.
- The Langmuir isotherm agreed with the equilibrium data better than the Freundlich and Temkin isotherm. The D-R model revealed that Energy for Cd^{2+}adsorption is greater than 8 kJ mol-1, implying that Cd^{2+} adsorption is a chemisorption process.
- The pseudo-second-order rate model accurately described the adsorption kinetics.
- For Cd^{2+} removal, a carboxyl, amide, and secondary amino multifunctional grafted cellulose nanocrystals derivative adsorbent (nanocomposites) was effectively produced. Furthermore, the functional groups work synergistically in Cd^{2+} adsorption onto the nanocomposites.

5.6. REFERENCES

Aden, M., Ubol, R.N., Knorr, M., Husson, J., & Euvrard, M. 2017. Efficent removal of nickel(II) salts from aqueous solution using carboxymethylchitosan-coated silica particles as adsorbent. *Carbohydr. Polym.* 173:372–382.

Aversano, G., D'Alessio, G., Coussement, A., Contino, F., & Parente, A. 2021. Combination of polynomial chaos and Kriging for reduced-order model of reacting flow applications. *Results Eng.* 10:100223.

Azad, H., Mohsennia, M., Cheng, C., & Amini, A. 2021. Facile fabrication of PVB-PVA blend polymer nanocomposite for simultaneous removal of heavy metal ions from aqueous solutions: Kinetic, equilibrium, reusability and adsorption mechanism. *J. Environ. Chem. Eng.* 9(5):106214.

Banza, M., Rutto, H., & Kabuba, J. Cobalt and Nickel Separation in Hydrometallurgy Using Modified Clinoptilolite with Dialkyl Phosphoric and Ethylenediaminetetraacetic Acid as an Ion Exchanger. Springer International Publishing.

Bohlouli, A., Afshar, M.R., Aboutalebi, M.R., & Seyedein, S.H. 2016. Optimization of tungsten leaching from low manganese wolframite concentrate using Response Surface Methodology (RSM). *Int. J. Refract. Met. Hard Mater.* 61:107–114.

Chen, Q., Zheng, J., Wen, L., Yang, C., & Zhang, L. 2019. A multi-functional-group modified cellulose for enhanced heavy metal cadmium adsorption: Performance and quantum chemical mechanism. *Chemosphere*. 224:509–518.

Cheng, K., Huang, C., Wei, Y., & Hsu, S. 2019. Novel chitosan – cellulose nano fi ber self-healing hydrogels to correlate self-healing properties of hydrogels with neural regeneration effects. *NPG Asia Mater. Springer US*.

Derikvandi, H. & Nezamzadeh-Ejhieh, A. 2017. Designing of experiments for evaluating the

interactions of influencing factors on the photocatalytic activity of NiS and SnS2: Focus on coupling, supporting and nanoparticles. *J. Colloid Interface Sci.* 490:628–641.

Dolatabadi, M., Mehrabpour, M., Esfandyari, M., Alidadi, H., & Davoudi, M. 2018. Modeling of simultaneous adsorption of dye and metal ion by sawdust from aqueous solution using of ANN and ANFIS. *Chemom. Intell. Lab. Syst.* 181:72–78.

Du, H., Liu, W., Zhang, M., Si, C., Zhang, X., & Li, B. 2019. Cellulose nanocrystals and cellulose nano fi brils based hydrogels for biomedical applications. *Carbohydr. Polym.* 209:130–144.

Franco, D.S.P., Duarte, F.A., Salau, N.P.G., & Dotto, G.L. 2020. Analysis of indium (III) adsorption from leachates of LCD screens using artificial neural networks (ANN) and adaptive neuro-fuzzy inference systems (ANIFS). *J. Hazard. Mater.* 384:121137.

Hernández-Hernández, L.E., Bonilla-Petriciolet, A., Mendoza-Castillo, D.I., & Reynel-Ávila, H.E. 2017. Antagonistic binary adsorption of heavy metals using stratified bone char columns. *J. Mol. Liq.* 241:334–346.

Igberase, E., Osifo, P., & Ofomaja, A. 2014. The adsorption of copper (II) ions by polyaniline graft chitosan beads from aqueous solution: Equilibrium, kinetic and desorption studies. *J. Environ. Chem. Eng.* 2(1):362–369.

Igwegbe, C.A., Mohmmadi, L., Ahmadi, S., Rahdar, A., Khadkhodaiy, D., Dehghani, R., & Rahdar, S. 2019. Modeling of adsorption of Methylene Blue dye on Ho-CaWO4 nanoparticles using Response Surface Methodology (RSM) and Artificial Neural Network (ANN) techniques. *MethodsX.* 6:1779–1797.

Ihsanullah, Abbas, A., Al-Amer, A.M., Laoui, T., Al-Marri, M.J., Nasser, M.S., Khraisheh, M., & Atieh, M.A. 2016. Heavy metal removal from aqueous solution by advanced carbon nanotubes: Critical review of adsorption applications. *Sep. Purif. Technol.* 157:141–161.

Kaboorani, A. & Riedl, B. 2015. Surface modification of cellulose nanocrystals (CNC) by a cationic surfactant. *Ind. Crop. Prod.* 65:45–55.

Kabuba, J. & Banza, M. 2020a. Results in Engineering Ion-exchange process for the removal of Ni (II) and Co (II) from wastewater using modi fi ed clinoptilolite : Modeling by response surface methodology and arti fi cial neural network. *Results Eng.*

Kabuba, J. & Banza, M. 2020b. Modification of clinoptilolite with dialkylphosphinic acid for the selective removal of cobalt (II) and nickel (II) from hydrometallurgical effluent. (June):1–11.

Khadhri, N., El, M., Saad, K., & Moussaoui, Y. 2019. Journal of Environmental Chemical Engineering Batch and continuous column adsorption of indigo carmine onto activated carbon derived from date palm petiole. *J. Environ. Chem. Eng.* 7(1):102775.

Lei, W., Zhou, X., Fang, C., Song, Y., & Li, Y. 2019. Eco-friendly waterborne polyurethane reinforced with cellulose nanocrystal from o ffi ce waste paper by two di ff erent methods. *Carbohydr. Polym.* 209:299–309.

Leudjo Taka, A., Klink, M.J., Yangkou Mbianda, X., & Naidoo, E.B. 2021. Chitosan nanocomposites for water treatment by fixed-bed continuous flow column adsorption: A review. *Carbohydr. Polym.* 255:117398.

Lu, B. qing, Li, M., Zhang, X. wen, Huang, C. mei, Wu, X. yan, & Fang, Q. 2018. Immobilization of uranium into magnetite from aqueous solution by electrodepositing approach. *J. Hazard. Mater.* 343:255–265.

Mo, C., Zhang, Q., Li, H., Yang, Z., Xu, H., Huang, G., Qu, A., & Chen, Y. 2021. Enhanced photodegradation ability and mechanism study of g-C3N4 by dual modified with sulfur-containing quantum dots doping after oxidization. *J. Photochem. Photobiol. A Chem.* 419:113462.

Moharrami, P. & Motamedi, E. 2020. Application of cellulose nanocrystals prepared from agricultural wastes for synthesis of starch-based hydrogel nanocomposites: Efficient and selective nanoadsorbent for removal of cationic dyes from water. *Bioresour. Technol.* 313:123661.

Musikavanhu, B., Hu, Z., Dzapata, R.L., Xu, Y., Christie, P., & Guo, D. 2019. Applied Surface Science Facile method for the preparation of superhydrophobic cellulosic paper. *Appl. Surf. Sci.* 496:143648.

Nordin, A.H., Wong, S., Ngadi, N., Zainol, M.M., Aien, N., Abd, F., & Nabgan, W. 2021. Journal of Environmental Chemical Engineering Surface functionalization of cellulose with polyethyleneimine and magnetic nanoparticles for efficient removal of anionic dye in wastewater. *J. Environ. Chem. Eng.* 9(1):104639.

Olad, A., Doustdar, F., & Gharekhani, H. 2020. Fabrication and characterization of a starch-based superabsorbent hydrogel composite reinforced with cellulose nanocrystals from potato peel waste. *Colloids Surfaces A Physicochem. Eng. Asp.* 601:124962.

Oyewo, O.A., Mutesse, B., Leswi, T.Y., & Onyango, M.S. 2019. Journal of Environmental Chemical Engineering Highly e ffi cient removal of nickel and cadmium from water using sawdust- derived cellulose nanocrystals. 7.

Rahaman, M.H., Islam, M.A., Islam, M.M., Rahman, M.A., & Alam, N.S. 2021. Biodegradable composite adsorbents of modified cellulose and chitosan to remove heavy metal ions from aqueous solution. *Curr. Res. Green Sustain. Chem.* :100119.

Saini, S., Chawla, J., Kumar, R., & Kaur, I. 2019. Response surface methodology (RSM) for optimization of cadmium ions adsorption using - C 16 - 6 - 16 incorporated mesoporous MCM - 41. *SN Appl. Sci. Springer International Publishing*. 1(8):1–10.

Salcedo, A.F.M., Ballesteros, F.C., Vilando, A.C., & Lu, M.C. 2016. Nickel recovery from synthetic Watts bath electroplating wastewater by homogeneous fluidized bed granulation process. *Sep. Purif. Technol.* 169:128–136.

Shahnaz, T., S., M.M.F., V.C., P., & Narayanasamy, S. 2020. Surface modification of nanocellulose using polypyrrole for the adsorptive removal of Congo red dye and chromium in binary mixture. *Int. J. Biol. Macromol.* 151:322–332.

Shojaeimehr, T., Rahimpour, F., Khadivi, M.A., & Sadeghi, M. 2014. A modeling study by response surface methodology (RSM) and artificial neural network (ANN) on Cu2+ adsorption optimization using light expended clay aggregate (LECA). *J. Ind. Eng. Chem. The Korean Society of Industrial and Engineering Chemistry*. 20(3):870–880.

Tang, J. 2016. Functionalized Cellulose Nanocrystals (CNC) for Advanced Applications.

Tang, X., Li, Q., Wu, M., Lin, L., & Scholz, M. 2016. Review of remediation practices regarding cadmium-enriched farmland soil with particular reference to China. *J. Environ. Manage.* 181:646–662.

Vishnu Priyan, V., Kumar, N., & Narayanasamy, S. 2021. Development of Fe3O4/CAC nanocomposite for the effective removal of contaminants of emerging concerns (Ce3+) from water: An ecotoxicological assessment. *Environ. Pollut.* 285:117326.

Voisin, H., Bergström, L., Liu, P., & Mathew, A.P. 2017. Nanocellulose-Based Materials for Water Purification.

Wang, S., Yu, J., Zhao, P., Li, J., & Han, S. 2021. Preparation and mechanism investigation of CdS quantum dots applied for copper ion rapid detection. *J. Alloys Compd.* 854:157195.

Xu, H., Wang, H., Lu, Y., Zeng, Y., Yang, Y., Zhang, Z., Wang, H., Wang, X., & Li, L. 2021. CeO2 quantum dots for highly selective and ultrasensitive fluorescence detection of 4-nitrophenol via the fluorescence resonance energy transfer mechanism. *Spectrochim. Acta. A. Mol. Biomol. Spectrosc.* 262:120115.

Zhang, L., Zeng, Y., & Cheng, Z. 2016. Removal of heavy metal ions using chitosan and modified chitosan: A review. *J. Mol. Liq.* 214:175–191.

CHAPTER SIX

MODELING OF ADSORPTION OF NICKEL (II) BY BLEND HYDROGELS (CELLULOSE NANOCRYSTALS AND CORN STARCH) FROM AQUEOUS SOLUTION USING ADAPTIVE NEURO-FUZZY INFERENCE SYSTEMS (ANFIS) AND ARTIFICIAL NEURAL NETWORKS (ANN)

ABSTRACT

The current study looks at the effectiveness of removing Nickel (II) from an aqueous solution using an adsorption method in a laboratory size reactor. An artificial neural network (ANN) and an adaptive neuro-fuzzy inference system (ANFIS) were used in this study to predict blend hydrogels adsorption potential in the removal of nickel (II) from aqueous solution. Four operational variables, including initial Ni (II) concentration (mg/L), pH, contact duration (min), and adsorbent dose (mg/L), were used as an input with removal percentage (%) as the only output, were studied to assess their impact on the adsorption study in the ANFIS model. In contrast, 70% of the data was used to build, 15% of the data was used in testing and validation to build the ANN model. Feedforward propagation with the Levenberg-Marquardt algorithm was employed to train the network. The use of (ANN) and (ANFIS) models for experiments was used to optimize, construct, and develop prediction models for Ni (II) adsorption using blend hydrogels (cellulose nanocrystals and corn starch). The results show that ANN and ANFIS models are promising prediction approaches that can successfully predict metal ions adsorption. According to this finding, the RMSE, AARE, ARE, MSE, and R^2 for Ni (II) in the training dataset were 0.061, 0.078, 0.017, 0.019, and 0.986, respectively for ANN. In the ANFIS model, the RMSE, AARE, ARE, MSE and R^2 were 0.0129, 0.0119, 0.028, 0.030, and 0.995, respectively. The morphology, functional groups, thermal characteristics, and crystallinity of blend hydrogels were all examined.

Keywords: artificial neural network (ANN); adaptive neuro-fuzzy inference system (ANFIS); Blend hydrogels; Nickel (II); Adsorption.

GRAPHICAL ABSTRACT

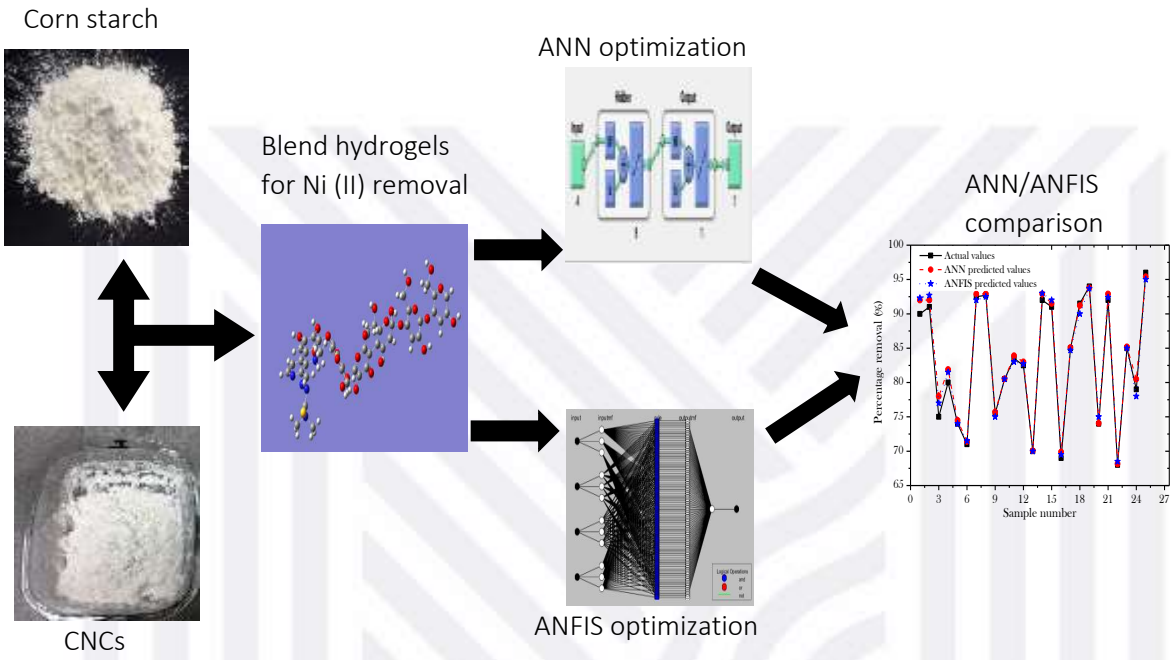

6.1. INTRODUCTION

heavy metal ions such as nickel (II) are prevalent and harmful contaminants in the aquatic system due to their toxicity. As a result, their large-scale emission from Textile effluents and wastewater from different industrial operations, such as pulp and paper processing, leather tanning, battery manufacture, and other sectors, is one of the most significant challenges that humans face with(Banza *et al.*, 2021). Ni (II) was used to study the simultaneous adsorption in an aqueous solution widely used in industrial applications such as battery manufacture. It is possible to eliminate this contaminant from the water using several different techniques. Precipitation, neutralization, electrochemical reduction, ion exchange, cementation, coagulation and flocculation, biosorption, and membrane processes are chemical techniques mostly used(Fosso-kankeu, 2018; Musamba *et al.*, 2018; Vishnu Priyan *et al.*, 2021). However, there are a few drawbacks and limits to this method. Adsorption is an excellent alternative approach because of its high efficiency, cost-effectiveness, ease of handling, and availability of adsorbents(Chen *et al.*, 2019).

With nanoparticles becoming more and more effective and innovative adsorbents, the need for their use has increased(Musikavanhu *et al.*, 2019). According to an understanding, superabsorbent hydrogels are three-dimensional cross-linked polymers that absorb and retain massive amounts of aqueous liquids(Du *et al.*, 2019). In recent years, polymeric adsorbents have been broadly applied for dye and heavy metal ions removal from water, with ion exchange, hydrogen bonding, and electrostatic interactions between heavy metal ions and the gel networks being the most prevalent mechanisms(Shalla *et al.*, 2018). In recent years, starch has been extensively applied to develop novel hydrogels for particular environmental applications. It is one of the most readily accessible and inexpensive polysaccharides with a significant number of hydroxyl groups. Micro- and nanofillers in the hydrogel matrix have also improved swelling properties and thermal and mechanical strength(Priyan *et al.*, 2020; Takagi *et al.*, 2013). To make reinforced hydrogel nanocomposites, materials such as carbon-nanomaterials, bentonites, graphene oxide, and iron oxide nanoparticles have been used(Liu & Kong, 2019; Priscila *et al.*, 2019; Senna *et al.*, 2016). Biopolymer hydrogel reinforcement has relied on nanometric dimensions, high aspect ratio, natural-based features, and distinctive structure of cellulose nanoparticles (CNCs) for decades(Danial *et al.*, 2015). Moreover, the radical OH

present on the structure of CNCs would enable their homogeneous integration into hydrogel matrixes via hydrogen bonding interactions between functional groups of CNCs and the host polymer(Ishak *et al.*, 2019; Lei *et al.*, 2018). Furthermore, CNCs have been recognized as a promising choice for wastewater treatment as a nano adsorbent nanomaterial.

Adaptive neuro-fuzzy inference systems (ANFIS) are a type of artificial intelligence (AI) that combines the learning skills of artificial neural networks (ANN) with the reasoning abilities of fuzzy systems(Franco *et al.*, 2020). As a result, it combines the benefits of both approaches into a single technique. In many engineering applications, a more efficient approach is achieved by combining fuzzy systems with artificial neural networks rather than applying a single methodology. To explain nonlinear behavior in complex systems, ANFIS is a strong tool for modeling, mapping, forecasting, problem-solving, and data mining the input and output values interaction. An ANFIS model is made up of two parts: the antecedent and the conclusion, which are linked together by fuzzy rules in a network form. It is generally recognized as a technology because of its broad capacity to simulate nonlinear variation, use in predicting the performance of various processes, and extrapolation based on historical data in a range of fields. Although a previous study applying the ANFIS model was carried out (Dolatabadi *et al.*, 2018; Franco *et al.*, 2020), there is no literature on a strategy for removing heavy metal ions such as Cu^{2+} with blends hydrogel using ANN, and ANFIS approaches.

As a result, the primary aim of this study is to anticipate the modeling of Ni (II) removal behavior using both models (ANN and ANFIS techniques). To begin, blend hydrogels are utilized as an adsorbent for Ni (II) adsorption from an aqueous solution. The input data are the operational factors: the starting Ni (II) concentrations, solution pH, contact duration, and adsorbent dose. Finally, experimental data output data are compared to predicted output data estimated from the two models.

6.2. EXPERIMENTAL

6.2.1 Materials

Cellulose nanocrystals used were extracted from waste papers via hydrolysis (≥90%). Unmodified corn starch of essential pure amylopectin contains the only trace of amylose. Nickel sulfate hexahydrate (≥98%), sodium hydroxide(>99%), hydrochloric acid (>99%),

and ammonium persulfate (>98%) were all purchased from Sigma-Aldrich. A pH meter (Hanna HI 8421) was used to adjust the pH of the solution. The Ultima 888 water distiller was used to produce distilled water. The amount of metal ions adsorbed was determined using Induced coupled plasma (ICP, Icap7000). Fourier transform infrared spectroscopy was used to explore the functional groups present in the hydrogel and the morphological changes (FTIR, Varian 7000). The morphological surface was assessed using scanning electron microscopy (SEM, Philips XL30FEG). X-ray diffraction was used to undertake both qualitative and quantitative approaches (XRD, Philips expert 0993). A thermal thermogravimetric analyzer was used to investigate thermal stability (TGA, NETZSCH5 209F3).

6.2.2 preparation of CNCs-starch hydrogel

20mg of Corn starch was poured into deionized water (250 mL) and agitated for 10 minutes to dissolve it at 50°C. The CNCs (20 mg) was added to the dispersed starch solution in 250 mL deionized water for 20 minutes. After that, the reaction flask was filled with 60 % KOH, stirred continuously for 15 minutes. The temperature was increased to 80 °C after adding ammonium persulfate (APS) 25 mg to the mixture to initiate radical polymerization. The result was rinsed with abundant deionized water and dried in an oven at 55°C after gelation took just 7 minutes. The proposed structure for the blend hydrogel is presented in **Figure 1.**

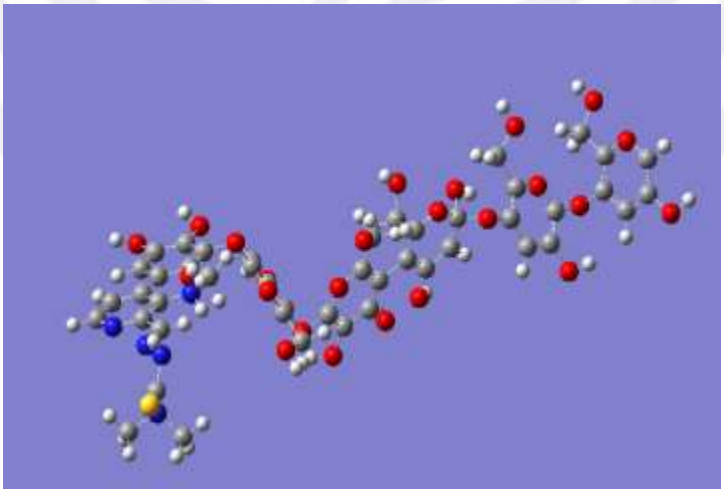

Figure 6.1: The proposed structure of the blend hydrogels (3D). Black, red, blue, yellow, and light black denote carbon, oxygen, nitrate, sulfur, and hydrogen atoms.

6.2.3 Adsorption experiments

Batch experiments were used to develop the adsorption method. Batch studies were carried out in 200 mL glass-stoppered Erlenmeyer flasks reactors holding test solutions at the appropriate level of Ni (II) concentration, contact duration, pH, and adsorbent dosage at room temperature (25±2°C). Quantities of a solution having a specific concentration of Solutions Ni (II) at the same time) was put into the reactor in each test. To maintain a consistent pH throughout the experiment, the pH of the solution was adjusted using dilute 0.1M HCl or NaOH. A shaker was used to agitate the solution at 185 rpm, adding the appropriate weight of adsorbent in the prescribed dose. The solid/liquid phases were then separated by centrifugation for 10 minutes at 2500 rpm.

The removal percentage (%) was assessed using the following equation:

$$\text{Removal (\%)} = \frac{(C_{in} - C_f)}{C_{in}} \times 100 \quad (6.1)$$

where C_{in} ($mg.L^{-1}$) denotes the initial Ni (II) concentration, C_f ($mg.L^{-1}$) denotes the concentration at time t. **Table 6.1** shows the range of variables used for ANN and ANFIS

Table 6.1: The range of variables used for the models

Input	Range	Output
1. pH	3-9	Removal percentage (%)
2. Concentration Ni (II)	50-500	
3. Time (min)	0-120	
4. dosage blend hydrogel (mg/L)	5-20	

6.3 ANALYSIS BY ANN AND ANFIS MODEL

To determine adsorption efficiency, all calculations were done with origin 2019b, and the modular artificial neural networks and a Neuro-fuzzy were constructed with a NN toolbox using MATLAB 2015a mathematical software. The training and prediction sets' RMSE, AARE, ARE, and MSE were also used to determine the two models and their parameter variations. The values of input neurons were standardized in the 0–1 range before completing the training (learning) process to avoid some training pathologies and guarantee that large weight values do not overload the network.

We have 26 experimental runs randomly split into training, validation, and test sets to assess the model's ability to predict unseen experiments that were not utilized for training (20-3-3). All of the samples were averaged. The traditional statistical measure for determining the proportion of variation between experimental and model predictions is R^2 (regression coefficient). R^2 is a value that ranges from 0 to 1. A number of R^2 close to 1 suggests that most of the difference between experimental and model predictions can be explained.

In contrast, a value of R^2 close to 0 indicates that only a tiny portion of the variation can be explained. The RMSE error function is a commonly used error function utilized as an objective function in most optimization approaches. The mean squared deviation (MSD), which aggregates the magnitudes of the deviations and is a good indicator of accuracy, is another name for this function. SSE is another often used error function, and it grows as the difference between experimental and model predictions grows(Ehteram *et al.*, 2021; Mohd Ali *et al.*, 2021; Zhu & Wang, 2022).

6.3.1 Artificial neural networks (ANN)

It is established a three-layer system with a four-neuron input layer (initial Ni (II) concentration, solution pH, contact duration, and adsorbent dosage), a hidden layer with nine distinct modes, and an output layer with one neuron (4-9-1) in **Figure 6.2(a).** Back-propagation (BP-ANN) is the most popular network, which uses a first-order gradient descent approach to train an algorithm for modeling experimental data. It's a decent algorithm for reducing errors at each iteration(Franco *et al.*, 2020). We selected The Marquardt–Levenberg learning approach among the many back-propagation (BP) techniques(Dolatabadi *et al.*, 2018). For all data sets in ANN, the log-sigmoid transfer function (log sig) in the hidden layer with four neurons in the first layer and a linear transfer function in the output node were utilized for Ni (II) removal simulation and prediction. The procedure for optimization by ANN is presented in **Figure 6. 2(b).**

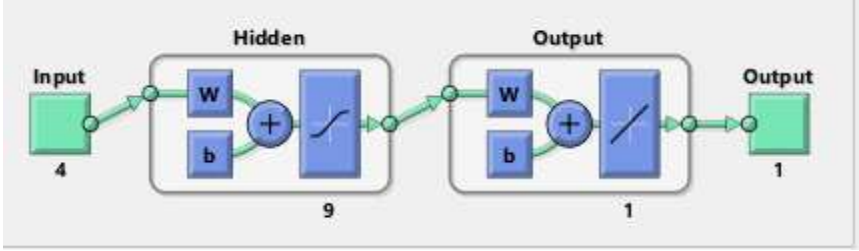

Figure 6.2(a): Architecture of ANN model.

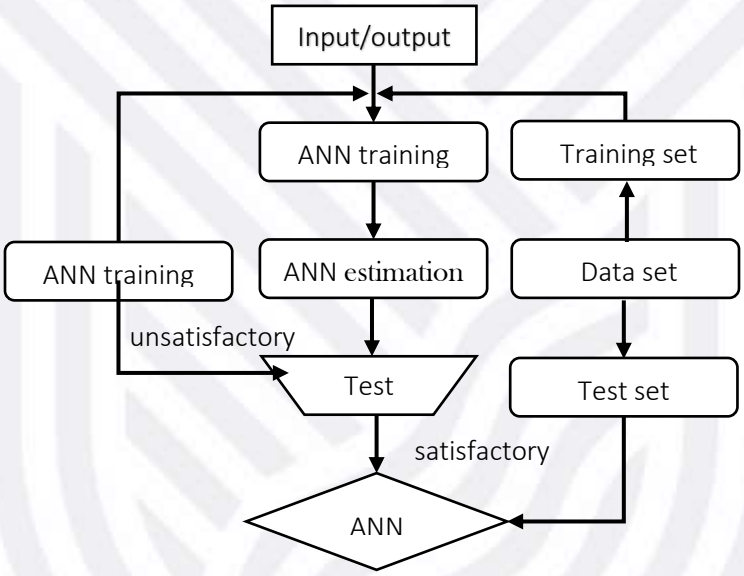

Figure 6.2(b): Procedure for optimization by ANN.

6.3.2 Adaptive neuro-fuzzy inference systems (ANFIS)

The neuro-fuzzy system's primary benefit is that it blends neural network characteristics with fuzzy logic. As a result, both limitations are eliminated. The explicit knowledge that can be gained and interpreted is dealt with by fuzzy logic, whereas the implicit knowledge is handled with neural networks. ANFIS combines the qualitative approach of fuzzy logic with the quantitative approach of neural networks. Integrating adaptive capabilities into a single system has certain drawbacks in addition to its benefits. A trial-and-error method is used to define membership parameters and rules in a fuzzy system. It was required to use the ANFIS system to develop an appropriate model between observed inputs and target values that would be accurate. As a part of this experiment, five layers have been identified as performing various functions: the product, the normalized layer, the fuzzy layer, the defuzzy layer, and the final layer(Ahmad *et al.*, 2021; Arora & Keshari, 2021;

Ehteram *et al.*, 2021; Mohd Ali *et al.*, 2021) are shown in **Figure 6.3(a).** The procedure for optimization by ANFIS is presented in **Figure 6. 3(b).**

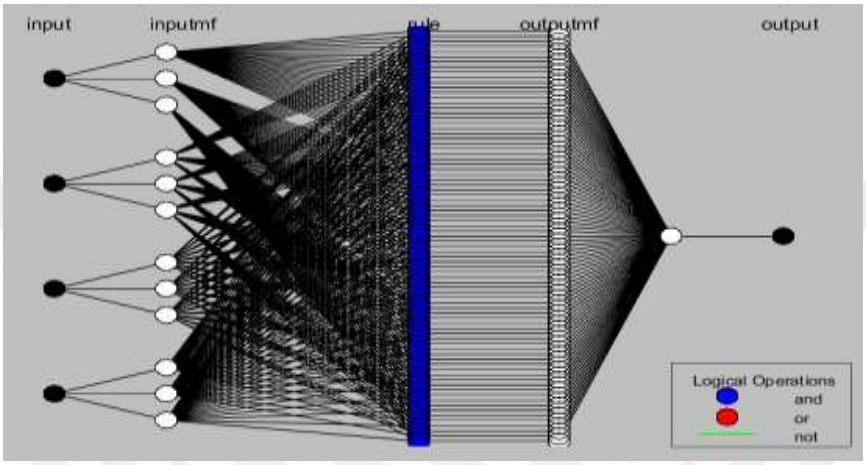

Figure 6.3(a): Architecture of ANFIS model.

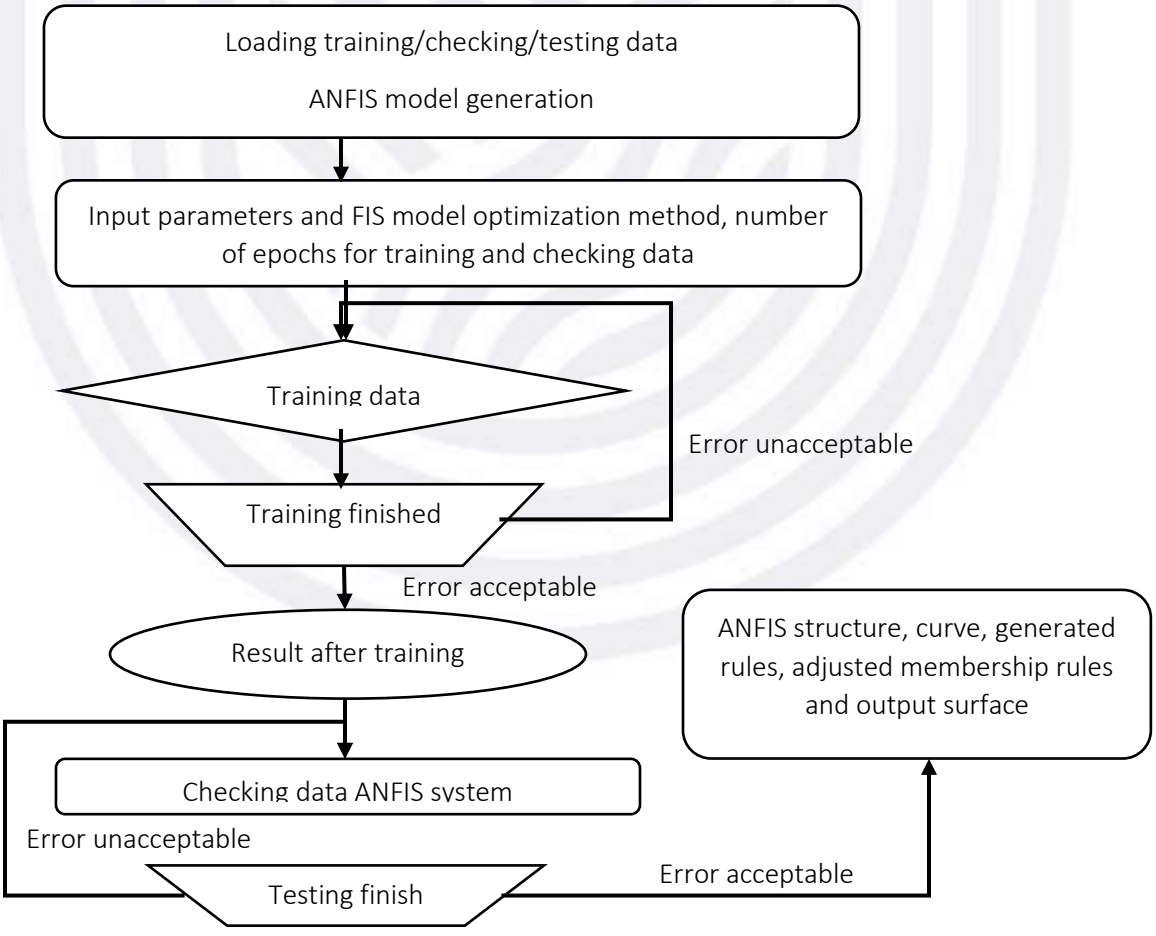

Figure 6.3(b): Procedure for optimization by ANFIS.

6.4. RESULTS AND DISCUSSION

6.4.1 ANN results

The interaction of the network with the training, testing, and validation data is seen in **Figure 6.4.** For training, testing, validation data, and the correlation coefficients were determined to be 0.99, 0.98, 0.98, and 0.98, respectively. In addition, the straight line shows the linear relationship. The model's predicted (output) data and experimental (target) data correlate. Findings imply that the actual data and the model-predicted data are in good agreement. As a result, suited for accurately predicting data, the overall correlation coefficient (0.98) demonstrates the created ANN model's outstanding prediction ability.

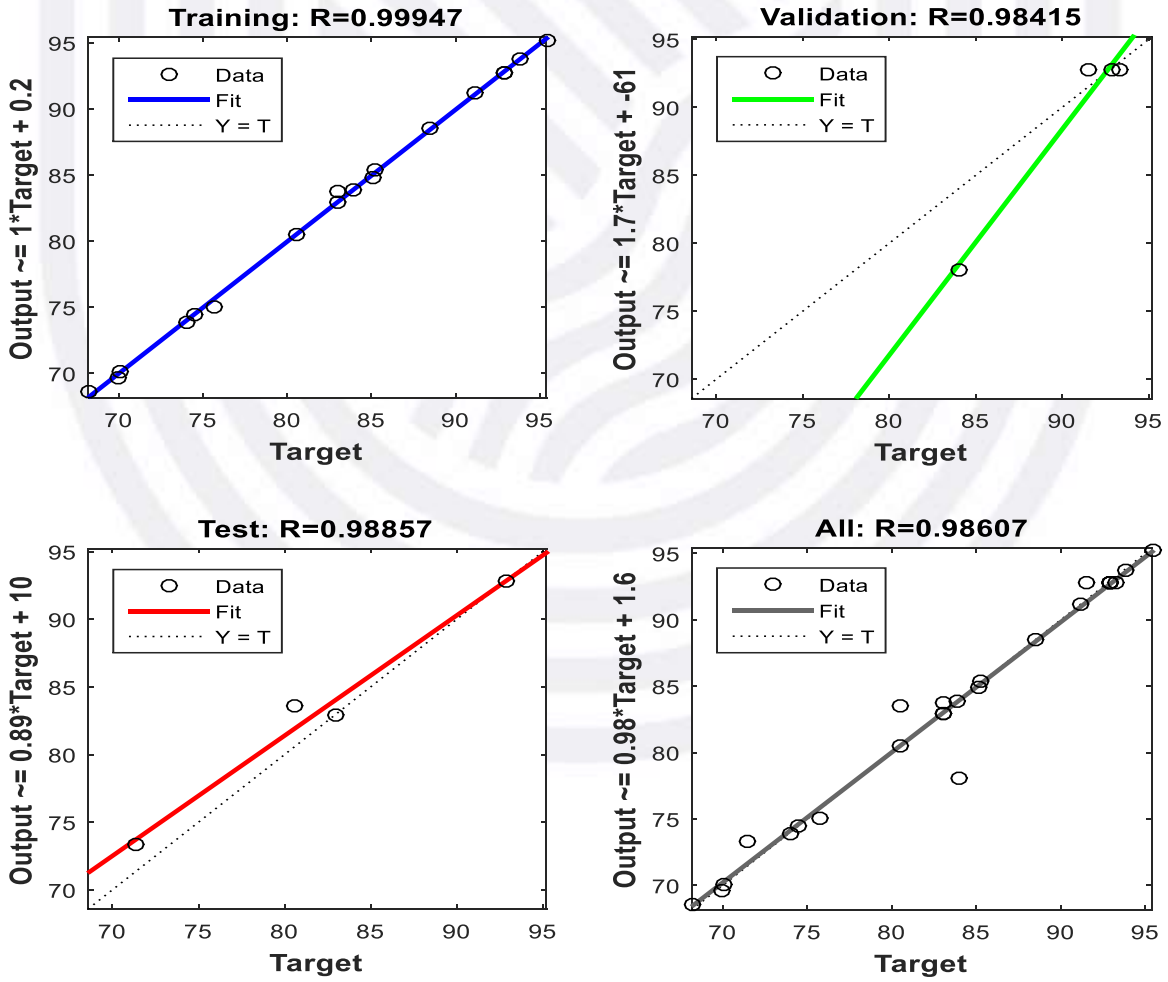

Figure 6.4: Regression analysis of neural network and corresponding target

6.4.2 ANFIS results

Figure 6.5 depicts the fundamental framework of the ANFIS model used in this investigation. The system generates 81 'and'-based rules for four input parameters comprising three membership functions (inputmf). They are then transformed into output by passing them through the same number of (outputmf). On the other hand, the ANFIS model's data prediction capacity has been shown in **Fig. 5** (rule viewer). For illustration, the absorption for pH 6, initial concentration 275 mg/L, contact time of 60 min, a dosage of 12.5 mg/L is about 91.00%. Within the data range, the model can predict all output data for every input parameter. Simultaneously, using the rule viewer, the inputs for a certainly needed output may be selected. As a consequence, the model can predict output data (absorption percentage) based on input variables (initial Ni (II) concentration, contact duration, pH, and adsorbent dosage) and vice versa. To predict the other parameter, the model can be modified for a minor change in either parameter.

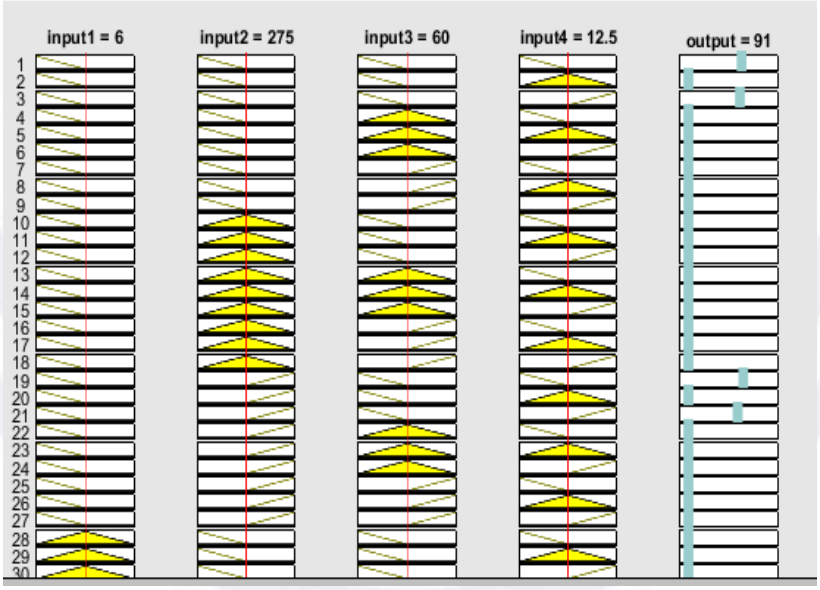

Figure 6.5: Rule viewer of the ANFIS model

6.4.2.1 influence of the input's parameters on the removal percentage

A significant element of ANFIS is its capacity to train itself using information from the current database to generate various graphs and contour plots. These figures show the relationship between the removal percentage and several factors described in the literature, such as (initial Ni (II) concentration, contact duration, pH, and adsorbent dosage. It was discovered that pH (input 1), contact duration (input 2), and adsorbent dosage (input 4) had a direct connection with the removal percentage of Ni (II), reaching a maximum value of 99 % (**Figure 6.6**). the relationship between pH and starting concentration is shown in **Figure 6.6(a).** The triangular nature contour plot indicated that pH and starting concentration had a considerable effect on removal percentage. Up to a pH of 6 and an initial concentration of 300 mg/L, a higher percentage removal was detected at lower pH and beginning concentration ranges. The reaction slowed when the pH was over six, and the starting concentration was over 300 mg/L. Cationic species may have occupied the blend hydrogel sites, slowing the approach of these ions to the surface and Ni (II) precipitates as hydroxide at higher pH(Gokmen *et al.*, 2021).

The ANFIS model shows in **Figure 6.6 (b-c)** the relationship between the contact duration, initial concentration, removal percentage, and additional factors such as pH. Increase the contact duration over 120 min increases the percentage removal, and the impact is particularly noticeable above 60 min for a constant pH, as shown in **Figure 6.6(b)**. At higher initial concentrations, from 300 to 500mg/L, a remarkably lower removal percentage has been seen. Due to the rise in driving power of the concentration gradient between the solid phase and adsorbate in the solution phase, **Figure 6.6(c)** shows maximum removal at contact duration of 120 min and pH of 6, on the other hand. This is due to the availability of active sites and solid electrostatic force between the positively charged Ni (II) and negatively charged blend hydrogel surface(Kabuba & Banza, 2020).

The RSM plots in **Figure 6.6(d)** show that a high removal percentage of 99 % was obtained with a dosage of 12.50 mg/L and an initial concentration of 300 mg/L, this may be due to the available active site of the blend hydrogel allowing penetration of Ni (II) penetration, and at higher dosage (greater than 300mg/L), there is a reduction in removal percentage due to the saturation of active sites of the blend hydrogel(Zong *et al.*, 2018)

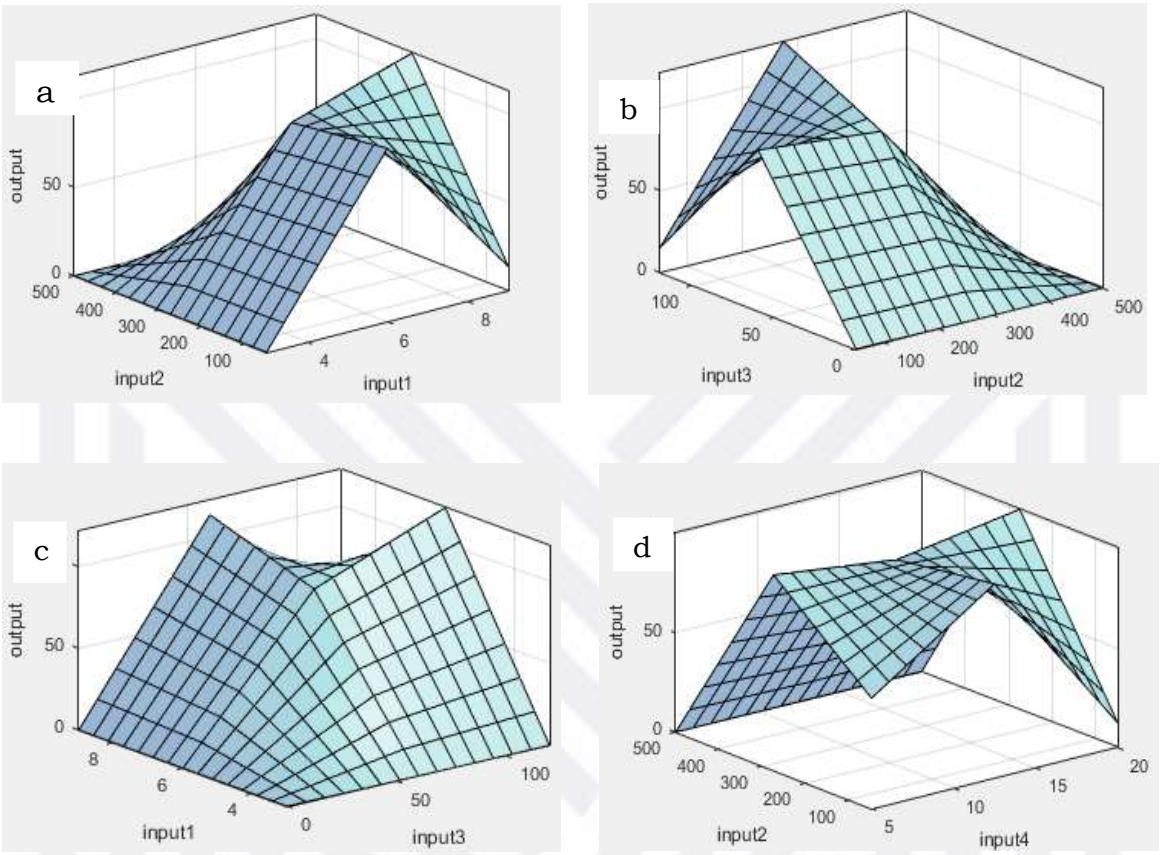

Figure 6.6: Effect of the interaction of various input parameters on the removal percentage of Ni (II), (a) pH and initial concentration, (b) contact duration and initial concentration, (c) contact duration and pH, (d) dosage and initial concentration.

6.4.3 predicted and actual data ANN and ANFIS

Table 6.2 shows the comparative and statistical analysis of the actual (experimental) data and the model predicted data for the removal percentage of Ni (II) using the blend hydrogels. According to the results, both models are capable of accurately predicting the characteristics of the adsorption. The RMSE, ARE, SSE, MSE, and R^2 values were all found to be 0.051, 0.031, 0.037, 0.049, and 0.986 for the ANN model, whereas the ANFIS model were all found to be 0.006, 0.018, 0.027,0.030, and 0.997.

Statistics show that both models have adequate statistical data, indicating that they can be applied in adsorption**. Table 6.2** demonstrates that ANFIS and ANN models accurately predicted both actual and predicted results.

$$\text{RMSE} \quad \sqrt{\frac{1}{N}\sum_{i=1}^{n}\left(\frac{\left(q_{e(exp)}-q_{e(pred)}\right)^2}{q_{e(exp)}}\right)} \tag{6.2}$$

$$\text{ARE} \quad \frac{100}{N}\sum_{i=1}^{n}\left(\left[\frac{\left(q_{e(exp)}-q_{e(pred)}\right)^{1}}{q_{e(exp)}}\right]\right) \tag{6.3}$$

$$\text{SSE} \quad \sum_{i=1}^{n}\left(q_{e(exp)}-q_{e(pred)}\right)^{2} \tag{6.4}$$

$$\text{MSE} \quad \frac{1}{N}\sum_{i=1}^{n}\left(q_{e(exp)}-q_{e(pred)}\right)^{2} \tag{6.5}$$

where N is the number of measurements, P is the number of model parameters, q_e(pred) is the predicted adsorption capacity in $mg.g^{-1}$, and q_e(exp) is the experimental adsorption capacity in $mg.g^{-1}$.

Table 6.2: Comparison of ANN and ANFIS model for Ni (II) removal

pH	Conc (mg/L)	Time(min)	Dosage (mg/L)	Actual (%)	ANN (%)	ANFIS (%)
6	250	120	10	92.00	91.2	91.7
6	250	60	10	92.01	91.7	92.07
3	50	0	20	78.52	77.05	77.9
9	50	120	5	81.94	83.82	82.89
3	500	0	20	74.51	74.28	75.14
9	50	0	20	71.47	70.90	70.12
6	250	60	10	92.92	92.24	92.82
6	250	60	10	92.97	92.51	92.77
9	50	120	20	75.70	75.28	76.27
3	50	0	5	80.54	80.25	80.54
6	50	60	10	83.92	83.85	83.73
3	500	0	5	83.08	82.25	82.79
9	500	0	20	70.05	70.02	70.08
6	250	60	10	92.92	93.07	92.81
6	250	60	10	91.52	91.18	91.72
9	50	0	5	69.93	69.93	69.71
9	250	60	10	85.12	85.25	85.27
6	250	60	20	91.24	91.33	91.52
6	250	60	5	93.86	92.87	93.26
9	500	120	20	74.05	73.56	73.28
6	250	60	10	92.91	92.24	91.71

RMSE (Root means square errors)	**1.29**	**0.61**
AARE (Absolute average relative errors)	**1.19**	**0.78**
ARE (Average relative errors)	**0.28**	**0.17**
MSE (Mean square errors)	**0.30**	**0.19**
R^2 (Regression coefficient)	**0.98**	**0.99**

Figure 6.7 depicts how well the two models fit correctly. The linear fit also indicates that both models have exceptional capabilities. Although both models can predict Ni (II) percentage removal, the ANN model had somewhat superior RMSE, AARE, ARE, and MSE values.

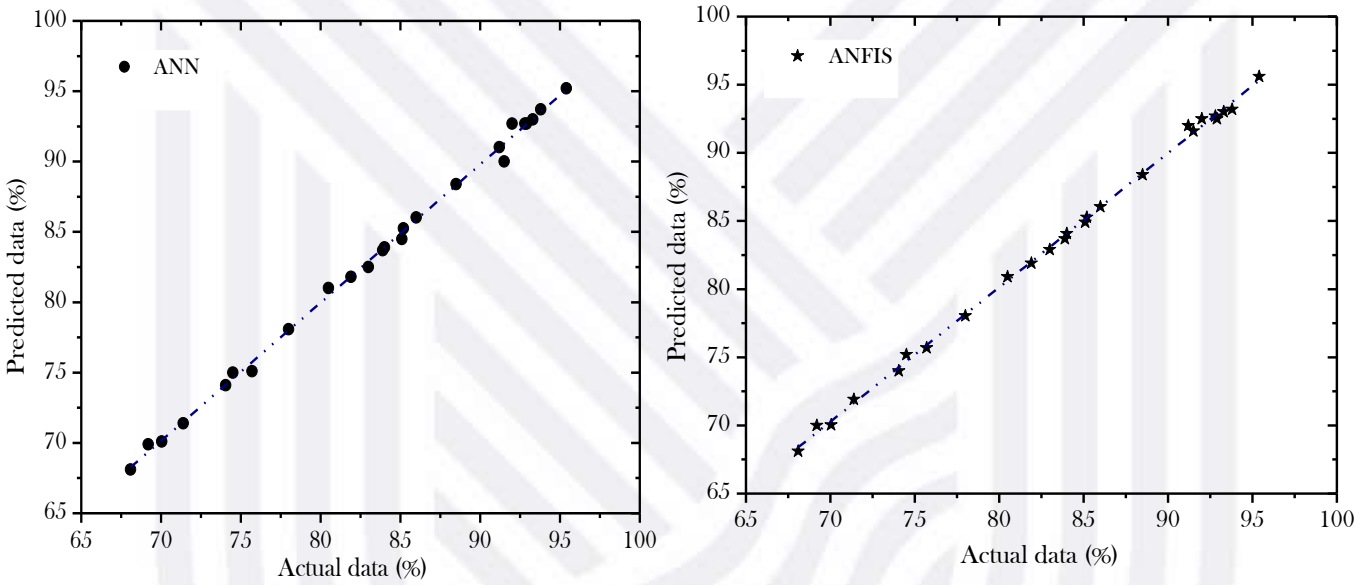

Figure 6.7: Comparison of the actual and predicted results for Ni (II) removal.

When compared to experimental results, the model's predictions necessarily apply to the removal of Ni (II) characteristics (for both ANFIS and ANN). **Figure 6.8** shows the behavioral pattern of the samples quite well. **Table 6.3** and **Figure 6.8** demonstrate that the ANFIS model performed exceptionally well for sample 10, but the ANN model performed very well for sample 23, where the absolute error was zero percent. Sample 4 showed mediocre performance with somewhat more significant absolute error (1.09 percent for ANFIS and 2.37 percent for ANN), but either model never surpassed the acceptable limit. The parameters and information based on the ANN and ANFIS models during the training are presented in **Table 6.3**.

Table 6. 3: The data used for ANN AND ANFIS model by backpropagation

ANN information		ANFIS information	
Characteristic	value	Characteristic	value
Number of epochs	20	Number of training pairs	10
Learning rule	Trainlm	Total number of parameters	117
Number of neurons	9	Number of linear parameters	81
Number of input nodes	4	Number of nodes	193
Number of output node	1	Number of nonlinear parameters	36
		Number of fuzzy rules	81

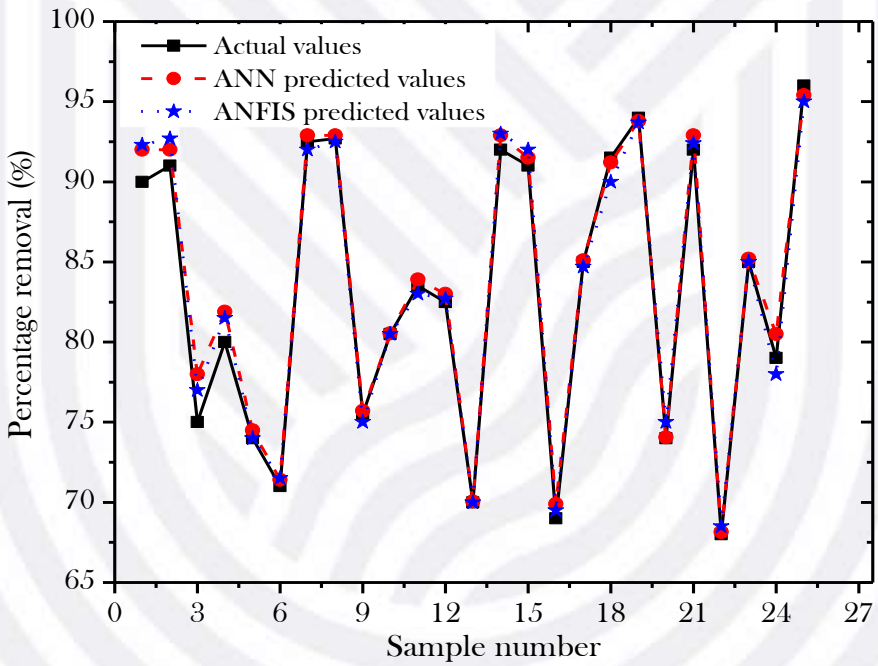

Figure 6.8:Comparison with ANN, ANFIS data with the actual data.

6.4.4 Characterization of the blend hydrogel

6.4.4.1 FTIR analysis

The O–H and C–H stretching vibrations, which originated from both starch and the grafting groups, were attributed to the distinctive peaks at 3490 cm^{-1} and 2933 cm^{-1} in the FTIR spectrum of the blend hydrogels (**Figure 6.9**). The C–O–C vibrations of the starch backbone and the pyranose ring of CNCs were represented by bands 1156 and 1036. C–S and S–O stretching vibrations of –SO_3H groups from grafted APS on the polymer backbone correspond to the maxima at 625, 1215, and 1394 cm^{-1}, respectively. In addition, the

vibrational peaks that occurred at 1450 cm^{-1}, 1560 cm^{-1}, and 1730 cm^{-1} were reported to stretching of COO- groups symmetrically and asymmetrically, as well as C=O, and COOH stretching vibration, respectively(Moharrami & Motamedi, 2020).

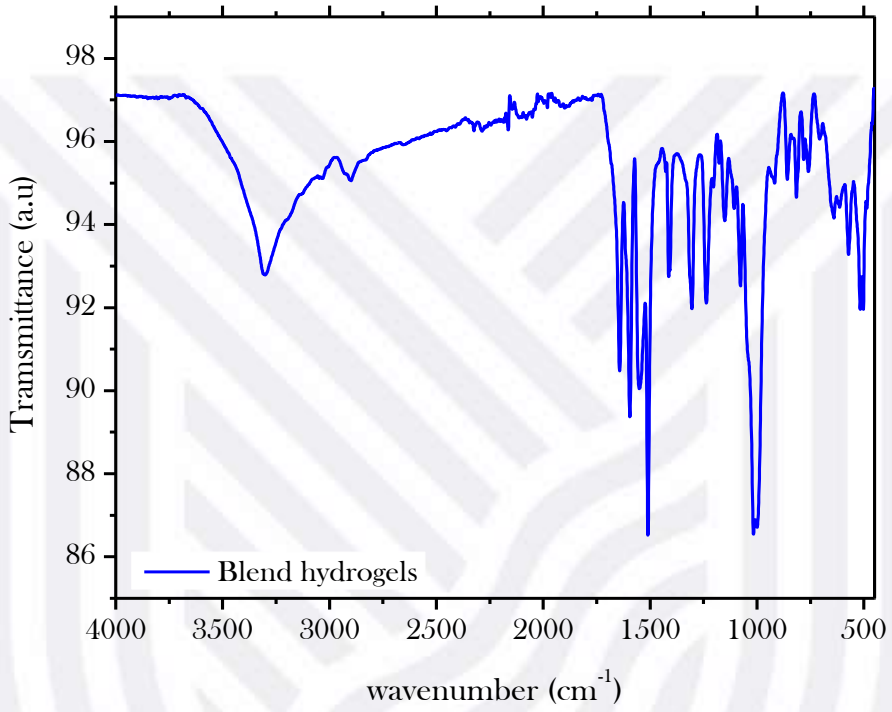

Figure 6.9: FTIR vibrational spectra of the blend hydrogels.

6.4.4.2 Morphological analysis

To explore the morphological characteristics of the blend hydrogels, the SEM technique was used and shown in **Figure 6.10**. The blend hydrogels have a porous surface. CNCs has been described in the literature to be a multifunctional crosslinking agent in polymeric matrixes. Due to APS involvement, new interactions are generated, and connections are broken in the polymeric matrix, impacting the sample's surface shape. Many CNC's and starch hydroxyl groups are active and can participate in the polymerization reaction and build the three-dimensional polymer network. Because of this, the interconnecting of polymeric chains may be avoided, and the hydrogen-bonding interaction between hydrophilic groups like - $CONH_2$, OH, and - COO can be reduced when CNC is present(Olad *et al.*, 2020).

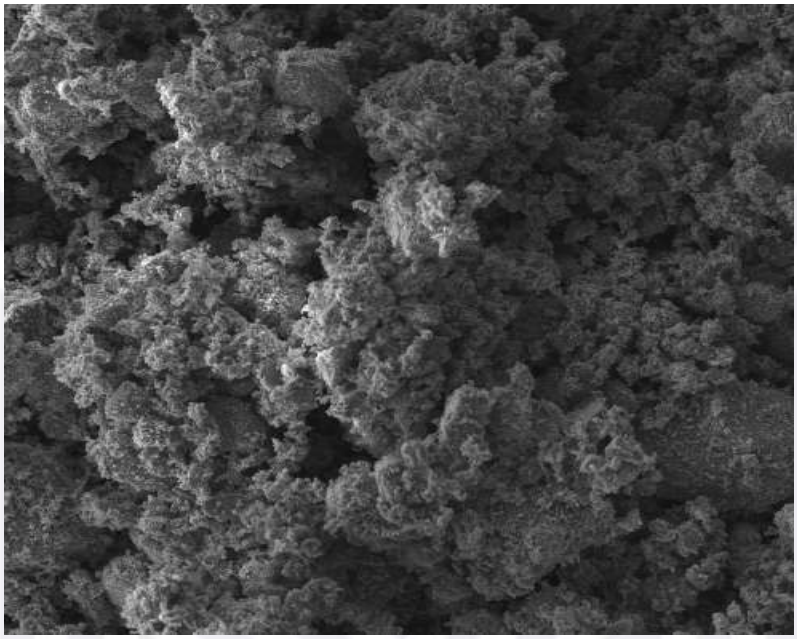

Figure 6.10: SEM image of the blend hydrogels.

6.4.4.3 XRD analysis

The presence of broad and weak peaks at two theta 28° and two theta 17° in the XRD patterns of the blend hydrogels (**Figure 6.11**) demonstrates the amorphous structure of the blend hydrogels materials (Olad *et al.*, 2020). Starch has a semi-crystalline structure, according to the observations. A prominent peak at two theta 17° indicates that starch has a B-type crystalline structure. However, in the presence of CNCs, the intensity of the hydrogel composite's distinctive peak (2 theta 28°) has considerably risen. Furthermore, the peak at two theta 40° might be attributed to the crystalline structure of the CNC(Gupta *et al.*, 2021).

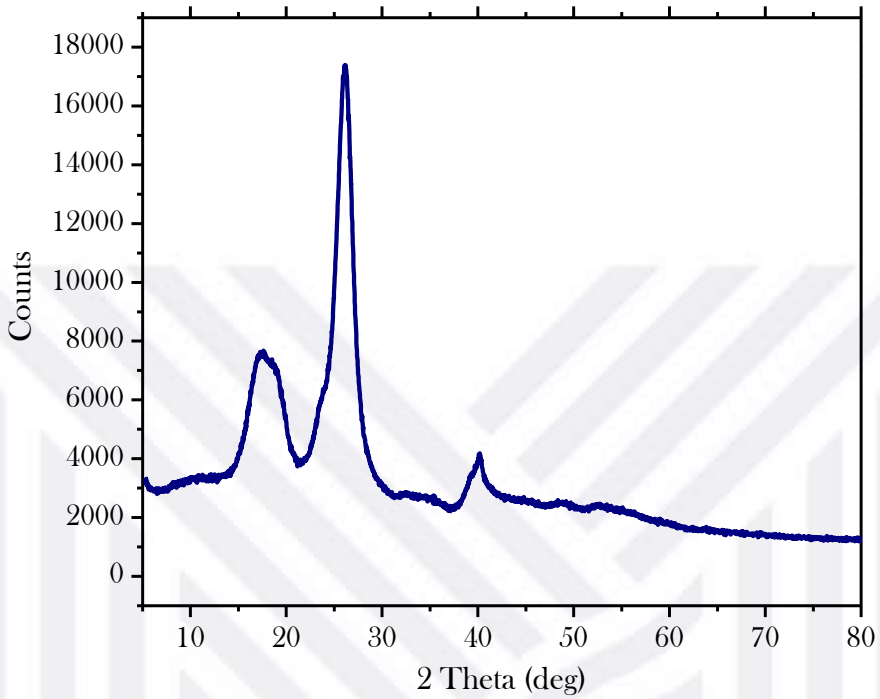

Figure 6.11: XRD Spectra of Blend hydrogels

6.4.4.4 TGA analysis

The TGA of the hydrogel is presented in **Figure 6.12**, which contains four phases of heat breakdown. The first phase (40°C to 100°C), the second phase (190°C to 300°C), the third phase (310°C to 380°C), and the last phase (400°C to 500°C). The first stage of weight loss is related to the loss of moisture through dehydration, and the second stage might be related to function group breakdown at the side chain. The third phase occurs, with a maximum temperature of 407.88, corresponding to the main chain scission. The last stage might be related to residual CNCs and starch breakdown.

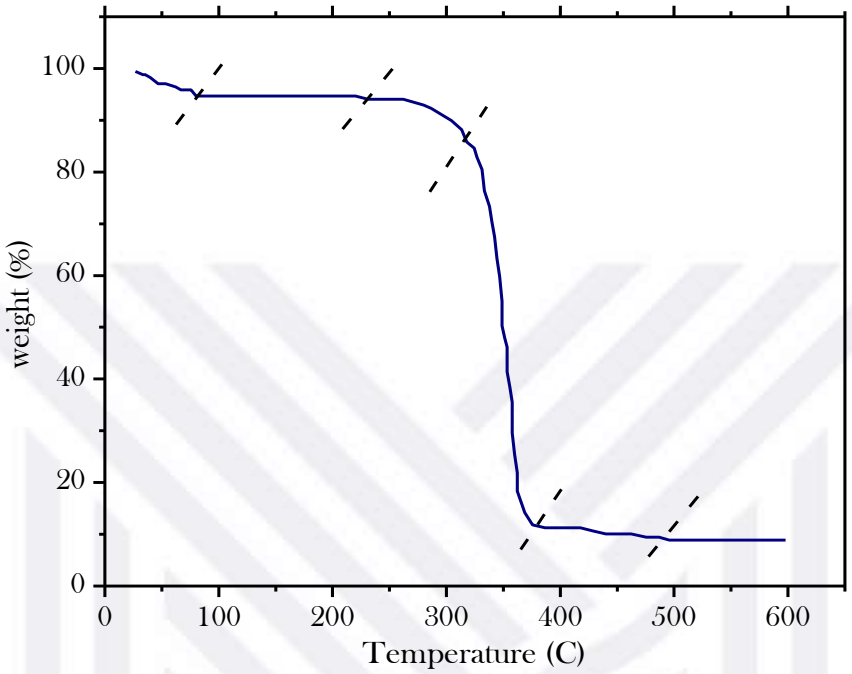

Figure 6.12: TGA curve of the Blend hydrogels

6.5. CONCLUSION

While the research achieved its primary objectives, it also opened new opportunities for investigation. Predicting the adsorption capacity of a particular adsorbent may be viable. ANFIS and ANN, two newly developed models, when compared to each other, have revealed which ones are most appropriate to be used in the effectiveness of the area of study. As a result of the research, the following conclusion can be reached:

For the ANFIS and ANN models, the regression coefficients (R^2) were 0.99 and 0.98, respectively. The findings show a good match between model-predicted and experimental data, showing that the models are suitable and compatible.

The ANFIS model's root-mean-square error (RMSE) between predicted and observed removal percentage values was 0.006, whereas the ANN model's RMSE was 0.051. For the ANFIS and ANN models, average relative errors (ARE) between predicted and experimental removal percentage values were determined to be 0.019 and 0.031, respectively. The Mean square errors (MSE) for ANFIS and ANN models, was found to be 0.019 and 0.030, respectively, between predicted and experimental removal percentages.

The Sum of square errors (SSE) for ANFIS and ANN models, between predicted and experimental removal percentage, was found to be 0.028 and 0.030, respectively.

The ANFIS model (R^2 = 0.99) outperformed the ANN model (R^2 = 0.98) in terms of overall efficiency, while both models are adequate. This might be because there were just a few datasets to operate with. In the case of the ANN model, working with a large number of datasets may be more efficient. The models are flexible, which means they can eliminate a lot of trial-and-error effort in predicting the removal percentage. It may also facilitate the scalable development of an adsorption process with the lowest trouble and constraint in terms of the required removal percentage.

The blend hydrogels exhibited a net-work structure and more uniform pores. Depending on the temperature of the analysis, the hydrogels displayed varying degrees of opacity and Ni (II) absorption capabilities. The carboxyl and amide group was present, and diffraction confirmed the presence of semi-crystalline and crystalline structures.

6.6. REFERENCES

Ahmad, M., Rashid, K., Tariq, Z., & Ju, M. 2021. Utilization of a novel artificial intelligence technique (ANFIS) to predict the compressive strength of fly ash-based geopolymer. *Constr. Build. Mater.* 301:124251.

Arora, S. & Keshari, A.K. 2021. ANFIS-ARIMA modelling for scheming re-aeration of hydrologically altered rivers. *J. Hydrol.* 601:126635.

Banza, M., Rutto, H., & Kabuba. Cobalt and Nickel Separation in Hydrometallurgy Using Modified Clinoptilolite with Dialkyl Phosphoric and Ethylenediaminetetraacetic Acid as an Ion Exchanger. Springer International Publishing.

Chen, Q., Zheng, J., Wen, L., Yang, C., & Zhang, L. 2019. A multi-functional-group modified cellulose for enhanced heavy metal cadmium adsorption: Performance and quantum chemical mechanism. *Chemosphere*. 224:509–518.

Danial, W.H., Abdul Majid, Z., Mohd Muhid, M.N., Triwahyono, S., Bakar, M.B., & Ramli, Z. 2015. The reuse of wastepaper for the extraction of cellulose nanocrystals. *Carbohydr. Polym.* 118:165–169.

Dolatabadi, M., Mehrabpour, M., Esfandyari, M., Alidadi, H., & Davoudi, M. 2018. Modeling of simultaneous adsorption of dye and metal ion by sawdust from aqueous solution using of ANN and ANFIS. *Chemom. Intell. Lab. Syst.* 181:72–78.

Du, H., Liu, W., Zhang, M., Si, C., Zhang, X., & Li, B. 2019. Cellulose nanocrystals and cellulose nano fi brils based hydrogels for biomedical applications. *Carbohydr. Polym.* 209:130–144.

Ehteram, M., Yenn Teo, F., Najah Ahmed, A., Dashti Latif, S., Feng Huang, Y., Abozweita, O.,

Al-Ansari, N., & El-Shafie, A. 2021. Performance improvement for infiltration rate prediction using hybridized Adaptive Neuro-Fuzzy Inferences System (ANFIS) with optimization algorithms. *Ain Shams Eng. J. Faculty of Engineering, Ain Shams University*. 12(2):1665–1676.

Fosso-kankeu, E. 2018. hybridized technique applied for AMD treatment. *Phys. Chem. Earth*. 105:170–176.

Franco, D.S.P., Duarte, F.A., Salau, N.P.G., & Dotto, G.L. 2020.Analysis of indium (III) adsorption from leachates of LCD screens using artificial neural networks (ANN) and adaptive neuro-fuzzy inference systems (ANIFS). *J. Hazard. Mater.* 384:121137.

Gokmen, F.O., Yaman, E., & Temel, S. 2021. Eco-friendly polyacrylic acid based porous hydrogel for heavy metal ions adsorption: characterization, adsorption behavior, thermodynamic and reusability studies. *Microchem. J.* 168:106357.

Gupta, A.D., Rawat, K.P., Bhadauria, V., & Singh, H. 2021. Recent trends in the application of modified starch in the adsorption of heavy metals from water: A review. *Carbohydr. Polym.* 269:117763.

Ishak, N.S., Ishak, K.M.K., Bustami, Y., & Rokiah, H. 2019. ScienceDirect Evaluation of Cellulose Nanocrystals (CNCs) as Protein Adsorbent in stick water. *Mater. Today Proc.* 17:516–524.

Kabuba, J. & Banza, M. 2020. Results in Engineering Ion-exchange process for the removal of Ni (II) and Co (II) from wastewater using modi fi ed clinoptilolite : Modeling by response surface methodology and arti fi cial neural network. *Results Eng.* 8:100189.

Lei, W., Fang, C., Zhou, X., Yin, Q., Pan, S., Yang, R., Liu, D., & Ouyang, Y. 2018. Cellulose nanocrystals obtained from office waste paper and their potential application in PET packing materials. *Carbohydr. Polym.* 181:376–385.

Liu, L. & Kong, F. 2019. In vitro investigation of the influence of nano-cellulose on starch and milk digestion and mineral adsorption. *Int. J. Biol. Macromol.* 137:1278–1285.

Moharrami, P. & Motamedi, E. 2020. Application of cellulose nanocrystals prepared from agricultural wastes for synthesis of starch-based hydrogel nanocomposites: Efficient and selective nanoadsorbent for removal of cationic dyes from water. *Bioresour. Technol.* 313:123661.

Mohd Ali, N.S., Hamzah, K., Idris, F., Basri, N.A., Sarkawi, M.S., Sazali, M.A., Rabir, H., Minhat, M.S., & Zainal, J. 2021. Power peaking factor prediction using ANFIS method. *Nucl. Eng. Technol.* (xxxx).

Musikavanhu, B., Hu, Z., Dzapata, R.L., Xu, Y., Christie, P., & Guo, D. 2019. Applied Surface Science Facile method for the preparation of superhydrophobic cellulosic paper. *Appl. Surf. Sci.* 496:143648.

Olad, A., Doustdar, F., & Gharekhani, H. 2020. Fabrication and characterization of a starch-based superabsorbent hydrogel composite reinforced with cellulose nanocrystals from potato peel waste. *Colloids Surfaces A Physicochem. Eng. Asp.* 601:124962.

Priscila, A., Silva, M., Vitória, A., Pontes, S.M.A., Pereira, A.L.S., De, M., Filho, M.S., Rosa, M.F., & Azeredo, H.M.C. 2019. Mango kernel starch fi lms as a ff ected by starch

nanocrystals and cellulose nanocrystals. 211:209–216.

Priyan, V.V., Shahnaz, T., Kunnumakkara, A.B., Rana, V., Saravanan, M., & Narayanasamy, S. 2020. Antioxidant, Anti-inflammatory and Biosorption Properties of Starch Nanocrystals In Vitro Study: Cytotoxic and Phytotoxic Evaluation. *J. Clust. Sci. Springer US*. 5.

Senna, M.M., Mostafa, A.E.K.B., Mahdy, S.R., & El-Naggar, A.W.M. 2016. Characterization of blend hydrogels based on plasticized starch/cellulose acetate/carboxymethyl cellulose synthesized by electron beam irradiation. *Nucl. Instruments Methods Phys. Res. Sect. B Beam Interact. with Mater. Atoms*. 386:22–29.

Shalla, A.H., Yaseen, Z., Bhat, M.A., Rangreez, T.A., & Maswal, M. 2018. Recent review for removal of metal ions by hydrogels. *Sep. Sci. Technol. Taylor & Francis*. 00(00):1–12.

Takagi, H., Nakagaito, A.N., & Bistamam, M.S.A. 2013. Extraction of cellulose nanofiber from waste papers and application to reinforcement in biodegradable composites. *J. Reinf. Plast. Compos.* 32(20):1542–1546.

Vishnu Priyan, V., Shahnaz, T., Suganya, E., Sivaprakasam, S., & Narayanasamy, S. 2021. Ecotoxicological assessment of micropollutant Diclofenac biosorption on magnetic sawdust: Phyto, Microbial and Fish toxicity studies. *J. Hazard. Mater.* 403:123532.

Zhu, X. & Wang, N. 2022. Hairpin RNA genetic algorithm based ANFIS for modeling overhead cranes. *Mech. Syst. Signal Process.* 165:108326.

Zong, L., Liu, F., Chen, D., Zhang, X., Ling, C., & Li, A. 2018. A novel pyridine based polymer for highly efficient separation of nickel from high-acidity and high-concentration cobalt solutions. *Chem. Eng. J.* 334:995–1005.

CHAPTER SEVEN

COMPARISON STUDY OF ANFIS, ANN, AND RSM AND MECHANISTIC MODELING FOR CHROMIUM (VI) REMOVAL USING MODIFIED CELLULOSE NANOCRYSTALS-SODIUM ALGINATE

ABSTRACT

The adaptive neuro-fuzzy inference system (ANFIS), artificial neural network (ANN), and response surface methodology (RSM) were used to develop an approach for assessing the Cr (VI) adsorption from wastewater using cellulose nanocrystals and sodium alginate. The adsorbent was characterized using Fourier transform infrared spectroscopy (FTIR) and Thermogravimetric analysis (TGA). The adsorption process was investigated using the ANFIS, ANN, and RSM models, considering the time, pH, concentration, and adsorbent dose. To examine the viability of the models, five statistical functions were applied. Cr (VI) absorption mechanism was described via four mechanistic models (Film diffusion, Weber and Morris, Bangham, and Dummwald-Wagner models). With R^2 values of 0.997, 0.990, and 0.989 for ANFIS, ANN, and RSM, respectively, predicted the Cr (VI) adsorption with incredible accuracy. Using the Central Composite Design (CCD), the significance of operating factors such as time, adsorbent dose, pH, and initial Cr (VI) concentration was investigated. The same concept was used to create a training set for ANN where the Levenberg-Marquardt, Variable learning rate, and Polak Ribiere conjugate algorithms were used. Further statistical indices supported ANFIS as the best prediction model for adsorption than ANN and RSM. The efficient algorithm optimized the process, which resulted in a 350 mg/g adsorption capacity. Film diffusion was identified as the rate-limiting process via mechanistic modelling.

Keywords: Adaptive neuro-fuzzy inference system, Artificial neural network, Response surface methodology, cellulose nanocrystals, sodium alginate, mechanistic modeling.

7.1 INTRODUCTION

Heavy metals have a density of more than 5 gr per cubic centimeter and atomic weights ranging from 63.0 to 200.0. Water pollution caused by the discharge of heavy metals into ecosystem metals has been a source of concern world(Ihsanullah *et al.*, 2016). Heavy metals are primarily found in wastewater from various chemical industries such as the production of steel, chemical manufacturing, fertilizer, mining, pulp, and pesticides, as well as metallurgy, mining, coal power, leather industries, and the manufacture of various polymers such as polyvinyl chloride(Dolatabadi *et al.*, 2018). The significant growth in industrialization has significantly contributed to the release of contaminants into the environment. Heavy metals, unlike organic pollutants, accumulates in human organisms since they are not biodegradable. Arsenic, chromium, copper, cadmium, lead, nickel, zinc, and mercury are toxic heavy metals crucial in industrial wastewater treatment(Kabuba & Banza, 2020a).

Chromium is considered one of the earth crust's most abundant elements, and it is estimated to be the sixth most abundant transition metal. Chromium is a metal found in natural deposits as ores containing other elements such as crocoite, ferric chromite, and chrome ochre(Zaman *et al.*, 2017). It's a well-known, very poisonous metal that may be found in drinking water. Chromium exists in various oxidation states, including 2+, 3+, and 6+, with the most stable being trivalent Cr(III) and hexavalent Cr(VI). Cr(III) is much less harmful than Cr(VI), because it is an essential component of human organisms(Ihsanullah *et al.*, 2016). Cr(VI), on the other hand, is exceedingly hazardous and may be found in a variety of industrial wastewater, causing severe nausea, vomiting, lung congestion, liver and kidney problems(Nordin *et al.*, 2021). Leather tanning, textile industries, metal polishing, electroplating, and chromate preparation require chromium metal (Zaman *et al.*, 2017).

As a result, industrial effluent discharge into the environment is a possible source of chromium pollution in wastewater. Refrigeration tower blowdown, electrolysis, mineral processing, and coating activities are examples of industrial sources. Dichromate ($Cr_2O_7^{2}$) and chromate (CrO_4^{2-}) ions are the most common forms of Cr(VI)(Shahnaz *et al.*, 2020). Cr(VI) can exist in water as chromate ion(CrO_4^{2-}), dichromate ($Cr_2O_7^{2}$) ions, chromic acid

(H_2CrO_4) and hydrogen chromate ion ($HCrO4^-$) depending on the pH of the solution. As a result of these detrimental impacts, the United States Environmental Protection Agency (USEPA) has categorized all chromium (VI) compounds as potential health hazards and set the allowable contaminant level in water at 0.1 mg/L. Because of the strict rules limiting the emission of this dangerous pollutant into water bodies, numerous solutions must be developed to decrease chromium (VI) to the permissible limit(Igberase *et al.*, 2017).

Chemical precipitation, electrolysis, ion exchange, coagulation, membrane separation, and adsorption are well-known and efficient traditional sewage treatment procedures(Kabuba & Banza, 2020a). However, because of constraints such as low efficacy, high operating costs, and the danger of secondary contamination, most of these technologies could not be widely deployed. The adsorption process has been extensively researched and widely implemented on a large scale because of its high efficiency, low cost, easy operation, and lack of polluting by-products(Fosso-kankeu, 2018). Various authors (Igberase *et al.*, 2017; Zaman *et al.*, 2017) have reported methods for adsorbing Cr(VI) from solution, including ion exchange, electrolysis, chemical precipitation, membrane separation and adsorption. Of these methods, the adsorption process seems to have great potential due to the ability to remove heavy metal ions from water and wastewater, its simplicity, easy operation, and the potential to be regenerated by some desorption processes.

Adsorbents based on natural polymers, in particular, are now gaining a lot of interest. Many of them were developed to address the disadvantages of synthetic polymers, such as their high cost of manufacture and challenges in regeneration. On the other hand, natural polymers can be highly effective, biodegradable, cost-effective, and recyclable, with no sludge formation and complete pollution reduction(Leudjo Taka *et al.*, 2021; Shojaeiarani *et al.*, 2019). Cellulose nanocrystals is biopolymers with a large surface area that is renewable and sustainable. Cellulose nanocrystals are derived from natural cellulose by acid hydrolysis is commonly applied in three industrial sectors: energy electronics, biomedical, and wastewater treatment(Kargarzadeh *et al.*, 2015). Cellulose nanocrystals various active OH groups have been physically and chemically modified using grafting, composite synthesis, and carboxylation(Kaboorani & Riedl, 2015). The last step is to soak cellulose nanocrystals in citric acid anhydrous. The resulting carboxylated cellulose nanocrystals retain the fundamental structure of cellulose while also displaying

beneficial properties such as high specific surface area, high hardness, and excellent stability.

Alginate is a naturally present biopolymer made of mannuronic acid and guluronic acid residues obtained from brown algae(Thomas *et al.*, 2018). Alginate is a potential biopolymer for various applications, such as drug administration, surgical dressing, and wastewater treatment. It has several desirable characteristics, including non-toxicity, biodegradability, biocompatibility, and low cost. Alginate may be modified physically and chemically to increase its structural performance and durability and generate new adsorptive structural features. Graft polymerization, composite, and the development of hydrogel beads are the most frequent ways for improving alginate's adsorption properties(Hu *et al.*, 2018).

However, the majority of Cr(VI) removal research focused on (OFAT) the one factor at a time technique. One factor at a time requires a long time to evaluate. It cannot predict the desired optimal adsorption efficiency as a series of contact between process variables.(Shahnaz *et al.*, 2020)used a factorial design to find the best conditions for removing Cr (VI). There has been no comparative investigation of Cr (VI) removal using complex modelling methods such as the adaptive neuro-fuzzy inference system (ANFIS), artificial neural network (ANN), and the response surface approach (RSM). As a result, our research is aimed towards reaching that goal.

Unlike one factor at a time, the response surface methodology (RSM) is a statistical method for optimizing a process in which a dependent output variable is impacted by a large number of independent input variables. The response is the name of the output variable. As an improved systematic approach to experimentation, RSM evaluates all process variables simultaneously while predicting an outcome. One of the essential aspects of RSM is the central composite design (CCD). The central composite design is a three-level experimental design that combines the axial and factorial design points in the experiments conducted. One of its key benefits is that it requires a few experimental runs to determine the optimal experimental conditions(Samuel *et al.*, 2020).

The artificial neural network (ANN) is a computational model that estimates the processing data of biological neurons. In addition to input and output layers, most neural network models have one or more hidden layers; the type of investigation affects the

number. A neural network's main characteristic is its capacity to perform internal computations to determine the targeted output from a set of input information. Since ANN may be applied in complex systems since it is reliable and efficient in representing the non-linear interactions among the variables and responses of diverse processes, by training the multiple input-output networks algorithm, the ANN can also assess multifactorial non-linear and complicated processes given sufficient data(Cojocaru *et al.*, 2021).

ANFIS is a neural network that is built on mathematical computation. Its operation is based on the Takagi-Sugeno fuzzy inference system, which allows it to handle complex and non-linear problems. It consists of a mixed system of neural networks and fuzzy systems which work together to provide accurate and better predictions from recorded input information. The fuzzy inference mechanism enhances the system's reliability and dependability, while the neural network regulates its flexibility(Arora & Keshari, 2021). In the latest years, there has been a growth in interest in using ANFIS in various processes. ANFIS was used by(Franco *et al.*, 2020) to investigate the indium (III) removal from leachates of LCD screens.(Zhu & Wang, 2022) ANFIS is based on a hairpin RNA genetic algorithm for simulating overhead cranes.

In addition, four mechanistic models (Weber and Morris, Dummwald-Wagner Film diffusion, and Bangham models) have been explored to establish the rate-controlling phase in the adsorption process. The coefficient of correlation was used to evaluate the models. As a result, the following are the goals of this work: (1) CNC modified adsorbent preparation and characterization; (2) modelling the adsorption capacity of Cr (VI) using ANFIS, ANN, and RSM; (3) comparison of the three models predictive capacities; and (4) determining the rate-controlling phase of the adsorption process using four mechanistic models.

7. 2 EXPERIMENTAL METHODOLOGY

7.2.1 Materials and equipment

Cellulose nanocrystals used were extracted from waste papers via hydrolysis (≥90%). Calcium chloride (>99%), sodium hydroxide(>99%), hydrochloric acid (>99%) and potassium dichromate (>99%) were all purchased from Sigma-Aldrich. The pH of the solution was controlled using a pH meter (Hanna HI 8421). Distilled water was produced

using the Ultima 888 water distiller. The quantity of metal ions adsorbed was assessed (ICP, Icap7000). The functional groups available in the CNC-Alg were explored using Fourier transform infrared spectroscopy (FTIR, Varian 7000), and the morphological surface was examined using scanning electron microscopy (SEM, Philips XL30FEG).

7.2.2 Preparation of Cellulose nanocrystals-sodium alginate adsorbent

After agitating at 60°C for 60 minutes, Alginate (2 g) was added to 100 mL H_2O to make a colloidal solution. Cellulose nanocrystals (4 g/200 mL, 50 mL) were ultrasonically dispersed for 20 minutes before adding to the Alg solution. The blended solution was agitated at a continuous high speed for 120 minutes to achieve uniform diffusion. The combined solution was put into a 250 mL (2%)$CaCl_2$ solution using a 10 mL syringe while being stirred mechanically. After 45 minutes, the developed cellulose nanocrystals and sodium alginate particles were transferred to a solution of 0.2% $CaCl_2$ to solidify. After 36 hours, the cellulose nanocrystals and sodium alginate particles were removed from the solution of $CaCl_2$ and rinsed numerous times with distilled water. The chemical structure of cellulose nanocrystals and sodium alginate particles was optimized using Gaussian 6.0 software (**Figure 1**)

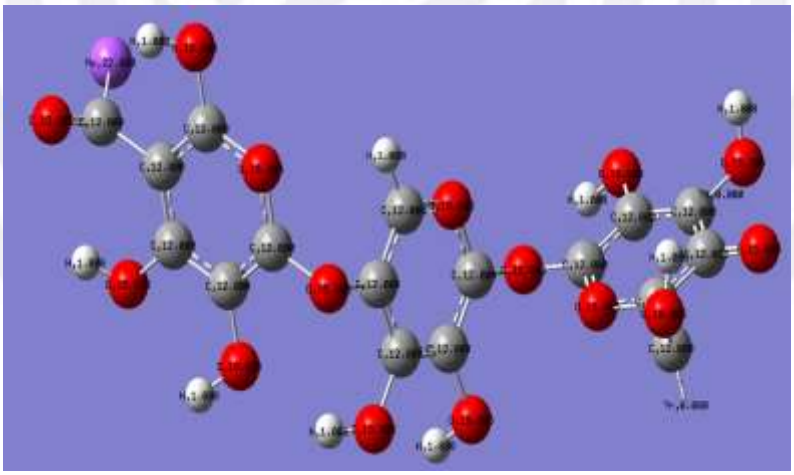

Figure 7.1. The proposed structure of Cellulose nanocrystals-sodium alginate

7.2.3 Adsorption experimental

Batch experiments were used to develop the adsorption method. Batch studies were carried out in 200 mL glass-stoppered flasks reactors holding test solutions at the appropriate required Cr (VI) concentration, contact time, adsorbent dose, and pH at room

temperature (27±2°C). The amounts of a solution with a particular Cr (VI) concentration were placed in the reactor. To maintain a consistent pH throughout the experiment, the pH of the solution was controlled using 0.1M NaOH or HCl. A shaker was used to agitate the solution at 180 rpm, adding the appropriate weight of adsorbent in the prescribed dose. The mixed phases were then subjected to centrifugation for 10 minutes at 1500 rpm.

The quantity of Cr (VI) adsorbed onto CNC-Alg (q_e) was determined using the Eq.7.1

$$q_e = \frac{(C_i - C_{eq}) \times V}{M} \quad (7.1)$$

where C_i (mg/L) denotes the starting concentration, C_{eq} (mg/L) denotes the equilibrium concentration, M (mg) denotes the mass of the nanocomposite used, and V (L) is the volume of the solution.

7. 2.4 Response surface methodology

RSM investigation of the adsorption process was performed using a central composite design (CCD). The four parameters employed as independent variables at a constant volume of 100 ml and a temperature of (27±2°C) were adsorbent dosage, contact time, concentration, and pH. The three levels of variance for these components are shown in **Table 7.1** (-1, 0, +1). Based on the experiments and past research findings, the experimental limit was determined(Kabuba & Banza, 2020b). The response variable was the adsorbent capacity (mg/g). The axial and factorial sets of experiments were performed in triplicate to improve the efficiency of the experimental design. In the RSM analysis, 21 experimental data sets were examined, including six central points. The core points ensured that the higher and lower values varied equally, the axial points ensured that the model prediction deviation was equal from the design center, and the center point facilitated data repeatability. The studies were carried out randomly to avoid systematic mistake(Onu *et al.*, 2021).

Table 7.1: Levels of independent variables for Cr (VI) adsorption

Variable	Coded	Coded level		
Time (min)	A	20	100	120
Dosage (g)	B	2	6	10
pH	C	3	6	9
Concentration (mg/L)	D	50	175	300

The response was estimated using an empirical relationship of the second-order polynomial, as shown in Eq. 2.

$$Y = \gamma_0 + \gamma_a A + \gamma_b B + \gamma_c C + \gamma_d D + \gamma_{aa} A^2 + \gamma_{bb} B^2 + \gamma_{cc} C^2 + \gamma_{dd} D^2 + \gamma_{ab} AB + \gamma_{ac} AC + \gamma_{ad} AD + \gamma_{bc} BC + \gamma_{bd} BD + \gamma_{CD} CD \quad (7.2)$$

Where Y is the expected response, γ_0 is the model constant, A, B, C and D are independent variables, γ_a, γ_b, γ_c and γ_d are linear coefficients and γ_{ab}, γ_{ac} γ_{ad} γ_{bc} and γ_{cd} are cross-product coefficients, and γ_{aa}, γ_{bb} γ_{cc} and γ_{dd} are the quadratic coefficients.

Design-Expert version 13 was employed for the experimental design, regression analysis, analysis of variance, and optimization of process factors in the adsorption of Cr (VI). The coefficient of regression (R^2) and the ANOVA p-value was used to assess the model's acceptability.

7.2.5 Artificial neural network

According to(Souza *et al.*, 2018), The RSM-generated experimental data set may be exploited to evaluate the ANN model correctly. Therefore, given a considerable number of data sets, ANN modelling performs better. As a result, the RSM collected data sets were doubled. Yielding a total of forty-two (42) data sets for the ANN analysis. For the ANN computation, Matlab software 2015 was employed. The network was trained using a Multi-Layer Perceptron (MPL). For modelling, the Levenberg-Marquardt back-propagation and Variable learning rate back-propagation algorithm were used (**Table 7.2**). The input, hidden (neurons), and output make up the network. The input factors were contact time, pH, dose, and concentration, while the adsorbent capacity was the output layer.

Trial and error were used to determine the number of neurons in the hidden layer, giving the lowest mean square error (MSE) and the highest correlation coefficient. This was done to guarantee that the model's predictions were as near as possible to the experimental data and avoid over-fitting. Large and small numbers of neurons were avoided since they might result in complex over-fitting and increased convergence speed(Zhu & Wang, 2022). About 70% of the data sources were chosen to train the neural network, 15% to test the neural network, and the other 15% to confirm the output. Additional data was assigned to the retraining, resulting in a better model and faster processing time.

The validating has been used to monitor the network's extension, which was terminated until no more progress was observed, while the testing provided an unbiased assessment of the network's functionality. Trainlm was utilized as the training method to normalize the bias value. To eliminate network error, the input parameters and response were standardized between 0 and 1(David Samuel *et al.*, 2021).

Table 7.2: Black propagation algorithm

BP algorithm	Function	MSE
Levenberg-Marquardt back propagation	*Trainlm*	0.002
Variable learning rate back-propagation	*Traingdx*	0.130
Polak Ribiere conjugate gradient backpropagation	*Traincgp*	0.121

7.2.6 Adaptive neuro-fuzzy inference system

The neuro-fuzzy system's primary benefit is to blend neural network characteristics with fuzzy logic. As a result, both limitations are eliminated. The explicit knowledge that can be gained and interpreted is dealt with by fuzzy logic, whereas the implicit knowledge is handled with neural networks. ANFIS combines the qualitative approach of fuzzy logic with the quantitative approach of neural networks. Integrating adaptive capabilities into a single system has certain drawbacks and benefits. A trial-and-error method defines membership parameters and rules in a fuzzy system(Ehteram *et al.*, 2021). The ANFIS model was generated using the fuzzy inference approach. The first and last layers of the ANFIS structure, respectively, represent the input parameters (time, adsorbent dose, pH, and concentration) and the output variable (adsorbent capacity). The model corresponded to first-order Sugeno inference systems in the second layer, which fuzzified input parameters by converting them into membership values using membership function parameters (MF). In the third layer, the model output was derived using a set of logical principles. In the third layer, the model output was computed using logical rules. The defuzzification of the inferred result to the actual target value was achieved in the fourth layer applying the output membership function(Onu *et al.*, 2021). In the fifth layer, only one node was used to display all received signals as the total output, which is the adsorbent capacity.

7. 2.7 Model performance indicator

The ANFIS, ANN, and RSM modelling findings were compared to performance indicators to provide a classification that identified the model with the highest predictive potential with the results obtained. The analysis used five high-performance statistical error functions (Equation 7.3-7.7). The chosen assessment indices were based on the characteristics of the data set that was used. A comparative parity analysis was also performed, which indicated particular deviation spots between the ANFIS, ANN, and RSM model predictions from the experimental results.

$$\text{RMSE} \quad \sqrt{\frac{1}{N}\sum_{i=1}^{n}\left(\frac{\left(q_{e(exp)}-q_{e(pred)}\right)^2}{q_{e(exp)}}\right)} \tag{7.3}$$

$$\text{ARE} \quad \frac{100}{N}\sum_{i=1}^{n}\left(\left[\frac{\left(q_{e(exp)}-q_{e(pred)}\right)^i}{q_{e(exp)}}\right]\right) \tag{7.4}$$

$$\text{SSE} \quad \sum_{i=1}^{n}\left(q_{e(exp)}-q_{e(pred)}\right)^2 \tag{7.5}$$

$$\text{MSE} \quad \frac{1}{N}\sum_{i=1}^{n}\left(q_{e(exp)}-q_{e(pred)}\right)^2 \tag{7.6}$$

$$\text{MPSD} = 100\sqrt{\frac{1}{N-P}\sum_{i=1}^{n}\left(\frac{\left(q_{e(exp)}-q_{e(pred)}\right)^2}{q_{e(exp)}}\right)i} \tag{7.7}$$

where the number of observations is N, the number of variables in the model is P, $q_{e(pred)}$ and $q_{e(exp)}$ are predicted and experimental adsorbent capacity, respectively.

7. 2.8 Mechanism modeling

Four mechanistic models were explored to reveal the rate-controlling phase in removing the Cr (VI) (see **Table 7.3**). In mechanistic modelling, the Bangham model, the Film diffusion (Boyd) model, the Dummwald-Wagner model, and the Weber and Morris (intra-particle) diffusion model were used(Onu *et al.*, 2021).

Table 7.3: Mechanistic models

Model	Equation	Eqn. Num.	Reference
Liquid film diffusion	$\ln(1-A)=-K_d t$	(8)	[3]
Weber and Morris	$q_X=K_X t^{0.5}+C_X$	(9)	[20]
Dumwald-Wagner	$\log(1-A^2)=(-K_{dw}/2.3V)t$	(10)	[21]
Bangham	$\log(C_a/C_a-q_{max})+\text{Log}(K_b m/2.3)t+\beta\log t$	(11)	[21]

7.3 RESULTS AND DISCUSSION

7.3.1 Characterization of the cellulose nanocrystals-alginate nanocomposites

7.3.1.1 FTIR analysis

As seen in **Figure 7.2**, the peaks at 3300, 1650, and 1400 cm^{-1} indicate the stretched vibration of O–H, the asymmetric vibration of C=O and symmetric vibrations of the carboxyl group, respectively. C–H stretching vibration peak was found to be between 3000and 2600 cm^{-1}, and C–O stretching vibration peak was found to be at 1200 cm^{-1}. The cellulose nanocrystals include a lot of COOH and OH, whereas Alginate has a lot of OH but very little COOH. This might imply that Alginate was successfully coated with cellulose nanocrystals while yet retaining some OH and COOH in the composite. The stretching vibration of CH_2 is responsible for the peak at 1350 cm-1. Other bands include 1020 cm^{-1} for morphological change in C-O and 850 cm^{-1} for the standard cellulose structure with glycoside connections in the glucose ring(Banza & Rutto, 2022).

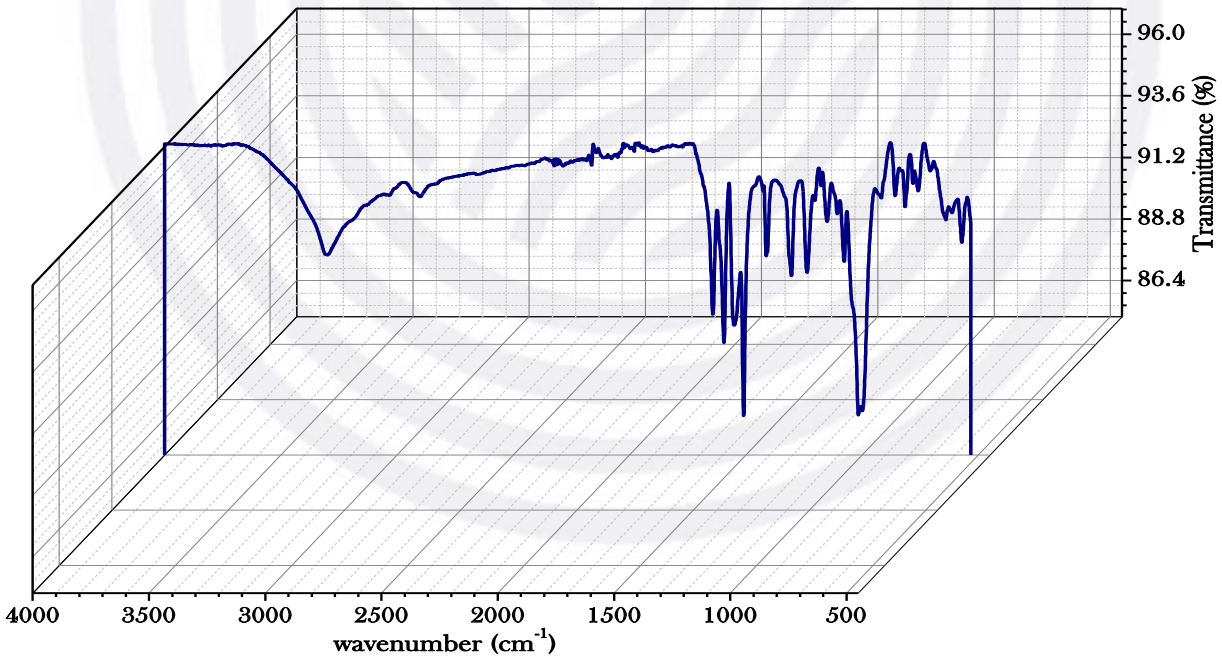

Figure 7. 2: FTIR vibrational spectra of the cellulose nanocrystals and Alginate

7.3.1.2 TGA Analysis

The TGA curves of cellulose nanocrystals-sodium alginate samples produced in an N_2 atmosphere at a 10 C min^{-1} heating rate are shown in **Figure 7. 3**. The weight loss for cellulose nanocrystals-sodium alginate was rapid at 150–200°C, followed by a more gradual reduction at 200–380°C. The breakdown of the pyranose rings in CCN's backbone is correlated with a distinctive degradation between 250 and 320 C. the last degradation stage occurred at 400–600°C, resulting in a 10% weight loss, which was consistent with the disintegration of Alginate and cellulose nanocrystals and demonstrated the effective synthesis process(Banza & Rutto, 2022).

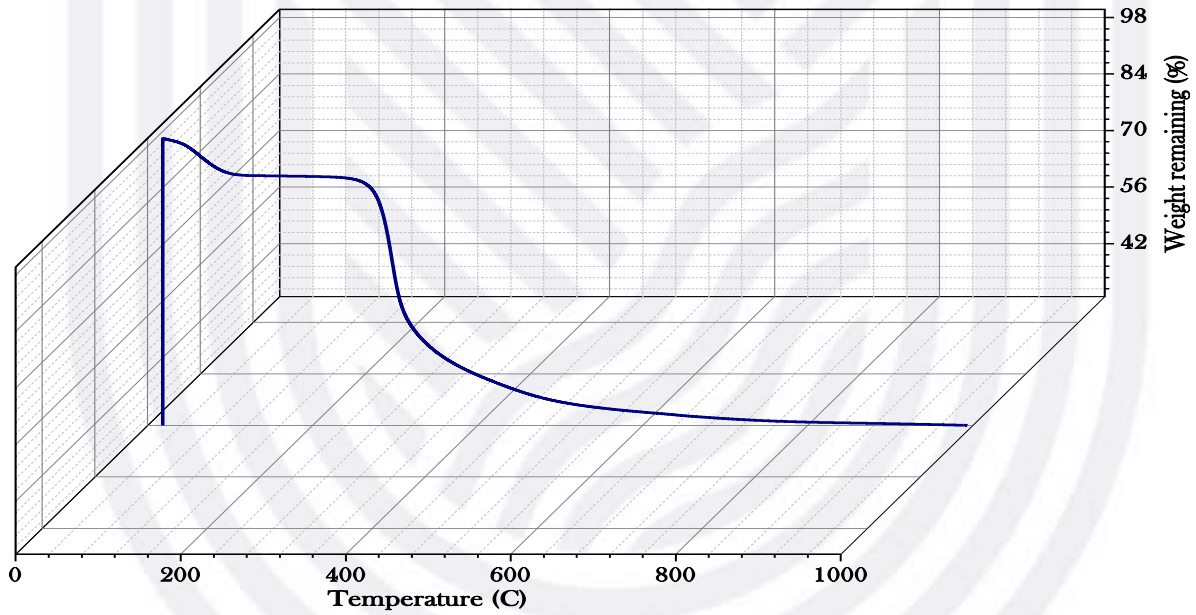

Figure 7. 3: TGA curve of the cellulose nanocrystals and Alginate

7.3.2 Experimental design result

An experimental design was adopted to investigate the individual and interacting impacts of the process factors. Table 3 shows the outcome of the experimental design. The majority of the responses produced from different runs were considered exceptional, demonstrating that the input parameters considerably impacted the response. At a contact time of 180 min, an adsorbent dose of 2g, a solution pH of 6, and a concentration of 50 mg/L, the maximum adsorption capacity of 265 mg/g was recorded.

7. 3.2.2 Response Surface Method plots

Graphical representations such as three-dimensional (3-D) and contour surface plots may be used to explore the interaction effects of the combination of input factors and response(David Samuel *et al.*, 2021). Fig.4 shows these plots. The graphs were used to demonstrate how the combined impacts of the process parameters on the adsorbent capacity of CNC-alginate adsorbent for Cr (VI) removal. The surface plots were developed by changing any two variables within the experimental region while keeping the other independent factors constant at their center points.

Fig. 4(a) and (b) show the interaction impact of contact time and dosage at a constant concentration of 175 mg/L and pH of 6. It was discovered that as both contact time and dosage expanded simultaneously, the adsorption capacity was raised to 466 mg/g. This is due to the availability of additional active adsorption sites for Cr (VI) capture, and the presence of sufficient time for the adsorption process are responsible for the increase in Cr (VI)(Shahnaz *et al.*, 2020). This was corroborated by the contour plot, which revealed that the optimal predicted adsorption capacity was 466 mg/g at a contact period of 180 minutes and a dosage of 2 g. The 3D plot's design showed a high interaction relationship between time and dosage.

Fig. 4(c) and (d) demonstrate the combined effects of pH and concentration at a contact time and dosage at CenterPoint's 150 minutes and 150 mg/L, respectively. The contour plot resembled a vertical line, indicating that the pH and concentration were interacting. Within the pH range used, the adsorption capacity dropped as pH increased. Lower pH and high concentration increased the adsorption capacity. This was because at acidic pH, the hydrogen bond degree of the CNCs/Alginate resulted in greater mobility and, as a result, an increase in adsorption due to electrostatic charge(Ahmadi *et al.*, 2021).

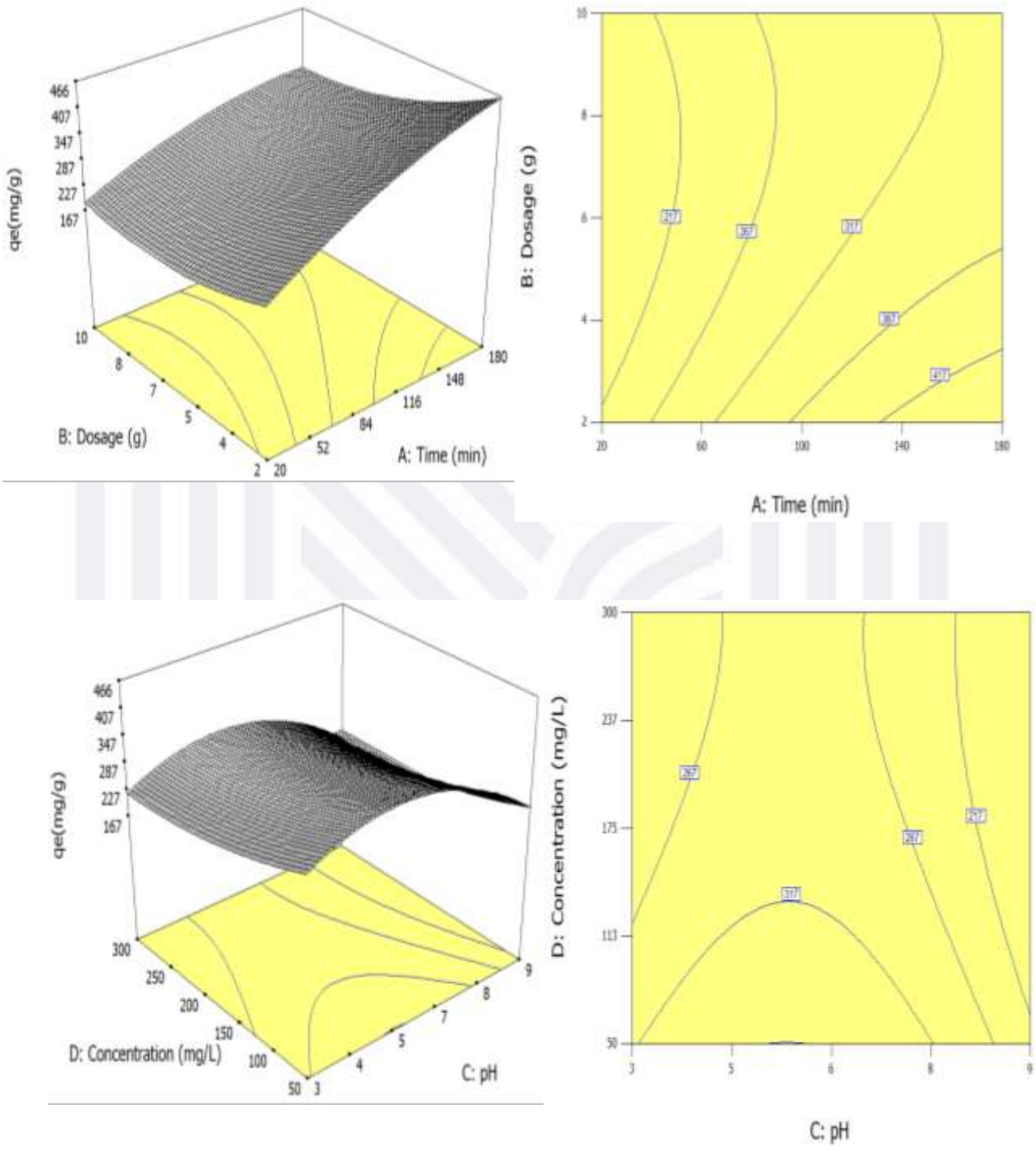

Figure 7. 4: The 3 D surface and contour plots of Cr (VI) adsorption

7. 3.2.3 Response surface modeling and ANOVA analysis

The RSM model study used the Design-Expert software's central composite design (CCD). In explaining the interaction between the output and input variables, the two-factor interactions, linear, cubic, and quadratic models, were compared using statistical model results. A high regression coefficient (R^2) and a low standard variation were used to find the optimum model for the adsorption process (Nosuhi & Nezamzadeh-Ejhieh, 2017). As shown in **Table 7.4**, the best model for describing Cr (VI) removal was a quadratic model with an R^2 value of 0.989 and a standard deviation of 1.62. Furthermore, the quadratic model's adjusted R^2 of 0.992 was close to the R^2, indicating strong significance and acceptable agreement between the input and output values(Zolgharnein *et al.*, 2017). The adjusted R^2 value was close to the predicted R^2, suggesting that the model and data were both adequate(Shahnaz *et al.*, 2020).

Table 7.4. Statistical overview of the models examined

Model	P-value	df	Standard deviation	R^2	R^2(Adj)	R^2(Pred)
Linear	0.0010	12	4.20	0.845	0.795	0.686
Quadratic	0.0001	4	1.62	0.989	0.992	0.995
Cubic	0.0322	2	1.84	0.954	0.938	0.934
2FI	0.0010	6	3.25	0.899	0.857	0.876

7.3.2.4 Anova (analysis of variance)

The findings of the analysis of variance are summarized in **Table 7.5**. It was used to determine the significance of the quadratic model and design variables. The p-value was used to determine the significance of each term in the quadratic model. A 95 % confidence level was employed in the p-value probability analysis. This implies that variables with p-values more than or equal to 0.05 are insignificant, and terms with p-values less than or equal to 0.05 are significant.

Fisher's F-test values determined the magnitude of the model's relevance and each quadratic model's independent input data. The ratio between the model's mean square was determined to achieve this. The greater the F-value for each significant model term, the greater the term's impact on the response. The p-value was less than 0.0001, and the F-

value was 93.45, suggesting that the quadratic model recommended was acceptable(Derikvandi & Nezamzadeh-Ejhieh, 2017).

The variables time (A), dosage (B), pH (C), and concentration (D) were significant, as were the interacting variables of AB, BC, AC, CD, AD, and BD, as well as the exponential variables of A^2, C^2, B^2, and D^2. For the interactive and exponential variables, Time had the most singularly significant influence, followed by the concentration on the adsorption of the Cr (VI). In contrast, dose and the combination of pH and dosage had the most significant effects. The RSM process's coefficient of variation was 2.10 per cent, indicating that the model equation was adequately predictable. The coefficient of variation was calculated by dividing the standard deviation by the mean of the output variable. A model is considered highly replicable if the coefficient of variation is below 10%, according to (Samuel & Okwu, 2019). Equation 7.12 shows the quadratic model equation that relates the Cr (VI) removal response to the independent input variables (pH, time, dosage, and initial concentration).

$$\text{Adsorption capacity (mg/g)} = 294.73 + 95.37A - 42.63B - 36.68C - 43.00D - 30.10A^2 + 38.53B^2 + 92.14C^2 + 24.03D^2 - 25.30AB - 11.92AC - 3.38AD - 30.51BC - 11.37BD + 3.38CD \quad (7.12)$$

The model equation might predict response for a given set of variables. It was also important for comparing the coefficients of the variables to see how they influenced the results. Any model term with a positive sign had a synergistic effect, whereas those with a negative value had an antagonistic effect. AD and CD were shown to be negligible in the ANOVA analysis in table 5. Equation 7.13 shows the complete model equation after removing the negligible component.

$$\text{Adsorption capacity (mg/g)} = 294.73 + 95.37A - 42.63B - 36.68C - 43.00D - 30.10A^2 + 38.53B^2 + 92.14C^2 + 24.03D^2 - 25.30AB - 11.92AC - 30.51BC - 11.37BD \quad (7.13)$$

Table 7.5. ANOVA

Source	Sum of Squares	DF	Mean Square	F-value	P-value
Model	2.06E+05	14	14716.92	532.95	< 0.0001
A	18909.98	1	18909.98	684.8	< 0.0001
B	3779.17	1	3779.17	136.86	< 0.0001
C	1410.55	1	1410.55	51.08	0.0004
D	18490	1	18490	669.59	< 0.0001
A2	1714.07	1	1714.07	62.07	0.0002
B2	3756.77	1	3756.77	136.05	< 0.0001
C2	12026.43	1	12026.43	435.52	< 0.0001
D2	1461.4	1	1461.4	52.92	0.0003
AB	593.46	1	593.46	21.49	0.0036
AC	238.57	1	238.57	8.64	0.0026
AD	120.13	1	120.13	4.35	0.0821
BC	1536.03	1	1536.03	55.63	0.0003
BD	1035.13	1	1035.13	37.49	0.0009
CD	91.13	1	91.13	3.3	0.1192
Residual	165.68	6	27.61		
Lack of Fit	155.68	2	77.84	31.14	0.0036

The observed values were compared to predicted values obtained by the model in Fig. 5a, while residual values were shown in Fig. 5b. The points were quite close to the straight line, showing that the actual and predicted response values are very well connected. According to the residuals plot, the majority of the data points were located within -1.0 and +1.0 points. According to these findings, the majority of residuals were found to be negligible. In Fig. 5c, the perturbation plot depicted the variation from the point of reference for input parameters. The mean at 300 mg/g adsorption capacity served as the reference point for this variation(Kabuba & Banza, 2020c). **Table 7.6** compares the three models with the experimental data set

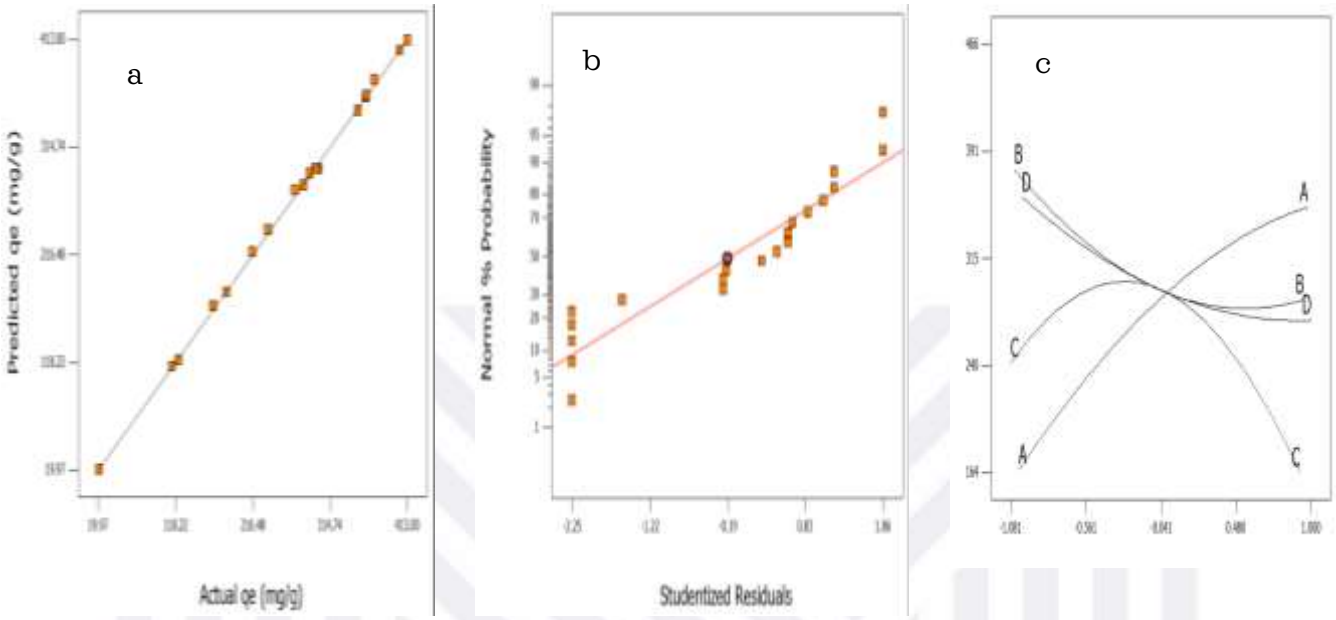

Figure 7. 5: RSM plots predicted vs actual (a), Normal plot (b) and Perturbation(c)

Table 7.6: RSM, ANN and ANFIS models

Run	Time (min)	Dosage (g)	pH	Concentration (mg/L)	qe (pred)	qe (exp) RSM	qe (exp) ANN	qe (exp) ANFIS
1	100	6	6	175	300	297	298	300
2	100	6	6	300	270	274	267	271
3	180	2	9	50	413	409	410	412
4	180	2	9	300	350	352	351	349
5	180	10	3	50	403	404	405	402
6	180	6	6	175	360	358	358	361
7	100	6	6	175	297	295	293	298
8	100	10	6	175	289	290	288	289
9	180	10	3	300	281	285	283	280
10	20	10	9	300	21	25	22	20
11	180	6	9	175	216	213	217	215
12	20	2	3	300	122	120	124	121
13	20	6	6	175	166	163	165	166
14	20	2	3	50	183	180	184	182
15	100	6	6	175	298	298	296	298
16	20	10	9	50	114	116	113	114
17	100	6	6	175	296	295	294	295
18	100	6	6	175	299	297	295	298
19	100	2	6	175	371	370	369	370
20	100	6	6	50	361	360	359	360
21	100	6	3	175	236	234	237	236

7.3.2.5 Modeling of artificial neural network

The ANN was tested using the parameters listed above, the slope, the validation test variable, which was used to determine the ANN's validity, and data analysis regression, which reveals how the ANN plots. The connection was examined, and the weights were re-initialized and modified if they were too tight or too loose. The training, testing, validating, and regression process was repeated until the fit was satisfactory. The outcome and error data were collected when the fitting was satisfactory, and the targets and outputs were compared(Ayoola *et al.*, 2020). To develop ANN, (Kabuba & Banza, 2020c)state that the following crucial characteristics must be determined: (1) Backpropagation training method selection, (2) data distribution, (3) ANN structure selection, and (4) starting weight selection(Cojocaru *et al.*, 2021).

• Algorithm for BP training selection

Three back-propagation training algorithms were examined to determine the best back propagation training method. The ANN Toolbox was used to import the data' laboratory findings. Most of the back-propagation training techniques used a three-layer NN with a linear transfer function at the output layer and a tangential sigmoid transfer function at the hidden layer. The Levenberg-Marquardt back-propagation training method was chosen because it has the minimum mean squared error, indicating that the algorithm's error is deficient. The regression correlation and the MSE were determined for NN cross-validation. The Levenberg-Marquardt back-propagation BP technique built the NN model for the experimental data. The neural network was trained using these data. The outcome matrix was generated via a forward pass (feed-forward back-propagation NN). The input matrix was sent forward through the network to generate each unit's output.

The outcome matrix was then matched to the required matrix, providing an error signal for each output. Appropriate modifications were performed for each network's weights to reduce the inaccuracy. After several rounds, the discrepancies between training and validation errors began to increase; the training was terminated. The algorithms Levenberg-Marquardt, Variable learning rate, and Polak Ribiere conjugate are shown in **Figures 6-8**.

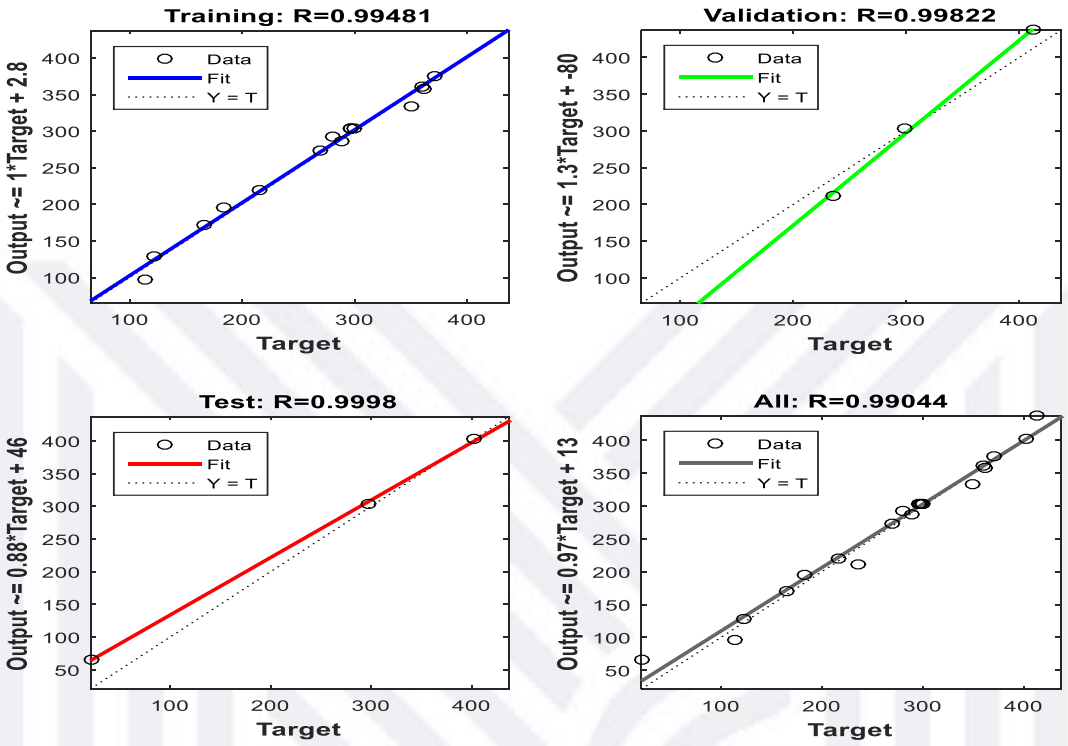

Figure 7.6: Training, validation, and test for Levenberg-Marquardt algorithm

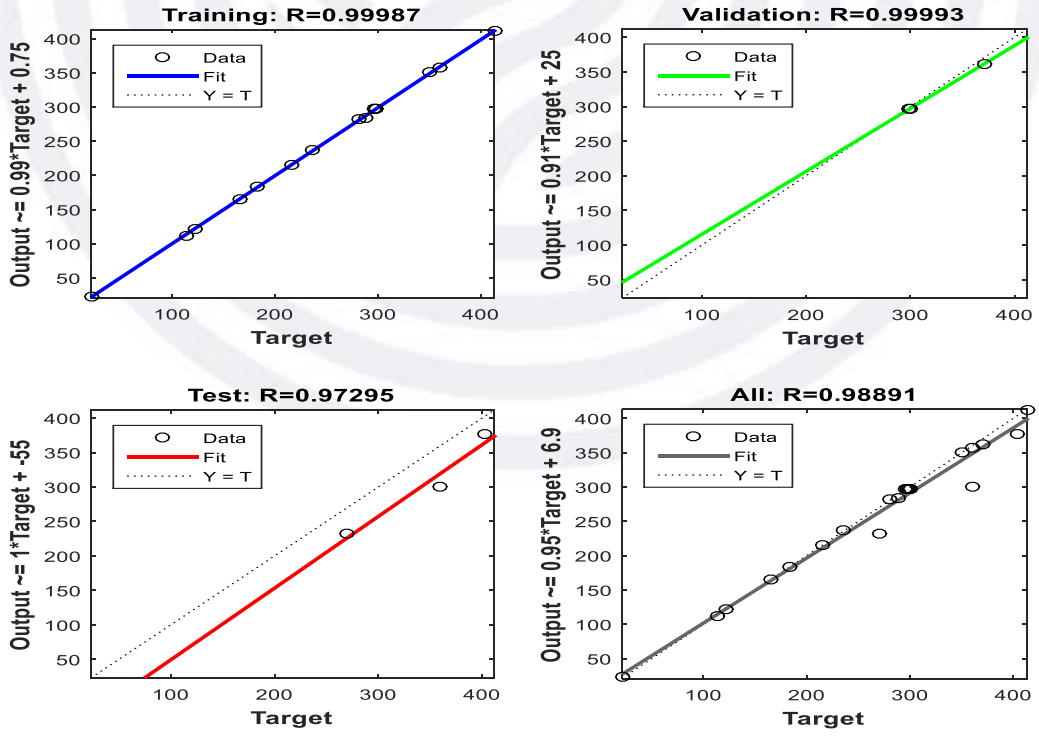

Figure 7.7: Training, validation, and test for Variable learning rate algorithm

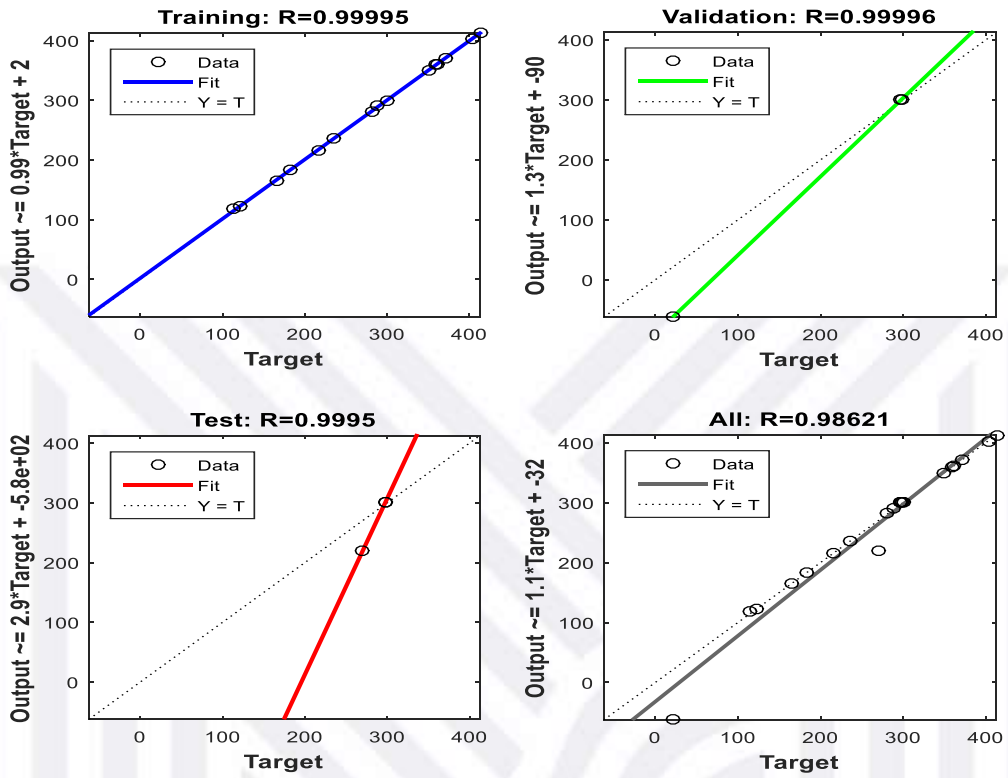

Figure 7. 8: Training, validation, and test for Polak Ribiere conjugate algorithm

The best method for training, testing, and validation was Levenberg-Marquardt, as illustrated in **Figure 7.9.** The R value for the Levenberg-Marquardt back-propagation method was 0.994 for training, 0.998 for validation, 0.999 during testing, and 0.990 for all phases. This suggests that the network's predicted output is substantially identical to the results of the laboratory analyses, as seen by the lower MSE. Because it had the minimum MSE value, this approach provided the best structure. This indicates that the Levenberg-Marquardt algorithm is appropriate for training the ANN Toolbox to predict Cr (VI) removal.

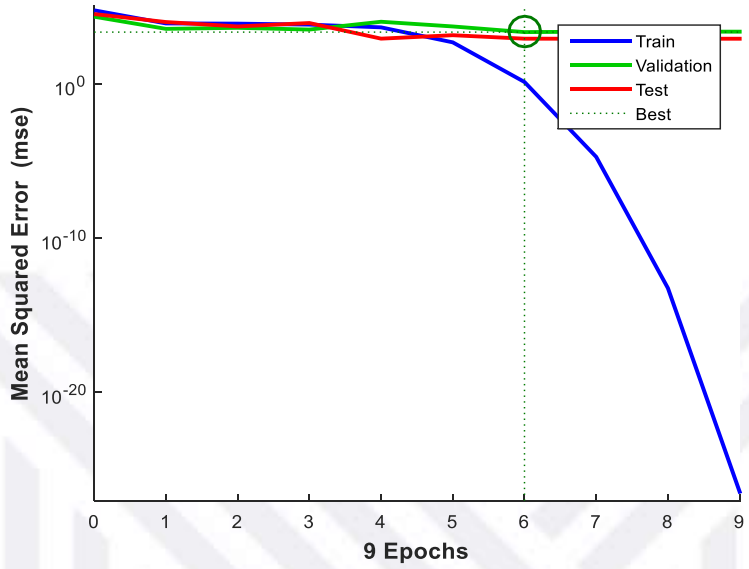

Figure 7.9: performance of the Levenberg-Marquardt algorithm

The ideal network architecture has to be developed to identify the best performance of the NN structure. The hidden neurons were calculated based on the training and prediction sets' minimal MSE values. Using the Levenberg-Marquardt back-propagation algorithm, the minimal value of MSE. The ideal structure: in the input layer (4 neurons), in the hidden layer (6 neurons), and the output layer 1neuron). The network was discovered to be completely linked. This indicates that every neuron for each layer was connected to every neuron in the next layer, as seen in Figure 10.

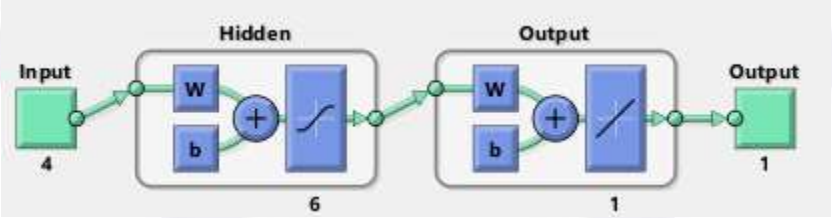

Figure 7. 10: ANN architecture of the adsorption process

7.3.2.6 Modeling of Adaptive neuro-fuzzy inference system

The ANFIS model was generated as a five-layered neural network using the fuzzy inference system approach. Fig. 11 shows the ANFIS structure, with the input parameters (time, dosage, pH, and concentration) and the response or outcome variable (adsorption capacity) represented by the first and last layers, respectively. The model is related to first-order Sugeno inference systems in the second layer, which filters input parameters

by transforming them into membership values using membership functions (MF). In the third layer, logical rules were used to determine the model's output. Output membership functions were used in the fourth layer to defuzzify the inferential output to actual output values. Only one node was used in the fifth layer, and the overall output was the total of all input variables(Dolatabadi *et al.*, 2018; Zhu & Wang, 2022).

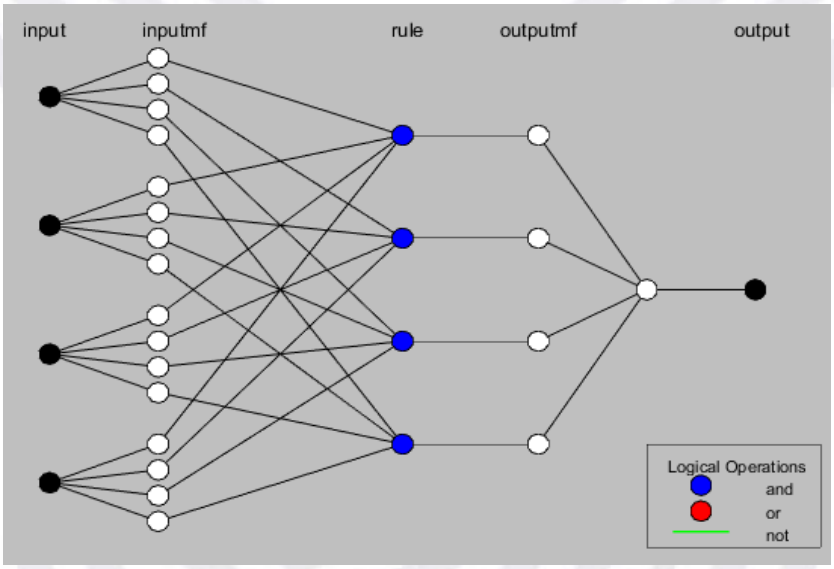

Figure 7. 11: Architecture of ANFIS model.

The ANFIS model's data prediction capacity has been shown in **Figure 7. 12** (rule viewer). For illustration, the absorption capacity for pH 6.14, the concentration of 175 mg/L, contact time of 100 min, a dosage of 12.5 is about 350 mg/g. The model can predict all output data for every input parameter within the data range. Simultaneously, the inputs for a certainly needed output may be selected using the rule viewer. As a consequence, the model can predict output data (absorption capacity) based on input variables (Cr (VI) concentration, time, pH, and adsorbent dose) and vice versa.

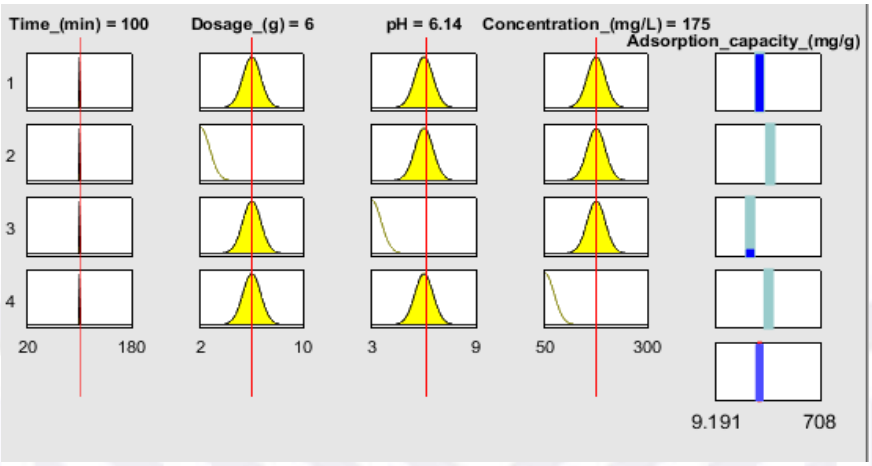

Figure 7.12: Rule viewer of the ANFIS model

Three membership functions (MFs) were assigned to each element in the input layer to create the FIS (**Figure 7.13**). The ANFIS modelling yielded a high correlation value of 0.997, indicating that the fuzzy inference system network can predict the absorption of Cr (VI) from solution using modified cellulose nanocrystals. The main advantage of ANFIS is that it reduces error by augmenting fuzzy controllers with self-learning abilities(Arora & Keshari, 2021). After seven epochs of training, the fuzzy network exhibited an error magnitude of 0.0005, confirming its suitability for modelling the removal of Cr (VI). Also, the low MSDE value obtained indicated that the training procedure was not over-fitting and that the ANFIS model can accurately predict the removal of Cr (VI) using adsorption.

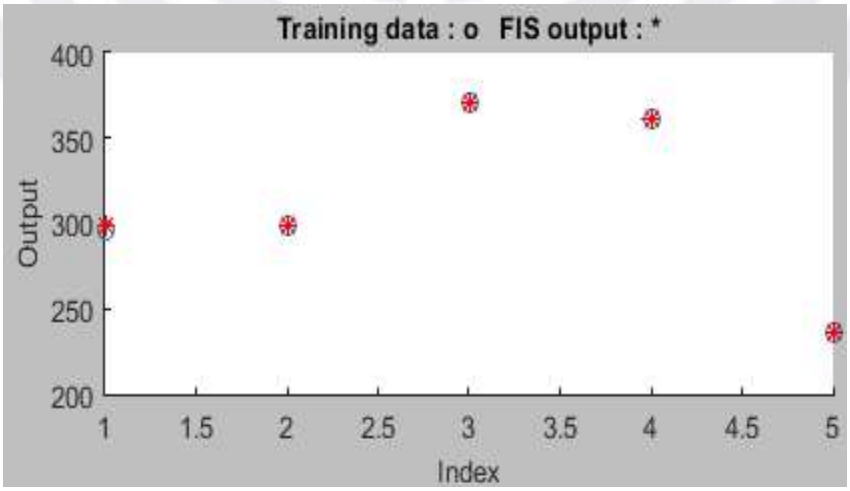

Figure 7.13: Predicted and Experimental data of the adsorption for ANFIS

7.3.3 Error analysis

To further investigate the model accuracy abilities, five statistical error functions were used to the model predictions with the data reported in **Table 7.7**. The RMSE, ARE, SSE, MSE, and MPSD error functions evaluated each model. The low values of these error functions proved the model's potential to predict. According to the findings, all of the models displayed insignificant error levels. The value of R^2 must be more than 0.8, according to (Zhu & Wang, 2022), to establish a satisfactory correlation between predicted and experimental data. To see if the R^2 was overstated, the adjusted-R2 was used, and the findings were satisfactory for all models, demonstrating their significance. ACCORDING TO THE STATISTICAL FINDINGS, the RSM and ANN were the least successful models in predicting the accuracy of the Cr (VI) adsorption process. The ANFIS model performed slightly better than the other two. The current study results were consistent with those of (Ahmad *et al.*, 2021; Dolatabadi *et al.*, 2018; Ehteram *et al.*, 2021), all reported that ANFIS was more reliable than ANN in predicting efficiency.

Table 7.7: Statistical error analysis of RSM, ANN, and ANFIS.

Error function	RSM	ANN	ANFIS
RMSE	0.011	0.008	0.007
ARE	0.471	0.375	0.371
SSE	0.023	0.022	0.017
MSE	0.021	0.020	0.015
MPSD	0.012	0.008	0.008
R2	0.989	0.990	0.997

7.3.4 Mechanistic modeling

Table 7.8 summarizes the model constants. The plotting of ln(1- A) versus time was used to assess the liquid film diffusion model. The rate factor was determined using the linear plot's gradient. The R^2 of 0.987 indicates that Cr (VI) removal was controlled by film diffusion, with time and proportionate approach to optimum being linearly related (Samadi *et al.*, 2014). The plotting of qt versus $t^{0.5}$ explored the Weber and Morris model. With increasing duration of solute uptake, the rate constant Kd dropped. The intra-particle diffusion model has a correlation value of 0.954. Since C is not equal to 0, intra-

particle diffusion was not the only limiting rate in the Cr (VI) removal. This is most likely due to a discrepancy in the Cr (VI) starting and ending mass transfer rates from solution to adsorbent (Race *et al.*, 2016).

The Dumwald-Wagner model was investigated using a plotting of $\log(1-A^2)$ as a function of time t. The Dumwald-Wagner model is an intra-particle model. The high fit of the near-linear fit indicated that pore dispersion was implicated in the removal mechanism. The line did not pass through the origin, showing that Cr (VI) adsorption onto adsorbent pores was not the only limiting rate step. These studies revealed that, while pore diffusion had a part in the adsorption process, the film dispersion was the most important rate-controlling phase of the adsorption process(Kabuba & Banza, 2020a). The Bangham method was assessed using the $\log (C_a/C_a - q_{max})$ as a factor of log t. The model was used to analyse if pore dispersion was the only rate-limiting step in the adsorption mechanism. A good model fit was shown by a high correlation value of 0.979, indicating that pore dispersion was involved in the adsorption mechanism. The lack of a perfect linear line in the double logarithm plot suggests that pore dispersion was not the primary rate-limiting phase(Al-Qahtani, 2016).

Table 7.8: mechanistic model parameters for Cr (VI) removal

Model	parameter	value
Liquid film diffusion	K_d (min^{-1})	0.085
	R^2	0.987
Weber and Morris	K_X ($mg/g.min^{0.5}$)	0.359
	C_X (mg/g)	12.25
	R^2	0.954
Dumwald-Wagner	K_{DW}	0.082
	R^2	0.932
Bangham	K_b	0.687
	β	0.210
	R^2	0.969

7.3.5 Comparison with other adsorbents

Table 7.9 compares the current study's findings with previously published chromium removal data from other researchers who used commonly accessible and low-cost adsorbents. The adsorption capacities of the adsorbents were employed as the basis. The present study's results were similar to those of other adsorbents. It has a reasonably high adsorption capacity of 350 mg/g. The findings determined that the cellulose nanocrystals and sodium alginate were low-cost and efficient adsorbents for removing Cr (VI)from an aqueous solution.

Table 7.9: Comparison of Cr(VI) removal with different adsorbents

Adsorbent	Adsorption cap. (mg/g)	Reference
Chitosan	154.88	Race *et al.*, 2016)
Nanocellulose	147.30	Ahmad *et al.*, 2021
Carbon nanotube	180.56	Ayoola *et al.*, 2020
Cellulose nanocrystals and sodium alginate	350.01	**This study**

7.4. CONCLUSION

The feasibility of RSM, ANN, and ANFIS prediction abilities in modelling Cr (VI) removal using cellulose nanocrystals and sodium alginate was investigated in this work. The presence of OH and COOH implies that Alginate was successfully coated with cellulose nanocrystals. The consistency in the disintegration of Alginate and cellulose nanocrystals demonstrated the effective synthesis process by FTIR and TGA analyses. Increased contact time in the adsorbent dose and concentration led to higher adsorption capacity but increases in pH above 6 resulted in lower adsorption capacity. The interaction impacts of the process variables were identified and their optimal conditions. Initial pH of 6, contact time of 100 min, initial Cr (VI) concentration of 175 mg/L, sorbent dose of 6 mg, and adsorption capacity of 350.23 mg/g were determined to be the optimal condition. ANN approaches with the BP algorithm are described and compared to experimental data. The Levenberg Marquardts Algorithm (4-6-1) with a tangent sigmoid transfer function at the hidden layer and a linear transfer function at the output layer produced the minimum MSE. In predicting EBT uptake, ANFIS, ANN, and RSM were shown to be accurate and similar. According to five statistical error indicators, the ANFIS model has the greatest

quality and reliability, followed by the ANN and RSM model. According to mechanistic modelling, the most likely rate-controlling phase of the removal process was film diffusion. The cellulose nanocrystals were shown to be a suitable adsorbent in this investigation.

7.5 REFERENCES

Ahmad, M., Rashid, K., Tariq, Z., & Ju, M. 2021. Utilization of a novel artificial intelligence technique (ANFIS) to predict the compressive strength of fly ash-based geopolymer. *Constr. Build. Mater.* 301:124251.

Ahmadi, S., Mesbah, M., Igwegbe, C.A., Ezeliora, C.D., Osagie, C., Khan, N.A., Dotto, G.L., Salari, M., & Dehghani, M.H. 2021. Sono electro-chemical synthesis of LaFeO3nanoparticles for the removal of fluoride: Optimization and modeling using RSM, ANN and GA tools. *J. Environ. Chem. Eng.* 9(4):105320.

Al-Qahtani, K.M. 2016. Water purification using different waste fruit cortexes for the removal of heavy metals. *J. Taibah Univ. Sci. Taibah University*. 10(5):700–708.

Arora, S. & Keshari, A.K. 2021. ANFIS-ARIMA modelling for scheming re-aeration of hydrologically altered rivers. *J. Hydrol.* 601:126635.

Ayoola, A.A., Hymore, F.K., Omonhinmin, C.A., Babalola, P.O., Fayomi, O.S.I., Olawole, O.C., Olawepo, A. V., & Babalola, A. 2020. Response surface methodology and artificial neural network analysis of crude palm kernel oil biodiesel production. *Chem. Data Collect.* 28.

Banza, M. & Rutto, H. 2022. Toxic / Hazardous Substances and Environmental Engineering Continuous fixed-bed column study and adsorption modeling removal of Ni , Cu , Zn and Cd ions from synthetic acid mine drainage by nanocomposite cellulose hydrogel. *J. Environ. Sci. Heal. Part A*. 0(0):1–13.

Cojocaru, C., Humelnicu, A.C., Pascariu, P., & Samoila, P. 2021. Artificial neural network and molecular modeling for assessing the adsorption performance of a hybrid alginate-based magsorbent. *J. Mol. Liq.* 337:116406.

David Samuel, O., Adekojo Waheed, M., Taheri-Garavand, A., Verma, T.N., Dairo, O.U., Bolaji, B.O., & Afzal, A. 2021. Prandtl number of optimum biodiesel from food industrial waste oil and diesel fuel blend for diesel engine. *Fuel*. 285:119049.

Derikvandi, H. & Nezamzadeh-Ejhieh, A. 2017. Designing of experiments for evaluating the interactions of influencing factors on the photocatalytic activity of NiS and SnS2: Focus on coupling, supporting and nanoparticles. *J. Colloid Interface Sci.* 490:628–641.

Dolatabadi, M., Mehrabpour, M., Esfandyari, M., Alidadi, H., & Davoudi, M. 2018. Modeling of simultaneous adsorption of dye and metal ion by sawdust from aqueous solution using of ANN and ANFIS. *Chemom. Intell. Lab. Syst.* 181:72–78.

Ehteram, M., Yenn Teo, F., Najah Ahmed, A., Dashti Latif, S., Feng Huang, Y., Abozweita, O., Al-Ansari, N., & El-Shafie, A. 2021.Performance improvement for infiltration rate prediction using hybridized Adaptive Neuro-Fuzzy Inferences System (ANFIS) with optimization algorithms. *Ain Shams Eng. J. Faculty of Engineering, Ain Shams University*.

12(2):1665–1676.

Fosso-kankeu, E. 2018. hybridized technique applied for AMD treatment. *Phys. Chem. Earth*. 105:170–176.

Franco, D.S.P., Duarte, F.A., Salau, N.P.G., & Dotto, G.L. 2020. Analysis of indium (III) adsorption from leachates of LCD screens using artificial neural networks (ANN) and adaptive neuro-fuzzy inference systems (ANIFS). *J. Hazard. Mater.* 384:121137.

Hu, Z., Mohamed, A., & Yu, D. 2018. International Journal of Biological Macromolecules Fabrication of carboxylated cellulose nanocrystal / sodium alginate hydrogel beads for adsorption of Pb (II) from aqueous solution. 108:149–157.

Igberase, E., Osifo, P., & Ofomaja, A. 2017. Chromium (VI) ion adsorption by grafted cross-linked chitosan beads in aqueous solution – a mathematical and statistical modeling study. *Environ. Technol.* 00(0):1–11.

Ihsanullah, Abbas, A., Al-Amer, A.M., Laoui, T., Al-Marri, M.J., Nasser, M.S., Khraisheh, M., & Atieh, M.A. 2016. Heavy metal removal from aqueous solution by advanced carbon nanotubes: Critical review of adsorption applications. *Sep. Purif. Technol.* 157:141–161.

Kaboorani, A. & Riedl, B. 2015. Surface modification of cellulose nanocrystals (CNC) by a cationic surfactant. *Ind. Crop. Prod.* 65:45–55.

Kabuba, J. & Banza, M. 2020a. Modification of clinoptilolite with dialkylphosphinic acid for the selective removal of cobalt (II) and nickel (II) from hydrometallurgical effluent. :1–11.

Kabuba, J. & Banza, M. 2020b. Results in Engineering Ion-exchange process for the removal of Ni (II) and Co (II) from wastewater using modi fi ed clinoptilolite : Modeling by response surface methodology and arti fi cial neural network. *Results Eng.* 8:100189.

Kabuba, J. & Banza, M. 2020c. Results in Engineering Ion-exchange process for the removal of Ni (II) and Co (II) from wastewater using modi fi ed clinoptilolite : Modeling by response surface methodology and arti fi cial neural network. *Results Eng.* 8:100189.

Kargarzadeh, H., Sheltami, R.M., Ahmad, I., Abdullah, I., & Dufresne, A. 2015. Cellulose nanocrystal : A promising toughening agent for unsaturated polyester nanocomposite. *Polymer (Guildf).* 56:346–357.

Leudjo Taka, A., Klink, M.J., Yangkou Mbianda, X., & Naidoo, E.B. 2021. Chitosan nanocomposites for water treatment by fixed-bed continuous flow column adsorption: A review. *Carbohydr. Polym.* 255:117398.

Nordin, A.H., Wong, S., Ngadi, N., Zainol, M.M., Aien, N., Abd, F., & Nabgan, W. 2021. Journal of Environmental Chemical Engineering Surface functionalization of cellulose with polyethyleneimine and magnetic nanoparticles for efficient removal of anionic dye in wastewater. *J. Environ. Chem. Eng.* 9(1):104639.

Nosuhi, M. & Nezamzadeh-Ejhieh, A. 2017. High catalytic activity of Fe(II)-clinoptilolite nanoparticales for indirect voltammetric determination of dichromate: Experimental design by response surface methodology (RSM). *Electrochim. Acta*. 223:47–62.

Onu, C.E., Nwabanne, J.T., Ohale, P.E., & Asadu, C.O. 2021. Comparative analysis of RSM,

ANN and ANFIS and the mechanistic modeling in eriochrome black-T dye adsorption using modified clay. *South African J. Chem. Eng.* 36:24–42.

Race, M., Marotta, R., Fabbricino, M., Pirozzi, F., Andreozzi, R., Cortese, L., & Giudicianni, P. 2016. Copper and zinc removal from contaminated soils through soil washing process using ethylenediaminedisuccinic acid as a chelating agent: A modeling investigation. *J. Environ. Chem. Eng.* 4(3):2878–2891.

Samadi, M.T., Zarrabi, M., Sepehr, M.N., Ramhormozi, S.M., Azizian, S., & Amrane, A. 2014. Removal of fluoride ions by ion exchange resin: Kinetic and equilibrium studies. *Environ. Eng. Manag. J.* 13(1):205–214.

Samuel, O.D. & Okwu, M.O. 2019. Comparison of Response Surface Methodology (RSM) and Artificial Neural Network (ANN) in modelling of waste coconut oil ethyl esters production. *Energy Sources, Part A Recover. Util. Environ. Eff.* 41(9):1049–1061.

Samuel, O.D., Okwu, M.O., Oyejide, O.J., Taghinezhad, E., Afzal, A., & Kaveh, M. 2020. Optimizing biodiesel production from abundant waste oils through empirical method and grey wolf optimizer. *Fuel*. 281:118701.

Shahnaz, T., S., M.M.F., V.C., P., & Narayanasamy, S. 2020. Surface modification of nanocellulose using polypyrrole for the adsorptive removal of Congo red dye and chromium in binary mixture. *Int. J. Biol. Macromol.* 151:322–332.

Shojaeiarani, J., Bajwa, D., & Shirzadifar, A. 2019. A review on cellulose nanocrystals as promising biocompounds for the synthesis of nanocomposite hydrogels. *Carbohydr. Polym.* 216:247–259.

Souza, P.R., Dotto, G.L., & Salau, N.P.G. 2018. Artificial neural network (ANN) and adaptive neuro-fuzzy interference system (ANFIS) modelling for nickel adsorption onto agro-wastes and commercial activated carbon. *J. Environ. Chem. Eng.* 6(6):7152–7160.

Thomas, D., Latha, M.S., & Thomas, K.K. 2018. Journal of Drug Delivery Science and Technology Synthesis and in vitro evaluation of alginate-cellulose nanocrystal hybrid nanoparticles for the controlled oral delivery of rifampicin. *J. Drug Deliv. Sci. Technol.* 46:392–399.

Zaman, H.A., Sharif, S., Kim, D.W., Idris, M.H., Suhaimi, M.A., & Tumurkhuyag, Z. 2017. Machinability of Cobalt-based and Cobalt Chromium Molybdenum Alloys - A Review. *Procedia Manuf.* 11:563–570.

Zhu, X. & Wang, N. 2022. Hairpin RNA genetic algorithm based ANFIS for modeling overhead cranes. *Mech. Syst. Signal Process.* 165:108326.

Zolgharnein, J., Dalvand, K., Rastgordani, M., & Zolgharnein, P. 2017. Adsorptive removal of phosphate using nano cobalt hydroxide as a sorbent from aqueous solution; multivariate optimization and adsorption characterization. *J. Alloys Compd.* 725:1006–1017.

CHAPTER EIGHT

CONTINUOUS FIXED-BED COLUMN STUDY AND ADSORPTION MODELLING REMOVAL OF Ni^{2+}, Cu^{2+}, Zn^{2+} and Cd^{2+} IONS FROM SYNTHETIC ACID MINE DRAINAGE BY NANOCOMPOSITE CELLULOSE HYDROGEL

ABSTRACT

Several authors have published research on the adsorption of harmful metal ions in batch mode using modified hydrogel in the literature; for large-scale operations, packed bed column studies are undertaken to produce data directly relevant to practical wastewater treatment. Due to their capacity to hold water in their porous structures, hydrogels are the most commonly used 3D polymer mesh materials for environmental remediation. The application of potential hydrogel for the absorption of Cu^{2+}, Ni^{2+}, Zn^{2+}, and Cd^{2+} ions from an aqueous solution in a packed bed adsorption column was studied in this work. The adsorbent was studied using Fourier transform infrared spectroscopy (FTIR), scanning electron microscope (SEM), X-ray diffraction (XRD), and the thermal thermogravimetric analyzer (TGA). The influence of breakthrough factors such as bed height, influent concentration and the feed flow rate was assessed. Bed Depth Service Time, Thomas, and Yoon-Nelson models were used to fit the experimental data. With an increase in bed height, removal efficiency, breakthrough, and exhaustion time rose but declined with increased flow rate and influent concentration. Bette performance was observed at a bed height of 25 cm, an influent metal ion concentration of 10 mg/l, and a flow velocity of 10 ml/min. In this work, the mathematical models used to describe experimental data were adequate.

Keywords: Hydrogel, metal ions adsorption, modelling, fixed-bed column, kinetic parameters, acid mine drainage.

8.1. INTRODUCTION

Water is a limited resource that is both crucial and needed on a global scale. As a result, having access to clean drinking water should be a top priority for maintaining a high quality of life. Water contamination and purification are presently vital issues for governments, researchers, and industries in this respect. Cu, Cd, Pb, Zn, and Ni are among the most hazardous metals. Researchers have shown that these metals have a detrimental impact on humans, aquatic life, plants, and the ecosystem. Acid mine drainage (AMD) is an acidic waste containing different ions such as copper, lead, chromium, zinc, cadmium, and nickel, which may contaminate surface and ground watercourses, jeopardizing the lives of humans, wildlife, plants, and aquatic species if particular care is not provided(Fosso-kankeu, 2018). Chemical precipitation, membrane separation, ion exchange, electrolysis, and adsorption have all been recommended in the past for the treatment of AMD. Other researchers have shown that these techniques are efficient at remediation, but they have drawbacks that limit their use. Although the techniques listed here can be used to treat AMD, it is essential to remember that the best adsorbent or treatment technique depends primarily on the initial concentration, capital investment, operational cost, and the AMD components of the treatment process environmental impact(Fosso-kankeu, 2018).

The most pressing problems are finding an effective technology for removing contaminants to ultra-low levels and purifying and recycling wastewater(Leudjo Taka *et al.*, 2021; Mengesha *et al.*, 2021; Musamba *et al.*, 2018). Because of its simplicity, cheap cost, and ability to recycle sorbent nanoparticles, the nanotechnology adsorption technique is now preferred as a promising method for water purification(Kargarzadeh *et al.*, 2015; Lei *et al.*, 2019; Shojaeiarani *et al.*, 2019). On the other hand, adsorption techniques are not fully used due to several constraints, including the surface area of adsorbent materials. The surface area of adsorbent materials has been proven to be the most critical element determining their adsorption capacity and effectiveness(Wu *et al.*, 2016). Adsorption technology is a purification process that uses adsorbents' high adsorption ability to remove pollutants. Large specific surface area, strong adsorption performance, remarkable selectivity, excellent chemical and thermal stability, low availability and reusability are the most common qualities needed of an effective adsorbent. The physical and chemical characteristics of contaminants, pH levels, coexisting substances,

temperature, contact time, and adsorbent dose all influence adsorption. Adsorption processes include ion exchange, electrostatic adsorption, hydrogen bonding, particular surface bonding, and chelation, as previously described.

The growing need for novel nanomaterials with large surface area, high adsorption capacity, high regeneration efficiency, and good antibacterial characteristics has gotten a lot of attention in this regard. Polymer nanocomposites are now regarded as promising nanomaterials with potential uses in wastewater treatment and other fields such as renewable energy, electronics, textile pharmaceuticals, and medicine. Macromolecular nanomaterials have a wide range of applications(Grishkewich *et al.*, 2017; Lei *et al.*, 2019; Yang *et al.*, 2016). Bio-based natural polymer nano-composites are the most preferred polymer nanocomposites because biopolymer matrices like cellulose nanocrystal and chitosan are ecologically friendly, biodegradable, biocompatible, easily accessible, easy to scale up, and inexpensive. Furthermore, when nanostructured elements were introduced into the polymer matrix, the performance of bio-based natural polymer nanocomposites was significantly improved. The inclusion of these nanostructured materials into the polymer matrix also aids in managing nanoparticle form, structural morphology, and size and the improvement of pollutant removal efficiency from wastewater(Abdelraof *et al.*, 2019; Raval *et al.*, 2016; Yang *et al.*, 2016).

Hydrogels are the most cost-effective materials for wastewater treatment. Because of its durability, density, and cost-effectiveness, the polymer material is frequently utilized. After numerous recoveries and reuses, the adsorption limits do not diminish. Hydrogels make sense in eliminating all pollutants from wastewater because of their high adsorption limit, mechanical strength, biodegradability, and reusability in various pH ranges. The amount of polar hydrophilic groups such as –OH, –COOH, $-CONH_2$, and $-SO_3H$ contribute to hydrogels' hydrophilic structure. These groups affix themselves to polymer chains in response to various stimuli. The reusability of hydrogel has been discovered to be highly exceptional. Previous research has demonstrated that adsorption-desorption cycle hydrogels with up to five adsorption cycles produce satisfactory outcomes(Gokmen *et al.*, 2021). Reusability is the essential feature of an adsorbent in wastewater treatment applications. The adsorption capacity of a substrate may be enhanced by increasing the surface characteristics in adsorption applications where hazardous particles are immobilized on a substrate and leads to better dispersion. Depending on the level of

exposure and interaction between the pollutants and the adsorbent, particles trapped on the substrate via adsorption play an active role in most situations. Wastewater and polluted water are treated using a wide range of physical and chemical treatment techniques. Pore size differences or chemical affinity between the substrate and the contaminant are employed in the processes(Nordin *et al.*, 2021).

Two of the most abundant renewable biomaterials suitable for this investigation are cellulose derived from waste papers and chitosan derived from the breakdown of chitin derived from crab exoskeletons(Danial *et al.*, 2015; Teramoto, 2019). Researchers have been studying the usage of cellulose and chitosan in different composite materials for decades. Both biopolymers have b-glycosidic connections and a very similar structure. Chitosan's flexibility allows it to be easily changed to modify or improve its characteristics in adsorption experiments; cross-linking chitosan renders it insoluble in acidic environments by tying the chains together with strong covalent bonds, enhancing its mechanical and chemical durability(Cheng *et al.*, 2019).

In this study, the cellulose nanocrystals hydrogel was used to evaluate the absorption efficiency of harmful metal ions from synthetic AMD. In industries, hazardous metal ion adsorption is usually done in a packed column to provide a continuous operation and high removal rate. Packed bed adsorption columns are simple, easy to use, can be regenerated, and do not produce sludge(Leudjo Taka *et al.*, 2021). How to anticipate the breakthrough curve in packed column adsorption is a critical problem since it provides critical information for designing a packed column adsorption system. However, mathematical modelling of a breakthrough curve is simple and requires minimal equipment, and it has attracted attention in recent years(Hernández-Hernández *et al.*, 2017). A variety of models have been employed to analyse and forecast breakthrough curves in a packed column system. The adsorption of metal ions from aqueous solution onto cellulose hydrogel in a packed column adsorption system was described in this work using the Bed Depth Service Time (BDST), Yoon–Nelson, and Thomas models.

8.2. EXPERIMENTAL

8.2.1 materials and equipment

All of the chemicals were analytical grade and were used without additional purification. The (CNCs) cellulose nanocrystals were extracted from millet husk via acid hydrolysis, Sigma-Aldrich supplied the gelatin powder from porcine skin (≥98%), Ethylenediaminetetraacetic acid(≥99%) as the cross-linking agent, the hydrochloric acid (>99%), acetic acid (>99%), and sodium hydroxide (>99%). A pH meter (Hanna HI 8421) was used to adjust the pH of the solution. The Ultima 888 water distiller was used in the school laboratory to produce distilled water. The amount of metal ions adsorbed was determined using Induced coupled plasma (ICP, Icap7000).

8.2.2 Synthetic AMD preparation

$CuSO_4 5H_2O$, $NiSO_4 6H2O$, $CdCl_2 H2O$, and $Zn(NO_3)_2 6H2O$ were used to make the stock solution. These initial 10–40 mg/L concentrations were obtained by diluting the stock solution further with distilled water. The pH of 4 was maintained in the synthetic AMD.

8.2.3 Hydrogel preparation

A cellulose and gelatin-based hydrogel composite was successfully generated due to the interaction between cellulose nanocrystals and gelatin. After thoroughly dissolving 10 wt% gelatin in hot water (45°C), a 50 ml cellulose nanocrystals suspension was put into the gelatin solution. Ethylenediaminetetraacetic acid 0.1M was used as a crosslinking agent. The reaction was carried out for 12 hours at 55 °C. After that, the hydrogel composite was washed with deionized water to remove any unreacted compounds before being stored at 4 degrees Celsius. The hydrogel's chemical 3D structure is shown in **Figure 8.1**

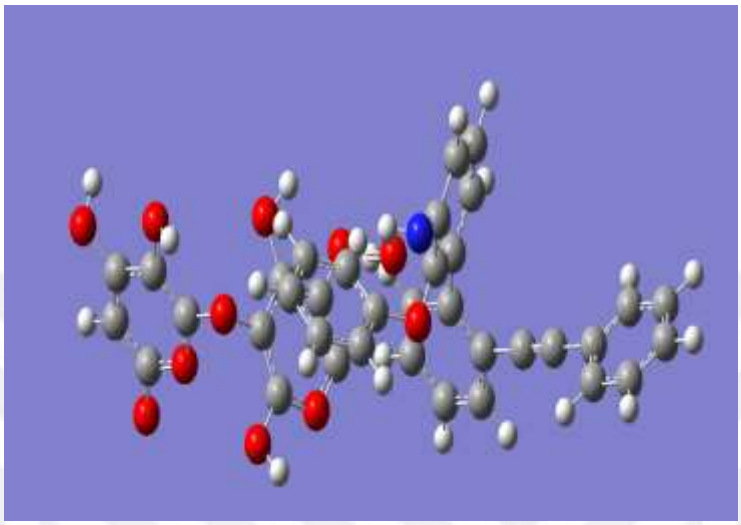

Figure 8.1: the proposed structure of the hydrogel(3D). Black, red, blue, and light black denote carbon, oxygen, nitrate, and hydrogen atoms.

8.2.4 Hydrogel characterization

The functional groups found in the hydrogel and the structural changes that resulted were investigated using Fourier transform infrared spectroscopy (FTIR, Varian 7000). Scanning electron microscopy was used to evaluate the morphological surface (SEM, Philips XL30FEG). The qualitative and quantitative investigations were carried out using X-ray diffraction (XRD, Philips expert 0993). The thermal stability was determined using a thermal thermogravimetric analyzer (TGA, NETZSCH5 209F3). The pore volume and surface area were determined using Brunauer-Emmett-teller (BET).

8.2.5 Adsorption studies in the continuous system

A clear polystyrene cylindrical column with an internal diameter of 4 cm and a depth of 40 cm was used for the continuous flow adsorption experiment. To confine the hydrogel inside the cylindrical column, a 100-meter plastic mesh was installed at both ends. To achieve the desired bed depth, the hydrogel was packed into the column. With the help of a peristaltic pump, the influent starting concentration was pushed upward through the column. The experiment was conducted at 30°C, with samples taken every 30 minutes and analyzed using an inductively coupled plasma (ICP). The experimental set-up is depicted in schematic form in Figure 2. The breakthrough time was defined as when the effluent concentration reached 10% of the original metal ion concentration. In comparison, the

exhaustion time was defined as when the effluent concentration reached 90% of the initial metal ion concentration.

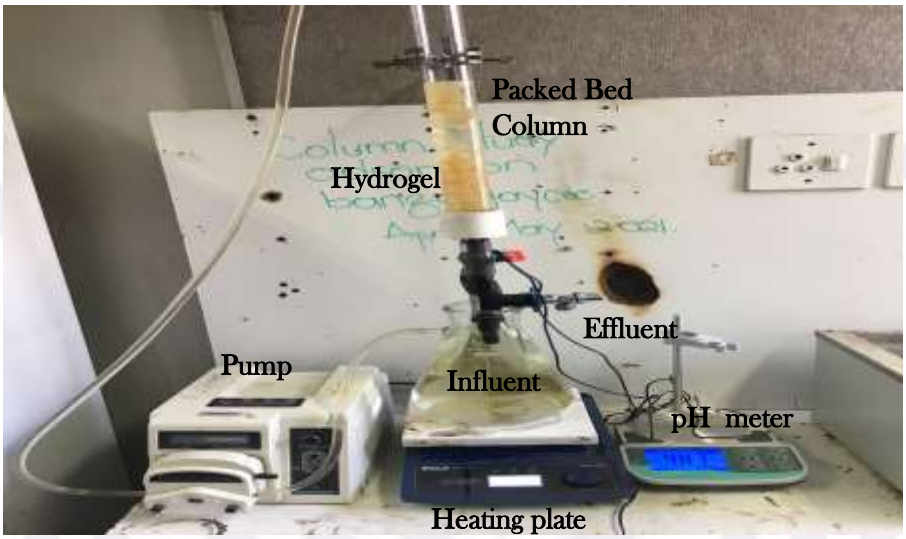

Figure 8.2: fixed packed bed column set-up diagram

8.2.5.1 Effect of bed height

Synthesized AMD was pumped upwards via columns with different bed heights of 10, 17, and 25 cm, corresponding to 20, 30, and 40 g of the hydrogel, respectively. The concentration of metal ions in the influent at 10 mg/L and the pH of the solution at 4. The metal ions concentration were determined using an ICP spectrophotometer after samples were taken at 30-minute intervals.

8.2.5.2 Effect of flow rate

Flow rates of 10, 20, and 30 ml/min were used to pump the influent solution through the columns in an up-flow direction. The bed height and pH level were kept constant at 40 g and 4, respectively. Metal ions concentrations were determined using an ICP spectrophotometer after samples were taken every 30 minutes.

8.2.5.3 Effect of Concentration

Metal ion concentrations of 10, 20 and 50 mg/L were used to examine the influence of influent concentration. Pumping the influent concentration upwards at a steady 10 ml/min was used. We kept the pH level of the solution at 4. After every 30 minutes, samples were taken and analyzed with an ICP spectrophotometer.

The amount of metal ions adsorbed onto hydrogel (q_e) was determined using the Equation below.

$$q_e = \frac{Q_{v.C_o}.Tb}{mH} \quad (8.1)$$

where Q_V (mL/min) denotes the flow rate, C_o (mg/L) denotes the concentration at equilibrium, Tb (min) denotes the breakthrough time, and mH (g) is the mass of the hydrogel.

The total removal percentage of metal ions as reported by Nisrine et al.(Khadhri *et al.*, 2019) is given in Equation (7.2)

$$\text{Removal percentage} = \frac{(C_O - C_e)}{C_O} \times 100 \quad (8.2)$$

where Co and Ce(mg/L) are the influent and effluent concentrations, respectively.

Bed height (Z), breakthrough time (Tb), and exhaustion time (Te) are used to calculate the critical bed height (Zm), which is also known as the height of the mass transfer zone is shown in Equation (7.3)(Khadhri *et al.*, 2019)

$$Z_m = Z\left(1 - \frac{T_b}{T_e}\right) \quad (8.3)$$

The volume of the effluent V_{ef} (mL) is given by Equation (7.4)

$$V_{ef} = Q_v Te \quad (8.4)$$

where Qv (mL/min) is the flow rate, and Te (min) is the exhaustion time

8.3. BREAKTHROUGH CURVE ANALYSIS

8.3.1. Bed Depth Service Time model

Hudchins adapted the Bohard-Adams model and produced the BDST model on the premise that intra-particle diffusion and external mass transfer resistance are irrelevant. The adsorbate is immediately adsorbed on the adsorbent surface(Hernández-Hernández *et al.*, 2017). This model is presented in Equation (7.5)

$$Tb = \frac{N_o}{C_o U_o} Z - \frac{1}{K_b C_o} Ln\left(\frac{C_o}{C} - 1\right) \quad (8.5)$$

where No (mg/L)represents the saturation concentration, Co(mg/L) represents the influent concentration, C (mg/L)represents the effluent concentration, K_b(L/mg/min) represents the adsorption rate constant, Z(cm) represents the bed depth. Tb represents the packed column breakthrough time concerning these conditions (min).

8.3.2. Yoon-Nelson model

This model is quite basic and does not require any particular information on the pollutant, the adsorbing medium, or the physical adsorption parameters. As a result, it's frequently used to define breakthrough curves, and it's based on the premise that the rate of reduction in each molecule's probability of adsorption is proportional to the chance of breakthrough(Igberase *et al.*, 2018). This model is expressed in Equation (7.6)

$$Ln\left(\frac{C}{C_o - C}\right) = k_Y t - \tau k_Y \quad (8.6)$$

t (min) is the breakthrough time, and k_Y (min^{-1}) is the rate constant. The k_Y and t are determined by the slope and intercept of the linear plot of Ln(C/(Co C)) vs t.

8.3.3. Thomas model

The Thomas model is one of the most widely used nowadays, and it is used to calculate a pollutant's rate constant and maximum adsorption capacity in a packed column. This model can predict the breakthrough curve, which helps build a packed column for the adsorption process. This model is based on the Langmuir kinetics of adsorption-desorption with no axial dispersion assumption and considers the rate of driving force to be a second-order reversible reaction(Pawar *et al.*, 2016). The Thomas model is expressed in Equation (7.7)

$$Ln\left(\frac{C_o}{C} - 1\right) = \frac{k_T q_e m_H}{Q_t} - K_T C_o t \quad (8.7)$$

where Qt is the flow rate, m is the quantity of adsorbent in the column, qe is the adsorption capacity, and kT is the Thomas rate constant. The slope and intercept of the straight-line plot of Ln(Co/C-1) vs t may be used to get the values of kT and qe, respectively.

8.3.4 Error analysis

The Residual root means square error (RMSE) and Marquardt's percent standard deviation (MPSD) tests of statistical analysis were used to show the adequacy of the

Thomas and Yoon–Nelson models. These are nonlinear approaches for comparing experimental data with model-predicted data, as shown in Equations (7.8) and (7.9).

$$\text{RMSE} = \sqrt{\sum_{i=1}^{n}\left(\frac{\left(q_{e(E)}-q_{e(P)}\right)^2}{N}\right)} \tag{8.8}$$

$$\text{MPSD} = 100\sqrt{\frac{1}{N-P}\sum_{i=1}^{n}\left(\frac{\left(q_{e(E)}-q_{e(P)}\right)^2}{q_{e(P)}}\right)i} \tag{8.9}$$

where N is the number of observations, P is the number of model parameters, and qe(E) and qe(P) are experimental and predicted uptake rates, respectively.

8.4. RESULTS AND DISCUSSION

8.4.1. Effect of bed height

The mass of adsorbent used in a packed bed column has a significant impact on metal ion adsorption. According to Leudjo et al. (Leudjo Taka *et al.*, 2021), a greater bed height broadens the mass transfer zone. **Figure 8.3** shows breakthrough curves for the adsorption of Cu^{2+}, Ni^{2+}, Zn^{2+}, and Cd^{2+} ions at varied bed heights of 10, 17, and 25 cm, which corresponds to 20, 30, and 40 g of hydrogel, respectively, and a constant flow rates and influent concentrations of 10 mL/min and 10 mg/L, respectively. The curves are usually in the shape of an 'S'. Breakthrough time, depletion time, and removal efficiency were found to be functions of bed height, as they appeared to increase with increased bed height. The breakthrough and depletion times correspond to effluent concentrations of 0.1 and 0.9 times influent metal ions, respectively. **Table 8.1** shows the effects of bed height on the parameters of column adsorption. For Cu^{2+}, Ni^{2+}, Cd^{2+}, and Zn^{2+}ions, an increase in bed height from 10 to 17 cm resulted in a corresponding rise in breakthrough time from 260 to 620 min, 230 to 520 min, 180 to 420 min, 150 to 360 min, respectively. As a result, raising the bed height resulted in a longer exhaustion time for Cu^{2+}, Ni^{2+}, Cd^{2+}, and Zn^{2+}ions, ranging from 390 to 680 minutes, 330 to 620 minutes, 300 to 570 minutes, 200 to 520 minutes, respectively. The axial dispersion phenomenon predominated in mass transfer at a lower bed height, reducing metal ion diffusion to the point where there was insufficient time for metal ions to diffuse onto hydrogel. However, increasing the bed height increased removal efficiency, breakthrough, and exhaustion time due to the availability of active sites, as more sites are produced as bed height is increased. This finding is significant because it

implies that a greater bed height should be considered for dependable bed performance(Pérez-morales & Sánchez-galván, 2019).

Table 8.1: Packed bed parameters of Cu^{2+}, Ni^{2+}, Cd^{2+}, and Zn^{2+}ions onto the hydrogel at variying bed heights (10, 17 and 25 cm)

Bed height (cm)	Metal ions	TB (min)	TE (min)	Vef (mL)	Zm (cm)	Removal efficiency (%)
10	Cu^{2+}	280	400	5600	6.47	95.24±1.46
	Ni^{2+}	250	430	3600	7.51	92.23± 1.30
	Cd^{2+}	190	340	4700	8.56	91.37±1.40
	Zn^{2+}	160	310	4300	10.52	88.96±1.02
17	Cu^{2+}	430	280	5200	6.28	98.16±1.88
	Ni^{2+}	370	550	4900	8.27	96.34±2.63
	Cd^{2+}	340	520	4300	8.80	94.78±1.97
	Zn^{2+}	280	430	3400	9.99	92.53±1.11
25	Cu^{2+}	640	840	3900	8.75	99.42±0.12
	Ni^{2+}	520	640	3700	6.87	99.23±1.46
	Cd^{2+}	430	580	3200	9.24	99.36±0.89
	Zn^{2+}	370	520	3000	10.30	98.94±0.48

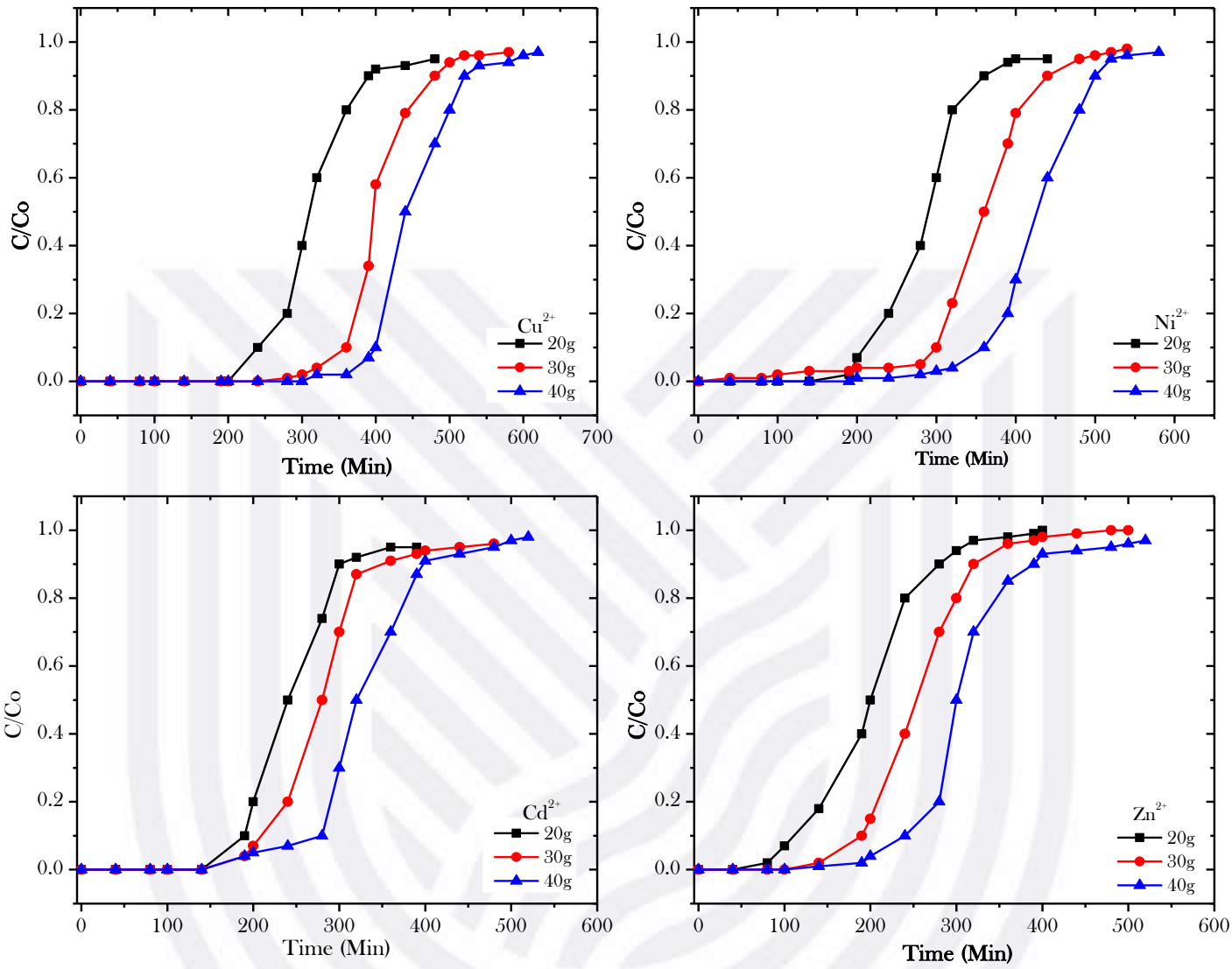

Figure 8.3: Effect of bed height on the breakthrough curves for Cu^{2+}, Ni^{2+}, Cd^{2+}, and Zn^{2+}ions adsorption onto hydrogel at pH of 4, the Flow rate of 10 mL/min, the influent concentration of 10 mg/L.

8.4.2. Effect of flow rate

The flow rate is critical in a continuous flow adsorption column because it regulates the retention period during which the adsorbate encounters the adsorbent surface. Furthermore, in most sectors, heavy metal ion removal from wastewater is accomplished in a continuous mode. As a result, studying the influence of flow rate becomes a vital criterion(Pérez-morales & Sánchez-galván, 2019). **Figure 8.4** depicts the breakthrough curves for Cu^{2+}, Ni^{2+}, Cd^{2+}, and Zn^{2+}ions adsorption onto hydrogel at varied flow rates of 10, 20, and 30 mL/min with constant starting concentration and a bed height of 10 mg/L and 17 cm, respectively. The trend in the plot of the ratio of effluent to influent concentration

versus time appears to follow a typical 'S' shape. As shown in **Table 8.2**, the metal ion flow rate significantly influences the bed column characteristics.

Consequently, the breakthrough time, depletion time and removal efficiency were reduced while the flow rate increased. For Cu^{2+}, Ni^{2+}, Cd^{2+}, and Zn^{2+}ions, the breakthrough time ranges from 440 to 320 min, 360 to 180 min, 330 to 150 min and 270 to 120 min at a flow rate of 10 - 20 mL/min. Exhaustion periods for the Cu^{2+}, Ni^{2+}, Cd^{2+}, and Zn^{2+} were similarly reduced from 560 to 430 minutes, 515 to 340 minutes, 490 to 310 minutes, and 450 to 260 minutes, respectively. Due to a lack of holding time for metal ions to interact with hydrogel. To further explain this result, at a lower flow rate, metal ions have a longer residence time in the column, giving them more time to access the active sites of the hydrogel. At a flow rate of 10 mL/min, the bed provided satisfactory results. However, increasing the flow rate leads to a poorer metal ion distribution in the column, resulting in inadequate time for the metal ions to diffuse into the adsorption sites(Pérez-morales & Sánchez-galván, 2019). At a greater flow rate, this resulted in an earlier breakthrough time(Lin *et al.*, 2021).

Table 8.2: Packed bed parameters of Cu^{2+}, Ni^{2+}, Cd^{2+}, and Zn^{2+}ions onto the hydrogel at a varying flow rate (10, 20 and 30 mL/min)

Flow rate (mL/min)	Metal ions	TB (min)	TE (min)	Vef (mL)	Zm (cm)	Removal efficiency (%)
10	Cu^{2+}	430	580	5600	9.30	99.01±0.32
	Ni^{2+}	370	520	3600	11.20	99.20±0.11
	Cd^{2+}	340	490	4700	11.48	98.75±0.43
	Zn^{2+}	280	460	4300	14.91	98.57±0.09
20	Cu^{2+}	370	520	5200	10.39	96.78±1.87
	Ni^{2+}	340	490	4900	10.98	94.89±2.14
	Cd^{2+}	240	430	4300	14.98	94.75±1.69
	Zn^{2+}	180	360	3400	16.87	93.89±1.98
30	Cu^{2+}	360	450	3900	8.75	89.72±4.89
	Ni^{2+}	190	370	3700	17.87	87.36±3.59
	Cd^{2+}	340	310	3200	17.83	85.67±4.56
	Zn^{2+}	120	280	3000	19.46	84.69±3.68

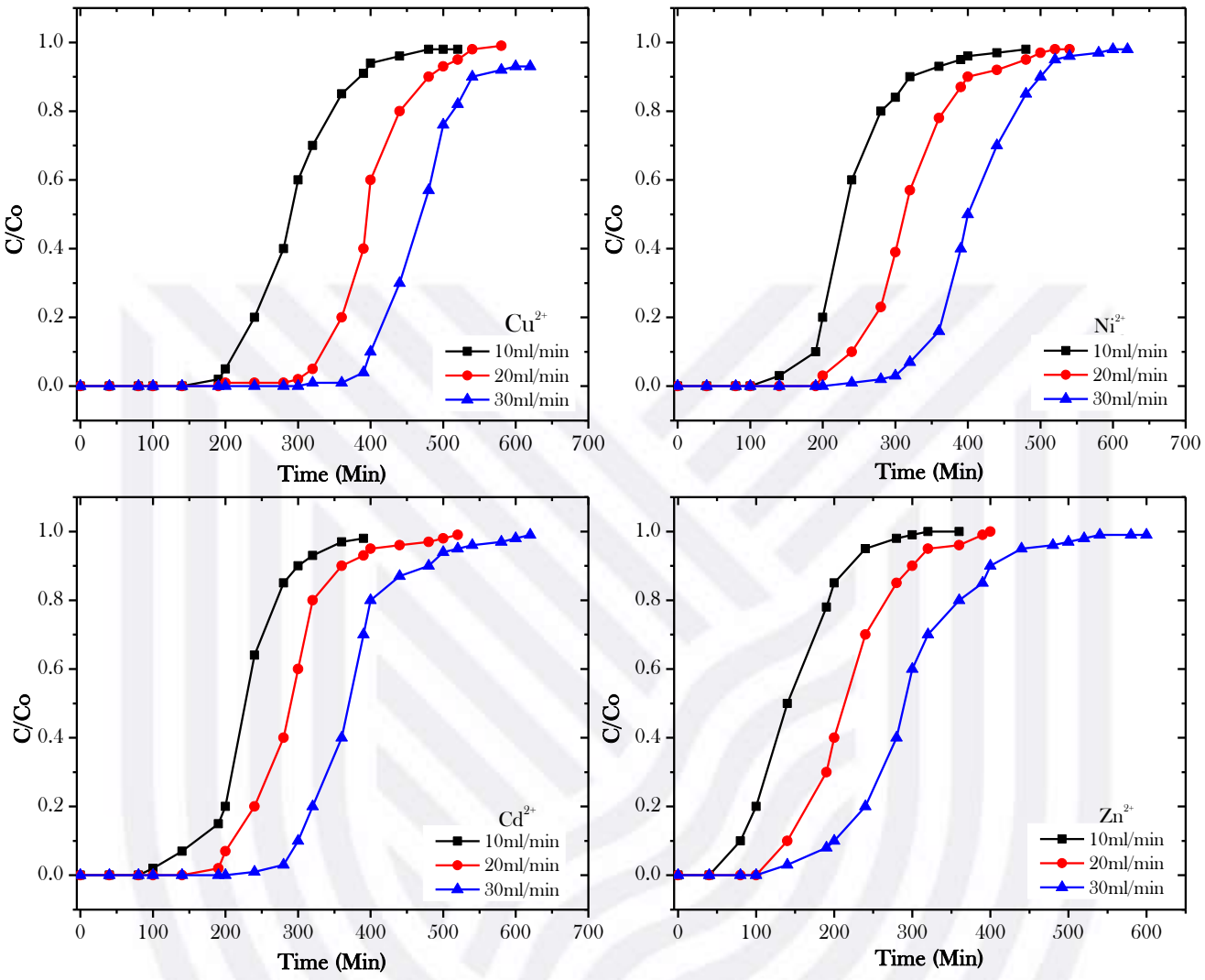

Figure 8.4: Effect of flow rate on the breakthrough curves for Cu^{2+}, Ni^{2+}, Cd^{2+}, and Zn^{2+}ions adsorption onto hydrogel at pH of 4, the concentration of 10 mg/L, bed height of 25 cm.

8.4.3. Effect of influent concentration

The breakthrough curves of Cu^{2+}, Ni^{2+}, Cd^{2+}, and Zn^{2+}ions adsorption onto the hydrogel at the various influent concentration (10- 50 mg/L) and bed height and constant flow rate of 25 cm and 10 mL/min, respectively was depicted in **Figure 8.5.** As influent concentration increased, removal efficiency, breakthrough time, and exhaustion time all decreased. **Table 8.3** shows the column adsorption parameters for different metal concentrations. Cu^{2+}, Ni^{2+}, Cd^{2+}, and Zn^{2+}ions have breakthrough durations ranging from 430 to 260 minutes, 350 to 220 minutes, 340 to 220 minutes, and 280 to 190 minutes, respectively, at influent concentrations of 10–50 mg/L. The exhaustion time took the following trend: Cu^{2+}(580–380 min), Ni^{2+}(510–360 min), Cd^{2+}(480–330 min) and Zn^{2+}(420–300 min). Other

researchers have observed this pattern in column adsorption studies(Leudjo Taka *et al.*, 2021; Lin *et al.*, 2021; Nahrul Hayawin *et al.*, 2020). However, the low mobility of metal ion molecules at lower influent metal ion concentrations required a longer retention time for the sites accessible for adsorption in the hydrogel to be depleted. Furthermore, when the influent concentration increases, the slope of the breakthrough curves accelerates, and the breakthrough time shortens. This observation can be explained by the fact that more adsorption sites were coated by metal ions, causing the hydrogel to become saturated faster.

Table 8.3: Packed bed parameters of Cu^{2+}, Ni^{2+}, Cd^{2+}, and Zn^{2+}ions onto the hydrogel at a varying concentration (10, 20 and 50 mg/L)

Influent concentration (mg/L)	Metal ions	TB (min)	TE (min)	Vef (mL)	Zm (cm)	Removal efficiency (%)
10	Cu^{2+}	430	580	5600	15.37	99.86±0.02
	Ni^{2+}	370	370	3600	11.30	99.00±0.31
	Cd^{2+}	340	480	4700	10.95	98.97±0.28
	Zn^{2+}	280	420	4300	13.47	98.85±1.32
20	Cu^{2+}	370	520	5200	10.35	97.98±1.48
	Ni^{2+}	310	480	4900	13.14	97.85±1.57
	Cd^{2+}	280	430	4300	12.75	96.35±1.78
	Zn^{2+}	220	340	3400	12.52	96.20±1.43
50	Cu^{2+}	280	400	3900	10.79	96.98±2.01
	Ni^{2+}	220	370	3700	14.67	96.34±2.12
	Cd^{2+}	220	340	3200	12.75	94.68±1.78
	Zn^{2+}	190	310	3000	14.13	94.25±1.46

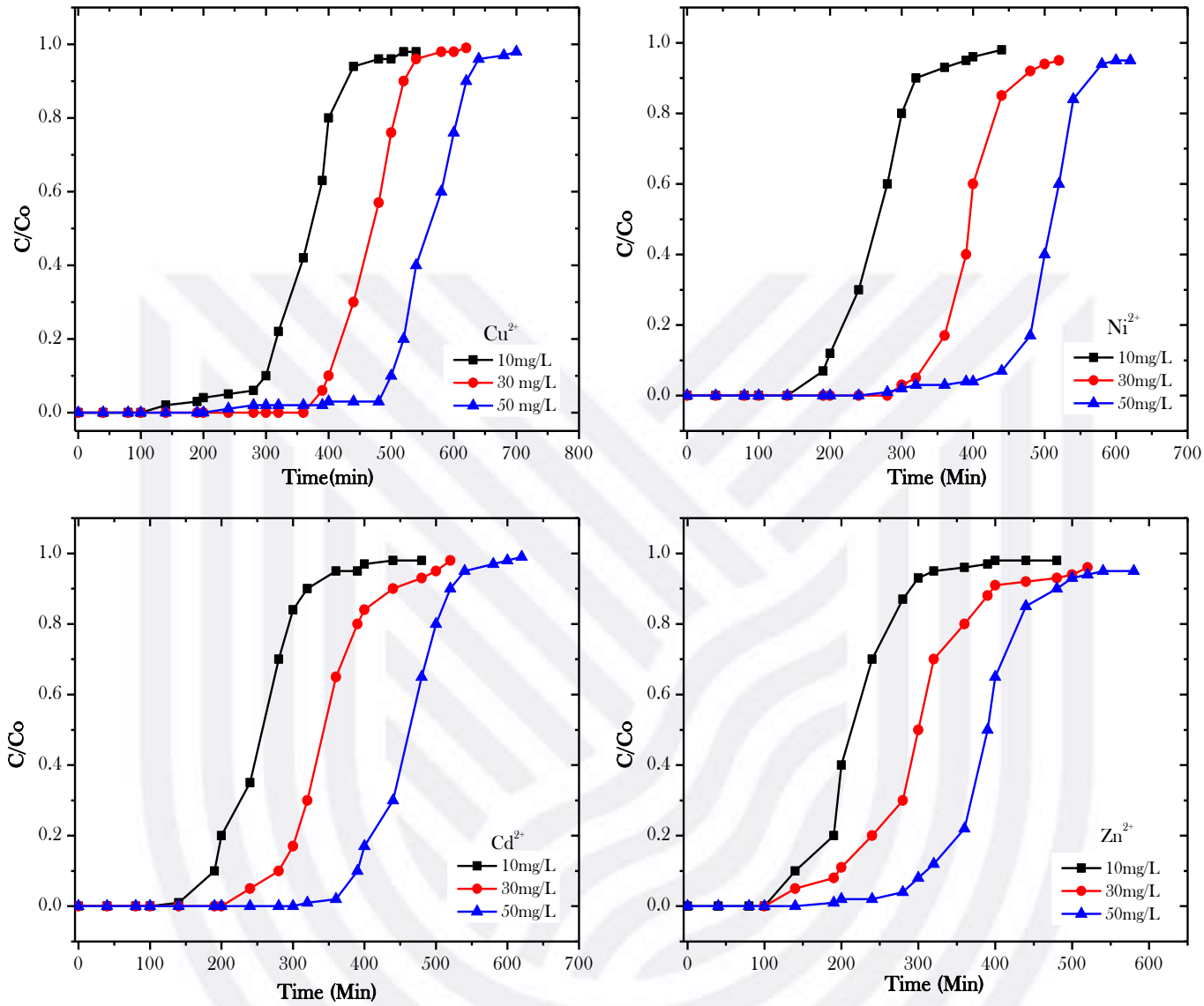

Figure 8.5: Effect of influent concentration on the breakthrough curves for Cu^{2+}, Ni^{2+}, Cd^{2+}, and Zn^{2+}ions adsorption onto hydrogel at pH of 4, the Flow rate of 10 mL/min, bed height of 25 cm.

8.4.5. Mathematical modelling approach

The prediction of column breakthrough, which determines the working lifespan of the bed, is the most relevant parameter in the design of a packed bed column adsorption system(Leudjo Taka *et al.*, 2021). **Table 8.4** shows the BDST parameters obtained from experimental data at different bed heights of 10, 17, and 25 cm, with constant flow rates and influent concentrations of 10 mL/min and 10 mg/L, respectively, while **Table 8.5** shows the parameters of the Thomas and Yoon- Nelson models obtained from experimental data when, influent metal ions concentration, flow rate and bed height were

varied. At a bed height of 25 cm, an influent concentration of 10 mg/L and a flow rate of 10 mL/min favourable breakthrough and removal efficiency values were observed. The correlation coefficient (R^2) was one of the indicators of the best fit model since the higher the R^2, the better the model fit. **Figure 8.6** shows the BDST model's plot of service time (min) vs bed depth (cm). The R^2 values (0.99) indicate that the BDST model adequately explains the experimental column adsorption data. As a result, Table 5 shows the values of the Thomas model's parameters and the R^2, RMSE, and MPSD values. The high R^2 values >0.940 indicate that the model is more applicable and nicely fits the experimental column data. The experimental q_e values were in good agreement with the predicted q_e values, indicating that the Yoon-Nelson model may be used to describe column data. The RMSE showed that the inaccuracies were minor, suggesting that the models were fitted correctly. The low MPSD values (0.00–6.53) and RMSE (0.00-0.29) indicate that the experimental and projected data are exceptionally well-aligned. External or internal diffusion is not the limiting step, according to the excellent fit of the Yoon-nelson model to experimental data (Azad *et al.*, 2021). Furthermore, the values of the Thomas model's parameters were established (**Table 8.5**). The form of a breakthrough curve is described by the rate constant K_T(Fallah & Taghizadeh, 2020). It was observed that as bed height raised, K_T values dropped, and as flow rate and influent metal ions concentration increased, K_T values increased. The R^2 values were ≥0.941, indicating that the fitting line of ln (C/(Co C)) versus time had a complete confidence level. The 50% breakthrough time (t) dropped as the flow rate, and influent metal concentration increased but increased as the bed height expanded. The experimental and predicted t values looked comparable, and the RMSE indicated that the differences between the experimental and predicted data were negligible.

The low MPSD values (0.00–6.53) and RMSE (0.00-0.29) further suggest that this model may be used to explain the adsorption of the metal ions in question onto the hydrogel in a column adsorption system. **Table 8.6** compares the adsorption capacity of various adsorbents found in the literature to that reported in this investigation. This study suggests that hydrogel might be suitable for removing harmful metal ions due to its high adoption capacity.

Table 8.4: BDST model parameters (pH=4, flow rate=10 mL/min, initial concentration= 10 mg/L and temperature= 27°C)

Metal ions	N_o(mg/L)	Ka(mg^{-1}/min)	R^2
Cu^{2+}	170.86±7.56	0.0043	0.992
Ni^{2+}	162.47±6.48	0.0024	0.997
Cd^{2+}	158.64±5.65	0.0075	0.991
Zn^{2+}	150.53±5.23	0.0013	0.994

Table 8.5. Thomas and Yoon-nelson model parameters for adsorption of Cu^{2+}, Ni^{2+}, Cd^{2+}, and Zn^{2+}ions onto hydrogel at varying bed heights 10, 17, 25 cm; flow rate 10, 20, 30 mL/min and concentration 10, 20, 50 mg/L.

		Thomas model						Yoon-Nelson model					
Bed height (cm)	Metal ions	K_T (mg/min)	q_e(E) (mg/g)	q_e(P) (mg/g)	RMSE	MPSD	R^2	K_Y (min^{-1})	T(E) (min)	T(P) (min)	RMSE	MPSD	R^2
10	Cu^{2+}	0.0042	460	449.50	0.018	1.49	0.952	0.023	360	361.52	0.011	1.45	0.992
	Ni^{2+}	0.0027	410	411.02	0.014	2.00	0.964	0.047	341	340.28	0.012	1.65	0.997
	Cd^{2+}	0.0060	310	309.76	0.018	2.20	0.945	0.041	257	255.00	0.010	2.00	0.996
	Zn^{2+}	0.0025	260	259.32	0.028	3.21	0.978	0.038	227	225.12	0.012	2.93	0.998
17	Cu^{2+}	0.0013	535	536.04	0.019	2.16	0.988	0.048	467	466.56	0.010	2.89	0.995
	Ni^{2+}	0.0034	460	461.08	0.028	1.91	0.992	0.075	432	432.09	0.009	0.07	0.990
	Cd^{2+}	0.0031	422	423.17	0.019	4.62	0.982	0.067	404	405.85	0.012	3.69	0.992
	Zn^{2+}	0.0039	347	348.89	0.021	6.53	0.994	0.054	347	345.99	0.017	5.63	0.989
25	Cu^{2+}	0.0013	640	640.98	0.019	3.69	0.953	0.083	678	678.54	0.008	2.06	0.994
	Ni^{2+}	0.0033	520	521.21	0.021	5.21	0.964	0.085	556	554.39	0.013	4.52	0.987
	Cd^{2+}	0.0031	430	431.23	0.032	5.30	0.937	0.089	480	480.23	0.007	5.23	0.999
	Zn^{2+}	0.0039	380	379.52	0.028	4.85	0.952	0.074	435	433.98	0.019	6.23	0.956
Flow rate (mL/min)	Cu^{2+}	0.0012	440	441.08	0.019	3.51	0.948	0.098	450	448.69	0.021	3.40	0.957
10	Ni^{2+}	0.0033	380	379.82	0.025	2.05	0.945	0.097	421	419.36	0.020	1.58	0.995
	Cd^{2+}	0.0031	350	351.28	0.017	5.48	0.973	0.088	387	385.29	0.019	4.32	0.982
	Zn^{2+}	0.0037	290	292.09	0.015	6.21	0.937	0.095	179	180.65	0.012	4.32	0.992
20	Cu^{2+}	0.0046	550	548.29	0.024	2.87	0.987	0.088	260	262.00	0.025	4.28	0.993
	Ni^{2+}	0.0024	492	494.02	0.018	3.08	0.947	0.083	420	419.99	0.017	2.71	0.988
	Cd^{2+}	0.0065	370	371.59	0.017	4.08	0.985	0.086	360	361.28	0.012	3.02	0.992
	Zn^{2+}	0.0014	290	292.27	0.015	2.98	0.988	0.072	300	300.56	0.009	2.31	0.996
30	Cu^{2+}	0.0044	670	669.97	0.016	3.00	0.942	0.083	451	450.09	0.012	1.45	0.999
	Ni^{2+}	0.0024	380	379.88	0.032	2.85	0.945	0.077	240	242.39	0.028	4.35	0.997
	Cd^{2+}	0.0075	320	319.97	0.019	3.87	0.912	0.072	205	206.00	0.017	3.75	0.968
	Zn^{2+}	0.0014	270	269.85	0.018	3.08	0.963	0.070	326	325.85	0.015	2.53	0.998
Influent concentration(mg/L)	Cu^{2+}	0.0097	430	429.39	0.021	2.89	0.972	0.094	495	496.38	0.010	2.00	0.958
10	Ni^{2+}	0.0092	380	382.00	0.025	4.87	0.987	0.098	432	434.29	0.029	5.23	0.963
	Cd^{2+}	0.0088	340	341.27	0.018	5.21	0.965	0.096	400	401.23	0.012	2.36	0.996
	Zn^{2+}	0.085	290	290.07	0.016	2.00	0.948	0.080	365	366.08	0.011	1.23	0.982
20	Cu^{2+}	0.0096	740	739.58	0.021	2.21	0.996	0.092	406	405.69	0.020	1.98	0.965
	Ni^{2+}	0.0087	620	621.29	0.029	2.98	0.947	0.088	348	347.89	0.029	2.69	0.988
	Cd^{2+}	0.0085	570	571.96	0.029	3.28	0.958	0.089	290	287.99	0.022	3.54	0.992
	Zn^{2+}	0.0070	460	458.69	0.035	3.08	0.987	0.087	220	219.22	0.017	2.28	0.965
50	Cu^{2+}	0.0092	820	821.32	0.022	2.69	0.945	0.083	345	344.72	0.019	2.01	0.960
	Ni^{2+}	0.0082	670	670.85	0.09	1.08	0.917	0.072	285	285.00	0.000	0.000	0.945
	Cd^{2+}	0.0075	640	641.20	0.019	4.29	0.944	0.074	258	255.65	0.020	5.69	0.948
	Zn^{2+}	0.0072	590	592.38	0.020	5.29	0.956	0.069	225	223.72	0.018	4.36	0.989

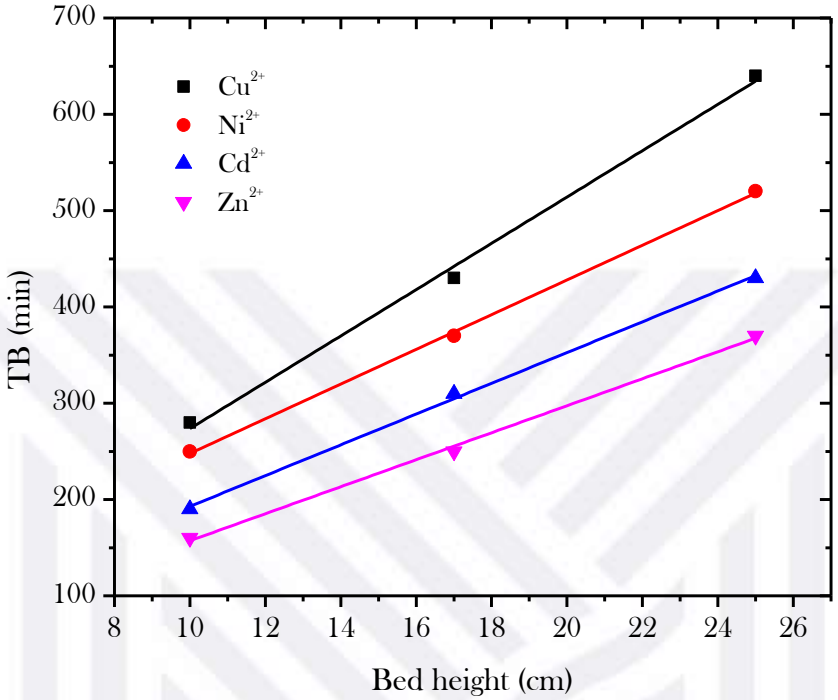

Figure 8.6: The BDST model's plot of service time (min) vs bed depth (cm)

Table 8.6: comparison of adsorption capacity of the hydrogel onto Cu^{2+}, Ni^{2+}, Cd^{2+}, and Zn^{2+}ions with other adsorbents

Metal ions	Adsorbent	Conc (mg/L)	Height (cm)	Q (ml/min)	q (mg/g)	reference
Cu^{2+}	Citrus peel	300	10	15	116.01	(Igberase *et al.*, 2018)
	clinoptilolites	300	30	10	127.29	(Igberase *et al.*, 2018)
	Hydrogel	**50**	**10**	**10**	**640.58**	**This study**
Ni^{2+}	Tea waste	200	-	10	11.13	(Kabuba & Banza, 2020)
	Ch-b	20	10	10	10.29	(Igberase *et al.*, 2018)
	Hydrogel	**50**	**10**	**10**	**411.02**	**This study**
Cd^{2+}	Sunflower waste	300	4.5	2	51.3	(Musamba *et al.*, 2018)
	GXXB	30	100	10	540	(Igberase *et al.*, 2018)
	Hydrogel	**50**	**10**	**10**	**809.76**	**This study**
Zn^{2+}	Pongamia oil	100	-	10	49.68	(Igberase *et al.*, 2018)
	GXXB	30	100	10	270	(Igberase *et al.*, 2018)
	Hydrogel	**50**	**10**	**10**	**292.09**	**This study**

8.4.6. characterization of the hydrogel

The FTIR spectrum of CNCs, gelatin and hydrogel is presented in **Figure 8.7**. The CNCs have exhibited distinctive bands at 3000 and 3550 cm^{-1} that reflect the significant elongation vibration band of the O-H function. The C-H elongation vibration band is found at 2980 cm^{-1}, corroborating the deformation band at 1500 cm^{-1}. The vibration shear of CH_2 may be seen in the region about 1450 cm^{-1}. With the distinctive band of about 880 cm^{-1} corresponding to the C-H of the aldehyde group as a support, this peak is characteristic of the carboxyl (C=O) elongation vibration band (1700 cm^{-1}). The C-O-C function is considered to be responsible for the peak at about 1000 cm^{-1}.

When looking at the gelatin FTIR spectra, the characteristic peaks around 2950 cm^{-1} are visible for the vibration band of O-H, 1600 cm^{-1} for amide I, 1000 cm^{-1} for the vibration band amide II, 750 cm^{-1} for the vibration band of amide III. The elongation vibration of C=O identifies the amide (I). A contributing band of C-N elongation vibration and C-C-N out-of-plane deformation was added. The amide (II) is identified by the C-N elongation vibration band and the out-of-plane vibration band. Finally, elongation and deformation vibration peak combinations from C-N and N-H describe an amide (III).

Comparing the values of several bands reveals a bathochromic effect in conjunction with a reduction in the intensity of some bands in the hydrogel spectrum. The band at 3300 cm^{-1} is associated with O-H vibration; the bands emerge between 1800 and 1000 cm^{-1}. These are caused by crosslinking-induced stretching vibration. The band at 1550 cm^{-1} is associated with the vibration C=N; overlapping absorption bands between 1150 cm-1 and 1350 cm^{-1} occur from the bending vibration mode of C-H groups coupling with the C-O and C-N absorption bands. For the hydrogel, they discovered a modest consistency of the carboxyl band at 1000 cm^{-1}, except for the strength of the band, which was reduced.

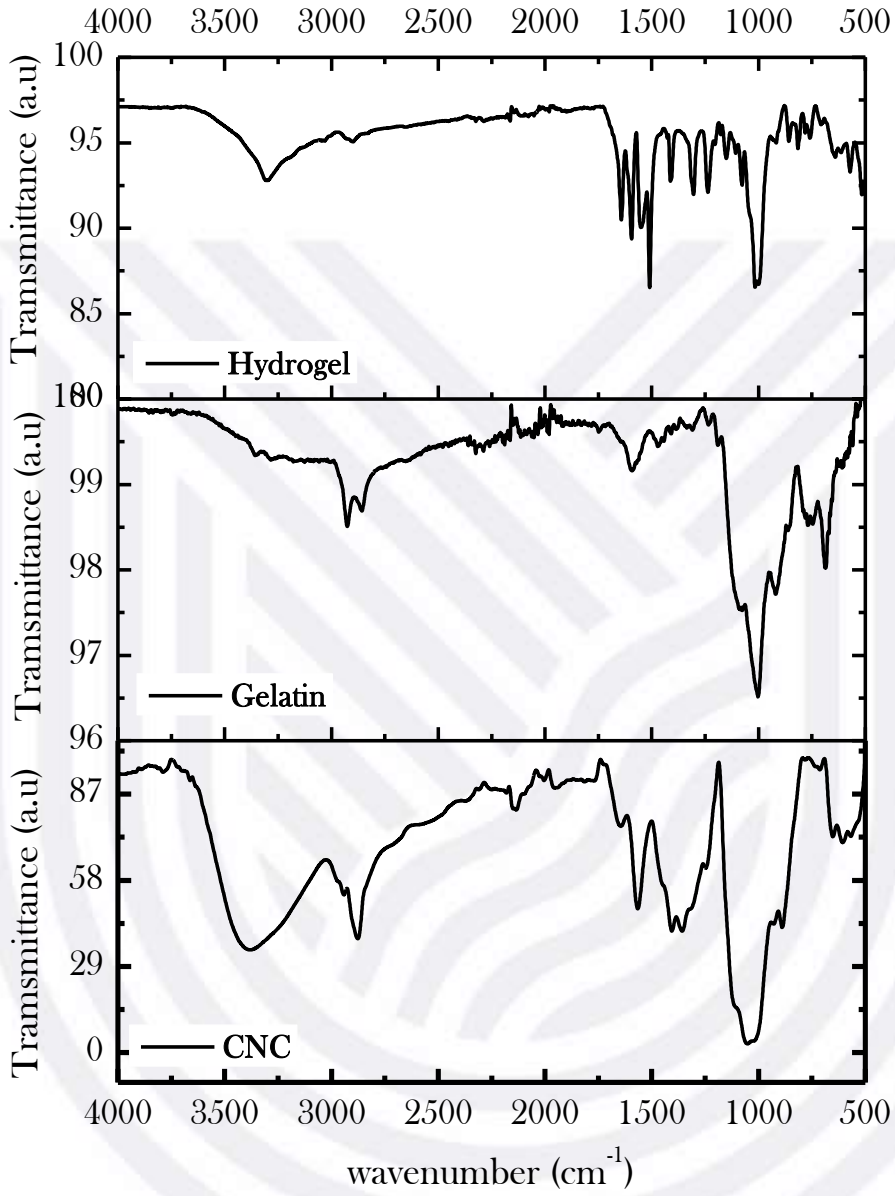

Figure 8.7: FTIR spectrum CNCs, Gelatin, and Hydrogel

A change in the morphological structure of the Gelatin, Cellulose and Hydrogel was seen using a scanning electron microscope (SEM). **Figure 8.8 (a), (b) and (c)** show the results. The presence of open pores is used to describe porosity, and these pores are linked to many properties, such as a porous structure's permeability and surface area. The SEM picture shows larger, more irregularly shaped particles in **Figure 8.8 (a) and (b)**. **Figure 8.8 (c)** depicts the cavities of various shapes and sizes and bigger holes between the particles, which will aid the solution's ability to permeate through. As a result of its high

porosity, the material is well-suited for the adsorption of heavy metal ions. The inclusion of these granules enhances the composite's surface area, making it better suited for metal ion adsorption. After crosslinking, a noticeable shift in surface morphology may be seen. Pore diffusion occurs during the process because of the increased contact with the adsorption surface provided by small pores and holes on the surface.

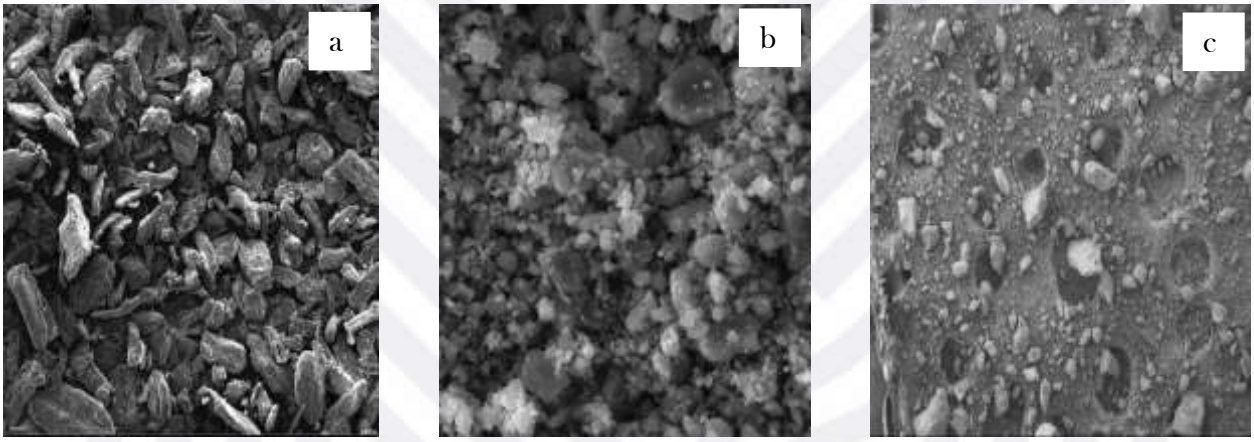

Figure 8.8: SEM image (a) CNCs, (b) Gelatin, (c) Hydrogel

TGA is used to examine the thermal characteristics of cellulose, gelatin, and hydrogel, as shown in **Figure 8.9.** Because the initial peak in the TGA curves is due to the evaporation of bound water and has nothing to do with the thermal breakdown temperature of polymers, we did not investigate it. The breakdown of the polypeptide chain in the second stage of gelatin film began at 280°C and reached a maximum mass loss at 400 °C. The breakage of glucoside linkages and hydrogen bonds during demethoxylation and dehydration was seen from 288 °C to 500°C in the second stage of CNCs. The second stage of the TGA curve of the hydrogel began at 285 °C and ended at 490 °C, which was lower than CNCs(Gu *et al.*, 2020). As a result, the introduction of gelatin appears to have broken the hydrogen bond and crystalline structure of cellulose, which is supported by XRD data.

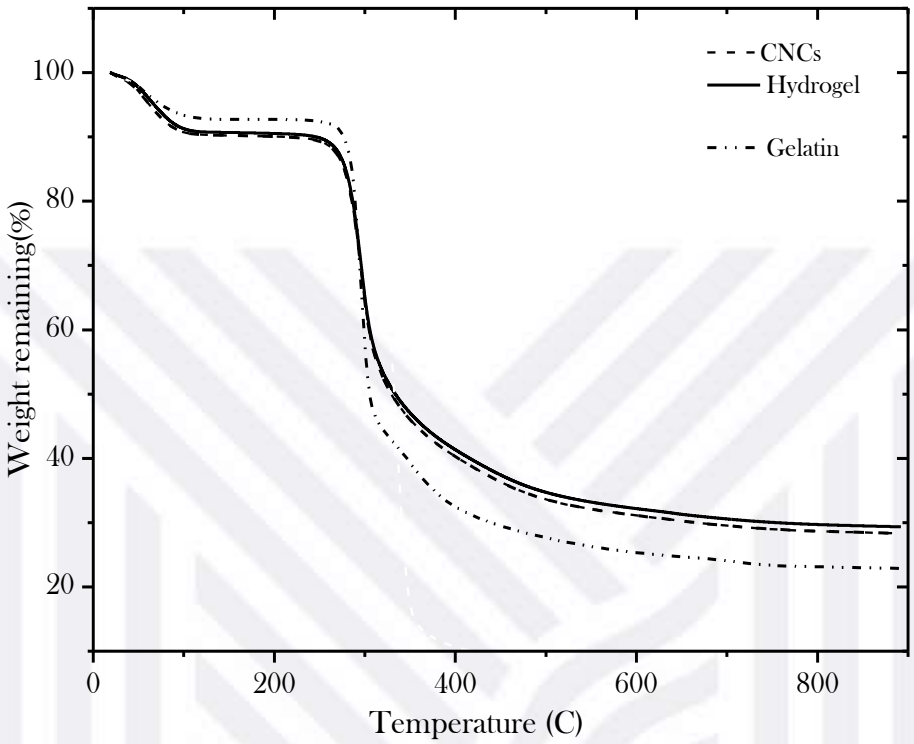

Figure 8.9: TGA curves CNCs, Gelatin, and Hydrogel

Figure 8.10 shows the XRD patterns of CNCs, gelatin, and hydrogel. At 2 theta 17°, 28°, and 40°, CNCs shows three distinct diffraction peaks, which are typically attributed to the (10), (100), and (200) planes of cellulose type I, respectively(Paulo *et al.*, 2019; Prado & Spinacé, 2019). The inter-helix distance of gelatin's triple helix is based on the peak at 2 theta 16°, and a broad diffraction peak at 27° is typical of the amorphous fraction of gelatin. These peaks are comparable to those seen in prior reports(Perumal *et al.*, 2019; Yao *et al.*, 2019). The peak at 2 theta 19° corresponding to the characteristic peak of gelatin and CNCs are identified in the XRD patterns of the hydrogel, and the peak at 2 theta 28° for gelatin may be overlapped with that of CNCs when gelatin is bonded onto the molecular chain of CNCs(Du *et al.*, 2019). The hydrogel results show that the original crystalline phase of CNCs was altered when it was linked with gelatin.

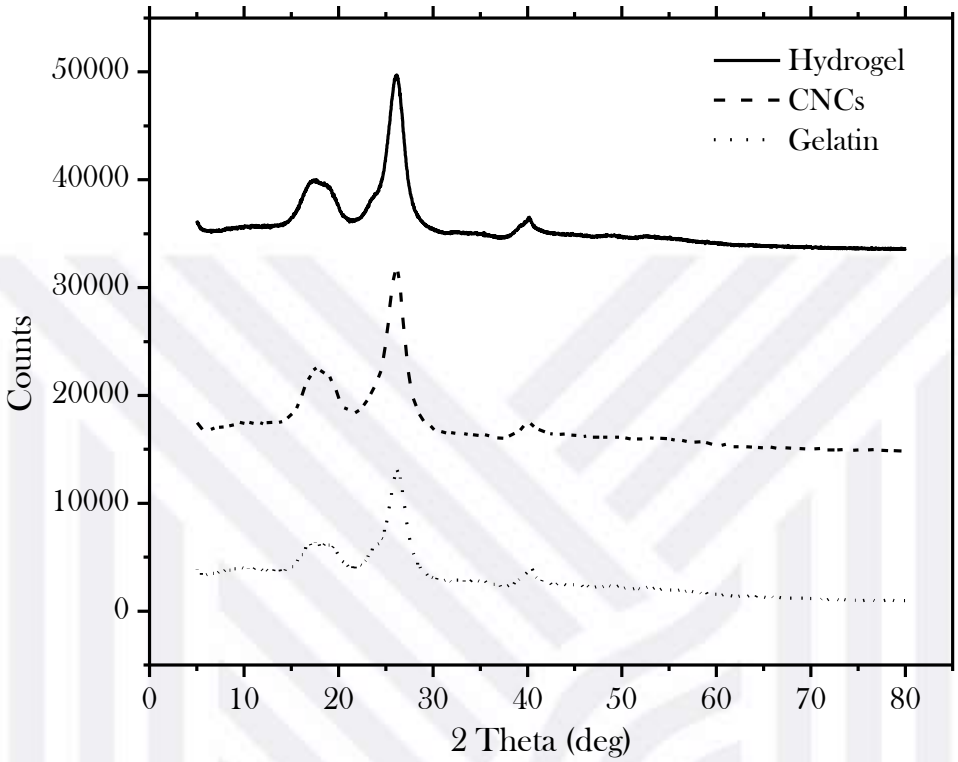

Figure 8.10: XRD patterns of CNCs, Gelatin, and Hydrogel

8.5. CONCLUSION

The packed bed column's technical feasibility for adsorption of Cu^{2+}, Ni^{2+}, $+Cd^{2+}$, and Zn^{2+} ions from its synthesized AMD by the hydrogel was evaluated. The hydrogel was considered to have the potential to interact very strongly with hazardous metal ions. This characteristic, together with the adsorbent's availability, cheap cost, and effective regeneration of the used adsorbent, sets it apart from numerous other adsorbents described in the literature by other researchers. The bed performed better at a bed height of 25 cm, an influent metal ion concentration of 10 mg/L, and a flow velocity of 10 mL/min. As a result, the packed bed experiment's breakthrough curve indicates that the breakthrough points were achieved sooner by raising the flow rate and influent concentration and later by increasing the bed height. The BDST, Yoon–Nelson, and Thomas model successfully explained the experimental data. The SEM, TGA, XRD, and FTIR findings for CNCs, gelatin and hydrogel were remarkable.

8.6 REFERENCES

Abdelraof, M., Hasanin, M.S., Farag, M.M., & Ahmed, H.Y. 2019. International Journal of Biological Macromolecules Green synthesis of bacterial cellulose / bioactive glass nanocomposites : Effect of glass nanoparticles on cellulose yield , biocompatibility and antimicrobial activity. *Int. J. Biol. Macromol.* 138:975–985.

Azad, H., Mohsennia, M., Cheng, C., & Amini, A. 2021. Facile fabrication of PVB-PVA blend polymer nanocomposite for simultaneous removal of heavy metal ions from aqueous solutions: Kinetic, equilibrium, reusability and adsorption mechanism. *J. Environ. Chem. Eng.* 9(5):106214.

Cheng, K., Huang, C., Wei, Y., & Hsu, S. 2019. Novel chitosan – cellulose nano fi ber self-healing hydrogels to correlate self-healing properties of hydrogels with neural regeneration effects. *NPG Asia Mater. Springer US*.

Danial, W.H., Abdul Majid, Z., Mohd Muhid, M.N., Triwahyono, S., Bakar, M.B., & Ramli, Z. 2015. The reuse of wastepaper for the extraction of cellulose nanocrystals. *Carbohydr. Polym.* 118:165–169.

Du, H., Liu, W., Zhang, M., Si, C., Zhang, X., & Li, B. 2019. Cellulose nanocrystals and cellulose nano fi brils based hydrogels for biomedical applications. *Carbohydr. Polym.* 209:130–144.

Fallah, N. & Taghizadeh, M. 2020. Continuous fixed-bed adsorption of Mo(VI) from aqueous solutions by Mo(VI)-IIP: Breakthrough curves analysis and mathematical modeling. *J. Environ. Chem. Eng.* 8(5):104079.

Fosso-kankeu, E. 2018. hybridized technique applied for AMD treatment. *Phys. Chem. Earth*. 105:170–176.

Gokmen, F.O., Yaman, E., & Temel, S. 2021. Eco-friendly polyacrylic acid based porous hydrogel for heavy metal ions adsorption: characterization, adsorption behavior, thermodynamic and reusability studies. *Microchem. J.* 168:106357.

Grishkewich, N., Mohammed, N., Tang, J., & Tam, K.C. 2017. Current Opinion in Colloid & Interface Science Recent advances in the application of cellulose nanocrystals. *Curr. Opin. Colloid Interface Sci.* 29:32–45.

Gu, L., Li, T., Song, X., Yang, X., Li, S., Chen, L., Liu, P., Gong, X., & Chen, C. 2020. Preparation and characterization of methacrylated gelatin / bacterial cellulose composite hydrogels for cartilage tissue engineering. 25:195–202.

Hernández-Hernández, L.E., Bonilla-Petriciolet, A., Mendoza-Castillo, D.I., & Reynel-Ávila, H.E. 2017. Antagonistic binary adsorption of heavy metals using stratified bone char columns. *J. Mol. Liq.* 241:334–346.

Igberase, E., Osifo, P., & Ofomaja, A. 2018. Mathematical modelling of Pb2+, Cu2+, Ni2+, Zn2+, Cr6+ and Cd2+ ions adsorption from a synthetic acid mine drainage onto chitosan derivative in a packed bed column. *Environ. Technol. (United Kingdom)*. 39(24):3203–3220.

Kabuba, J. & Banza, M. 2020. Results in Engineering Ion-exchange process for the removal of Ni (II) and Co (II) from wastewater using modi fi ed clinoptilolite : Modeling by

response surface methodology and arti fi cial neural network. *Results Eng.* 8:100189.

Kargarzadeh, H., Sheltami, R.M., Ahmad, I., Abdullah, I., & Dufresne, A. 2015. Cellulose nanocrystal : A promising toughening agent for unsaturated polyester nanocomposite. *Polymer (Guildf).* 56:346–357.

Khadhri, N., El, M., Saad, K., & Moussaoui, Y. 2019. Journal of Environmental Chemical Engineering Batch and continuous column adsorption of indigo carmine onto activated carbon derived from date palm petiole. *J. Environ. Chem. Eng.* 7(1):102775.

Lei, W., Zhou, X., Fang, C., Song, Y., & Li, Y. 2019. Eco-friendly waterborne polyurethane reinforced with cellulose nanocrystal from o ffi ce waste paper by two di ff erent methods. *Carbohydr. Polym.* 209:299–309.

Leudjo Taka, A., Klink, M.J., Yangkou Mbianda, X., & Naidoo, E.B. 2021. Chitosan nanocomposites for water treatment by fixed-bed continuous flow column adsorption: A review. *Carbohydr. Polym.* 255:117398.

Lin, J., Su, T., Chen, J., Xue, T., Yang, S., Guo, P., Lin, H., Wang, H., Hong, Y., Su, Y., Peng, L., & Li, J. 2021. Efficient adsorption removal of anionic dyes by an imidazolium-based mesoporous poly(ionic liquid) including the continuous column adsorption-desorption process. *Chemosphere*. 272:129640.

Mengesha, D.N., Appiah-Ntiamoah, R., & Kim, H. 2021. Azo-dye derived oxidized-nitrogen rich carbon sheets with high adsorption capability for dye effluent under both batch and continuous conditions. *Chemosphere*. 279:130463.

Nahrul Hayawin, Z., Ibrahim, M.F., Nor Faizah, J., Ropandi, M., Astimar, A.A., Noorshamsiana, A.W., & Abd-Aziz, S. 2020. Palm oil mill final discharge treatment by a continuous adsorption system using oil palm kernel shell activated carbon produced from two-in-one carbonization activation reactor system. *J. Water Process Eng.* 36:101262.

Nordin, A.H., Wong, S., Ngadi, N., Zainol, M.M., Aien, N., Abd, F., & Nabgan, W. 2021. Journal of Environmental Chemical Engineering Surface functionalization of cellulose with polyethyleneimine and magnetic nanoparticles for efficient removal of anionic dye in wastewater. *J. Environ. Chem. Eng.* 9(1):104639.

Paulo, J., Oliveira, D., Pinheiro, G., Lisie, S., Cleber, F., Renato, A., Dias, G., & Zavareze, R. 2019. International Journal of Biological Macromolecules Cellulose nanocrystals from rice and oat husks and their application in aerogels for food packaging. *Int. J. Biol. Macromol* 124:175–184.

Pawar, R.R., Lalhmunsiama, Bajaj, H.C., & Lee, S.M. 2016. Activated bentonite as a low-cost adsorbent for the removal of Cu(II) and Pb(II) from aqueous solutions: Batch and column studies. *J. Ind. Eng. Chem. The Korean Society of Industrial and Engineering Chemistry*. 34:213–223.

Pérez-morales, J.M. & Sánchez-galván, G.2019. Continuous dye adsorption and desorption on an invasive macrophyte (Salvinia minima). *Environmental Science and Pollution Research*. :5955–5970.

Perumal, S., Atchudan, R., Yoon, D.H., Joo, J., & Cheong, I.W. 2019. Spherical Chitosan/Gelatin Hydrogel Particles for Removal of Multiple Heavy Metal Ions from

Wastewater. *Ind. Eng. Chem. Res. American Chemical Society*. 58:9900–9907.

Prado, K.S. & Spinacé, M.A.S. 2019. International Journal of Biological Macromolecules Isolation and characterization of cellulose nanocrystals from pineapple crown waste and their potential uses. *Int. J. Biol. Macromol.* 122:410–416.

Raval, N.P., Shah, P.U., & Shah, N.K. 2016. Adsorptive removal of nickel(II) ions from aqueous environment: A review. *J. Environ. Manage.* 179:1–20.

Shojaeiarani, J., Bajwa, D., & Shirzadifar, A. 2019. A review on cellulose nanocrystals as promising biocompounds for the synthesis of nanocomposite hydrogels. *Carbohydr. Polym.* 216:247–259.

Teramoto, Y. 2019. Material development using the inherent features of nano-cellulose and nano-chitin : Necessity of simple processes and cross-disciplinary collaboration. *Adv. Powder Technol. The Society of Powder Technology Japan*. (xxxx).

Wu, Y., Fan, Y., Zhang, M., Ming, Z., Yang, S., & Arkin, A. 2016. Functionalized agricultural biomass as a low-cost adsorbent : Utilization of rice straw incorporated with amine groups for the adsorption of Cr (VI) and Ni (II) from single and binary systems. *Biochem. Eng. J.* 105:27–35.

Yang, J., Duan, J., & Bjo, L.Z. 2016. Spherical nanocomposite particles prepared from mixed cellulose – chitosan solutions. :3105–3115.

Yao, Y., Wang, H., Wang, R., & Chai, Y. 2019. International Journal of Biological Macromolecules Novel cellulose-gelatin composite fi lms made from self-dispersed microgels : Structure and properties. *Int. J. Biol. Macromol.* 123:991–1001.

CHAPTER NINE

Original contribution and recommendations for future studies

9.1 Original contribution

Developing sustainable wastewater treatment platforms based on eco-friendly and biodegradable nanomaterials and biopolymers can significantly reduce carbon emissions and secondary pollutants. According to several research, cellulose nanocrystals are attractive candidates for the adsorption of pollutants in wastewater. The difficulty in extracting CNCs after adsorption, however, restricts their utility in large-scale water treatment procedures. The introduction of CNCs into matrices with increased adsorption capacities is very desirable in this context. Furthermore, unmodified CNCs have low selectivity towards a wide range of water pollutants, therefore surface functionalization is required to provide this selectivity.

The following five key aims of this thesis have been defined in light of all of these significant factors: (a) the extraction of cellulose nanocrystals from millet husk waste and waste papers. (b) the development of green and biodegradable adsorbent such as nanocomposites and blend hydrogel. (c) batch adsorption tests were used to evaluate the adsorption properties of CNCs nanocomposites for selective removal of heavy metal ions and the blend hydrogels understanding of heavy metal ions adsorption behavior in a fixed bed column adsorption. (d) quantum mechanism, mechanistic , and kinetics study for adsorption. (e) modeling of adsorption process using response surface methodology, artificial neural network, and adaptive neuro-fuzzy inference system.

Development of CNCs nanocomposites

- cellulose nanocrystals been treated with succinic anhydride and EDTA.
- cellulose nanocrystals and chitosan.
- cellulose nanocrystals and starch.
- cellulose nanocrystals and sodium alginate.
- cellulose nanocrystals and gelatin.

Understanding the adsorption behavior of heavy metal ions removal by modified CNCs in batch and fixed bed column adsorption

The influence of various parameters such as contact time, adsorbent dosage, initial concentration, pH, and temperature on the dye adsorption characteristics of CNCs nanocomposites were determined. Adsorption kinetic data fitted well to pseudo-second-order kinetic model and intra-particle diffusion and elovich model were used to explain the mechanism of adsorption. The preferred adsorption sites were determined using the binding energy gaps HOMO-LUMO. absorption mechanism was described via four mechanistic models such as Film diffusion, Weber and Morris, Bangham, and Dummwald-Wagner models. CNCs nanocomposites were also found to be reusable more than 95% regeneration efficiency even after five adsorption cycles. The carboxylate functional group is primarily engaged in the coordination and selective removal of metal ions

The impact of several column operating factors on breakthrough curves, such as starting concentration, bed depth, and flow rate, was investigated. Breakthrough curves showed a sudden increase followed by a slow fall before increasing in concentration continuously until saturation was reached. The column operational parameters were discovered to influence this behaviour. To confirm that this was not an artifact due to the column design parameters, the existence of this phenomenon was verified by changing the flow direction, the diameter of the column and composition of adsorbent. It was determined that this, in fact, was not an artifact, but a property of the hydrogel themselves. The shrinkage of the bed over time was observed during the experiment. It was found that hydrogels undergo osmotic swelling followed by a charge shielding assisted shrinkage during the dye adsorption which affected the packing of the fixed bed resulting in the particular phenomenon observed in the breakthrough curve. It was found that this particular phenomenon assisted in improving the performance of the adsorbent, as lower void fraction meant more contact between the bulk fluid and adsorbent.

Adsorption is also dependent on several ionic parameters such as electronegativity, ionic radius, hydration radius, degree of hydration, and ionic strength in the aqueous phase. More electronegativity at the surface means more cation ion exchange, which improves adsorption. In addition, the degree of hydration and hydration radius affect the ion exchange process. Large ionic radius favors rapid saturation of adsorption sites due to

steric congestion on the surface. When ionic strength is increased, the distribution coefficients (Kd) decrease and the initial metal concentrations of metals rise, resulting in a reduction in the adsorption process.

Modeling adsorption with RSM, ANN and ANFIS

Because RSM provides a configuration and arrangement that provides useful information on the interaction between numerous process factors, ANFIS predicts more accurately than RSM. Nonetheless, the ANFIS model has far more modelling capability than the RSM model, and the optimal solution recorded by ANFIS was significantly superior to the one recorded by RSM. As a result, this research suggests that ANFIS be used to evaluate the influence of operating parameters on different lignocellulose materials and biogas yields produced during optimization.

9.2 Recommendations for future studies

In summary, the development and application of CNCs included nanocomposites for water treatment applications was the focus of this thesis. Based on the findings of the investigation, the following recommendations for further research are made. Because of the ionically crosslinked character of these nanocomposites, their practical usage in an aqueous environment with a high concentration of competing binding ions may be limited since competitive binding can cause COOH to be extracted from the matrix. However, following all of the experiments employing various concentrations heavy metal ions, no visible change in the nanocomposite stability was detected. As a result, more research may be done to develop superior nanocomposite for better performance in an aqueous environment with a larger concentration of competing binding ions.

a novel recyclable adsorbent based on CNCs and sodium alginate was developed and their adsorption characteristics for heavy metal ions was evaluated using batch adsorption studies. Preliminary experiments have shown a decrease in the heavy metal ions removal % with an increase in the salt concentration. This will restrict the application of CNCs-alginate in real wastewater samples which contains higher salt concentration. As a result, more design experiments should be conducted in order to change the properties of this adsorbent for application in this condition. Furthermore, efforts have been undertaken to enhance the loading of CNCs in the nanocomposite. Preliminary investigations have showed that greater loadings improve the capacity to absorb heavy metal ions. batch

adsorption investigations employing greater modified CNCs loadings can give insight on the optimum CNCs loading threshold limit for a nanocomposite with maximal adsorption capability.

The design consideration for the development of these new adsorbents can be made based on the type of pollutant needed to be removed. The application of pure and surface functionalized CNCs may be expanded further by creating new filtering platforms comprised of interchangeable CNC loaded cartridges. The CNCs contained in these cartridges may be tailored to the water pollutant to be eliminated. The adsorption features of CNCs integrated nanocomposites were thoroughly investigated as part of this PhD thesis study. These insights can be used to the field of controlled release. Some studies have already proven that CNCs are excellent candidates for molecule binding and controlled release. Modeling the control release characteristics of these nanocomposites can provide insight into the role of CNCs in molecule binding and controlled release. By functionalizing CNCs, it is possible to demonstrate that the controlled release and stimuli-responsive features of these nanocomposites may be enhanced.

The nanocomposites' stimuli-responsive nature is useful for the regulated release of agrochemicals. The pH of the soil environment can be exploited to activate agrochemical release from the nanocomposite. CNCs can be functionalized by grafting pH-responsive polymers such as poly(acrylic acid) onto their surfaces. The insertion of these functionalized CNCs will cause the pH of the nanocomposite to change. The grafted poly(acrylic acid) chains will also add more negative charges on the surface CNCs, which will improve binding and control of positively charged agrochemicals.

More algorithms such as Fletcher-Reeves conjugate gradient back-propagation, Powell-Beale conjugate gradient back-propagation, Scaled conjugate gradient back-propagation, BFGS quasi-Newton back-propagation, and One step secant back-propagation from ANN, factorial, D-optimal, and hybrid design from RSM, The hybrid algorithm such as forward pass (LSM) and a backward pass (GDM) from ANFIS need to be explored for accuracy and better prediction of the process.

APPENDICES

APPENDIX A : Cellulose nanocrystals modifications

Cellulose nanocrystals modified with succinic anhydride and ethylenediaminetetraacetic acid

Nanocomposite (cellulose nanocrystals and chitosan)

Blend Hydrogels (cellulose nanocrystals and starch)

Hydrogel (cellulose nanocrystals and gelatin)

Biodegradability studies on the cellulose nanocomposites

APPENDIX B : Results for selective removal of Cr (VI)

pH	Removal	qe	Time	Removal	qe	Concentration	Removal	qe
	(%)	(mg/g)	(min)	(%)	(mg/g)	(mg/L)	(%)	(mg/g)
2	75	260	0	63	205	0	97	0
3	77.5	265	100	90	260	100	97	100
4	90	275	200	92	265	200	95	175
5	97	280	300	95	270	300	90	250
6	97	280	400	95	270	400	80	300
8	97	280	500	95	270	500	75	325

Dosage	Removal	qe	Temperature	Removal	qe	Recycles	qe
(mg/L)	(%)	(mg/g)	K	(%)	(mg/g)		(mg/g)
0	45	450	293	90	255	1	257
5	80	300	298	92.5	256	2	256
10	85	200	303	94	257	3	254
15	90	120	308	95	257	4	251
20	92	100	312	95	258	5	225
25	92	100				6	220

APPENDIX C : Continuous fixed -bed column study

a) Effect of flow rate

Time Min	**C/Co** 10ml/min	**C/Co** 20ml/min	**C/Co** 30ml/min	**Time** Min	**C/Co** 10ml/min	**C/Co** 20ml/min	**C/Co** 30ml/min
0	0	0	0	0	0	0	0
40	0	0	0	40	0	0	0
80	0	0	0	80	0	0	0
100	0	0	0	100	0	0	0
140	0	0	0	140	0.03	0	0
190	0.02	0	0	190	0.1	0	0
200	0.05	0.01	0	200	0.2	0.03	0
240	0.2	0.01	0	240	0.6	0.1	0.01
280	0.4	0.01	0	280	0.8	0.23	0.02
300	0.6	0.02	0	300	0.84	0.39	0.03
320	0.7	0.05	0.01	320	0.9	0.57	0.07
360	0.85	0.2	0.01	360	0.93	0.78	0.16
390	0.91	0.4	0.04	390	0.95	0.87	0.4
400	0.94	0.6	0.1	400	0.96	0.9	0.5
440	0.96	0.8	0.3	440	0.97	0.92	0.7
480	0.98	0.9	0.57	480	0.98	0.95	0.85
500	0.98	0.93	0.76	500		0.97	0.9
520	0.98	0.95	0.82	520		0.98	0.95
540		0.98	0.9	540		0.98	0.96
580		0.99	0.92	580			0.97
600			0.93	600			0.98
620			0.93	620			0.98
640				640			
680				680			
700				700			
740				740			
780				780			
800				800			

Time Min	**C/Co** 10ml/min	**C/Co** 20ml/min	**C/Co** 30ml/min	**Time** Min	**C/Co** 10ml/min	**C/Co** 20ml/min	**C/Co** 30ml/min
0	0	0	0	0	0	0	0
40	0	0	0	40	0	0	0
80	0	0	0	80	0.1	0	0
100	0.02	0	0	100	0.2	0	0
140	0.07	0	0	140	0.5	0.1	0.03
190	0.15	0.02	0	190	0.78	0.3	0.08
200	0.2	0.07	0	200	0.85	0.4	0.1
240	0.64	0.2	0.01	240	0.95	0.7	0.2
280	0.85	0.4	0.03	280	0.98	0.85	0.4
300	0.9	0.6	0.1	300	0.99	0.9	0.6
320	0.93	0.8	0.2	320	1	0.95	0.7
360	0.97	0.9	0.4	360	1	0.96	0.8
390	0.98	0.93	0.7	390		0.99	0.85
400		0.95	0.8	400		1	0.9
440		0.96	0.87	440			0.95
480		0.97	0.9	480			0.96
500		0.98	0.94	500			0.97
520		0.99	0.95	520			0.98
540			0.96	540			0.99
580			0.97	580			0.99
600			0.98	600			0.99
620			0.99	620			
640				640			
680				680			
700				700			
740				740			
780				780			
800				800			

b)Effect of bed height

Time Min	**C/Co** 20g	**C/Co** 30g	**C/Co** 40g	**Time** Min	**C/Co** 20g	**C/Co** 30g	**C/Co** 40g
0	0	0	0	0	0	0	0
40	0	0	0	40	0	0	0
80	0	0	0	80	0	0	0
100	0	0	0	100	0	0	0
140	0.02	0	0	140	0	0	0
190	0.03	0	0	190	0.07	0	0
200	0.04	0	0	200	0.12	0	0
240	0.05	0	0.01	240	0.3	0	0
280	0.06	0	0.02	280	0.6	0	0.01
300	0.1	0	0.02	300	0.8	0.03	0.02
320	0.22	0	0.02	320	0.9	0.05	0.03
360	0.42	0	0.02	360	0.93	0.17	0.03
390	0.63	0.06	0.02	390	0.95	0.4	0.04
400	0.8	0.1	0.03	400	0.96	0.6	0.04
440	0.94	0.3	0.03	440	0.98	0.85	0.07
480	0.96	0.57	0.03	480		0.92	0.17
500	0.96	0.76	0.1	500		0.94	0.4
520	0.98	0.9	0.2	520		0.95	0.6
540	0.98	0.96	0.4	540			0.84
580		0.98	0.6	580			0.94
600		0.98	0.76	600			0.95
620		0.99	0.9	620			0.95
640			0.96	640			
680			0.97	680			
700			0.98	700			
740				740			
780				780			
800				800			

Time Min	**C/Co** 20g	**C/Co** 30g	**C/Co** 40g	**Time** Min	**C/Co** 20g	**C/Co** 30g	**C/Co** 40g
0	0	0	0	0	0		0
40	0	0	0	40	0		0
80	0	0	0	80	0		0
100	0	0	0	100	0	0	0
140	0.01	0	0	140	0.1	0.05	0
190	0.1	0	0	190	0.2	0.08	0.01
200	0.2	0	0	200	0.4	0.11	0.02
240	0.35	0.05	0	240	0.7	0.2	0.02
280	0.7	0.1	0	280	0.87	0.3	0.04
300	0.84	0.17	0	300	0.93	0.5	0.08
320	0.9	0.3	0.01	320	0.95	0.7	0.12
360	0.95	0.65	0.02	360	0.96	0.8	0.22
390	0.95	0.8	0.1	390	0.97	0.88	0.5
400	0.97	0.84	0.17	400	0.98	0.91	0.65
440	0.98	0.9	0.3	440	0.98	0.92	0.85
480	0.98	0.93	0.65	480	0.98	0.93	0.9
500		0.95	0.8	500		0.94	0.93
520		0.98	0.9	520		0.96	0.94
540			0.95	540			0.95
580			0.97	580			0.95
600			0.98	600			
620			0.99	620			
640				640			
680				680			
700				700			
740				740			
780				780			
800				800			

c)Effect of Concentration

Time Min	**C/Co** 10mg/L	**C/Co** 30mg/L	**C/Co** 50mg/L	**Time** Min	**C/Co** 10mg/L	**C/Co** 30mg/L	**C/Co** 50mg/L
0	0	0	0	0	0	0	0
40	0	0	0	40	0	0	0
80	0	0	0	80	0	0	0
100	0	0	0	100	0	0	0
140	0.02	0	0	140	0	0	0
190	0.03	0	0	190	0.07	0	0
200	0.04	0	0	200	0.12	0	0
240	0.05	0	0.01	240	0.3	0	0
280	0.06	0	0.02	280	0.6	0	0.01
300	0.1	0	0.02	300	0.8	0.03	0.02
320	0.22	0	0.02	320	0.9	0.05	0.03
360	0.42	0	0.02	360	0.93	0.17	0.03
390	0.63	0.06	0.02	390	0.95	0.4	0.04
400	0.8	0.1	0.03	400	0.96	0.6	0.04
440	0.94	0.3	0.03	440	0.98	0.85	0.07
480	0.96	0.57	0.03	480		0.92	0.17
500	0.96	0.76	0.1	500		0.94	0.4
520	0.98	0.9	0.2	520		0.95	0.6
540	0.98	0.96	0.4	540			0.84
580		0.98	0.6	580			0.94
600		0.98	0.76	600			0.95
620		0.99	0.9	620			0.95
640			0.96	640			
680			0.97	680			
700			0.98	700			
740				740			
780				780			
800				800			

Time Min	**C/Co** 10mg/L	**C/Co** 30mg/L	**C/Co** 50mg/L	**Time** Min	**C/Co** 10mg/L	**C/Co** 30mg/L	**C/Co** 50m/L
0	0	0	0	0	0		0
40	0	0	0	40	0		0
80	0	0	0	80	0		0
100	0	0	0	100	0	0	0
140	0.01	0	0	140	0.1	0.05	0
190	0.1	0	0	190	0.2	0.08	0.01
200	0.2	0	0	200	0.4	0.11	0.02
240	0.35	0.05	0	240	0.7	0.2	0.02
280	0.7	0.1	0	280	0.87	0.3	0.04
300	0.84	0.17	0	300	0.93	0.5	0.08
320	0.9	0.3	0.01	320	0.95	0.7	0.12
360	0.95	0.65	0.02	360	0.96	0.8	0.22
390	0.95	0.8	0.1	390	0.97	0.88	0.5
400	0.97	0.84	0.17	400	0.98	0.91	0.65
440	0.98	0.9	0.3	440	0.98	0.92	0.85
480	0.98	0.93	0.65	480	0.98	0.93	0.9
500		0.95	0.8	500		0.94	0.93
520		0.98	0.9	520		0.96	0.94
540			0.95	540			0.95
580			0.97	580			0.95
600			0.98	600			
620			0.99	620			
640				640			
680				680			
700				700			
740				740			
780				780			
800				800			

APPENDIX D: SEM results

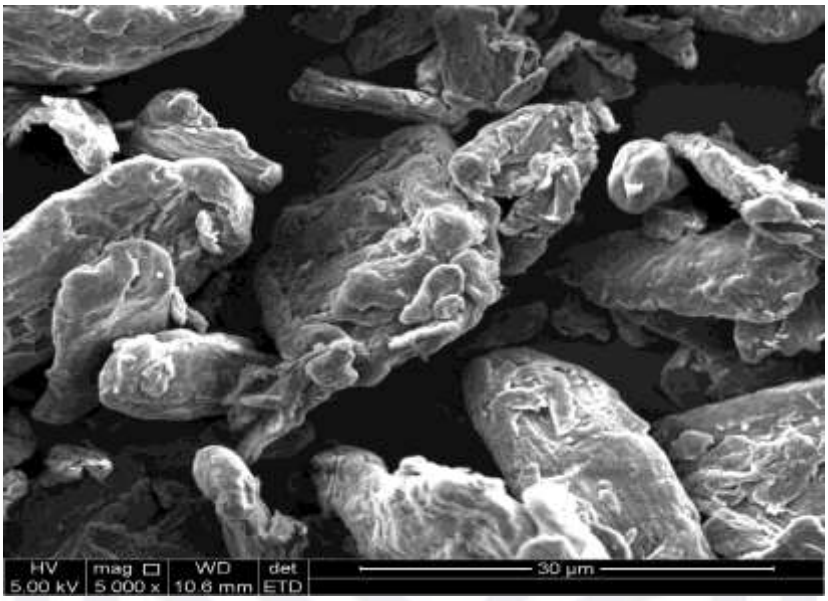

Cellulose nanocrystals

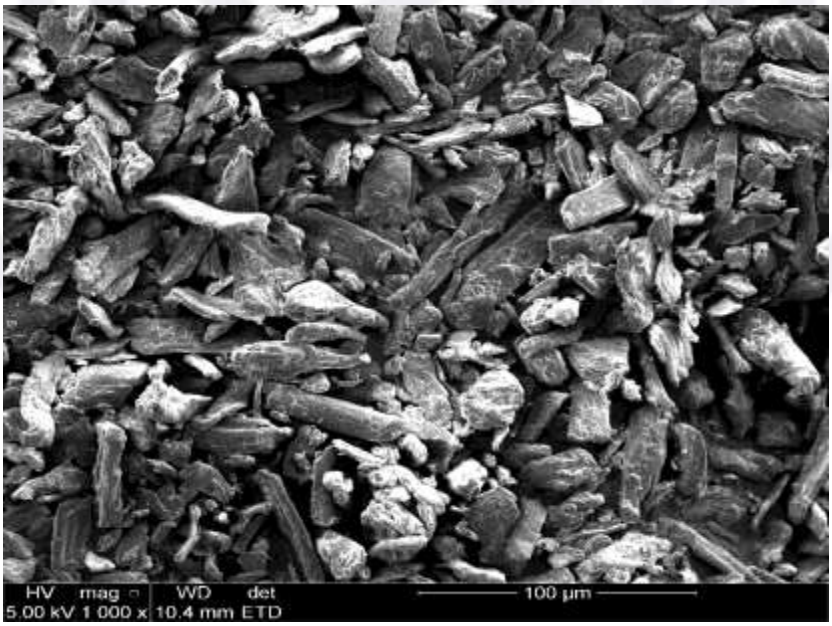

Starch

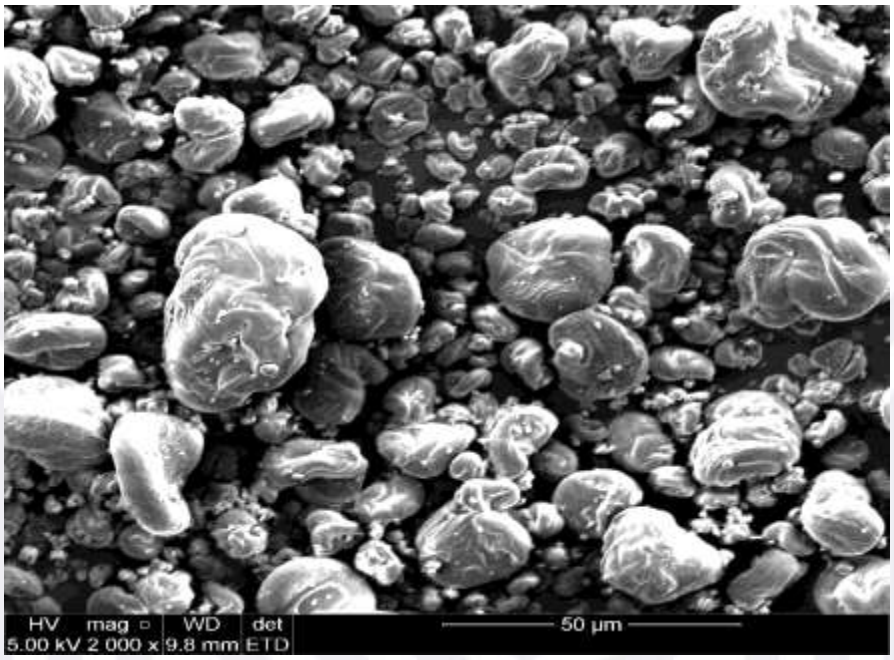

Chitosan

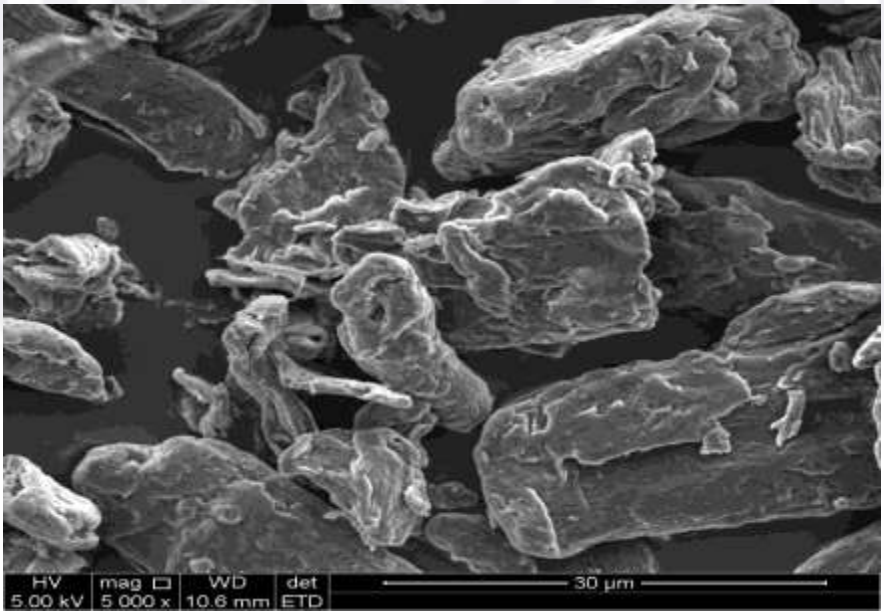

Gelatin